Saving seas by seeing ships *p. 1148*

Microbes against plastic pollution *pp. 1154 & 1196*

Timing is key in synergizing cancer treatments *p. 1204*

Science

$15
11 MARCH 2016
sciencemag.org

AAAS

SPECIAL ISSUE

FORENSICS

Evidence on trial p. 1128

CONTENTS

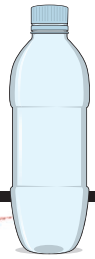

1154 & 1196

Soda bottles for dinner

11 MARCH 2016 • VOLUME 351 • ISSUE 6278

SPECIAL SECTION

Forensics

NEWS

1128 Evidence on trial
By M. Enserink

1130 Sizing up the evidence
By K. Servick

1133 When DNA is lying *By D. Starr*

1134 How hair can reveal a history
By H. Armitage and N. Rogers

1136 A trail of microbes
By K. Kupferschmidt

1138 Who dropped the bomb? *By R. Stone*

1140 Whose voice is that?
By N. Rogers

1141 Clues from the ashes
By L. Wade

1143 The microbial death clock
By K. Kupferschmidt

1144 The Bitcoin busts
By J. Bohannon

SEE ALSO

▸ PODCAST

ON THE COVER

Bullets fired from the same pistol by the Prince George's County Police Department, in Maryland, show similar but not identical markings—an example of the ambiguity that plagues much crime-scene evidence. The bullets were fired as part of a research effort to bring greater rigor to forensic analysis, conducted by the National Institute of Standards and Technology. See page 1128. For more on the process behind the cover image, see http://scim.ag/1LPKy4C. *Photo: Matthew Rakola*

NEWS

IN BRIEF

1120 News at a glance

IN DEPTH

1122 **MARS ORBITER TO SNIFF FOR METHANE**
Mission aims to settle whether gas exists—and whether it could hint at life
By E. Hand

1123 **EVIDENCE GROWS FOR ZIKA VIRUS AS PREGNANCY DANGER**
Lab experiments and new clinical data suggest that fast-spreading virus attacks developing brain *By G. Vogel*

1124 **IN SEARCH OF SPACETIME MEGAWAVES**
Timing in celestial radio beacons could reveal gravitational tsunamis *By D. Clery*

1126 **WHY HIGH 'GOOD CHOLESTEROL' CAN BE BAD NEWS**
A faulty transport system sometimes causes high HDL *By J. Couzin-Frankel*
▸ RESEARCH ARTICLE P. 1166

1127 **PLANS FOR NEW RESEARCH HUB GET CRITICAL RECEPTION**
Scientists welcome new money but worry about lack of transparency
By L. Margottini

INSIGHTS

PERSPECTIVES

1148 **ENDING HIDE AND SEEK AT SEA**
New technologies could revolutionize ocean observation *By D. J. McCauley* et al.

1150 **THE INVISIBLE DIMENSION OF FUNGAL DIVERSITY**
Can microbial taxa be defined from environmental molecular sequences?
By D. Hibbett

1152 **THE TIME IS RIGHT FOR MULTIPHOTON ENTANGLED STATES**
A chip-based microresonator enables time-bin entanglement *By A. C. Peacock and M. J. Steel*
▸ REPORT P. 1176

1153 **UNRAVELING A PATHWAY TO AUTISM**
A signaling pathway that controls protein synthesis may be a target for autism therapeutics *By J. P. H. Burbach*
▸ REPORT P. 1199; RESEARCH ARTICLE BY F. YI *ET AL.* 10.1126/science.aaf2669

1154 **FEEDING ON PLASTIC**
A bacterium completely degrades poly(ethylene terephthalate)
By U. T. Bornscheuer
▸ REPORT P. 1196

Downloaded from on March 10, 2016

Published by AAAS

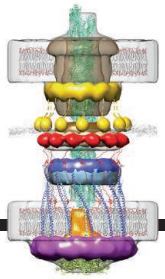

1165
Protein machines that move bacteria

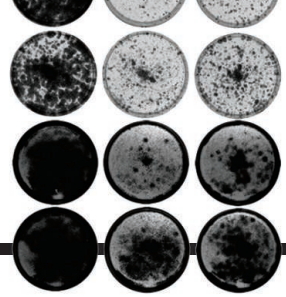

1208 & 1214
Metabolic rewiring in cancer cells

1156 TO SEE THE WORLD IN A GRAIN OF SPINS
A universal simulator is developed that can model the workings of any classical spin system *By S. Wehner*
▸ REPORT P. 1180

BOOKS *ET AL.*

1158 THE IMPORTANCE OF BEING LITTLE
By E. Christakis, reviewed by K. Hirsh-Pasek and R. M. Golinkof

1159 INSIDE GRADUATE ADMISSIONS
By J. R. Posselt, reviewed by S. Beilock

LETTERS

1160 STREAMLINING CHINA'S PROTECTED AREAS
By J. Li et al.

1160 SOCIAL COST OF CARBON: GLOBAL DUTY
By C. Guivarch et al.

1161 REFORMING CHINA'S SCIENCE AWARDS
By G. Qi et al.

1161 TECHNICAL COMMENT ABSTRACTS

RESEARCH

IN BRIEF

1162 From *Science* and other journals

RESEARCH ARTICLES

1165 BACTERIAL PILI
Architecture of the type IVa pilus machine *Y.-W. Chang* et al.
RESEARCH ARTICLE SUMMARY; FOR FULL TEXT: dx.doi.org/10.1126/science.aad2001

1166 HEART DISEASE
Rare variant in scavenger receptor BI raises HDL cholesterol and increases risk of coronary heart disease *P. Zanoni* et al.
▸ NEWS STORY P. 1126

1171 CHEMICAL PHYSICS
Wavelike charge density fluctuations and van der Waals interactions at the nanoscale *A. Ambrosetti* et al.

REPORTS

1176 QUANTUM OPTICS
Generation of multiphoton entangled quantum states by means of integrated frequency combs *C. Reimer* et al.
▸ PERSPECTIVE P. 1152

1180 SPIN MODELS
Simple universal models capture all classical spin physics *G. De las Cuevas and T. S. Cubitt*
▸ PERSPECTIVE P. 1156

1184 TOPOLOGICAL MATTER
Quasiparticle interference of the Fermi arcs and surface-bulk connectivity of a Weyl semimetal *H. Inoue* et al.

1188 ZEOLITES
Accelerated crystallization of zeolites via hydroxyl free radicals *G. Feng* et al.

1192 FUNGAL ENZYMES
Early-branching gut fungi possess a large, comprehensive array of biomass-degrading enzymes *K. V. Solomon* et al.

1196 BIODEGRADATION
A bacterium that degrades and assimilates poly(ethylene terephthalate) *S. Yoshida* et al.
▸ PERSPECTIVE P. 1154

1199 NEURODEVELOPMENT
CLK2 inhibition ameliorates autistic features associated with SHANK3 deficiency *M. Bidinosti* et al.
▸ PERSPECTIVE P. 1153; RESEARCH ARTICLE BY F. YI *ET AL.* 10.1126/science.aaf2669

1204 CANCER BIOLOGY
Schedule-dependent interaction between anticancer treatments *S. Chen* et al.

CANCER THERAPY

1208 Disordered methionine metabolism in MTAP/CDKN2A-deleted cancers leads to dependence on PRMT5 *K. J. Mavrakis* et al.

1214 *MTAP* deletion confers enhanced dependency on the PRMT5 arginine methyltransferase in cancer cells *G. V. Kryukov* et al.

1218 TRANSCRIPTION
Measurement of gene regulation in individual cells reveals rapid switching between promoter states *L. A. Sepúlveda* et al.

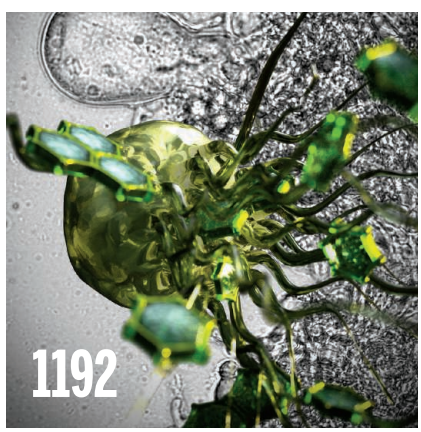

DEPARTMENTS

1117 EDITORIAL
Tackling toxics
By Arlene Blum

1119 EDITOR'S NOTE
PREview of new products
By Marcia McNutt

1230 WORKING LIFE
The water watchdog
By Rachel Bernstein

Science Staff 1114
New Products 1223
Science Careers 1224

IMAGE: (BOTTOM RIGHT) PETER ALLEN/UCSB

SCIENCE (ISSN 0036-8075) is published weekly on Friday, except the last week in December, by the American Association for the Advancement of Science, 1200 New York Avenue, NW, Washington, DC 20005. Periodicals mail postage (publication No. 484460) paid at Washington, DC, and additional mailing offices.

Copyright © 2016 by the American Association for the Advancement of Science. The title SCIENCE is a registered trademark of the AAAS.

Domestic individual membership and subscription (51 issues): $165 ($74 allocated to subscription). Domestic institutional subscription (51 issues): $1522; Foreign postage extra: Mexico, Caribbean (surface mail) $55; other countries (air assist delivery) $89. First class, airmail, student, and emeritus rates on request. Canadian rates with GST available upon request, GST #1254 88122. Publications Mail Agreement Number 1069624. **Printed in the U.S.A.**
Change of address: Allow 4 weeks, giving old and new addresses and 8-digit account number. **Postmaster:** Send change of address to AAAS, P.O. Box 96178, Washington, DC 20090–6178. **Single-copy sales:** $15.00 current issue, $20.00 back issue prepaid includes surface postage; bulk rates on request. **Authorization to photocopy** material for internal or personal use under circumstances not falling within the fair use provisions of the Copyright Act is granted by AAAS to libraries and other users registered with the Copyright Clearance Center (CCC) Transactional Reporting Service, provided that $35.00 per article is paid directly to CCC, 222 Rosewood Drive, Danvers, MA 01923. The identification code for *Science* is 0036-8075. *Science* is indexed in the *Reader's Guide to Periodical Literature* and in several specialized indexes.

Published by AAAS

Science
AAAS
1200 New York Avenue, NW, Washington, DC 20005
Bateman House, 82-88 Hills Road, Cambridge, UK CB2 1LQ

Editor-in-Chief Marcia McNutt
Executive Editor Monica M. Bradford **News Editor** Tim Appenzeller
Managing Editor, Research Journals Katrina L. Kelner
Deputy Editors Barbara R. Jasny, Andrew M. Sugden(UK), Valda J. Vinson, Jake S. Yeston

Research and Insights

SR. EDITORS Caroline Ash(UK), Gilbert J. Chin, Lisa D. Chong, Julia Fahrenkamp-Uppenbrink(UK), Pamela J. Hines, Stella M. Hurtley(UK), Paula A. Kiberstis, Marc S. Lavine(Canada), Kristen L. Mueller, Ian S. Osborne(UK), Beverly A. Purnell, L. Bryan Ray, Guy Riddihough, H. Jesse Smith, Jelena Stajic, Peter Stern(UK), Phillip D. Szuromi, Sacha Vignieri, Brad Wible, Nicholas S. Wigginton, Laura M. Zahn **ASSOCIATE EDITORS** Brent Grocholski, Keith T. Smith **ASSOCIATE BOOK REVIEW EDITOR** Valerie B. Thompson **ASSOCIATE LETTERS EDITOR** Jennifer Sills **CHIEF CONTENT PRODUCTION EDITOR** Cara Tate **SR. CONTENT PRODUCTION EDITORS** Harry Jach, Lauren Kmec **CONTENT PRODUCTION EDITORS** Jeffrey E. Cook, Chris Filiatreau, Cynthia Howe, Barbara P. Ordway, Catherine Wolner **SR. EDITORIAL COORDINATORS** Carolyn Kyle, Beverly Shields **EDITORIAL COORDINATORS** Joi S. Granger, Lisa Johnson, Anita Wynn **PUBLICATIONS ASSISTANTS** Aneera Dobbins, Jeffrey Hearn, Dona Mathieu, Le-Toya Mayne Flood, Shannon McMahon, Scott Miller, Caitlyn Phillips, Jerry Richardson, Rachel Roberts(UK), Alice Whaley(UK), Brian White **EXECUTIVE ASSISTANT** Anna Bashkirova **ADMINISTRATIVE SUPPORT** Janet Clements(UK), Lizanne Newton(UK), Maryrose Madrid, John Wood(UK)

News

NEWS MANAGING EDITOR John Travis **INTERNATIONAL EDITOR** Richard Stone **DEPUTY NEWS EDITORS** Daniel Clery(UK), Robert Coontz, Elizabeth Culotta, David Grimm, David Malakoff, Leslie Roberts **CONTRIBUING EDITOR** Martin Enserink(Europe) **SR. CORRESPONDENTS** Jeffrey Mervis, Elizabeth Pennisi **NEWS WRITERS** Adrian Cho, Jon Cohen, Jennifer Couzin-Frankel, Carolyn Gramling, Eric Hand, Jocelyn Kaiser, Catherine Matacic, Kelly Servick, Robert F. Service, Erik Stokstad(Cambridge, UK), Emily Underwood **INTERNS** Hanae Armitage, Patrick Monahan, Nala Rogers **CONTRIBUTING CORRESPONDENTS** Michael Balter(Paris), John Bohannon, Warren Cornwall, Ann Gibbons, Mara Hvistendahl, Sam Kean, Eli Kintisch, Kai Kupferschmidt(Berlin), Andrew Lawler, Christina Larson(Beijing), Mitch Leslie, Charles C. Mann, Eliot Marshall, Virginia Morell, Dennis Normile(Shanghai), Heather Pringle, Tania Rabesandratana(London), Gretchen Vogel(Berlin), Lizzie Wade(Mexico City) **CAREERS** Donisha Adams, Rachel Bernstein(Editor) **COPY EDITORS** Julia Cole, Dorie Chevlen, Jennifer Levin (Chief) **ADMINISTRATIVE SUPPORT** Jessica Adams

Executive Publisher Rush D. Holt
Interim Publisher Bill Moran **Chief Digital Media Officer** Rob Covey

BUSINESS OPERATIONS AND PORTFOLIO MANAGEMENT DIRECTOR Sarah Whalen **PRODUCT DEVELOPMENT DIRECTOR** Will Schweitzer **PRODUCT DEVELOPMENT ASSOCIATE** Hal Moore **BUSINESS SYSTEMS AND FINANCIAL ANALYSIS DIRECTOR** Randy Yi **MANAGER OF FULFILLMENT SYSTEMS** Neal Hawkins **SYSTEMS ANALYST** Nicole Mehmedovich **ASSISTANT DIRECTOR, BUSINESS OPERATIONS** Eric Knott **MANAGER, BUSINESS OPERATIONS** Jessica Tierney **SENIOR BUSINESS ANALYST** Cory Lipman **BUSINESS ANALYSTS** Sandy Kim, Meron Kebede **FINANCIAL ANALYST** Robert Clark **DIRECTOR, COPYRIGHTS LICENSING SPECIAL PROJECTS** Emilie David **PERMISSIONS ASSOCIATE** Elizabeth Sandler **RIGHTS, CONTRACTS, AND LICENSING ASSOCIATE** Lili Kiser

MARKETING DIRECTOR Elise Swinehart **ASSOCIATE DIRECTOR OF ACQUISITION AND RETENTION** Julianne Wielga **MARKETING ASSOCIATE** Elizabeth Sattler **SR. MARKETING EXECUTIVE** Jennifer Reeves **ASSOCIATE DIRECTOR, CREATIVE SERVICES** Tzeitel Sorrosa **ART ASSOCIATE** Seil Lee **JR. ART ASSOCIATE** Kim Huynh **ASSISTANT COMMERCIAL EDITOR** Selby Frame **MARKETING PROJECT MANAGER** Angelissa McArthur **PROGRAM DIRECTOR, AAAS MEMBER CENTRAL** Peggy Mihelich **FULFILLMENT SYSTEMS AND OPERATIONS** membership@aaas.org **MANAGER, MEMBER SERVICES** Pat Butler **SPECIALISTS** Terrance Morrison, Latasha Russell **MANAGER, DATA ENTRY** Mickie Napoleoni **DATA ENTRY SPECIALISTS** Brenden Aquilino, Fiona Giblin

PUBLISHER RELATIONS MANAGER Catherine Holland **PUBLISHER RELATIONS, EASTERN REGION** Keith Layson **PUBLISHER RELATIONS, WESTERN REGION** Ryan Rexroth **SALES RESEARCH COORDINATOR** Aiesha Marshall **MANAGER, SITE LICENSE OPERATIONS** Iquo Edim **SENIOR OPERATIONS ANALYST** Lana Guz **FULFILLMENT ANALYST** Judy Lillibridge **ASSOCIATE DIRECTOR, MARKETING** Christina Schlecht **MARKETING ASSOCIATE** Isa Sesay-Bah

WEB TECHNOLOGIES SR. DEVELOPER Chris Coleman **DEVELOPERS** Dan Berger, Jimmy Marks, Ryan Jensen **SR. PROJECT MANAGER** Trista Smith **PROJECT MANAGER** Nick Fletcher

DIGITAL MEDIA DIRECTOR OF ANALYTICS Enrique Gonzales **DIGITAL REPORTING ANALYST** Eric Hossinger **SR. WEB PRODUCER** Sarah Crespi **WEB PRODUCER** Alison Crawford **VIDEO PRODUCER** Nguyen Nguyen **SOCIAL MEDIA PRODUCER** Brice Russ

DIRECTOR OF OPERATIONS PRINT AND ONLINE Lizabeth Harman **DIGITAL/PRINT STRATEGY MANAGER** Jason Hillman **QUALITY TECHNICAL MANAGER** Marcus Spiegler **PROJECT ACCOUNT MANAGER** Tara Kelly **DIGITAL PRODUCTION MANAGER** Lisa Stanford **ASSISTANT MANAGER DIGITAL/PRINT** Rebecca Doshi **SENIOR CONTENT SPECIALISTS** Steve Forrester, Antoinette Hodal, Lori Murphy, Anthony Rosen **CONTENT SPECIALISTS** Jacob Hedrick, Kimberley Oster

DESIGN DIRECTOR Beth Rakouskas **DESIGN EDITOR** Marcy Atarod **SENIOR DESIGNER** Garvin Grullón **DESIGNER** Chrystal Smith **GRAPHICS MANAGING EDITOR** Alberto Cuadra **SENIOR SCIENTIFIC ILLUSTRATORS** Chris Bickel, Katharine Sutliff **SCIENTIFIC ILLUSTRATOR** Valerie Altounian **SENIOR ART ASSOCIATES** Holly Bishop, Nathalie Cary, Preston Huey **PHOTOGRAPHY MANAGING EDITOR** William Douthitt **PHOTO EDITORS** Leslie Blizard, Christy Steele

DIRECTOR, GLOBAL COLLABORATION, CUSTOM PUBLICATIONS, ADVERTISING Bill Moran **EDITOR, CUSTOM PUBLISHING** Sean Sanders: 202-326-6430 **ADVERTISING MARKETING MANAGER** Justin Sawyers: 202-326-7061 science_advertising@aaas.org **ADVERTISING SUPPORT MANAGER** Karen Foote: 202-326-6740 **ADVERTISING PRODUCTION OPERATIONS MANAGER** Deborah Tompkins **SR. PRODUCTION SPECIALIST/GRAPHIC DESIGNER** Amy Hardcastle **SR. TRAFFIC ASSOCIATE** Christine Hall **SALES COORDINATOR** Shirley Young **ASSOCIATE DIRECTOR, COLLABORATION, CUSTOM PUBLICATIONS/CHINA/TAIWAN/KOREA/SINGAPORE** Ruolei Wu: +86-186 0082 9345, rwu@aaas.org **COLLABORATION/CUSTOM PUBLICATIONS/JAPAN** Adarsh Sandhu + 81532-81-5142 asandhu@aaas.org **EAST COAST/E. CANADA** Laurie Faraday: 508-747-9395, FAX 617-507-8189 **WEST COAST/W. CANADA** Lynne Stickrod: 415-931-9782, FAX 415-520-6940 **MIDWEST** Jeffrey Dembski: 847-498-4520 x3005, Steven Loerch: 847-498-4520 x3006 **UK EUROPE/ASIA** Roger Goncalves: TEL/FAX +41 43 243 1358 **JAPAN** Katsuyoshi Fukamizu(Tokyo): +81-3-3219-5777 kfukamizu@aaas.org **CHINA/TAIWAN** Ruolei Wu: +86-186 0082 9345, rwu@aaas.org

WORLDWIDE ASSOCIATE DIRECTOR OF SCIENCE CAREERS Tracy Holmes: +44 (0) 1223 326525, FAX +44 (0) 1223 326532 tholmes@science-int.co.uk **CLASSIFIED** advertise@sciencecareers.org **U.S. SALES** Tina Burks: 202-326-6577, Nancy Toema: 202-326-6578 **EUROPE/ROW SALES** Sarah Lelarge **SALES ASSISTANT** Kelly Grace **JAPAN** Hiroyuki Mashiki(Kyoto): +81-75-823-1109 hmashiki@aaas.org **CHINA/TAIWAN** Ruolei Wu: +86-186 0082 9345 rwu@aaas.org **MARKETING MANAGER** Allison Pritchard **MARKETING ASSOCIATE** Aimee Aponte

AAAS BOARD OF DIRECTORS, CHAIR Geraldine L. Richmond **PRESIDENT** Barbara A. Schaal **PRESIDENT-ELECT** Susan Hockfield **TREASURER** David Evans Shaw **CHIEF EXECUTIVE OFFICER** Rush D. Holt **BOARD** Cynthia M. Beall, May R. Berenbaum, Carlos J. Bustamante, Stephen P.A. Fodor, Claire M. Fraser, Michael S. Gazzaniga, Laura H. Greene, Elizabeth Loftus, Mercedes Pascual

SUBSCRIPTION SERVICES For change of address, missing issues, new orders and renewals, and payment questions: 866-434-AAAS (2227) or 202-326-6417, FAX 202-842-1065. Mailing addresses: AAAS, P.O. Box 96178, Washington, DC 20090-6178 or AAAS Member Services, 1200 New York Avenue, NW, Washington, DC 20005

INSTITUTIONAL SITE LICENSES 202-326-6730 **REPRINTS:** Author Inquiries 800-635-7181 **COMMERCIAL INQUIRIES** 803-359-4578 **PERMISSIONS** 202-326-6765, permissions@aaas.org **AAAS Member Services** 202-326-6417 or http://membercentral.aaas.org/discounts

Science serves as a forum for discussion of important issues related to the advancement of science by publishing material on which a consensus has been reached as well as including the presentation of minority of conflicting points of view. Accordingly, all articles published in *Science*—including editorials, news and comment, and book reviews—are signed and reflect the individual views of the authors and not official points of view adopted by AAAS or the institutions with which the authors are affiliated.

INFORMATION FOR AUTHORS See pages 624 and 625 of the 5 February 2016 issue or access www.sciencemag.org/authors/science-information-authors

SENIOR EDITORIAL BOARD
Gary King, *Harvard University,* **Susan M. Rosenberg,** *Baylor College of Medicine,*
Ali Shilatifard, *Northwestern University Feinberg School of Medicine*

BOARD OF REVIEWING EDITORS (Statistics board members indicated with **(S)**

Adriano Aguzzi, *U. Hospital Zürich*
Takuzo Aida, *U. of Tokyo*
Leslie Aiello, *Wenner-Gren Foundation*
Judith Allen, *U. of Edinburgh*
Sonia Altizer, *U. of Georgia*
Sebastian Amigorena, *Institut Curie*
Kathryn Anderson, *Memorial Sloan-Kettering Cancer Center*
Meinrat O. Andreae, *Max-Planck Inst. Mainz*
Paola Arlotta, *Harvard U.*
Johan Auwerx, *EPFL*
David Awschalom, *U. of Chicago*
Clare Baker, *University of Cambridge*
Jordi Bascompte, *University of Zurich*
Facundo Batista, *London Research Inst.*
Ray H. Baughman, *U. of Texas, Dallas*
David Baum, *U. of Wisconsin*
Carlo Beenakker, *Leiden U.*
Kamran Behnia, *ESPCI-ParisTech*
Yasmine Belkaid, *NIAID, NIH*
Philip Benfey, *Duke U.*
May Berenbaum, *U. of Illinois*
Gabriele Bergers, *U. of California, San Francisco*
Bradley Bernstein, *Massachusettes General Hospital*
Peer Bork, *EMBL*
Bernard Bourdon, *Ecole Normale Supérieure de Lyon*
Chris Bowler, *École Normale Supérieure*
Ian Boyd, *U. of St. Andrews*
Emily Brodsky, *U. of California, Santa Cruz*
Ron Brookmeyer, *U. of California Los Angeles* **(S)**
Christian Büchel, *U. Hamburg-Eppendorf*
Joseph A. Burns, *Cornell U.*
Carter Tribley Butts, *U. of California, Irvine*
Gyorgy Buzsaki, *New York U. School of Medicine*
Blanche Capel, *Duke U.*
Mats Carlsson, *U. of Oslo*
Ib Chorkendorff, *U. of Denmark*
David Clapham, *Children's Hospital Boston*
Joel Cohen, *Rockefeller U., Columbia U.*
James J. Collins, *MIT*
Robert Cook-Deegan, *Duke U.*
Lisa Coussens, *Oregon Health & Science U.*
Alan Cowman, *Walter & Eliza Hall Inst.*
Robert H. Crabtree, *Yale U.*
Roberta Croce, *Vrije Universiteit*
Janet Currie, *Princeton U.*
Jeff L. Dangl, *U. of North Carolina*
Tom Daniel, *U. of Washington*
Frans de Waal, *Emory U.*
Stanislas Dehaene, *Collège de France*
Robert Desimone, *MIT*
Claude Desplan, *New York U.*
Dennis Discher, *U. of Pennsylvania*
Gerald W. Dorn II, *Washington U. School of Medicine*
Jennifer A. Doudna, *U. of California, Berkeley*
Bruce Dunn, *U. of California, Los Angeles*
William Dunphy, *Caltech*
Christopher Dye, *WHO*
Todd Ehlers, *U. of Tuebingen*
David Ehrhardt, *Carnegie Inst. of Washington*
Tim Elston, *U. of North Carolina at Chapel Hill*
Gerhard Ertl, *Fritz-Haber-Institut, Berlin*
Barry Everitt, *U. of Cambridge*
Ernst Fehr, *U. of Zurich*
Anne C. Ferguson-Smith, *U. of Cambridge*
Michael Feuer, *The George Washington U.*
Toren Finkel, *NHLBI, NIH*
Kate Fitzgerald, *U. of Massachusetts*
Peter Fratzl, *Max-Planck Inst.*
Elaine Fuchs, *Rockefeller U.*
Daniel Geschwind, *UCLA*
Karl-Heinz Glassmeier, *TU Braunschweig*
Ramon Gonzalez, *Rice U.*
Julia R. Greer, *Caltech*
Elizabeth Grove, *U. of Chicago*
Nicolas Gruber, *ETH Zurich*
Kip Guy, *St. Jude's Children's Research Hospital*
Taekjip Ha, *U. of Illinois at Urbana-Champaign*
Christian Haass, *Ludwig Maximilians U.*
Michael Hasselmo, *Boston U.*
Martin Heimann, *Max-Planck Inst. Jena*
Yka Helariutta, *U. of Cambridge*
James A. Hendler, *Rensselaer Polytechnic Inst.*
Janet G. Hering, *Swiss Fed. Inst. of Aquatic Science & Technology*
Kai-Uwe Hinrichs, *U. of Bremen*
David Hodell, *U. of Cambridge*
David Holden, *Imperial College*
Lora Hooper, *UT Southwestern Medical Ctr. at Dallas*
Tamas Horvath, *Yale University*
Raymond Huey, *U. of Washington*
Fred Hughson, *Princeton U.*
Auke Ijspeert, *EPFL Lausanne*
Stephen Jackson, *USGS and U. of Arizona*
Steven Jacobsen, *U. of California, Los Angeles*
Kai Johnsson, *EPFL Lausanne*
Peter Jonas, *Inst. of Science & Technology (IST) Austria*
Matt Kaeberlein, *U. of Washington*
William Kaelin Jr., *Dana-Farber Cancer Inst.*
Daniel Kahne, *Harvard U.*
Daniel Kammen, *U. of California, Berkeley*
Abby Kavner, *U. of California, Los Angeles*
Masashi Kawasaki, *U. of Tokyo*
V. Narry Kim, *Seoul National U.*
Joel Kingsolver, *U. of North Carolina at Chapel Hill*
Robert Kingston, *Harvard Medical School*
Etienne Koechlin, *Ecole Normale Suprieure*
Alexander Kolodkin, *Johns Hopkins U.*
Thomas Langer, *U. of Cologne*
Mitchell A. Lazar, *U. of Pennsylvania*
David Lazer, *Harvard U.*
Thomas Lecuit, *IBDM*
Virginia Lee, *U. of Pennsylvania*
Stanley Lemon, *U. of North Carolina at Chapel Hill*
Ottoline Leyser, *Cambridge U.*
Wendell Lim, *U.C. San Francisco*
Marcia C. Linn, *U. of California, Berkeley*
Jianguo Liu, *Michigan State U.*
Luis Liz-Marzan, *CIC biomaGUNE*
Jonathan Losos, *Harvard U.*
Ke Lu, *Chinese Acad. of Sciences*
Christian Lüscher, *U. of Geneva*
Laura Machesky, *CRUK Beatson Inst. for Cancer Research*
Anne Magurran, *U. of St. Andrews*
Oscar Marin, *CSIC & U. Miguel Hernández*
Charles Marshall, *U. of California, Berkeley*
C. Robertson McClung, *Dartmouth College*
Graham Medley, *U. of Warwick*
Tom Misteli, *NCI*
Yasushi Miyashita, *U. of Tokyo*
Mary Ann Moran, *U. of Georgia*
Richard Morris, *U. of Edinburgh*
Alison Motsinger-Reif, *NC State U.* **(S)**
Thomas Murray, *The Hastings Center*
Daniel Neumark, *U. of California, Berkeley*
Kitty Nijmeijer, *U. of Twente*
Pär Nordlund, *Karolinska Inst.*
Helga Nowotny, *European Research Advisory Board*
Ben Olken, *MIT*
Joe Orenstein, *U. of California Berkeley & Lawrence Berkeley National Lab*
Harry Orr, *U. of Minnesota*
Pilar Ossorio, *U. of Wisconsin*
Andrew Oswald, *U. of Warwick*
Steve Palumbi, *Stanford U.*
Jane Parker, *Max-Planck Inst. of Plant Breeding Research*
Giovanni Parmigiani, *Dana-Farber Cancer Inst.* **(S)**
John H. J. Petrini, *Memorial Sloan-Kettering Cancer Center*
Samuel Pfaff, *Salk Institute for Biological Studies*
Joshua Plotkin, *U. of Pennsylvania*
Albert Polman, *FOM Institute AMOLF*
Philippe Poulin, *CNRS*
Jonathan Pritchard, *Stanford U.*
David Randall, *Colorado State U.*
Felix Rey, *Institut Pasteur*
Trevor Robbins, *U. of Cambridge*
Jim Roberts, *Fred Hutchinson Cancer Research Ctr.*
Barbara A. Romanowicz, *U. of California,Berkeley*
Amy Rosenzweig, *Northwestern University*
Mike Ryan, *U. of Texas, Austin*
Mitinori Saitou, *Kyoto U.*
Shimon Sakaguchi, *Kyoto U.*
Miquel Salmeron, *Lawrence Berkeley National Lab*
Jürgen Sandkühler, *Medical U. of Vienna*
Alexander Schier, *Harvard U.*
Vladimir Shalaev, *Purdue U.*
Robert Siliciano, *Johns Hopkins School of Medicine*
Denis Simon, *Arizona State U.*
Uri Simonsohn, *U. of Pennsylvania*
Alison Smith, *John Innes Centre*
Richard Smith, *U. of North Carolina* **(S)**
John Speakman, *U. of Aberdeen*
Allan C. Spradling, *Carnegie Institution of Washington*
Jonathan Sprent, *Garvan Inst. of Medical Research*
Eric Steig, *U. of Washington*
Paula Stephan, *Georgia State U. and National Bureau of Economic Research*
Molly Stevens, *Imperial College London*
V. S. Subrahmanian, *U. of Maryland*
Ira Tabas, *Columbia U.*
Sarah Teichmann, *Cambridge U.*
John Thomas, *North Carolina State U.*
Shubha Tole, *Tata Institute of Fundamental Research*
Christopher Tyler-Smith, *The Wellcome Trust Sanger Inst.*
Herbert Virgin, *Washington U.*
Bert Vogelstein, *Johns Hopkins U.*
Cynthia Volkert, *U. of Göttingen*
David Wallach, *Weizmann Inst. of Science*
Ian Walmsley, *U. of Oxford*
Jane-Ling Wang, *U. of California, Davis* **(S)**
David A. Wardle, *Swedish U. of Agric. Sciences*
David Waxman, *Fudan U.*
Jonathan Weissman, *U. of California, San Francisco*
Chris Wikle, *U. of Missouri* **(S)**
Ian A. Wilson, *The Scripps Res. Inst.* **(S)**
Timothy D. Wilson, *U. of Virginia*
Rosemary Wyse, *Johns Hopkins U.*
Jan Zaanen, *Leiden U.*
Kenneth Zaret, *U. of Pennsylvania School of Medicine*
Jonathan Zehr, *U. of California, Santa Cruz*
Len Zon, *Children's Hospital Boston*
Maria Zuber, *MIT*

BOOK REVIEW BOARD
David Bloom, *Harvard U.,* **Samuel Bowring,** *MIT,* **Angela Creager,** *Princeton U.,*
Richard Shweder, *U. of Chicago,* **Ed Wasserman,** *DuPont*

EDITORIAL

Tackling toxics

Most Americans believe that if a chemical is in their cosmetics, their coat, or their couch, someone is making sure it's safe for their health. In reality, little toxicity information or regulation is required for 80,000 industrial chemicals used in commerce in the United States. To address this, legislation to update the ineffective 1976 Toxic Substance Control Act (TSCA) is currently moving through Congress. The hope is that it will lead to improved regulation of chemicals, but the extent and timeliness of the reform are not certain. In the meantime, the widespread use of harmful chemicals continues to pose a threat to our health and environment.

In 1977, Bruce Ames and I published a report that a flame retardant in children's pajamas called "brominated Tris" was a mutagen and potential carcinogen. Three months later, it was banned from children's pajamas, only to be replaced by "chlorinated Tris." We determined that this too was a mutagen, and it was removed from pajamas. Such regrettable substitution of a harmful chemical with a less-studied cousin is like "a game of whack-a-mole," according to Donald Kennedy (former editor-in-chief of *Science* and former commissioner of the U.S. Food and Drug Administration).* Unfortunately, highly fluorinated chemicals are now getting the regrettable substitution treatment. These chemicals provide stain and water repellency in outdoor clothing, nonstick cookware, furniture, carpet, cosmetics, and food contact paper. However, they are highly mobile, have no known degradation pathways in the environment, and can persist indefinitely.

"Do we need this chemical, given the potential for harm?"

Perfluorooctanoic acid, commonly called C8, has an estimated half-life of 2.3 years or more in humans and is associated with cancer, elevated serum cholesterol levels, and other health problems. C8 was phased out of consumer products in the United States last year, a half-century after toxicologists first revealed its potential for harm. It was replaced with numerous perfluorohexanoic acid (C6) compounds that are more rapidly excreted by humans but also show extreme environmental persistence. Are these replacements safe? There is limited research thus far on the toxicity of the C6 alternatives. However, they are increasing in the environment and in human blood, and they share the potential toxicity of their C8 relatives.

One solution to the regrettable substitution problem is to address entire families or classes containing toxic chemicals rather than tackling them one at a time. For example, the Green Science Policy Institute, an organization of scientists that promotes the responsible use of chemicals, has called for a 50% reduction over the next 5 years in the use of six families of chemicals in consumer products, whose studied members have been found to be harmful: highly fluorinated chemicals, antimicrobials, flame retardants, bisphenols and phthalates, organic solvents, and certain metals.† Before using such substances in products, we should ask "Do we need this chemical, given the potential for harm?"

The good news is that companies are starting to act: Kaiser Permanente, IKEA, Levi Strauss & Co., and Crate and Barrel are phasing out highly fluorinated and other chemical classes of concern from the products they buy, produce, and/or sell.

Scientists can contribute by evaluating health and environmental impacts across a chemical's life cycle and looking for safer alternatives. They can make policy recommendations and collaborate on consensus documents. In 2015, 230 scientists from 40 countries signed the Madrid Statement,‡ expressing concern regarding the persistence and toxicity of both the highly fluorinated C8 chemicals and the C6 alternatives. Scientists can catalyze dialogue and action among manufacturers, retailers, and large purchasers and have an immediate impact in reducing the use of harmful chemicals.

Such actions by the scientific community can, along with meaningful TSCA reform, improve the health of the population and the environment. Most important of all, it will make our planet healthier and safer for future generations.

– Arlene Blum

Arlene Blum is founder and executive director of the Green Science Policy Institute, Berkeley, CA. E-mail: arlene@GreenSciencePolicy.org

*D. Kennedy, *Science* **318**, 1217 (2007). †http://greensciencepolicy.org/topics/six-classes/.
‡A. Blum *et al.*, *Environ. Health Perspect.* **5**, A108 (2015).

10.1126/science.aaf5468

PHOTOS: (INSET) FRED FROESE/ISTOCKPHOTO; (TOP) JOHN KOKOSCA

Downloaded from on March 10, 2016

Published by AAAS

EDITOR'S NOTE

PREview of new products

Marcia McNutt is Editor-in-Chief, Science *Journals*

This week, the *Science* family of journals launches some new and important initiatives. The first is that when authors visit the manuscript submittal portal for *Science*, *Science Translational Medicine*, and *Science Signaling*, they will notice an additional choice: *Science Immunology*. The newest member of the *Science* family is open for submissions!

Under the leadership of Editor Dr. Angela Colmone, who formerly handled the immunology content for *Science Translational Medicine*, *Science Immunology* aims to drive discovery and illuminate function across the ever-expanding field of immunology. The journal welcomes contributions involving research in all organisms and model systems, including humans, and particularly encourages articles on cancer immunology. Although interested in traditional models, the journal encourages nontraditional approaches as well. An Editorial Advisory Board is led by Dr. Abul Abbas from the University of California, San Francisco, and Dr. Federica Sallusto, Università della Svizzera Italiana, Switzerland. The Federation of Clinical Immunology Societies will be affiliated with *Science Immunology* to provide advice on journal direction. Journal policies will follow those of the other *Science* family journals. *Science Immunology*'s first articles will appear online in midsummer 2016, and for a trial period they will be freely available to all.

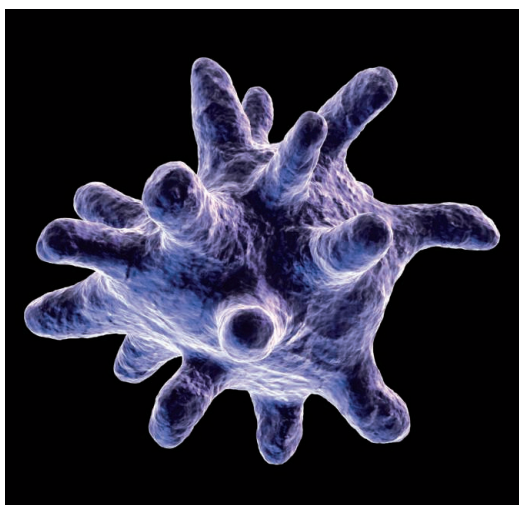

"...Science Immunology *aims to drive discovery... across the ever-expanding field of immunology.*"

Alert readers will notice another major change this week—the addition of the Peer Review Evaluation (PRE) badge displayed on papers published by the *Science* family of journals, retroactive to 1 January 2016. Many scientists have been disheartened by reports of journals failing in peer review, or authors committing fraud through the use of peer-review rings to get published without critical scrutiny. These examples raise the question: "Whom can you trust?" PRE seeks to uphold the standards of peer review by placing more transparency on the process. The digital PRE badge permits the reader to view how many reviewers saw the paper, how many rounds of review it received, how many editors were involved in the decision, and journal-specific items such as whether a statistical expert reviewed the paper. The icon also provides links to more standard information such as the journal's peer-review policies and the relevant industry initiatives that the journal supports. Use of PRE is a sign that a journal is committed to quality and transparency in peer review. In addition to the *Science* family of journals, PRE is available on journals published by the American Diabetes Association and *The Journal of Bone & Joint Surgery*.*

At the same time as the *Science* family of journals is implementing PRE, we are also asking the first and corresponding authors to provide Open Researcher and Contributor IDs (ORCIDs) when they submit their revised papers through the submittal portal. ORCIDs are free, easy to use, and fast to obtain,† and are rapidly becoming an international standard for uniquely identifying authors, thus removing confusion that can arise with common author names, when authors change their names, and when authors change institutions and/or are inconsistent about publishing with or without initials. Use of ORCIDs also means that authors get credit for citations consistently.

The new responsive website for the *Science* family of journals reflects a design that is faster and better suited for smartphones and tablets. There is now a consistent look and feel between the various journals, making navigation between them easier. As our digital content continues to grow, the new website is truly an ideal venue for the scientific community to relay discoveries, commentaries, news, and beyond to our global audience.

– Marcia McNutt

*See www.pre-val.org for more information or contact PRE@aaas.org. †http://orcid.org

10.1126/science.aaf6194

PHOTOS: (INSET) ISTOCKPHOTO; (TOP) STACEY PENTLAND PHOTOGRAPHY

Downloaded from on March 10, 2016

Published by AAAS

NEWS

> “Even good journals slip up. What makes them good journals is how they deal w/ slip-ups. I hope @PLOSONE learns & improves from #Creatorgate”
>
> **@Neuro_Skeptic**, about a paper retracted last week that cited “the Creator” in a study of hand movement. The authors, all Chinese, blame a mistranslation.

IN BRIEF

Brazil starts work on Antarctic station

Artist’s conception of the new station on King George Island, at the tip of the Antarctic Peninsula.

Four years after its only year-round Antarctic research station went up in flames, Brazil has started work on a new $100 million scientific stronghold in the southernmost continent. The previous station had been in operation for 30 years until a fire gutted 70% of it; in the aftermath, the government installed 45 emergency operational modules to keep Brazilian science in Antarctica afloat. The new base, expected to be completed in 2018, will share the same location and name—Comandante Ferraz—as the previous station. It has a sleek futuristic design, with 17 laboratories and accommodations for about 65 people. But scientists worry that a looming funding squeeze will crimp research by the time the station is up and running. Glaciologist Jefferson Simões, coordinator of the National Institute of Science and Technology for the Cryosphere in Porto Alegre, hopes the new station won’t become an “empty house.” The last time the federal government issued a call for research in Antarctica was in 2013, and that pot of money is expected to dry up in the next 6 months, he says. “That’s the big question now: What are we going to do after October, when the money runs out?” http://scim.ag/BrazilAnt

AROUND THE WORLD

China to invest more in science

BEIJING | China will invest heavily in science and technology over the next 5 years, and will cut red tape hampering science spending in the hope that innovation will help the country weather its economic slowdown. Speaking on 5 March at the National People’s Congress, Chinese Premier Li Keqiang gave an overview of the country’s vision for economic development, part of its new 5-year plan for 2016 to 2020. The plan boosts science spending by 9.1% in 2016 to 271 billion yuan ($41 billion); by 2020, it says, R&D investment will account for 2.5% of gross domestic product, compared with 2.05% in 2014. The plan also reduces bureaucratic barriers for scientists, improves environmental protection while curbing carbon emissions and other pollutants, and cites a long list of national priorities, including building national science centers and space programs and expanding high-speed rail. However, the plan offers few concrete details on how such measures will be implemented or funded.
http://scim.ag/Chinabudget

EPA nixes pesticide’s approval

WASHINGTON, D.C. | The Environmental Protection Agency (EPA) has announced its intent to cancel its conditional approval of flubendiamide, an insecticide used on more than 200 U.S. crops under several brand names, including Synapse. EPA

Approval was canceled because the pesticide could harm aquatic life, EPA says.

PHOTOS: (TOP TO BOTTOM) BRAZILIAN NAVY; © MICHAEL DWYER/ALAMY STOCK PHOTO

Downloaded from on March 10, 2016

Published by AAAS

granted Bayer CropScience conditional approval to sell the pesticide in 2008, pending further studies. It now says that the product breaks down into a more harmful chemical that can persist in the deep sections of freshwater streams and lakes, threatening benthic creatures. The company says EPA is relying on "overly conservative and unrealistic theoretical modeling" without real-world proof of harm, and has challenged the cancellation. While the two sides wait for an administrative hearing Bayer can continue to sell the chemical. Environmental groups and industry are closely watching the case, because flubendiamide is one of thousands of pesticides that have gained a green light while studies are pending, but the first for which EPA has pulled its approval.

Proper use of the p-value

ALEXANDRIA, VIRGINIA | In science's ongoing reproducibility crisis, misuse of the "p-value"—with 0.05 often considered a magical threshold for "statistical significance"—is particularly reviled. The American Statistical Association weighed in this week by releasing "six principles" on how to interpret p-values, marking the first time the organization has taken an official position on the matter. The principles were derived from more than a year of discussion by a consensus committee made up of 26 statistical experts. Among the new pro-tips: A p-value smaller than 0.05 doesn't necessarily mean that your hypothesis is true. And it doesn't say whether the results are due to chance alone, as is commonly believed. Also, the size of a p-value doesn't tell you anything about the significance of a result; even if the hypothesized effect is real, the effect could be so small it's barely worth publishing.

FINDINGS

Mosquitoes overwinter in D.C.

The mosquito *Aedes aegypti* is a major vector for transmitting certain diseases, including dengue, chikungunya, and Zika. It has been in the United States for some 375 years, but its presence has been thought to be seasonal in states such as Maryland and Virginia, given its low tolerance for cold. However, a recent study, which examined the genotypes of 70 larval and adult *A. aegypti* mosquitoes collected each summer in Washington, D.C., from 2011 through 2014, suggests that a small population of *A. aegypti* mosquitoes are year-round residents of the city. The mosquitoes likely survived the winters by inhabiting humanmade underground spaces, the team reports in *The American Journal of Tropical Medicine and Hygiene*.

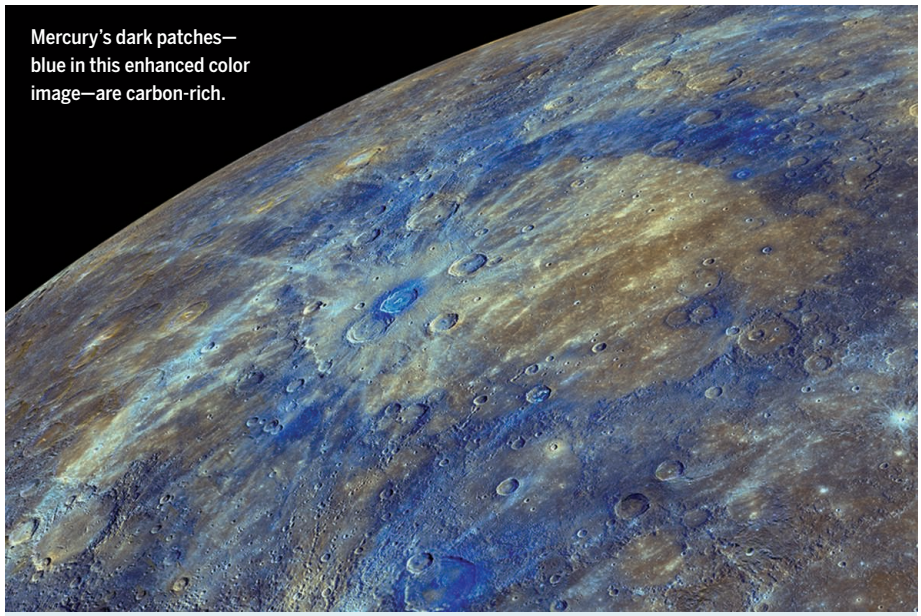

Mercury's dark patches—blue in this enhanced color image—are carbon-rich.

PHOTO: NASA/JOHNS HOPKINS UNIVERSITY APPLIED PHYSICS LABORATORY/CARNEGIE INSTITUTION OF WASHINGTON

Mercury is covered in pencil lead

Mercury is darker than the moon—although the innermost planet lacks the iron that gives the moon its dark patches. Instead, Mercury's darkening agent is carbon, in the form of graphite (known to schoolchildren as pencil lead), scientists reported this week in *Nature Geoscience*. Using NASA's MESSENGER orbiter, they found evidence for a few percent of carbon—a much higher fraction than is typically found on Earth, the moon, and Mars. The observations came from the last days of the MESSENGER mission, just before it crashed into the surface in 2015, when the spacecraft got up close and personal to large craters (shown) where the darkening agent is most prevalent. The craters expose remnants of Mercury's original, 4.5-billion-year-old crust, which formed as the planet solidified from a ball of molten magma. Most minerals crystallizing out of the magma ocean would sink, but graphite would have floated to the top.

NEWSMAKERS

Three Qs

Scott Halstead, 86, is one of the world's foremost authorities on mosquito-borne viruses, including dengue and chikungunya. *Science* spoke with Halstead, an investigator at the Uniformed Services University of the Health Sciences in Bethesda, Maryland, about the likely fate of the Zika virus. **http://scim.ag/HalsteadZika**

Q: Zika, chikungunya, and yellow fever seem to disappear for years and then return. Why?
A: The nature of these zoonotic diseases is that they involve primates. If you dug into it you'd probably find it has something to do with the weather and the fruiting of trees and the monkey populations. Herd immunity in humans must be very important, too, and population size. The herd immunity [threshold] for dengue, chikungunya, and Zika is about 80%; when 80% of the population is immune, transmission is being blocked four out of five times. That one out of five times is not enough to keep the disease going.

Q: How long is chikungunya going to stay around? Zika?
A: Five years, max. The only model I have is India. I watched when chikungunya went from Africa to India in 1963 and it disappeared from India in about 5 years. Zika's the same.

Q: By the time there's a Zika vaccine, you're suggesting Brazil's population may be largely immune.
A: Based on the observations that I've made and that anybody can see with their own eyes if they look at the data, this virus is just going to burn itself out. There's only a need for a vaccine in the acute emergency.

Published by AAAS

PLANETARY SCIENCE

Mars orbiter to sniff for methane

Mission aims to settle whether gas exists—and whether it could hint at life

By **Eric Hand**

For more than a decade, Mars scientists have chased a will-o'-the-wisp: methane. On Earth, the gas is made mostly by microbes, and detecting it on Mars could mean the planet once hosted, or still hosts, similar life. But glimpses of martian methane have been elusive—and perhaps illusive. Next week, Europe and Russia plan to launch an orbiter that could help resolve the mystery—not only by verifying the presence of the gas, but by tracing its sources, sinks, and seasonal variations.

The European Space Agency's (ESA's) Trace Gas Orbiter (TGO), scheduled to lift off from Baikonur, Kazakhstan, as early as 14 March and arrive at Mars in October, carries spectrometers with unprecedented sensitivity to methane and other trace gases. Besides settling the methane question, the TGO is aiming for another first: a Mars landing by a country other than the United States. A small lander called Schiaparelli is along for the ride; if all goes as planned, it will touch down on the Meridiani Planum, a dark, smooth plain girding the planet's belly. Scientifically, the lander will do little more than take weather measurements for a few days. But, if successful, Schiaparelli will blaze a path for a planned ESA rover in 2018.

The search for Mars methane began in 2004, when researchers announced that Mars Express, ESA's first Mars orbiter, had detected methane in concentrations as high as 10 parts per billion (ppb). Two other detection claims soon followed, from groups using Earth-based telescopes.

The reports pointed to a current or very recent methane source, because ultraviolet (UV) light destroys the molecules within several hundred years. And the shifting, evanescent plumes suggested that the methane was emerging in concentrated bursts, and was somehow immune to winds that should mix the methane evenly across the planet in a matter of days. Living organisms aren't the only possible source. Methane could also come from subsurface chemical reactions between rock and water, or the breakdown of organic matter contained in dust and micrometeorites that pelt the planet.

The arrival of NASA's Curiosity rover in 2012 added to the mystery. Two years ago, the rover team measured a spike of 7 ppb, lasting a couple of months. But since then, concentrations have settled into a faint background of 0.5 ppb, with little variation.

Many researchers were skeptical of the early measurements (*Science*, 22 June 2012, p. 1500), saying that Mars Express lacked the resolution to clearly see methane, and that ground-based astronomers faced too daunting a task in subtracting Earth's atmospheric methane to reveal Mars's. And the puzzling results from Curiosity haven't settled anything, says Ann Carine Vandaele of the Royal Belgian Institute for Space Aeronomy in Brussels. "They clearly demonstrate that we do not understand anything about methane on Mars," she says.

Vandaele hopes that the TGO, which is expected to operate through 2022, will help. The orbiter will rely on two spectrometers—a Belgian instrument called NOMAD and a Russian one called ACS—that can detect methane concentrations as low as 20 parts per trillion. Their extreme sensitivity comes from an ability to stare into the sun. Looking across the limb of the planet, the sensors will watch as the sun rises and sets through the thin atmosphere. The bright backlighting should make the absorption lines associated with methane stand out sharply. Providing the atmosphere is dust-free, the measurements should reach almost all the way down to the surface, where methane concentrations would be the highest.

Both instruments can also stare straight down and look for methane absorption lines in light reflected off the surface. This

Plumbing the martian atmosphere

Instruments on the Mars Trace Gas Orbiter will look for faint whiffs of methane in two directions. In limb mode, the sun is used as a backlight, and the methane signal stands out sharply. In nadir mode, reflected light off the surface offers better spatial resolution but the methane signal is weaker.

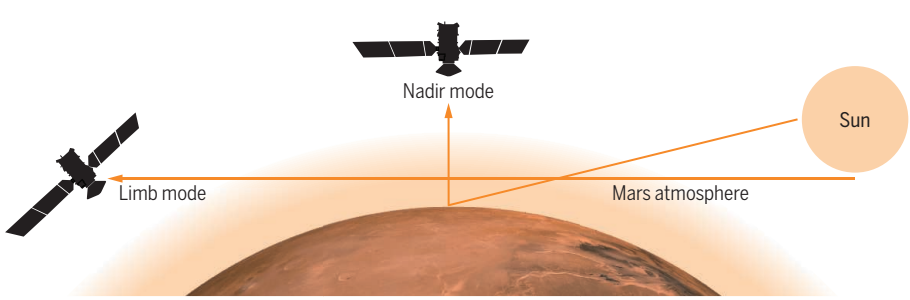

CREDITS: (IMAGE) ESA/ATG MEDIALAB; (DIAGRAM) NASA

Downloaded from on March 10, 2016

Published by AAAS

Artist's conception of the European Space Agency's Trace Gas Orbiter above Mars.

will allow high-resolution mapping, which could be key to spotting methane seeps, if they exist. But the mapping mode's sensitivity is relatively low; Vandaele expects that the look-down observations won't detect concentrations below 11 ppb. "That's a big problem," says Chris Webster, the leader of Curiosity's methane detection instrument at the Jet Propulsion Laboratory in Pasadena, California, because it means the TGO won't be able to map methane if it remains at or below the levels detected by the rover. On the other hand, Webster says the TGO team should be able to convert the limb mode observations into lower-resolution maps.

Methane is not the TGO's only quarry. It will also search for sulfur-bearing compounds, a signal of volcanism that, if found in conjunction with methane, could imply that the methane has a geological rather than a biological origin. Both spectrometers will monitor how carbon dioxide and water vapor move through the atmosphere, and ACS will measure temperature. Those observations will help fine-tune martian climate models, says TGO project scientist Håkan Svedhem in Noordwijk, the Netherlands, making them "more precise and more useful for predictions."

The TGO is part of a two-mission, €1.2 billion program called ExoMars, which was originally supposed to be run jointly with the United States. But NASA pulled out in 2012 because of budget troubles. ESA turned to Russia, which in return for placing scientific instruments aboard the spacecraft offered two Proton rocket launches, the first for the TGO and the second, scheduled for 2018, for a rover that will drill into the subsurface and look for life.

The Schiaparelli lander is key to that plan, because it will test many of the technologies needed to land the rover, including a parachute and radar altimeter. Schiaparelli is scheduled to detach from the TGO 3 days before it enters Mars's orbit. Then, on 19 October, the lander will plummet for 6 minutes through the thin atmosphere, slowed by the usual but always hair-raising methods of parachute and retrorocket. A camera will snap a picture 10 seconds or so before touchdown, and as the lander strikes the surface at 10 kilometers per hour, an underbelly of honeycombed aluminum will crumple, cushioning the blow.

How confident is Thierry Blancquaert, Schiaparelli manager at the European Space Research and Technology Centre in Noordwijk, that the lander will arrive safely? "I don't have a number," he says. "I would say 'likely' or 'very likely.'" ■

PHOTO: © PERCIO CAMPOS/EPA/CORBIS

INFECTIOUS DISEASE

Evidence grows for Zika virus as pregnancy danger

Lab experiments and new clinical data suggest that fast-spreading virus attacks developing brain

By **Gretchen Vogel**

Since late last year, when doctors in Brazil warned that a wave of serious birth defects might be linked to a little-known virus called Zika, researchers have struggled to pin down the link. Some in the media have questioned whether the reported increase in birth defects is real; others, particularly environmental activists, have suggested the virus is an innocent bystander, unfairly blamed for defects caused by chemicals or other factors. With three studies published last week, chances that the virus has been wrongly accused are fading.

Two independent groups showed that, at least in the lab, the virus eagerly infects developing brain cells, suggesting a mechanism by which it could cause the most striking of the observed birth defects: microcephaly, in which babies are born with abnormally small heads and brains. The work "is going to be very important," says Madeline Lancaster, who studies human brain development at the Medical Research Council Laboratory of Molecular Biology in Cambridge, U.K. The results "are quite consistent with what you're seeing in the babies with microcephaly."

A third study, following several dozen pregnant women in Brazil who had become infected with Zika virus, directly links the infection to an increase in brain defects. It also suggests that the virus can harm a developing fetus in other ways, possibly by attacking the placenta and slowing down the supply of nutrients. "These are the data we have been waiting for," says Daniel Lucey, an expert on global health at Georgetown University in Washington, D.C.

Zika virus, named after a forest in Uganda where it was first isolated decades ago, usually causes only mild symptoms in people, including fever and rash. But the virus's spread across northeastern Brazil last year coincided with a striking increase in microcephaly (*Science*, 8 January, p. 110), and many of the mothers reported having had symptoms consistent with Zika infection earlier in their pregnancies. Researchers have also identified the virus in amniotic fluid of pregnant women whose fetuses were diagnosed with microcephaly, in the brain tissue of a fetus with the disorder, and in the placentas of women infected during their pregnancy. Still, it has been difficult to prove a link to the birth defects, in part because blood tests for Zika virus are only accurate for about a week after infection.

Brazil saw a sudden increase in babies born with microcephaly after the Zika virus spread there last year.

To gauge the virus's possible effects on the developing brain, researchers in one of the new studies coaxed induced pluripotent stem (iPS) cells to grow into immature brain cells called human cortical neural progenitor cells. (iPS cells are adult cells that have been reprogrammed into stem cells that can grow into most of the tissues in the body.) They then exposed the neural progenitor cells to a lab strain of Zika virus. Three days later, 85% of the

Downloaded from on March 10, 2016

Published by AAAS

cells in the culture dishes were infected, neuroscientists Hongjun Song and Guo-li Ming at Johns Hopkins University in Baltimore, Maryland; virologist Hengli Tang at Florida State University in Tallahassee; and their colleagues reported on 4 March in *Cell Stem Cell*. In contrast, when the virus was applied to other kinds of cells—including fetal kidney cells, embryonic stem cells, and undifferentiated iPS cells—it infected fewer than 10% of the cells by day 3.

The virus hijacked the neural progenitor cells, Song says, using their machinery to replicate itself and spread quickly to new cells. The infected cells grew more slowly and had abnormal cell division cycles, which could also contribute to microcephaly, the team reported.

In a separate set of experiments, researchers found similar impacts on two other lab models of developing brain tissue. In a preprint posted online in *PeerJ* on 2 March, neuroscientist Patricia Garcez and stem cell researcher Stevens Rehen at the D'Or Institute for Research and Education in Rio de Janeiro, Brazil, report growing human iPS cells into clusters of neural stem cells called neurospheres, as well as into 3D organoids that resemble a miniature developing human brain. Infections with Zika virus (isolated from a Brazilian patient) killed most of the neurospheres and left the few survivors small and misshapen. Infected organoids grew to less than half their normal size.

> *"The news isn't just bad. It's terrible."*
>
> **Daniel Lucey**, Georgetown University

Lancaster says the fate of the lab-grown cells mirrored what was seen in earlier studies of organoids derived from stem cells that carried gene mutations linked to microcephaly. "You have two very different causes of microcephaly, but you see something very similar happening: a depletion of neural stem cells, and that would lead to fewer neurons" in the developing brain, she says.

The first published clinical data from infected pregnant women suggest that microcephaly is not the only type of damage the virus can cause. In an ongoing study, researchers at the Oswaldo Cruz Foundation in Rio de Janeiro have been enrolling pregnant women who develop a rash. Of the first 88 women, 72 tested positive for Zika virus, the team reported on 4 March in *The New England Journal of Medicine*.

Although none of the fetuses of the 16 women who tested negative for Zika have shown any abnormalities on ultrasound examinations, 12 of the 42 infected women who agreed to receive additional ultrasounds developed complications. Five had fetuses with abnormal brain growth, and one baby was born with microcephaly and eye problems. Several other fetuses were small for their developmental age. Two whose mothers were infected late in pregnancy were stillborn. Other issues included a lack of amniotic fluid and eye problems that may indicate blindness. This range of problems suggests that risks for pregnant women could be broader than doctors have realized, says Karin Nielsen of the University of California, Los Angeles, who helped coordinate the study with colleagues from the Oswaldo Cruz Foundation. In particular, she says, Zika infections late in pregnancy seem able to attack the placenta, producing damage that can kill an otherwise healthy fetus. Nielsen proposes a new name for the suite of symptoms: Zika virus congenital syndrome.

Still, many scientists suspect that Zika has accomplices that exacerbates its effects. Both Garcez's and Song's teams are now repeating their experiments with other viruses, including dengue, a relative of the Zika virus that is prevalent in the same regions. Previous exposure to other related viruses—even the vaccine for yellow fever—might also affect how Zika infection affects pregnant women and their babies. Genetic factors may also play a role.

Even if other factors contribute to the prenatal damage, the new findings are sobering news for countries across the Americas where Zika has spread in the last half-year: They are bracing for their own waves of birth defects. Colombia has seen its first Zika-related cases of microcephaly in recent weeks. "The news isn't just bad," Lucey says. "It's terrible."

Public health officials are rushing to respond to the threat and identify questions that need answering. The World Health Organization (WHO) convened a meeting last week in Washington, D.C., to outline Zika virus research priorities. That was followed this week by a WHO meeting in Geneva, Switzerland to discuss how to spur companies to develop better diagnostic tests, a vaccine, and ways to control the mosquitoes that spread the virus.

At the Geneva meeting, WHO physician Bruce Aylward, who the agency has tapped to lead its responses to major new outbreaks, noted that in February WHO declared an international public health emergency based on just the possibility of an association between Zika virus and microcephaly. Although WHO isn't ready to formally declare the virus guilty, he said, "a lot has happened since then. The data are all moving in one direction." ■

GRAVITATIONAL WAVES

In search of spacetime megawaves

Timing in celestial radio beacons could reveal gravitational tsunamis

By **Daniel Clery**

Last month, the detection of gravitational waves from merging black holes made headlines and tweetstorms around the world. But a hunt for much bigger game was already afoot.

The black holes responsible for last month's discovery weighed a few dozen times as much as our sun. Black holes millions or billions that massive, however, lurk at the centers of most galaxies—and they merge, too. Spotting the ensuing gravitational tsunamis takes an entirely different kind of detector from the Laser Interferometer Gravitational-Wave Observatory (LIGO), the Earth-based device that triumphed last month—one that stretches to the stars.

Three teams of radio astronomers are watching the heavens for hints of these megawaves, and their latest results suggest that increasing sensitivity could lead to a detection sometime in the next decade. "Eventually we will detect something," says Michael Kramer, director of the Max Planck Institute for Radio Astronomy in Bonn, Germany. "It's like peering through fog. We'll clear the smokescreen in time."

Astronomers think that over the history of the universe, galaxies have grown by consuming smaller galaxies or merging with their neighbors. When that happens, the supermassive black holes at their centers wind up orbiting each other, just like the pair of black holes LIGO detected. Because such dark behemoths move much more slowly, they produce long, loping gravitational waves. Whereas LIGO detected waves thousands of kilometers long, supermassive black holes would throw off waves measured in light-years.

To detect these much longer waves requires a much bigger detector. LIGO measured differences in the length of its two 4-kilometer arms caused by a passing gravitational wave. For waves from a supermassive binary, observers need "arms" hundreds of light-years long.

Downloaded from on March 10, 2016

Published by AAAS

They get them from highly magnetized, spinning neutron stars called pulsars. Pulsars pulse because they emit very powerful beams of electromagnetic radiation that sweep around like lighthouse beams. Observers on Earth see a flash of radiation once per rotation, at intervals so regular that pulsars can serve as highly accurate cosmic clocks. A passing gravitational wave, by stretching and squeezing space between Earth and the pulsars, should change the pulses' travel time—and cause the clocks to waver.

Three groups formed to exploit this promise in the mid-2000s, using the largest radio telescopes on three continents, including Australia's 64-meter Parkes radio telescope and the 500-meter telescope in Arecibo, Puerto Rico. But despite all that telescopic firepower, none of the efforts has yet sensed a ripple. "We would have expected to see them by now," Kramer says.

One challenge: Only about 50 of the most metronomic pulsars—"millisecond pulsars" that rotate hundreds of times per second—are suitable for the gravitational wave search. And even those "are not all equally good," says Alberto Sesana of the University of Birmingham in the United Kingdom. "Our sensitivity is dominated by a handful of good ones."

To improve accuracy, the three teams agreed to pool their data in a collaboration dubbed the International Pulsar Timing Array (IPTA), which has just released its first analysis, from a batch of data collected up until 2013. In a paper posted on the arXiv.org preprint server in February, IPTA researchers reported that their measurements are sensitive to a "strain" of 1.7×10^{-15}. In real terms, that means they can tell whether the distance to a distant pulsar changes by less than 100 meters per light-year of distance. "That is two times better than the individual data sets that went into it," Sesana says. Some models of supermassive black hole binaries predicted that gravitational waves would be detected at that level of sensitivity, but the IPTA analysis saw nothing.

Australia's Parkes telescope can see some of the most regular pulsars in the sky, so it sets the tightest limits on gravitational waves.

While IPTA was processing the combined data, individual teams forged ahead to produce better results with more up-to-date data. The North American group, called NANOGrav, set a limit of 1.5×10^{-15}, and Australia's Parkes Pulsar Timing Array (PPTA) got it down to 1.0×10^{-15}. Kramer and Sesana, who are both part of the European Pulsar Timing Array as well as IPTA, predict that speedier data processing will eventually make IPTA's results more competitive. "IPTA is more than the sum of the individual arrays," Kramer says.

Yet the fact that all of these efforts have come up empty-handed has some researchers talking about widening the search. The PPTA team, which monitors a few of the best pulsars and so sets the tightest limits (*Science*, 25 September 2015, p. 1522), says one possible explanation for the lack of wave sightings is that friction from surrounding gas and stars may cause supermassive binaries to merge more quickly than theorists had estimated. In that case, searches should focus on shorter waves, which would require more frequent observations. "We've started a dedicated timing program of our best pulsar at Parkes, timing it more frequently, for longer integrations in the short wavelength band. We hope that these observations lead to the first hint of a gravitational wave background," says Ryan Shannon of Curtin University, Perth, in Australia.

The NANOGrav team, in contrast, says in a paper published in February in *The Astrophysical Journal* that the key to success lies in monitoring a larger array of pulsars so that researchers can correlate results from many pulsar pairs. "A small array of the most accurate pulsars can place phenomenal constraints on the background, but is not well equipped for detection," says Stephen Taylor of NASA's Jet Propulsion Laboratory in Pasadena, California. The team estimates this approach has an 80% chance of detecting gravitational waves in the next 10 years.

New and better observatories will be key, because they can discover more pulsars and make more regular and more accurate timing measurements. Several are on the horizon, including MeerKAT in South Africa, a precursor to the Square Kilometer Array (SKA); the 500-meter Aperture Spherical Telescope (FAST) in China; and the SKA itself, which will begin observing in the early 2020s. "Everyone is looking forward to the SKA," Sesana says. "It will really provide a huge leap in sensitivity." ■

How to catch a gravitational wave: teamwork and timing

Astronomers hope to detect the very long, faint gravitational waves from binary supermassive black holes by monitoring the timing of distant pulsars. The measurements require lots of time on the biggest radio telescopes in the world. Three teams in Europe, Australia, and North America are engaged in the chase.

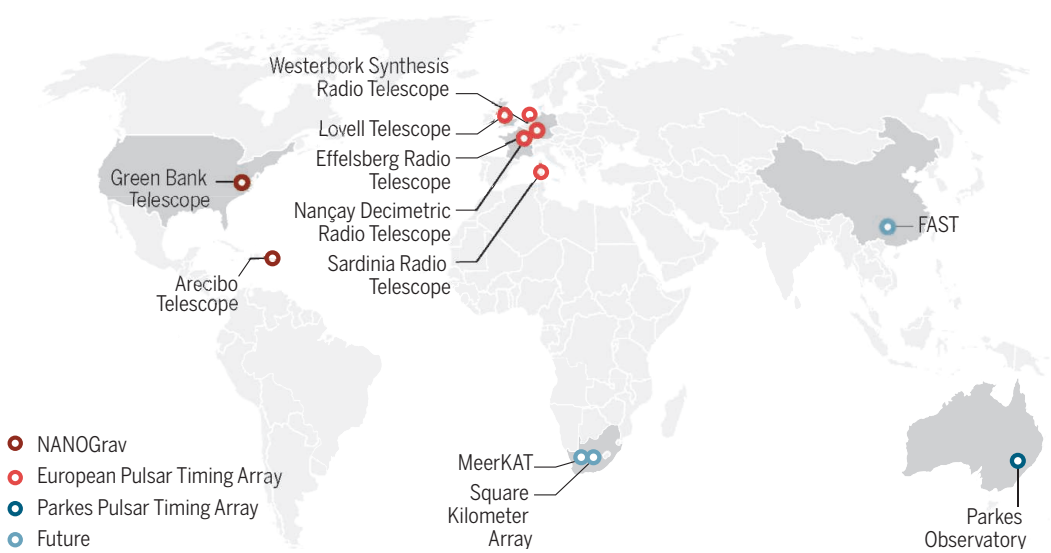

CREDITS: (PHOTO) © R. IAN LLOYD/MASTERFILE/CORBIS; (MAP) ADAPTED BY P. HUEY/*SCIENCE*

Published by AAAS

When the cholesterol transport system falters, arteries may become clogged with plaque (green).

PHOTO: EYE OF SCIENCE/SCIENCE SOURCE

LIPID BIOLOGY

Why high 'good cholesterol' can be bad news

A faulty transport system sometimes causes high HDL

By **Jennifer Couzin-Frankel**

The 67-year-old woman had sky-high high-density lipoprotein (HDL), the form of cholesterol long seen as protective against heart disease, and yet her arteries were lined with plaque. Her paradoxical case has helped motivate a team of scientists to show how high HDL can sometimes be a signal not of heart health, but of the opposite: a cholesterol system unable to siphon the fatty particles from circulation.

In the last 10 years, HDL particles have confounded scientists. The normal role of these bundles of protein and fat is to ferry cholesterol from the rest of the body to the liver, which eliminates it from the body. More of something good should mean better health, and people who naturally have higher HDL levels are usually better off. But drugs that increase HDL cholesterol have flopped in clinical trials, and genes that help raise it don't seem to track with less heart disease. "Nothing with HDL's ever simple," says Jay Heinecke, a biochemist at the University of Washington, Seattle, who has studied it for years.

In this week's issue of *Science*, Daniel Rader, a geneticist and lipidologist at the University of Pennsylvania, and his colleagues suggest that the amount of HDL is less important than how efficiently it gets moved from arteries into the liver. Rader's inspiration was a mouse model developed by Monty Krieger at the Massachusetts Institute of Technology in Cambridge about 20 years ago. The mouse's developers had deleted a gene called *SCARB1*, resulting in animals with startlingly high HDL and, just as startlingly, severely clogged arteries. "Mice actually get heart attacks," Heinecke says. That's because the system for moving cholesterol out of the body is broken in these mice.

Normally, HDL particles gather cholesterol from immune cells that line the arteries, and then deposit their load in the liver so that the cycle can begin again. The protein made by the *SCARB1* gene, known as SR-B1, helps make that deposit happen. Mice without SR-B1 have HDL particles swollen with cholesterol, which struggle to draw more of it away from the arterial wall.

Radar wondered whether the same thing might be happening in some people. He and his colleagues began by sequencing genes in 852 people with very high HDL and more than 1000 controls. They found one person—the 67-year-old woman—who had no functioning copies of the *SCARB1* gene and had more plaque on her arteries than an average woman her age. Her HDL was 152 mg/dl, well above the average of about 62 mg/dl among women in her age group. Eighteen others had just one functional copy of *SCARB1* instead of the usual two, and most of them also had high HDL. Detailed studies of nine people with *SCARB1* mutations, including the woman, suggested that as in the mice, their abundant HDL failed to transport cholesterol effectively through the body.

Rader then reached out to colleagues who had collected DNA on hundreds of thousands of people for studies of lipids and heart disease. Among them, he found another 284 people who had only one functioning copy of *SCARB1*. (No one else was like that first woman, with both copies missing.) Most of these people also had higher than average HDL. These people were also about 80% more likely than controls to have coronary artery disease—about the same increase in risk seen with traditional risk factors like diabetes and hypertension.

"This is a key indication of what people have suspected from animal studies," says Alan Tall, an HDL researcher at Columbia University. It appears that HDL is higher "because the flux is blocked," not because HDL is excelling at keeping cholesterol out of the arteries.

Still, because Rader could find so few people without fully functioning *SCARB-1*, and because the potential effects of the mutations on heart health appeared fairly modest, the link between faulty HDL transport and cardiac troubles is still tenuous, he and others say. And HDL's behavior in a petri dish doesn't necessarily reflect what it's doing inside the body, suggests Jan Albert Kuivenhoven, who studies the genetics of lipid metabolism at the University Medical Center Groningen in the Netherlands. "We have no good ways to do the tests with HDL that can really tell what's happening" in a person, Kuivenhoven says.

HDL remains extraordinarily complex, Rader and Kuivenhoven say. It's possible that HDL-raising drugs failed in clinical trials because of the type of HDL the drugs produced—doctors detected more large HDL particles than expected. Overall, however, there's little question that high HDL still tracks with a healthier heart for most people—except, Rader says, when it doesn't.

Ultimately, he says, we'd like to be able to say, "Your HDL is high because X, and that's good thing," and in someone else, "Your HDL is high because of Y, and that's a bad thing." Now, he and others want to nail down exactly what those factors might be—and, potentially, how to head them off. ■

Downloaded from on March 10, 2016

Published by AAAS

ITALY

Plans for new research hub get critical reception

Scientists welcome new money but worry about lack of transparency

By **Laura Margottini**, *in Rome*

It sounded like a gift to Italian research: a brand-new center for the life sciences, lavishly funded by the government and housed at the stylish site of a former world expo in Milan, Italy's fashion and science capital. The effort would receive €1.5 billion over the next decade and focus on genomics, personalized medicine, cancer, and neurodegenerative diseases.

But plans for the Human Technopole Italy 2040 (HT), revealed by Italian Prime Minister Matteo Renzi on 24 February, have drawn mostly criticism. Many researchers applaud the government for investing in science, which has suffered from drastic budget cuts and political neglect. But they object to the lack of transparency with which the plan was hatched. And some worry that it won't benefit the best researchers and institutes, but those with the best connections.

"While national research is agonizing, the prime minister pulls the HT out of his hat," Elena Cattaneo, an internationally recognized stem cell researcher at the University of Milan and senator for life, wrote in the daily newspaper *La Repubblica* recently. She called the center an example of "political improvisation and of how public funding for research shouldn't be managed." Return on Academic ReSearch, an association of scientists, has criticized the "unbalanced concentration of resources in the Milan area, while the rest of the country is dying."

Backers, however, see the HT as a bold bid to save Italian science. It "represents the best opportunity for medical, scientific and civil progress in Italy since the Second World War," oncologist Umberto Veronesi, who helped create the plan, wrote in *La Repubblica*.

The HT helped solve a problem for Italy's government: What to do with the 110-hectare site in the northwest of Milan vacated by Expo 2015, which drew 22 million people between May and October. The plan, developed by the Italian Institute of Technology (IIT) in Genoa, together with universities and institutes in Milan and elsewhere in northern Italy, calls for seven new centers focusing on medical genomics, agriculture and food science, big-data analysis, and nanoscience, to be run by IIT. Labs are also planned at hospitals, research centers, and universities in the Milan area, and institutes elsewhere in Italy may be involved as well—including the National Research Council—but how is unclear.

"Our mandate is to open labs solely in Milan for now," says IIT's scientific director, Roberto Cingolani, adding that scientists from elsewhere are welcome to use the HT's facilities. The center would recruit some 1500 researchers from around the world and seek investments from biotech, pharmaceutical, food, and high-tech companies.

The "Tree of Life" at the World Expo 2015 site in Milan, Italy, where the Human Technopole is planned.

Nobody disputes that Italian science can use a shot in the arm. Government spending for universities has decreased by more than 10% since 2009, to some €6.9 billion this year. Over the same period, a key funding stream, the Research Projects of National Interest, went down from about €100 million to €30 million annually. In a recent letter in *Nature*, physicist Giorgio Parisi of the University of Rome La Sapienza and 69 other scientists urged the European Union to put pressure on Italy to spend 3% of its gross domestic product on research; an online petition making the same request has already gathered 55,000 signatures.

But the HT isn't what Parisi and others were hoping for. The plan was developed without any debate in parliament or the academic world and approved in emergency legislation; media stories have suggested that pharma executives and Milan research institutes convinced Renzi to support it. Even today, details remain vague. A blueprint produced by IIT is awaiting review by a government panel, Cingolani says, but it has not been published. "An investment of this magnitude should involve the scientific community, not just a small number of people," Parisi says.

Some say IIT's record doesn't bode well for its stewardship of the new center. Launched in 2003, IIT has a €96 million annual budget from the Ministry of Economic Development to foster innovation. Because it is a private foundation, it can disburse money for research and hire researchers without issuing public calls, unlike Italy's universities. It has set up labs at universities and research institutes around the country, often based on unclear criteria, says Giovanni Bachelet, a physicist at La Sapienza and a former member of the Chamber of Deputies for the Democratic Party. ITT "is funded through public money so it should be accountable for anything it does," Bachelet says. If the HT is run in the same way, it won't live up to its promises, he says.

Cingolani, who has headed IIT since 2005, dismisses those worries. IIT is run according to the highest international standards and does hire its scientists through public calls, he says. He points to a string of successes, including 130 European grants, 350 patent applications, 60 collaborations with industry, and 12 startups. The HT will bring huge technological and medical advancements to the country, he says.

But the skeptics are unconvinced. "Italian research is becoming a desert," says Massimo Dominici, an oncologist and hematologist at the University of Modena and Reggio Emilia, "but that doesn't mean water should be poured in without following international standards." ■

PHOTO: © ATLANTIDE PHOTOTRAVEL/CORBIS

Downloaded from on March 10, 2016

Published by AAAS

Downloaded from on March 10, 2016

Published by AAAS

EVIDENCE ON TRIAL

By **Martin Enserink**

On 27 February, a court ordered the District of Columbia to pay $13.2 million to Santae Tribble, who spent 28 years in prison based on bogus science. After a taxi driver was murdered in Southeast Washington in 1978, a witness had seen the killer wearing a stocking mask. In a stocking found a block away, police found a hair that matched Tribble's "in all microscopic characteristics," an analyst for the Federal Bureau of Investigation testified. Chances that it came from someone else were "one in 10 million," a prosecutor told the jury. Tribble was convicted.

But a DNA analysis 31 years later showed that the 13 hairs in the stocking came from three different people, none of them Tribble, and from a dog. His incarceration wrecked Tribble's life: The judge in this year's decision found that it contributed to severe depression, heroin addiction, and HIV and hepatitis infections, according to *The Washington Post*. His story is just one of many. Forensic hair analysts have systematically overstated their evidence for decades, the Department of Justice has found, landing hundreds of innocent people in jail and some on death row.

Hair analysis is only one of many flawed forensic fields: A 2009 report from the National Research Council found that the analysis of many types of evidence—from footprints and tire tracks to bullet marks and blood splatters—lacks a solid foundation. Even DNA evidence, seen as the gold standard, can land innocent people in jail, now that new technologies can detect minuscule amounts of genetic material.

Forensic analysts are trying to do better. Many fields are testing the accuracy of existing methods and developing new ones that are more science-based. Statisticians have embarked on an ambitious effort to express the strength of so-called pattern evidence, such as fingerprints, in a more scientific way.

Meanwhile, some scientists are developing the forensic tools of tomorrow. Microbiologists are examining the possibility that the mix of bacteria living in and on the human body is so personal that it could help identify individuals. Computer scientists are helping to unmask criminals who use cryptocurrency, such as Bitcoin. Even hair has a forensic future: New analytical techniques stop short of identifying people but may provide reliable clues about a person's origins, history, or lifestyle.

Given the history of forensics, new techniques will need to be validated more thoroughly than past methods were. And whether the methods are new or familiar, analysts, lawyers, and judges will all need to adopt a more scientific way of thinking. Bad forensic science has already wrecked too many lives.

PHOTO: TED KINSMAN/SCIENCE PHOTO LIBRARY

Published by AAAS

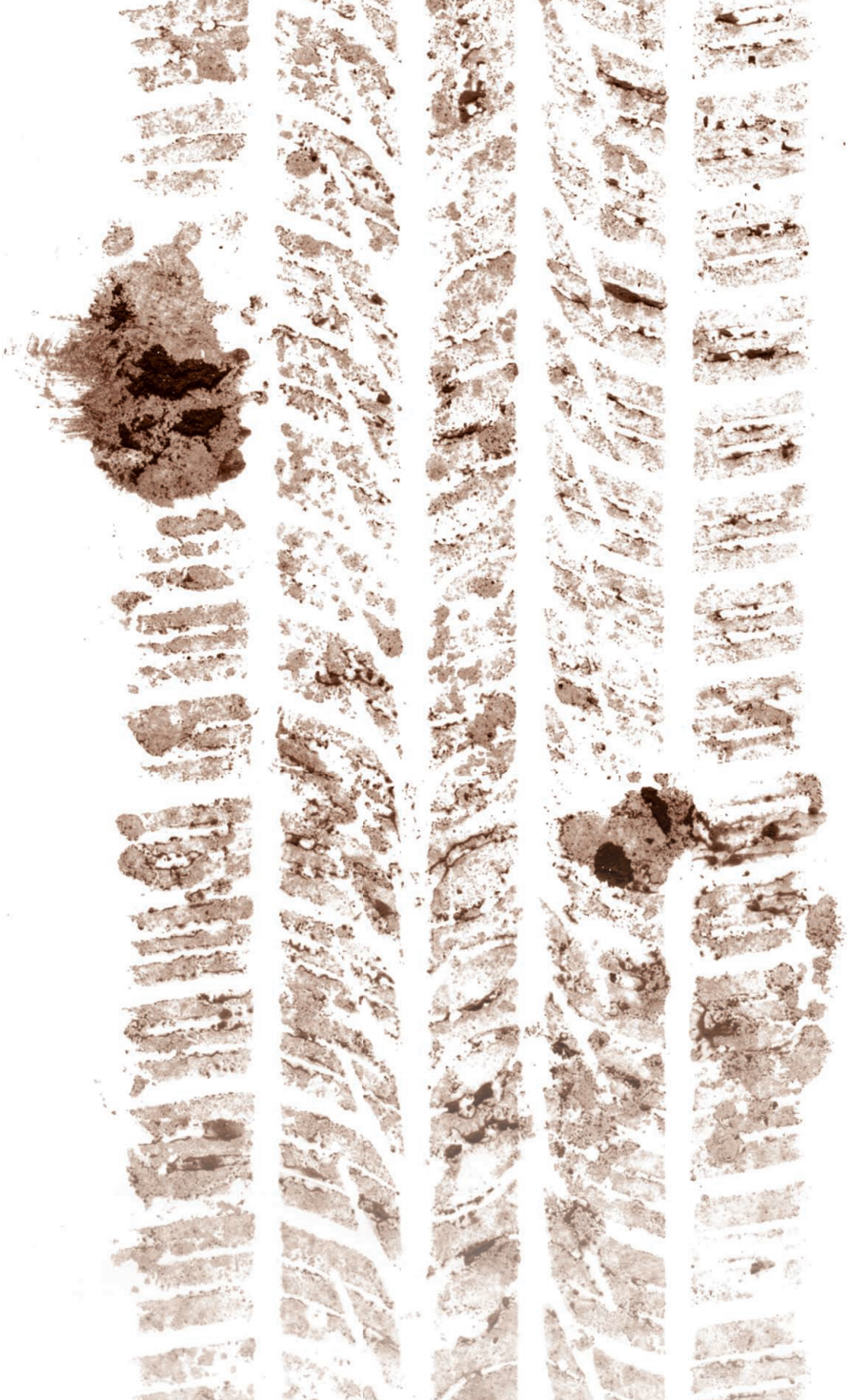

SIZING UP THE EVIDENCE

Statisticians are on a mission to reverse a legacy of junk science in the courtroom

By **Kelly Servick**

Forensic scientists have often overstated the strength of evidence from tire tracks, fingerprints, bullet marks, and bite marks.

On a September afternoon in 2000, a man named Richard Green was shot and wounded in his neighborhood south of Boston. About a year later, police found a loaded pistol in the yard of a nearby house. A detective with the Boston Police Department fired the gun multiple times in a lab and compared the minute grooves and scratches that the firing pin and the interior of the gun left on its cartridge casings with those discovered on casings found at the crime scene. They matched, he would later say at a pretrial hearing, "to the exclusion of every other firearm in the world."

The detective's finding might have bolstered federal racketeering charges for two alleged gang members implicated in various crimes on that street. But the defendants' lawyers challenged its admissibility. The patterns on the cartridges from the lab weren't identical to those from the crime scene, they pointed out. So how could the detective be sure that the shots hadn't been fired from another gun?

The short answer, if you ask any statistician, is that he couldn't. There was some unknown chance that a different gun struck a similar pattern. But for decades, forensic examiners have sometimes claimed in court that close but not identical ballistic markings could conclusively link evidence to a suspect—and judges and juries have trusted their expertise. Examiners have made similar statements for other forms of so-called pattern evidence, such as fingerprints, shoeprints, tire tracks, and bite marks.

But such claims are ill-founded, a committee at the National Academy of Sciences (NAS) concluded in 2009. "No forensic method has been rigorously shown to have the capacity to consistently, and with a high degree of certainty, demonstrate a connection between evidence and a specific individual or source," the panel wrote. In other words: Judges and juries were sometimes sending people to jail based on bogus science.

The committee's report sent shockwaves through the legal system, and forensic science is now grinding toward reform. A series of expert working groups, assembled by the National Institute of Standards and Technology (NIST) and the Department of Justice, has begun to gather and endorse standards for collecting and evaluating different kinds of evidence. What is needed, says Constantine Gatsonis, a statistician at Brown University, who chaired the NAS

PHOTO: MATTHEW RAKOLA

Downloaded from on March 10, 2016

Published by AAAS

committee, is statistical rigor. "When somebody tells you, 'I think this is a match or not a match,' they ought to tell you an estimate of the statistical uncertainty about it," he says.

Last May, NIST awarded $20 million to a team of about 30 statisticians and legal professionals to help develop tools for analyzing the strength of an apparent match. Called the Center for Statistics and Applications in Forensic Evidence (CSAFE), it will collaborate with NIST statisticians to develop statistical methods that describe how strongly a shoeprint in the dirt links the owner of a certain pair of sneakers to a crime scene, for example, or how many fingerprints other than the suspect's might have left a similar pattern on a murder weapon.

MANY FORENSIC DISCIPLINES have been plagued with high-profile errors. An ongoing review of the Federal Bureau of Investigation's (FBI's) microscopic hair comparisons, in which forensic scientists look for distinguishing features such as the thickness, texture, and pigment in a hair strand, has revealed erroneous statements in more than 90% of cases before 2000 in which FBI examiners gave testimony. Often, analysts said that hair could be associated with a specific person—which hair analysis cannot prove. At least five of the cases reviewed so far ended in convictions later reversed with DNA evidence.

The analysis of bite mark patterns has been shown to be so weak scientifically that a state commission in Texas recently recommended banning it from the courtroom. In one high-profile case, a man named Ray Krone was convicted of murder after prosecutors used bite marks on the victim's neck and breast to link Krone to the crime; he served 10 years in prison before DNA evidence showed that he was innocent.

Even more-established methods, such as fingerprint comparison, have faced criticism. Many fingerprint analysts use standard procedures to mark different levels of detail in a suspect's fingerprint and in a "latent print" left at a crime scene. But making a so-called individualization—a conclusion that the prints are from the same source—is "where it gets a little fuzzy," says Glenn Langenburg, a forensic scientist and fingerprint examiner at the Minnesota Bureau of Criminal Apprehension in St. Paul. After examiners look at enough prints known to be from the same source and from different sources, "their brain gets calibrated" to some internal threshold of similarity, he says.

The fuzziness shows in their findings. One study of 169 fingerprint examiners found 7.5% false negatives—in which examiners concluded that two prints from the same person came from different people—and 0.1% false positives, where two prints were incorrectly said to be from the same source. When some of the examiners were retested on some of the same prints after 7 months, they repeated only about 90% of their exclusions and 89% of their individualizations.

Testing examiner accuracy using known samples can give the judge or jury a sense of general error rates in a field, but it can't describe the level of uncertainty around a specific piece of evidence. Right now, only DNA identification includes that measure of uncertainty. (DNA analyses are based on 13 genetic variants, or alleles, that are statistically independent, and known to vary widely among individuals.) Mixtures of genetic material from multiple people can complicate the analysis (see story,

How strong is the resemblance between those fingerprints?

Many statisticians aim to express the strength of forensic evidence as a likelihood ratio, which contrasts the probability of observing a given pattern under different scenarios. This model, under development by researchers at South Dakota State University in Brookings, uses two large databases to evaluate similarities between fingerprints.

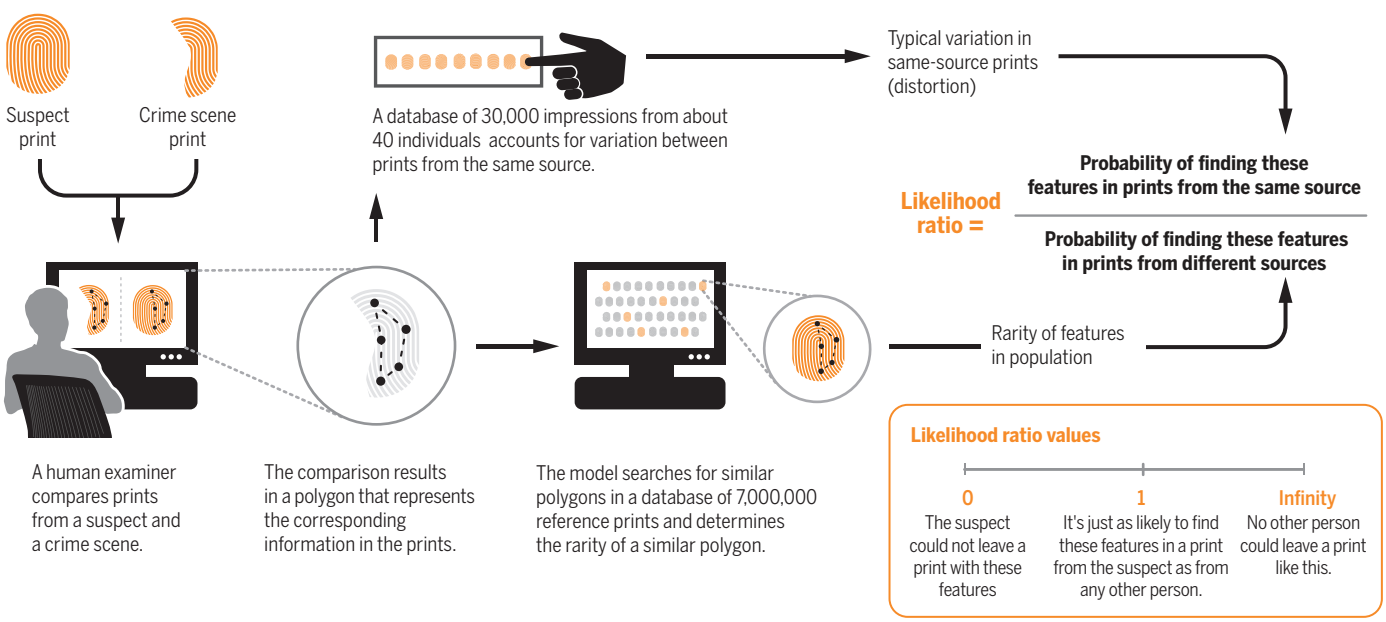

GRAPHIC: G. GRULLÓN/*SCIENCE*

Published by AAAS

p. 1133), but DNA profiling is "a relatively easy statistical problem to solve," says Nicholas Petraco, an applied mathematician at City University of New York's John Jay College of Criminal Justice in New York City. Pattern evidence doesn't operate under the same rules, he says. "What's an allele on a tool mark?"; "What's an allele on a hair or fiber?"

To estimate how frequently a given feature occurs in pattern evidence, researchers will need large databases. Carriquiry and her CSAFE colleagues will begin by exploring digital collections, such as images of bullet and casing marks assembled by NIST researchers, and one of the world's largest collections of crime scene shoeprints, kept by the Israeli police force. The team must also decide what aspects of an image are relevant for comparison. For example, sole patterns indicating the brand and model of a shoe may not be as informative for a comparison as acquired characteristics such as damage or wear patterns.

A large database and a set of rules for feature selection could then feed a statistical model that describes how unusual the set of similarities between two samples really is, relative to similarities between two randomly selected samples from the population. Ideally, says Carriquiry, the model would produce a "likelihood ratio." That would allow an examiner to say, for example, that the similarities between two fingerprints are 10,000 times more likely to occur if they came from the same finger than if they came from different ones.

For fingerprints, that kind of assessment seems within reach. A model under development by forensic scientist Cedric Neumann and statistician Christopher Saunders at South Dakota State University in Brookings can estimate a likelihood ratio for prints once a trained examiner marks their similarities (see diagram, p. 1131). The approach still isn't quite ready for use in court, says Neumann, in part because its results vary too widely depending on which features an examiner selects as relevant. Tighter standards for examiners could resolve the problem, he says.

For other types of evidence, the approach may never work, some scientists say. For instance, a relevant database of shoeprints might not be practical, says Lesley Hammer, a forensic scientist in Anchorage, Alaska, who specializes in footwear and tire track analysis. The database would have to keep up with an ever-changing market of brand-name and counterfeit products, document distinctive features like wear or damage patterns, and possibly even account for regional variations in shoe frequency—the likelihood of a snow boot turning up in Hawaii versus North Dakota, for example.

WHAT STATISTICIANS manage to compute with their new models will have little value if forensic examiners, jurors, judges, and lawyers don't know how to interpret statistical claims. That's why CSAFE collaborator Brandon Garrett, a law professor at the University of Virginia in Charlottesville, has begun to study how jurors perceive a forensic examiner's testimony.

In a 2013 study, for instance, online participants had to rate the likelihood of a defendant's guilt in a hypothetical robbery based on different kinds of testimony from a fingerprint examiner. It didn't seem to matter whether they were simply told that a print at the scene "matched" or was "individualized" to the defendant, or whether the examiner offered further justification—the chance of an error is "so remote that it is considered to be a practical impossibility," for example. In all those cases, jurors rated the likelihood of guilt at about 4.5 on a 7-point scale. "As a lawyer, I would have thought the specific wording would have mattered more than it did," Garrett says. But if subjects were told that the print could have come from someone else, they seemed to discount the fingerprint evidence altogether.

"When Neumann and his colleagues tested out their fingerprint likelihood ratios on mock jurors, participants recognized that making an "identification" was fundamentally different from providing a probability statement. But they didn't seem to distinguish between a strong likelihood ratio (one in 100,000) and a weaker one (one in 1000) when estimating the probability that a suspect was the source of a print. Neumann suspects that numbers can still be useful for describing testimony, but that lawyers and cognitive psychologists will have to team up to figure out the best presentation.

The final decision about what kinds of statements jurors can ponder, though, is up to judges, who often confer with lawyers and forensic examiners to decide what evidence is admissible. CSAFE aims to reach all these players through a campaign to boost statistical literacy. Last week, the statisticians conducted training for practitioners across Florida crime labs at the Palm Beach County Sheriff's Office, and they intend to launch similar courses around the United States.

Some judges are already pretty savvy about statistics. In the Boston racketeering case, federal district court judge Nancy Gertner found the detective's conclusion that only one gun on the entire planet could have produced the imprints on the bullet cartridges "preposterous." She believed the evidence should have been excluded completely. But Gertner—now a professor at Harvard University—feared that an appeals court would reverse that move, so she "reluctantly" ruled that the detective could describe ways in which the bullet casings looked similar, but not conclude that they came from the same pistol. Ultimately, a jury said there was no evidence of a racketeering operation; Gertner cleared the defendants of the more serious federal charges and their cases were moved to state court.

What's troubling, Gertner says, is that when judges accept junk science, an appeals court rarely overrules them. Attaching a numerical probability to evidence, as CSAFE hopes to do, "would certainly be interesting," she says. But even a standard practice of critically evaluating evidence would be a step forward. "The pattern now is that the judges who care about these issues are enforcing them, and the judges who don't care about these issues are not." ■

What not to say in the courtroom

Several phrases often used to describe similarities in evidence are falling out of favor as statisticians begin to influence examiners and judges.

"TO A REASONABLE DEGREE OF SCIENTIFIC CERTAINTY"
A customary way to express the strength of scientific testimony that has "zero meaning," says Carnegie Mellon University in Pittsburgh, Pennsylvania, statistician Stephen Feinberg, a member of the U.S. National Commission on Forensic Science, which is urging the legal community to abandon the phrase.

"IT'S A MATCH."
A misleading fixture of TV crime dramas. "The correct testimony is, 'I've looked at these two things, and they look similar,'" says Brandon Garrett, a law professor at the University of Virginia in Charlottesville.

"THERE IS A 0% ERROR RATE."
Never true, says Alicia Carriquiry, a statistician at Iowa State University in Ames: "There's always a chance, even if it's infinitesimal, that there's a different explanation for your evidence."

"IDENTIFICATION"/"INDIVIDUALIZATION"
Often used in fingerprint analyses, these terms, too, "imply absolute certainty of the conclusion," the U.S. Army's Defense Forensic Science Center explained last year when it announced that it would no longer use them.

Published by AAAS

PHOTO: MIKE ROGERS

WHEN DNA IS LYING

DNA analysis has helped free thousands of wrongly convicted people. But sometimes DNA lands innocent people in prison, Greg Hampikian warns

By **Douglas Starr**

On a Tuesday morning in Boise, biologist Greg Hampikian is on speakerphone with Christopher Tapp, an inmate at the Idaho State Correctional Institution in Kuna. Tapp is in prison for a murder he swears he did not commit. Many others think he's innocent as well—lawyers, journalists, an organization of former judges; even the victim's mother. No one has fought for him longer than Hampikian, a researcher at Boise State University (BSU).

"How're you doing, Chris?" Hampikian begins.

"I'm having a good time at summer camp," Tapp says gamely. "Although you know me … I'm in the hole again"—solitary. "There was a mutual misunderstanding between me and someone else." He mentions that he and his wife are getting divorced.

"I'm really sorry Chris, that's a lot to deal with," Hampikian says. "You know my offer still stands. I'll pay tuition for any courses you want to take." A pause. "You know we got a decision from the court to move forward with a new DNA test. But the court is only allowing us a limited amount and we have to decide which test is the right one."

Tapp has been in jail since 1998, serving a 25-years-to-life sentence for the murder of a 19-year-old woman named Angie Dodge; he confessed after a series of lengthy interrogations that several experts have described as coercive. Police found plenty of male DNA at the scene, and it did not match Tapp. But the prosecutor and jury believed his confession.

"I don't think people are evil," Hampikian says, "but once they're convinced of a story, they protect it."

Hampikian, who holds joint appointments in biology and criminal justice at BSU and heads the Idaho Innocence Project, has been helping people like Tapp for more than 20 years. He works with defense attorneys and police around the world, trying to free innocent people by exploiting the power of DNA forensics—or by exposing its pit-

Published by AAAS

Downloaded from on March 10, 2016

falls. As the nation's only Innocence Project director who's also a scientist, "he's absolutely essential to what we do," said Aimee Maxwell, executive director of the Georgia Innocence Project in Decatur, which Hampikian helped establish.

In Tapp's case, Hampikian has pushed for the use of a new, controversial DNA technique that he believes may yet identify the real killer and exonerate Tapp. In other instances, such as the notorious Amanda Knox conviction in Italy, he has shown how DNA evidence was false or misconstrued. "Just because it's DNA doesn't mean it's good science," he says.

HAMPIKIAN, 54, who looks a bit like the comedian Bill Maher, is affable, funny, and likes aphorisms. On science and religion: "Theologians are willing to die for their beliefs but scientists are willing to let their beliefs die."

His involvement with forensic science was a multiyear courtship. He had done research on the Y chromosome in Australia and was teaching at Clayton State University in Morrow, Georgia, in 1993 when an associate of famed criminologist Henry Lee asked him whether science could determine the sex of a person based on traces of saliva left at a crime scene. (It could.) Later, he was so captivated by the story of Calvin Johnson, who was exonerated by DNA in 1999 after spending 16 years in prison for rape, that he helped Johnson write an autobiography, *Exit to Freedom*. "The idea that you could free someone with a little bit of this snotlike stuff was a notion that seemed thrilling to me," he says.

Hampikian joined the original board of the Georgia Innocence Project, launched in 2002. In 2004, he moved to BSU, where, in addition to teaching and doing research in genetics, he helped found the Idaho Innocence Project. He used DNA to help exonerate at least a dozen wrongfully convicted people in the United States, Taiwan, and Italy. He's had losses as well. Four of his clients were eventually executed.

DNA evidence is so powerful because it has firm roots in science and is backed by statistics. Analysts focus on 13 or more places in the genome, called loci, where humans are extraordinarily diverse. Each locus contains a "short tandem repeat," a bit of DNA that is repeated multiple times. The exact number of repeats at each locus varies from person to person and can range anywhere between the low single digits to the mid-50s. Because we get one copy of each chromosome from our mother and one from our father, there are two numbers of repeats for each locus, which appear as peaks on an electropherogram, a chart produced by a genetic analyzer.

The chance that two people have the same pairs at all 13 loci is astronomically low. It's a bit like pulling the handles of two slot machines with 13 cylinders each—all containing dozens of symbols—and hoping they match up right down the line. To reduce the risk of false matches even further, the Federal Bureau of Investigation (FBI) will soon release new guidelines calling for DNA forensics to use 20 or more locations.

Its accuracy has made DNA evidence virtually unassailable. A landmark report published by the National Research Council in 2009 dismissed most forensics as unproven folk-wisdom but singled out DNA as the one forensic science worthy of the name. Yet in recent years Hampikian and other geneticists have begun to question the technology. Thanks to a series of advances—including the polymerase chain reaction, which can multiply tiny amounts of DNA—it's now possible to detect DNA at levels thousands of times lower than when DNA fingerprinting was developed in the 1980s. Investigators can even collect "touch DNA" from fingerprints on. A mere 25 or 30 cells will sometimes suffice.

This heightened sensitivity can easily create false positives. Analysts are picking up DNA transferred from one person to another by way of an object that both of them have touched, or from one piece of evidence to another by crime scene investigators, lab techs—or when two items jostled against each other in an evidence bag.

That was the case with Amanda Knox, a U.S. student accused of stabbing her U.K. housemate Meredith Kercher to death in Perugia, Italy. Authorities had accused a local young man named Rudy Guede of sexually assaulting and killing Kercher. The evidence against him was overwhelming—palm prints, fingerprints, and his DNA on the victim and throughout her room—and he was eventually found guilty. But Italian prosecutors also charged Knox and her boyfriend Raffaele Sollecito with murder. Traces of Sollecito's DNA had been found on the clasp of a bra belonging to Kercher, suggesting that he had taken part in the sexual assault, while a knife in Sollecito's kitchen drawer showed

ILLUSTRATION: G. GRULLON/*SCIENCE*

FORENSIC FRONTIERS

How hair can reveal a history

By **Hanae Armitage** *and* **Nala Rogers**

Forensic hair analysis has developed a bad reputation. The technique has relied on traits such as color, thickness, and curvature to link a suspect to a crime scene. But an ongoing reanalysis of old cases by the U.S. Justice Department found that analysts have often overstated their case in the courtroom; several people convicted based on a hair sample were later found to be innocent.

Now, sophisticated analytical techniques are giving hair a new role in forensics. The goal is no longer matching a suspect to a crime scene but using hair to infer physical characteristics or even the travel history of an unknown criminal or victim. Most hairs found at crime scenes don't have enough DNA in them for analysis; "doing a chemical analysis and trying to determine some trait about the individual … is really the only alternative," says Glen Jackson, a forensic scientist at West Virginia University in Morgantown.

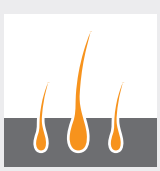

Keratin, the main component of human scalp hair, contains all 21 amino acids, but the ratios depend on the body's biochemistry and differ from person to person. Hydrolyzing the amino acids and measuring their quantities yields a profile that, when compared with a database, gives an indication of a person's sex, age, body mass index, and region of origin, Jackson says—although the accuracy varies by trait and more work is needed.

The ratios of isotopes—atoms of the same element that differ in the number of neutrons—in hair can also yield clues. The ratios of hydrogen and oxygen isotopes in drinking water vary from region to region and are captured in hair. As a result, isotopic analysis of hair can provide clues about where a person has been in the previous months—or years, if the hair is long enough. In 2008, a Utah company called Isoforensics discovered that "Saltair Sally," an unidentified woman found dead in Utah in 2000, had repeatedly moved between the Pacific Northwest and the Salt Lake City area before she died—a clue that helped identify her in 2012. "People are coming to us and saying 'Hey, I heard about this technique and I've got a cold case from 1976. Do you think it will help?'" says Isoforensics President Lesley Chesson. ■

Published by AAAS

Knox's DNA on the handle and Kercher's DNA on the blade.

Hampikian reviewed the lab's procedures and data for the defense team. He noted that the bra clasp hadn't been collected until 46 days after the murder, and not until several crime scene investigators had picked it up, passed it around and then put it back down on the floor to photograph its position—all of which could have caused Sollecito's DNA to end up on the clasp. And although plenty of Knox's DNA was on the knife handle (she had used it in cooking), the amount of DNA from Kercher on the blade was vanishingly small—less than half the amount FBI considered valid for testing.

Hampikian's critique was signed by nine other prominent geneticists and made public. Meanwhile, he had his students mimic part of the investigation. They collected five soda cans from the office of BSU's dean of arts and sciences after lunch and put them in individual evidence bags. Then, without changing gloves, they put five newly bought knives into separate evidence bags. Like the Italians, Hampikian's group looked for DNA at levels below the FBI-recommended minimum. They found DNA from a member of the dean's staff on one of the knife blades. Yet that person had not touched or even been in the same room with the knives.

Nevertheless, the Italian court found Knox and Sollecito guilty. They spent 4 years in prison before being freed by an appeals court, only to later be found guilty again. Last spring, after Italian DNA experts reviewed the case, an Italian high court pronounced both innocent.

DNA ANALYSIS can become even trickier when a mix of DNA from various potential suspects is found in a single crime scene sample. With a simple sample, analysts look at two sets of peaks at a given locus: one for the victim and one for the perpetrator. With mixtures, they're looking at bunches of peaks, with no indication of which pairs go together, or which source they came from—aside from those of the known victim. At that point the analysis becomes highly subjective.

Studies have confirmed this. In 2013, geneticist Michael Coble of the National Institute of Standards and Technology in Gaithersburg, Maryland, set up a hypothetical scenario in which a mix of DNA from several people had been found on a ski mask left at a crime scene after a series of robberies. Coble asked 108 labs across the country to determine whether a separate DNA sample, which he posited had come from a suspect in the robberies, was also part of the mix. Seventy-three of the labs got it wrong, saying the suspect's DNA was part of the mix when, in fact, it was not. "It's the Wild West out there," Coble says. "Too much is left to the analysts' discretion."

Amanda Knox was convicted of murder in Italy based on a vanishingly small amount of DNA found on a knife.

Hampikian conducted a similar study using DNA evidence from a real crime: the case of Kerry Robinson, a Georgia man serving 20 years for taking part in a gang rape. The victim had identified a man named Tyrone White as one of her attackers. Indeed, in a DNA mixture at the crime scene, White's DNA matched 11 of the 13 alleles that did not belong to the victim. White confessed; as part of a plea bargain he implicated Robinson, against whom he had a grudge. Robinson had two alleles in common with DNA found on the victim's body, both "at the borderline of detection," says Hampikian, who testified that Robinson was "absolutely excluded."

For the study, Hampikian and U.K. psychologist Itiel Dror asked 17 analysts at a reputable U.S. lab to interpret the electropherograms from the case, without specifying their origin. Twelve of the analysts excluded Robinson from the mixture, four said they could draw no conclusion, and only one said Robinson's DNA was in the mix. Hampikian's lab also tested the DNA of four employees from a local TV news station; all four had at least two alleles in common with the crime scene, like Robinson. One of them, a 26-year-old white female, had three.

"Greg was fantastic," says Robinson's attorney, Rodney Zell of Zell & Zell law firm in Atlanta. "He knows his stuff and is a great witness." Even so, an appeals court judge ruled against Robinson's appeal last summer. Zell appealed that decision to the Supreme Court of Georgia, where it's now pending. Meanwhile, Tyrone White has served his reduced sentence and walked free.

"I DON'T THINK people are evil," Hampikian says, "but once they're convinced of a story they protect it." On the phone with Chris Tapp, he's explaining why it's been so hard to overturn his conviction. Yet Hampikian thinks recent scientific advances in DNA forensics could still free him.

Idaho Falls police detained Tapp because he was a friend of their prime suspect, who was eventually released. Assuming Working on the theory that several people must have attacked Angie Dodge, police offered Tapp immunity if he would reveal the name of the other assailant. Over the weeks, Tapp gave them several dozen names, but DNA ruled out each new suspect. Eventually police withdrew Tapp's immunity, leaned on him until he confessed, and charged him. They said Tapp held Dodge's arms down while one or two other men assaulted and killed her.

In order to mount an appeal, Tapp's lawyers must produce evidence that was not available at the time of the trial. One approach is a search process called famil-

500
nanograms
Amount of DNA needed for fingerprinting when the technique was first published in 1985. It corresponds to about one drop of blood or 100,000 cells.

0.1
nanogram
The amount that, in some cases, suffices today. It corresponds to about 20 cells, a number that could be found in a fingerprint.

CREDITS: (PHOTO) REUTERS/ALESSIA PIERDOMENICO; (DATA) A. J. JEFFREYS *ET AL.*, *NATURE* **316** (4 JULY 1985) © 1985 NATURE PUBLISHING GROUP; WWW.PROMEGA.DE

Published by AAAS

ial DNA. If police can't match DNA from a crime scene to FBI's national database, loosening their search criteria may lead to a so-called partial match—possibly a relative of the perpetrator, which could provide an investigative lead. Civil rights advocates object to this procedure because it means that simply being related to an offender can make you a person of interest; Maryland and the District of Columbia have banned the practice. But it has solved some important cases, including that of a Californian serial killer nicknamed the Grim Sleeper.

In the case of Angie Dodge, Idaho Falls police checked the crime scene DNA against FBI's database and did not find a match. (It's not entirely clear whether they searched for a partial match as well.) At Hampikian's suggestion, they also conducted what he calls a "genealogical search." Police had a forensics lab produce a profile of 35 loci on the Y chromosome from semen found at the crime scene; then they obtained a subpoena to have Ancestry.com, the world's largest genealogy company, compare the profile with a Y chromosome database that the copany had bought in 2012 from a Mormon genealogy foundation.

One man, a Mississippi resident with no criminal record, matched at 34 of the 35 locations. He was too old to fit the killer's profile but police took an interest in one of his sons, Michael Usry, Jr., a 36-year-old filmmaker in New Orleans, Louisiana, who produced gory murder films and who had passed through Idaho near the time of the murder in 1996. They obtained a court order to sample Usry's DNA in 2014—but the test results excluded him. Tapp's attorney, John Thomas, says he is looking into legal approaches to expand the familial searching. (Usry, meanwhile, has become so interested in Tapp's case that he announced plans to make a film about it.)

Last spring, Thomas got court permission to try another avenue: have a laboratory do "touch DNA" testing of swabs that had been taken from Dodge's hands. If Tapp's DNA isn't found in them, that would disprove the prosecutors' claim that he held her down while she was killed. "We're going to keep attacking the state's theory piece by piece," Hampikian says. He worries that the court might reject the new evidence, as they have in previous appeals. He worries that Tapp won't go free until his parole in 2026. But he puts on a brave phone voice for him as he explains the options.

Tapp says: "I appreciate everything you guys are doing, and thank ..." but the line cuts off before he can finish his sentence. ■

Douglas Starr is co-director of the Program in Science Journalism at Boston University.

A TRAIL OF MICROBES

The unique mix of bacteria you leave behind wherever you go might be used to identify you

By **Kai Kupferschmidt**

One morning last summer, evolutionary biologist Jose Lopez was having coffee on the back porch of his house in Hollywood, Florida, when two burglars climbed in through a front window and did what home invaders usually do: They rifled through drawers, disconnected the TV to carry it off, and even opened the fridge to have a Coke.

This wasn't an ordinary break-in, however. The invaders were employees of the local sheriff's office, and the burglary was part of a science project. Later, forensics experts swooped in to swab down surfaces and handles in the house. In a laboratory at the University of Chicago (UC) in Illinois, colleagues of Lopez's isolated DNA from these swabs and fished out parts of one particular stretch named 16S rDNA—a sequence that is distinctive for almost every bacterial species. By amplifying and sequencing these bits, the scientists were able to identify hundreds of different species in each swab.

After eliminating the species left by the house's legitimate residents—including a cat—they were left with a new kind of physical evidence: the microbial DNA deposited by the thieves as they moved through the rooms. Because the mix of species and strains in a person's microbiome is highly individual, such molecular signatures might be used to place someone at a crime scene, says Jack Gilbert, a microbial ecologist at UC. And

PHOTOS: (LEFT TO RIGHT) SCIENCE SOURCE; MATTHEW RAKOLA

Downloaded from on March 10, 2016

Published by AAAS

Touching a phone, or just walking through a room, will leave behind hundreds of microbial species, sometimes including *Staphylococcus aureus* (inset).

because the microbiome varies by gender, age, and lifestyle, the data could also be used to build up a picture of a suspect.

The field is in its infancy; so far, the only crime it has helped solve occurred on the hit TV show *CSI: Miami*. Some scientists are skeptical that microbial signatures are individual enough to be used as evidence in court. "I think we are very far from using the microbiome in forensic analysis. If it will ever be used," says microbiologist Jacques Ravel of the University of Maryland, Baltimore. Others are more optimistic. "We have enough data to suggest it is well worth exploring," says David Relman, who studies human and animal microbiomes at Stanford University in Palo Alto, California.

HOPES THAT MICROBIOMES could help solve crimes date from a study published in 2010 in the *Proceedings of the National Academy of Sciences*, which showed that bacterial DNA recovered from computer keyboards matched the microbiomes found on their owners' fingertips. The authors also sampled bacteria from nine computer mice and used the results to pick the owners out of a database of 270 microbiomes. "This was the first paper to demonstrate that people leave a highly unique and identifiable signature," Gilbert says.

Adding to the microbiome's appeal for forensics, people shed bacteria constantly and indiscriminately. "You're shedding them from your face, spitting them out from your mouth, breathing them out though your nose," Gilbert says. They aren't confined by gloves or clothes. "Your trousers or your pants are like a loose fish net material to bacteria. As soon as you sit down, your bottom or your vaginal microbiota is expelled onto that surface and it is actually reasonably persistent until the next person sits down," Gilbert says. In a 2015 paper, scientists measured the airborne bacteria surrounding volunteers in a sanitized chamber and were able to identify some of the subjects by their microbial cloud.

All told, researchers have sampled microbiomes from thousands of people, mostly volunteers from Europe and the United States, and found that the relative abundances of microbial species are highly individual. Even identical twins can be told apart. One reason our microbiome is so highly personal is that it's partly determined by our genome and immune system. Chance plays a role as well. In the first 3 or 4 years of life, humans seem to pick up a unique set of bacteria from the vast natural diversity they're exposed to; that mix remains fairly stable all their lives, says Peer Bork, a computational biologist at the European Molecular Biology Laboratory in Heidelberg, Germany.

Yet the question is whether these signatures can be used to identify a person beyond a reasonable doubt, as human DNA evidence can. Bork thinks that will be possible, but not with the 16S rDNA technique alone, because it mostly picks up differences between bacterial species. Instead, he thinks investigators need to fully sequence all the DNA swabbed from a crime scene and from suspects' microbiomes, to detect small differences between strains of the same species. "You and I both have *E. coli,* but I have a slightly different strain than you," Bork says. "We carry about a thousand different species in the microbiome. If we look at differences in all of them, we may well be able to distinguish 8 billion people." So far, Bork's group has studied about 3500 individuals using this strategy; all of them were unique. But because it entails extensive sequencing, this approach comes with a higher price tag.

Another problem is that both individual bacteria and the composition of microbial communities change over time. The signature a murderer left at a crime scene a decade ago may not exactly match his microbial cloud today. Moving to a different country changes the microbiome as well, and antibiotics can radically alter it. Smart criminals might pop a few pills before they strike, "like criminals who used to burn their fingertips with acid and other unpleasant techniques," says Rob Knight of the University of California, San Diego, one of the leaders of the new field.

> ***"Your trousers or your pants are like a loose fish net material to bacteria."***
>
> **Jack Gilbert**, University of Chicago

To help solve crimes, forensic analysts would need the equivalent of a fingerprint library: a database of known microbiome profiles to which they can compare evidence from a crime scene. "We would need 8 billion stool or skin samples," Bork says. "I'm not sure how practical that is." But Gilbert doesn't think that's a big problem. He says such databases could be built up the same way they have been for fingerprints: gradually, starting with convicted criminals.

Even if microbiologists can't pinpoint one particular culprit, a microbiome left at a crime scene may hold important clues. Is the perpetrator a man or a woman? Does he smoke? Where does she live? "Unlike fibers or fragments of hair, the microbiome contains an awful lot of information," Gilbert says. For instance, a small study he did with collaborators in Shanghai, China, found big differences between the skin microbiomes of people living in urban, suburban, and rural areas.

In the fake break-in, Gilbert compared the signatures of the two intruders with a database of a few thousand people that he has built up; based on the relative abundance of particular taxonomic groups, he predicted that one of the burglars had at least 10 alcoholic drinks a week and that the other was on migraine medication. He was right on both counts. "When I heard that, I was in shock," says George Duncan, a DNA expert at the Broward County Sherriff's office who had organized the burglary. These kinds of leads could be very valuable to police, he says.

Bork notes, however, that "at the moment many of these associations are very shaky." For instance, two groups have reported that the microbiomes of diabetes patients can be distinguished from that of nondiabetics. But a careful analysis by Bork's group, published in *Nature* in December 2015, showed that what scientists had detected was not a signature from the disease, but from the common diabetes drug metformin.

Gilbert is trying to improve his database by recruiting more people in Chicago and Florida with jobs or lifestyles that leave a particularly strong mark on the microbiome, such as bakers, farmers, vegetarians, and vegans. To help the field along further, Rhonda Roby of the J. Craig Venter Institute in Rockville, Maryland, has received a grant of more than $900,000 from the National Institute of Justice to build a microbiome database containing thousands or even tens of thousands of samples for the forensics community.

One thing is for sure, Ravel says: Scientists will need to tread carefully. Junk science has landed innocent people in jail in the past; the last thing microbiologists should do is add another flawed technique to the forensic arsenal, he says. "You don't want to start accusing and messing up the lives of many people just because they have a microbiome similar to the one found at the crime scene." ■

Published by AAAS

WHO DROPPED THE BOMB?

Postdetonation forensics may help provide answers if the nuclear nightmare becomes a reality

By **Richard Stone**

Last summer, an atomic bomb detonated in a city on the U.S. Eastern seaboard, killing tens of thousands and plunging the nation into despair. As first responders and the military grappled with the aftermath, elite teams of scientists raced to analyze the blast for clues to precisely what kind of bomb had gone off and who bore responsibility for the act.

That was the premise of an exercise—the first of its kind—held in July and August 2015 to test a new network of sensors that would collect data during a surprise nuclear strike. The Mighty Saber simulation was a sobering acknowledgment of many experts' belief that an attack on U.S. soil is more likely than ever—yet tracing responsibility would be far harder than it was during the Cold War, when the chief threat was annihilation by the Soviet Union.

"The scenario has changed," says Thomas Cartledge, a nuclear engineer with the U.S. Defense Threat Reduction Agency (DTRA) in Fort Belvoir, Virginia. "Now, if you see a mushroom cloud go off in New York City, you won't know who did it, or what kind of weapon they used." Possibilities include a warhead diverted from the U.S. arsenal or smuggled into the country by terrorists, or a bomb delivered by an enemy state such as North Korea, which has threatened to nuke the White House.

Researchers have reproduced trinitite, the green-hued glass left by the first U.S. nuclear blast, for use in forensic studies.

The conceivable need to unmask a perpetrator and mount a response is propelling the emerging area of postdetonation forensics. "Someone's going to get the pointy end of the stick. You want to make sure the right entity gets it," says Howard Hall, director of the Institute for Nuclear Security at the University of Tennessee, Knoxville. He and other nuclear detectives are devising new sensors, manufacturing artificial fallout to hone analytical techniques, and

PHOTO: MATTHEW RAKOLA

Downloaded from on March 10, 2016

Published by AAAS

studying how the glass formed in the furnace of an atomic blast would vary depending on the nature of the bomb and the city where it detonated.

The most likely nuclear terrorism scenario, experts say, is a bomb set off on a city street. Past experience offers only a sketchy picture of the resulting devastation. The atomic bombs the United States dropped on Hiroshima and Nagasaki in 1945 detonated about 500 meters above those cities. During the subsequent half-century, while the United States refined its atomic arsenal, nearly all tests were in the air or underground, not in citylike environments. Researchers did study fallout and how it forms, but they were seeking clues about how to prevent or alleviate radiation illness, not identify the perpetrator. "Scientists were not interested in figuring out what kind of device had detonated, because they already knew that," says analytical chemist Michael Kristo, a nuclear forensics expert at Lawrence Livermore National Laboratory in California.

Still, the testing program was a proving ground for postdetonation forensics. The U.S. national labs "put together some very good radiochemical procedures for analyzing debris," says Hall, a radiochemist. Fallout is a mélange of the vaporized environment—soil and structures that were near the blast—laced with fission products (radioisotopes created when fissile materials like uranium or plutonium fission), activation products (radioisotopes formed when the blast radiation transmutes shielding and other bomb components), and residual nuclear material. The precise constituents vary according to a weapon's design—whether it's a simple gun-triggered uranium device, for example, or an intricate hydrogen bomb.

"Each type of weapon has a distinct fingerprint," says Michael Pochet, a U.S. Air Force electrical engineer detailed to DTRA. In plutonium bombs, for example, the fissile isotope is plutonium-239, made in nuclear reactors and extracted by reprocessing spent fuel, which contains a mix of plutonium isotopes and other actinides like americium. Detecting those nuclei indicates that the bomb's core was plutonium. Their proportions hold clues to the bomb's history, says Joel Ullom, a physicist at the U.S. National Institute of Standards and Technology in Boulder, Colorado, who, with colleagues at Los Alamos National Laboratory in New Mexico, has developed a superconducting sensor that speedily differentiates plutonium isotopes.

The ratio between plutonium isotopes and americium-241, a decay product of plutonium-241, "can tell you the time since the plutonium was chemically purified," Ullom says. Americium is removed during reprocessing, so as the freshly separated plutonium ages, americium starts accumulating again. Hall, meanwhile, is developing faster methods to analyze lanthanides, the 15 rare earth elements that, with the radioactive actinides, are key constituents of fallout. The mix of lanthanides and actinides reveals information about the weapon's shielding, for example, and the energy of the neutrons that bombarded it. He intends to fit his gas phase separation apparatus onto a "flyaway lab": a skid that can be deployed quickly in the event of an attack.

To ground-truth these analytical techniques, researchers at Livermore and other national labs are producing surrogate fallout representing different bomb types. The scientists have pressed into service the National Ignition Facility at Livermore, one

Forensics of a nuclear blast

If an atomic bomb were to detonate in a U.S. city, nuclear sleuths would use a wide range of tools to puzzle out the nature of the bomb and who was responsible. Each weapon type has a distinct fingerprint encompassing the waveforms it emits and the fallout it unleashes.

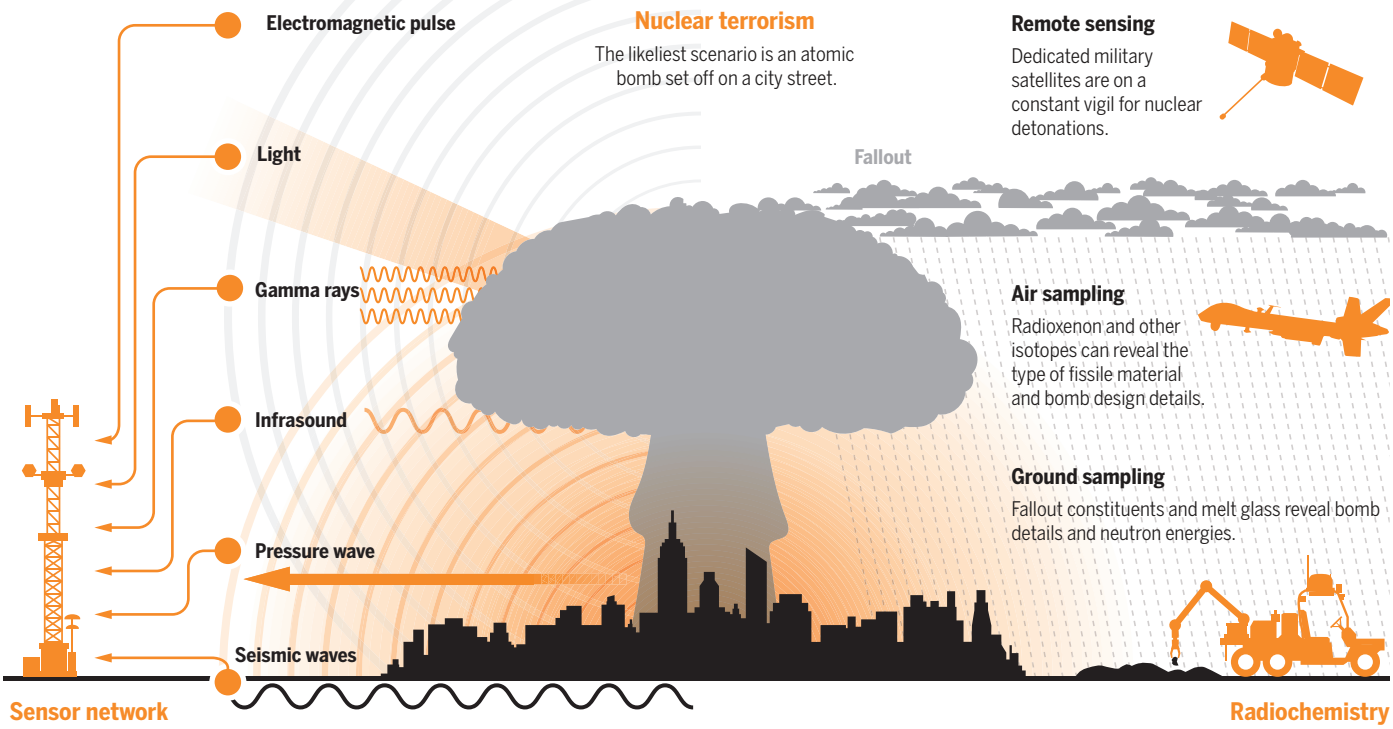

GRAPHIC: A. CUADRA/*SCIENCE*

Published by AAAS

of the world's most powerful lasers, which Kristo calls "a ready source" of neutrons at energies comparable to those produced in the deuterium-tritium fusion reactions that power a hydrogen bomb.

Hall's team is cooking up another type of test sample for postdetonation forensics: artificial melt glass. The real thing forms when an atomic inferno instantly melts anything having the misfortune of being at ground zero. The glass varies with the explosion site, but different bomb specs also produce unique melt glasses, providing clues about what happened. Hall's group has developed a recipe book of melt glass for any geographic location based on a "witch's brew" of the bomb's fissile material and explosive yield, its detonation point, and the local geology and construction materials.

The team reproduced trinitite, the green-hued glass left by the Trinity test, the first U.S. nuclear detonation, which took place in 1945 at the White Sands Missile Range in New Mexico. They have also baked up specimens for Houston, Texas, where the glass-dominated architecture would yield a grayish glass if nuked, and for New York City, whose iron-heavy construction leads to a darker, volcanic-looking glass.

ATOMIC BLASTS ALSO UNLEASH an electromagnetic pulse—a blitzkrieg of gamma rays, x-rays, and radio waves that instantly fries most nearby electronics—as well as intense light, seismic waves, air pressure waves, and infrasound. All may provide information on the type of bomb and its origin. In the 1940s, scientists began designing sensors to capture these signals, first at White Sands and then primarily at the Nevada Test Site, where the United States detonated 928 bombs.

Now, DTRA is leading a government-wide effort to upgrade those sensors and link them up in an array, called Discreet Oculus, which can be deployed in and around cities. "We've repurposed the sensors for an urban environment," Cartledge says. That required devising algorithms to account for how cityscapes deflect or absorb various types of waves, for instance, and filtering out noise from sources such as subways, the vibrations of which could interfere with interpreting vibrations from the detonation.

Mighty Saber set out to test the ability of Discreet Oculus to identify the type of bomb in a surprise attack. The exercise's premise was that a bomb had been diverted from the U.S. arsenal and detonated. "We pulled in weapon designers to see what those signals would be," Pochet says. In late 2013, several dozen experts began ginning up a fallout profile and modeling how waves would propagate and attenuate in a real U.S. city. DTRA won't say which city it was; Cartledge refers to it as Gotham. "No city wants to know it was used as a model for a nuclear attack," he says.

Based on these models, DTRA sent data simulating what Discreet Oculus sensors would record during the explosion to the Air Force Technical Applications Center on Patrick Air Force Base in Florida, which distributed it to four teams of experts from the center and the U.S. national labs. "We said, 'Here's the data, go and do your analyses'," Cartledge says. The task was to identify the bomb, and time was of the essence. "In real life," Pochet says, "we would be working against the clock, struggling to keep up with the news cycle." The exercise ran for 25 days; all four teams figured it out, Cartledge says. He won't specify how quickly but says, "We need to be faster."

DTRA HAS ALREADY INSTALLED Discreet Oculus in several U.S. cities, where the arrays are undergoing testing. They are expected to be operational and transferred to the U.S. Air Force in 2018. DTRA has also begun working on a portable version called Minikin Echo that could be deployed for events like the Olympics.

Although postdetonation forensics may well finger a bomb design, that knowledge by itself wouldn't always unmask the perp. A gun-triggered uranium bomb, for example, could be fashioned by any of a number of terrorist outfits with modest technological expertise, such as the Islamic State group, providing they can lay their hands on several kilograms of highly enriched uranium. That's "where intel comes in," Hall says. But to have any chance of unraveling the details of a nuclear attack, investigators have to lay the scientific groundwork—while hoping it will never be needed. ■

ILLUSTRATION: G. GRULLON/*SCIENCE*

FORENSIC FRONTIERS

Whose voice is that?

By **Nala Rogers**

On the night George Zimmerman fatally shot 17-year-old Trayvon Martin in Sanford, Florida, a 911 call captured the sound of someone screaming. But who? An expert for the prosecution testified it was Martin, begging for help in his last moments. But at a pretrial hearing, several scientists said the recording quality was too poor to tell. The call was not admitted as evidence.

The case illustrates the problems in speaker recognition, a forensic field with a checkered history that is trying to find solid scientific ground. Police and lawyers "can't tell the difference between somebody who's deluded or who is a charlatan, and somebody who is actually doing solid scientific work," says Geoffrey Stewart Morrison, an independent forensic scientist and former chair of the Forensic Acoustics Subcommittee of the Acoustical Society of America in Vancouver, Canada.

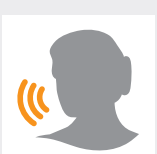

In the 1960s, analysts began converting recordings into images using spectrograph machines and making subjective judgments about how similar they looked—a method once commonly used in courts but now widely discredited. More reliable alternatives have emerged. Signal processing engineers developed automated systems that typically measure the frequency components of speech every few milliseconds. Phonetics experts break up recordings based on individual sounds, then analyze the elements using statistical tests or their own judgments.

Automated systems now work very well—some banks rely on them to identify their clients—but only if you clearly speak a standard sentence into a microphone. Comparing real-world samples is much more error-prone, says Hirotaka Nakasone, a senior scientist in the Federal Bureau of Inivestigation's voice recognition program who testified in the Trayvon Martin case. The same person will sound different during a bar fight versus speaking calmly in an interrogation room, and recording quality is often poor. That's why the admissibility of voice recognition systems in courts is contentious, although the systems are widely used in criminal investigations.

To improve accuracy, scientists are studying how factors like inebriation, emotional state, and recording devices influence voice samples. They are also testing how well existing systems perform and developing standards for things like data selection and the presentation of results. For example, a panel chaired by Nakasone is working on standards for the U.S. National Institute of Standards and Technology. The field is moving away from subjective systems, Morrison says: "Automatic systems are more robust to cognitive bias and are more easily tested." ■

Published by AAAS

PHOTO: RICHARD COOK/BBC ARCHIVES

CLUES FROM THE ASHES

Were the bodies of 43 missing Mexican students burned at a dumpsite? Fire investigator José Torero says the science doesn't add up

By **Lizzie Wade**, *in Mexico City*

On 12 July 2015, José Torero found himself standing in the municipal dump outside the town of Cocula in the Mexican state of Guerrero, tallying up everything he didn't see. Burn marks on the trees. Melted plastic. Anything that, to his trained eye, would indicate that 10 months before, the Cocula dump could have been the site of a massive fire that burned 43 bodies to ash.

Torero, who was born in Peru and now teaches at the University of Queensland (UQ), St. Lucia, in Brisbane, Australia, had come to investigate a crime that shocked the world: the disappearance of 43 students from the Ayotzinapa Normal School, a rural teacher's college near Tixtla, Guerrero. According to Mexico's attorney general (AG), the crime culminated in the students' bodies being incinerated at the Cocula dump.

But what Torero found—or rather, didn't find—at the alleged scene of the crime has threatened to unravel the government's story and has left the fate of the missing 43 even more mysterious than before. His investigation has also put a fresh spotlight on the forensic science of fire investigation, an area where Torero is seen as a world expert.

Although tens of thousands of fires are examined yearly around the world for arson, few investigations employ state-of-the-art science. Many are done by firefighters who rely on their own experience with how fire behaves, rather than scientific studies, says John Lentini, an independent fire investigator based in Islamorada, Florida. Lentini himself helped raise major doubts about the evidence used to convict Cameron Todd Willingham, a man executed in Texas for setting the fire that killed his family. "The field is not very advanced," Lentini says.

Fire encompasses "biology, chemistry, heat transfer, fluid mechanics, chemical combustion, behavior of structures, behav-

Difficult fire investigations are often highly politicized, José Torero says.

Downloaded from on March 10, 2016

Published by AAAS

ior of materials. Scientifically speaking, it's a problem of enormous complexity," Torero says. Few investigations take into consideration state-of-the-art research in each of these fields. Worse, Lentini says, many investigators set out trying to prove an established theory of the crime, rather than ruling out hypotheses with the help of models and experiments, as Torero does.

TORERO GOT INTERESTED IN FIRE after he left Peru to study engineering at the University of California, Berkeley, where he met researchers working on fire safety problems for the International Space Station. "It was a combination of the NASA thing—it catches everybody's attention—and the fact that the problem in and of itself was incredibly complicated and unique."

Tires or wood couldn't have provided the heat needed to completely burn 43 bodies at the Cocula dump, says Torero, who believes incineration in a crematorium is a more likely scenario.

During a postdoc with the European Space Agency, Torero's interests began to shift. "What really brought me into more 'down-to-earth' work," he says, was a 1999 fire in the tunnel under Mont Blanc in the French Alps that killed 38 people. In its wake, Torero dedicated himself to the intersection of fire safety and engineering, studying how disastrous fires start and spread as well as engineering strategies to prevent them. After teaching at the University of Maryland, College Park, and the University of Edinburgh, he became the head of the School of Civil Engineering at UQ in 2012.

When it comes to forensic work, Torero dedicates himself to cases "that have a significant social impact." In the aftermath of the 9/11 attacks, he studied the structural weaknesses that allowed fire to bring down the Twin Towers in hopes of improving skyscraper design. In 2011, he investigated a fire that killed 81 inmates in Chile's San Miguel prison. Guards had seen smoke but had failed to open the padlock that kept prisoners trapped in the burning cell. "They were blamed for not taking action and not being able to rescue the inmates," Torero remembers.

After recreating the blaze in the laboratory and using computer models to understand its behavior, his team concluded that by the time the guards saw smoke, the padlock was too hot to open and the prisoners were already dead. "They would never have had the time," Torero says. His conclusions refocused blame away from the individual guards and onto the overcrowded prison conditions that allowed the fire to endanger so many lives.

Torero got involved in the Ayotzinapa case at the request of a group of five independent experts (known in Mexico as the Interdisciplinary Group of Independent Experts, or GIEI) convened by the Inter-American Commission on Human Rights to examine both the disappearances and how Mexico's AG has handled the investigation. The trouble began on the night of 26 September 2014, when students hijacked five commercial buses to transport them to a demonstration in Mexico City—an illegal but widely tolerated practice by students at Mexico's politically radical teachers' colleges. The students convened in the town of Iguala, where they came under gunfire by municipal and, allegedly, federal police. Some students escaped, others were killed while trying to flee, and 43 disappeared.

According to the AG, the missing students were kidnapped by the Guerreros Unidos drug cartel with help from the local police and under orders from Iguala's mayor, who had family ties to the gang. They were then executed and their bodies incinerated in the Cocula dump in the early hours of 27 September 2014, the AG says. The executioners gathered some of the remains into trash bags and allegedly dumped them into a nearby river, where they were later recovered; other remains were found in the dump itself.

The remains—mostly ash with a few bone fragments—were sent to a lab at the University of Innsbruck in Austria, where scientists have been able to make positive DNA identifications of two of the missing students. Still, doubts continued to swirl around the government's story, especially because no independent investigators were present when the remains were found, calling into question the chain of custody. The GIEI panel was asked to help resolve the doubts.

"A LOT of the more difficult [fire] cases are highly politicized," Torero says, and Ayotzinapa is no exception. "Politically, you need an answer, and you have to provide that answer now." In the case of Ayotzinapa, arrested cartel members had confessed —under torture, the GIEI suspects—to burning 43 bodies in the Cocula dump. "The [AG's] entire investigation was driven to try to prove or create evidence that what the testimonies were saying was correct," Torero says.

For example, the government's report presents rocks found in the Cocula dump that had been cracked from heat as evidence supporting the confessions. The problem, Torero says, is that "I could have gotten the same cracked rock with a small fire, with an old fire, in a number of different ways"—none of which the AG ruled out.

More things were amiss. Cartel members said they incinerated all 43 bodies at the same time on a pyre made of wood and tires. Past studies done with pig carcasses and human corpses revealed that when a body is burned on a pyre, the fat serves as fuel, but it doesn't provide enough heat to burn up all of the organic matter, Torero says. Yet the remains studied in Austria had virtually no organic matter left. (That's why the lab has been able to make only two DNA identifications so far.) "The only way you eliminate all that is if you have a source of heat that doesn't depend on the fat," Torero says.

Wood and tires could not have supplied so much heat: Torero calculated that the

PHOTO: REUTERS/HENRY ROMERO

Published by AAAS

perpetrators would have needed to burn 20,000 to 40,000 kilograms of wood or 9000 to 18,000 tires to provide the necessary energy. Instead, the state of the remains "is typical of incineration in a furnace," Torero says, such as those used in crematoriums. No crematoriums near Iguala have yet been investigated as possible crime scenes.

Then Torero went to the Cocula dump himself. He saw some partially burned tires and melted plastic, but they were more in line with what he would expect to see after a series of small fires. Most telling, in his view, were the trees. Leaves burned off in a fire can grow back in 10 months, but when a big fire scorches a tree trunk, that scar never goes away; scientists can even see burn scars centuries later in tree rings. None of the trees bordering the dump showed such damage.

Demonstrators marched in Mexico City on 26 December 2015 to demand justice for the 43 students, whose fate remains unclear.

TORERO ANNOUNCED his findings on 6 September 2015, when the GIEI released its full report: "The hypothesis that 43 bodies were burned in that dump is impossible." The Argentine Forensic Anthropology Team, which is monitoring the Ayotzinapa investigation on behalf of the victims' families, recently released its own report supporting Torero's assessment. And Lentini believes Torero "almost certainly came to the right conclusion."

AG Arely Gómez did not comment on Torero's findings but did open a second forensic investigation of the Cocula site. Several international fire science experts contacted for this story declined to comment because they are participating in that new inquiry. The AG's office told *Science* that it expects to release the results in early April.

Working 10 months after the fact with a questionable chain of custody, Torero knew he wasn't going to be able to reconstruct what happened at the dump. "It's like having three pieces of a 10,000-piece puzzle," he says. Still, for some families it was valuable to have their doubts about the government's story confirmed. "We're poor, but we're not stupid," a mother of one of the victims said at a press conference following Torero's announcement. "Our children weren't burned there!" For now, that's the only thing they can be sure about. ■

FORENSIC FRONTIERS

The microbial death clock

By **Kai Kupferschmidt**

When you die, a new life begins for the billions of microbes you carry with you. Unchecked by your immune system, waves of species start multiplying and breaking down your body. Microbes from the environment join in as well. Geneticist Jessica Metcalf of the University of Colorado, Boulder, hopes this macabre procession can provide a microbial clock that can help investigators tell the time of death more precisely than they can with current methods, which rely on body temperature, rigor mortis, and insects.

Early in the decay, for instance, bacteria from the Moraxellaceae family and the genus *Acinetobacter* begin gorging on dying human cells. Soon after, the Rhizobiaceae family, often involved in breaking down nitrogen sources, takes over. The gases produced by these bacteria cause the body to bloat and eventually rupture, allowing oxygen in and giving aerobic species the upper hand. Microscopic worms also start to multiply, probably feasting on the bacterial biomass now covering the corpse.

Metcalf first showed that she could use microbes, combined with a statistical model, to pinpoint the time of death of mice to within 3 days, even weeks after death. Then her team took samples from four human bodies at a so-called body farm, where cadavers are placed outside so that forensic scientists can study how they decompose. In a paper published in *Science* (8 January, p. 158), they reported that, again, the microbial dance was predictable enough to set a clock. "Over 25 days our error rate is about 2 to 4 days," says Rob Knight of the University of California, San Diego, who is collaborating with Metcalf. In a large new project, the researchers will expose 36 bodies, three at each of three different body farms, in all four seasons. That will help them further calibrate their clock further and tell them how it is affected by the environment. ■

CREDITS: (PHOTO) REUTERS/EDGARD GARRIDO; (ILLUSTRATION) G. GRULLÓN/*SCIENCE*

Published by AAAS

THE BITCOIN BUSTS

Its anonymity made Bitcoin popular among criminals. But even with cryptocurrency, researchers can follow the money

By **John Bohannon**

Bitcoin, the Internet currency beloved by computer scientists, libertarians, and criminals, is no longer invulnerable. As recently as 3 years ago, it seemed that anyone could buy or sell anything with Bitcoin and never be tracked, let alone busted if they broke the law. "It's totally anonymous," Martti Malmi, one of Bitcoin's earliest developers and investors, boasted in June 2013. "The FBI does not have a prayer of a chance of finding out who is who."

The Federal Bureau of Investigation (FBI) and other law enforcement begged to differ. Ross Ulbricht, the 31-year-old American who created Silk Road, a Bitcoin market facilitating the sale of $1 billion in illegal drugs, was sentenced to life in prison in February 2015. In March, the assets of 28-year-old Czech national Thomas Jiikovský were seized; he's suspected of laundering $40 million in stolen Bitcoins. Two more fell in September 2015: 33-year old American Trendon Shavers pleaded guilty to running a $150 million Ponzi scheme—the first Bitcoin securities fraud case—and 30-year-old Frenchman Mark Karpelès was arrested and charged with fraud and embezzlement of $390 million from the now shuttered Bitcoin currency exchange Mt. Gox.

The majority of Bitcoin users are law-abiding people motivated by privacy concerns or just curiosity. But Bitcoin's anonymity is also a powerful tool for financing crime: The virtual money can keep shady transactions secret. The paradox of cryptocurrency is that its associated data create a forensic trail that can suddenly make your entire financial history public information.

Academic researchers helped create the encryption and software systems that make Bitcoin possible; many are now helping law enforcement nab criminals. These experts operate in a new field at the crossroads of computer science, economics, and forensics, says Sarah Meiklejohn, a computer

The Bitcoin Embassy in Tel Aviv, Israel, opened in 2013 to support a community of Bitcoin enthusiasts.

PHOTO: REUTERS/BAZ RATNER

Downloaded from on March 10, 2016

Published by AAAS

scientist at University College London who co-chaired an annual workshop on financial cryptography in Barbados last month. "There aren't that many of us," she notes. "We all know each other."

When Bitcoin first emerged, law enforcement officers were "panicking," Meiklejohn says. "They thought these technologies were dangerous and made it harder for them to do their job." But as the arrests and convictions have rolled in, "there's a steady shift toward seeing cryptocurrency as a tool for prosecuting crimes." Even in the strange new world of Bitcoin, FBI Assistant General Counsel Brett Nigh said in September 2015, "investigators can follow the money."

UNLIKE MONEY ISSUED by governments, Bitcoin has no Federal Reserve, no gold-backing, no banks, no physical notes. Created in a 2008 academic paper by a still unknown person using the name Satoshi Nakamoto, Bitcoin "is an intellectual artifact," says Patrick McDaniel, a computer scientist at Pennsylvania State University (Penn State), University Park. "It's the frontier of economics."

Strictly speaking, Bitcoins are nothing more than amounts associated with addresses, unique strings of letters and numbers. For example, "1Ez69SnzzmePmZX3WpEzMKTrcBF2gpNQ55" represents nearly 30,000 Bitcoins seized during the Silk Road bust—worth about $20 million at the time—that were auctioned off by the U.S. government on 1 July 2014.

Those Bitcoins have been split up and changed hands numerous times since then, and all of these transactions are public knowledge. The past and present ownership of every Bitcoin—in fact every 10-millionth of a Bitcoin—is dutifully recorded in the "blockchain," an ever-growing public ledger shared across the Internet. What remains hidden are the true identities of the Bitcoin owners: Instead of submitting their names, users create a code that serves as their digital signature in the blockchain.

The job of keeping the system running and preventing cheating is left to a volunteer workforce known as Bitcoin miners. They crunch the numbers needed to verify every transaction. Added to this is an ever-growing math task known as "proof of work," which keeps the miners honest. The calculations are so intense that miners use specialized computers that run hot enough to keep homes or even office buildings warm through the winter. The incentive for all this effort is built into Bitcoin itself. The act of verifying a 10-minute block of transactions generates 25 new Bitcoins for the miner. This is how Bitcoins are minted.

Just like any currency, Bitcoin's real-world value emerges as people trade it for goods, services, and other currencies. If you're not a miner, you can only get Bitcoins from someone who already has them. Companies have sprung up that sell Bitcoins—at a profitable rate—and provide ATM machines where you can convert them into cash. And of course, you can sell something in return for Bitcoins. As soon as both parties have digitally signed the transaction and it is recorded in the blockchain, the Bitcoins are yours.

As *Science* went to press, Bitcoin's market capitalization, a measure of the amount of money invested in it, stood at $5.6 billion. That money is very safe from theft, as long as users never reveal their private keys, the long—and ideally, randomly generated—numbers used to generate a digital signature. But as soon as a Bitcoin is spent, the forensic trail begins.

BY 2013, millions of dollars' worth of Bitcoins were being swapped for illegal drugs and stolen identity data on Silk Road. Like a black market version of Amazon, it provided a sophisticated platform for buyers and sellers, including Bitcoin escrow accounts, a buyer feedback forum, and even a vendor reputation system. The merchandise was sent mostly through the normal postal system—the buyer sent the seller the mailing address as an encrypted message—and the site even provided helpful tips, such as how to vacuum-pack drugs.

Investigators quietly collected every shred of data from Silk Road—from the images and text describing drug products to the Bitcoin transactions that appear in the blockchain when the deals close. Ultimately, investigators needed to tie this string of evidence to one crucial, missing piece of data: the Internet Protocol (IP) addresses of the computers used by buyers or sellers.

The challenge is that the Bitcoin network is designed to blur the correspondence between transactions and IP addresses. All Bitcoin users are connected in a peer-to-peer network over the Internet. Data flow between their computers like gossip in a crowd, spreading quickly and redundantly until everyone has the information—with no one but

Following the Bitcoin breadcrumbs

Although Bitcoin is designed to protect privacy, it nonetheless generates abundant public data. Investigators try to connect the transactions publicly recorded in the Bitcoin blockchain to sales on online drug markets and, ultimately, to sellers.

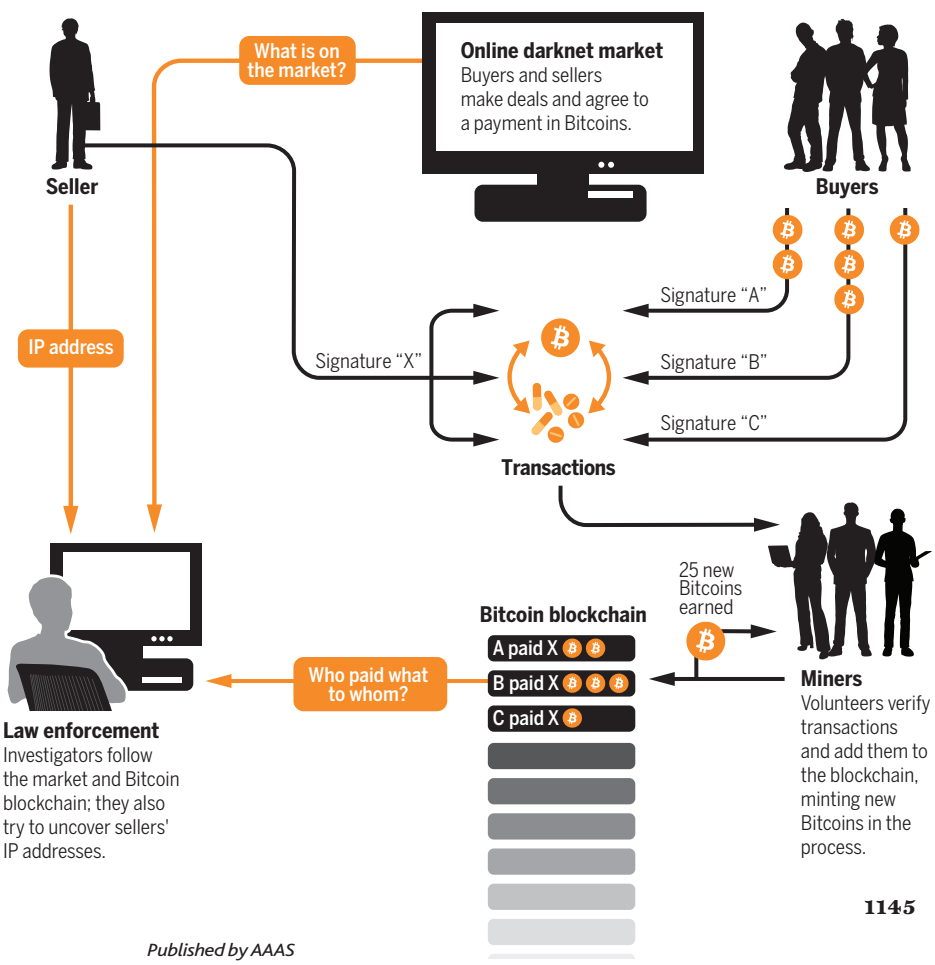

GRAPHIC: C. SMITH/*SCIENCE*

Published by AAAS

the originator knowing who spoke first.

This system worked so well that it was carelessness, not any privacy flaws in Bitcoin, that led to the breakthrough in the investigation of Silk Road. When Ulbricht, the ringleader, was hiring help to expand his operation, he used the same pseudonym he had adopted years before to post announcements on illegal drug discussion forums; that and other moments of sloppiness made him a suspect. Once FBI tracked his IP address to a San Francisco, in California, Internet cafe, they caught him in the act of logging into Silk Road as an administrator.

Other criminals could take solace in the fact that it was a slip-up; as long as you used Bitcoin carefully, your identity was protected behind the cryptographic wall. But now even that confidence is eroded.

Among the first researchers to find a crack in the wall were the husband-and-wife team of Philip and Diana Koshy. In 2014, as graduate students in McDaniel's lab at Penn State, they built their own version of the software that buyers and sellers use to take part in the Bitcoin network. It was especially designed to be inefficient, downloading a copy of every single packet of data transmitted by every computer in the Bitcoin network. "We wanted to see everything," Philip Koshy says.

If the data flowing through the network were perfectly coordinated, with everyone's computer sending and receiving data as frequently as the rest, then it might be impossible to link Bitcoin addresses with IP addresses. But there is no top-down coordination of the Bitcoin network, and its flow is far from perfect. The Koshys noticed that sometimes a computer sent out information about only one transaction, meaning that the person at that IP address was the owner of that Bitcoin address. And sometimes a surge of transactions came from a single IP address—probably when the user was upgrading his or her Bitcoin client software. Those transactions held the key to a whole backlog of their Bitcoin addresses. Like unraveling a ball of string, once the Koshys isolated some of the addresses, others followed.

Ultimately, they were able to map IP addresses to more than 1000 Bitcoin addresses; they published their findings in the proceedings of an obscure cryptography conference. It is unusual for an academic paper to cause both *The New York Times* and the U.S. Department of Homeland Security to come calling. "It was crazy," Philip Koshy says. Their technique has not yet appeared in the official record of a criminal case, but the Koshys say they have observed so-called fake nodes on the Bitcoin network associated with IP addresses in government data centers in Virginia, suggesting that investigators there are hoovering up the data packets for surveillance purposes too. (The pair has since left academia for tech industry jobs.)

AS CRIMINALS HAVE EVOLVED more sophisticated methods to use Bitcoin, researchers have followed apace. Meiklejohn—who says she regularly works with law enforcement but is "not comfortable discussing the details"—was one of the first researchers to explore Bitcoin "mixing" services. The basic idea is to protect the anonymity of transactions by swapping many people's Bitcoin stashes with each other, as in a shell game. The forensic trail shows the money going in but then goes cold because it is impossible to know which Bitcoins belong to whom on the other end. "So in principle, this is a solution to Bitcoin's anonymity problem," Meiklejohn says.

Bitcoin Foundation Vice Chairman Charlie Shrem (right) leaves the Manhattan federal courthouse in New York City in January 2014. Shrem was later sentenced to 2 years in prison for laundering money on Silk Road.

But even mixing has weaknesses that forensic investigators can exploit. Soon after Silk Road shut down, someone with administrative access to one of the newly emerging black markets walked away with 90,000 Bitcoins from user escrow accounts. The thief tried to use a mixing service to launder the money, but wasn't patient enough to hide the tracks, Meiklejohn says. "It's difficult to push large amounts of Bitcoin through mixing services secretly. It's extremely noticeable no matter how you do it." Thomas Jiikovský, the man under investigation by Czech police, is suspected to be the thief in question.

The beauty of Bitcoin, from a detective's point of view, is that the blockchain records all. "If you catch a dealer with drugs and cash on the street, you've caught them committing one crime," Meiklejohn says. "But if you catch people using something like Silk Road, you've uncovered their whole criminal history," she says. "It's like discovering their books."

Exactly that scenario is playing out now. On 20 January of this year, 10 men were arrested in the Netherlands as part of an international raid on online illegal drug markets. The men were caught converting their Bitcoins into Euros in bank accounts using commercial Bitcoin services, and then withdrawing millions in cash from ATM machines. The trail of Bitcoin addresses allegedly links all that money to online illegal drug sales tracked by FBI and Interpol.

IF BITCOIN'S PRIVACY shortcomings drive users away, the currency will quickly lose its value. But the demand for financial privacy won't disappear, and new systems are already emerging. "I don't feel people have the right to know, unless disclosed, how much cash is in my wallet, just like I don't feel anyone should know what conversations I'm having with anyone else," says Ryno Matthee, a software developer based in Somerset, South Africa.

Matthee is part of a team launching a new anonymous online market called Shadow this year, which will use its own cryptocurrency, ShadowCash. The goal is not to facilitate illegal transactions, Matthee says. It will be up to the users, who administer the system, to police it, he says, but to help prevent abuse, "we are going to try our best to filter out known keywords for drugs or worse."

Shadow is far from the only Bitcoin competitor. Scores of alternative cryptocurrencies now exist. And some experts predict that one may finally go mainstream. Some banks already rely on a cryptocurrency called Ripple for settling large global money transfers. And the U.S. government "has been engaging with the cryptocurrency community and learning from them," says Bill Gleim, head of machine learning at Coinalytics, a company based in Menlo Park, California.

Gleim believes the federal government will issue its own cryptocurrency, "maybe as soon as late 2016." If so, it is likely to require users to verify their real-world identities. That could defeat the purpose of cryptocurrency in the eyes of privacy advocates and criminals. Or maybe not: In this technological game of cat and mouse, the next move may go to the criminals. ■

PHOTO: © LUCAS JACKSON/REUTERS

Published by AAAS

Downloaded from on March 10, 2016

MARINE GOVERNANCE

Ending hide and seek at sea

New technologies could revolutionize ocean observation

By **Douglas J. McCauley,[1]* Paul Woods,[2] Brian Sullivan,[3] Bjorn Bergman,[2] Caroline Jablonicky,[1] Aaron Roan,[3] Michael Hirshfield,[4] Kristina Boerder,[5] Boris Worm[5]**

The ocean remains the least observed part of our planet. This deficiency was made obvious by two recent developments in ocean governance: the emerging global movement to create massive marine protected areas (MPAs) (*1*) and a new commitment by the United Nations (UN) to develop a legally binding treaty to better manage high-seas biodiversity (*2*). Both policy goals cause us to confront whether it is meaningful to legislate change in ocean areas that we have little capacity to observe transparently. Correspondingly, there has been a surge in interest in the potential of publicly accessible data from automatic ship identification systems (AIS) to fill gaps in ocean observation. We demonstrate how AIS data can be used to empower and propel forward a new era of spatially ambitious marine governance and research. The value of AIS, however, is inextricably linked to the strength of policies by which it is backed.

POLICY AIS was conceived as a navigational safety aid to prevent ship collisions. AIS transponders publicly broadcast information about a ship's identity, position, and course. The recently gained capacity for mass detection of AIS messages by satellite (S-AIS) makes it possible to observe vessel activity anywhere in the world. In coastal regions, AIS data can be viewed near real time for free, and historical AIS data can be publicly purchased from data vendors. Nonprofit organizations are working on making select AIS data products available for free, and global funders are providing developing nations with access to AIS data (*3*).

The open technologies used by AIS, and its global use, distinguish it from other regionally administered "closed-access" systems [e.g., vessel monitoring systems (VMS)] that do not pool data across jurisdictional regions, transmit data at lower rates, and tightly restrict data access. AIS, however, is not without shortcomings: It is not instantaneous (delays range from minutes to 1 hour), satellite coverage dictates data density, and it doesn't transmit data on the operation of fishing gear [see table S1 for a full comparison of observation systems (*4*)]. Hence, AIS is best viewed as a transparent, global complement to existing closed-access systems. Since 2004, the United Nations' International Maritime Organization (IMO) AIS requirements have fostered compliance for the largest

PHOTO: © CSI PRODUCTIONS/ALAMY STOCK PHOTO

Published by AAAS

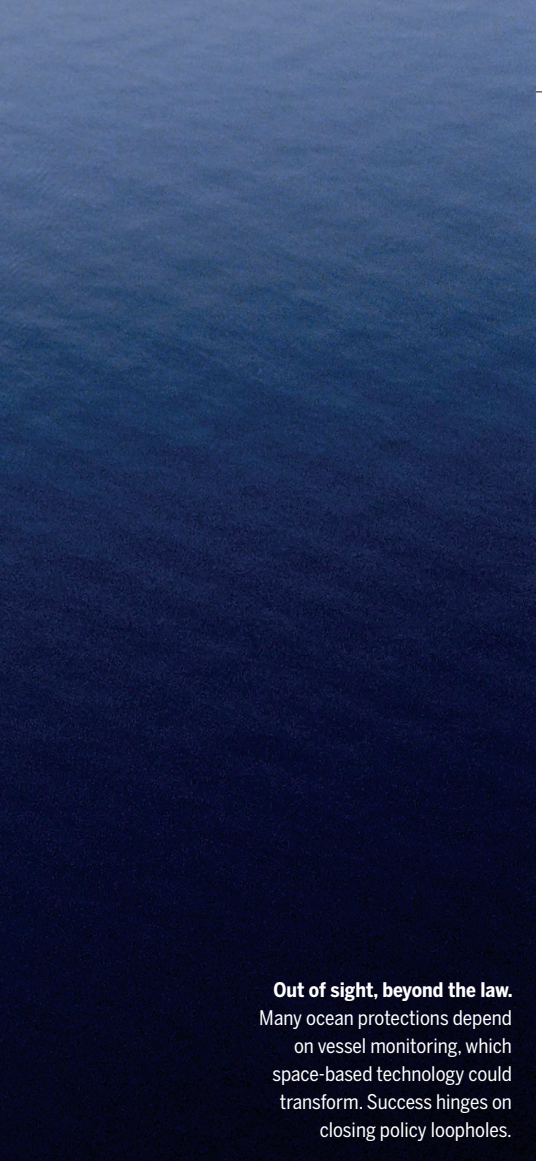

Out of sight, beyond the law. Many ocean protections depend on vessel monitoring, which space-based technology could transform. Success hinges on closing policy loopholes.

ocean-going vessels and passenger liners, but numerous vessels, notably many fishing vessels, slip through the cracks in existing IMO policy (*5*).

PROTECTED AREAS, HIGH SEAS, AND MORE. Nineteen "mega-MPAs" (>100,000 km^2) have been created or announced in the past 6 years, collectively amounting to more area than all MPAs previously gazetted. If we are to move from the ~3% of the ocean currently delineated to the 10% target for 2020 set by the Convention on Biological Diversity (*6*–*8*), megapark establishment will continue.

AIS provides the first tenable option for publicly accessible observation of mega-MPAs. We examined S-AIS activity data of known fishing vessels present within Kiribati's Phoenix Island Protected Area (PIPA), a California-sized MPA (i.e., ~410,000 km^2) that was closed to all commercial fishing on 1 Jan 2015 (*4*). Our data showed substantial fishing activity before closure, and a sharp drop at closure (Fig. 1). Six months of post-closure monitoring revealed only one case of fishing activity in PIPA, and this vessel was interdicted and fined by Kiribati. About 97% of vessels observed fishing in PIPA pre-closure consistently used AIS postclosure, allowing additional insight into how fishermen responded to MPA closure (*4*).

S-AIS estimates of fishing effort in the PIPA region derived using algorithms that separate fishing from nonfishing behaviors (e.g., transiting) were positively correlated with effort reported from fisheries observers, [$P < 0.0001$ (*4*)] AIS, however, underestimates observer-derived effort, the latter presumably a more complete, but more resource-intensive, measure mirroring results from Atlantic land-based AIS (*9*).

About 64% of the ocean lies outside of national jurisdiction. These waters harbor unique aspects of marine biodiversity, including highly endangered species (*6*, *10*, *11*). Concern about ineffective high-seas management has been increasing and has prompted consideration of closing the high seas entirely to harvest (*12*). In recognition of these issues, the UN adopted a landmark resolution in June 2015 that commences negotiations toward a treaty to better manage high-seas biodiversity (*2*, *7*, *13*).

S-AIS provides a low-cost global mechanism for making such a treaty meaningful and enforceable. To provide a first illustration, we summarized 648,591 S-AIS messages transmitted during 2014 of purse seine vessels working across 26 million km^2 of high seas in the tropical Pacific (*4*). Purse-seiners represent the largest commercial fishery in this high-seas region. S-AIS revealed hot spots of purse seine activity surrounding both the Galapagos Marine Reserve and PIPA (fig. S8).

There are many ways by which AIS could improve marine science and management beyond tracking fishing. AIS provides data about diverse ocean users, from cargo vessels to whale-watching boats, that can be used to develop zoning solutions that maximize biodiversity gains while minimizing industry impact (*14*). Additional AIS applications include use by sustainable seafood certifiers wishing to promote fisheries that transparently share harvest data, governments fulfilling seafood traceability requirements, local authorities aiming to decrease collisions between ships and marine megafauna, and overseeing development of seabed mining operations.

LOOPHOLES, POLICIES, AND PRIVACY. Fully reaping the benefits of AIS for ocean governance depends on correcting two key weaknesses: (i) only a small fraction of vessels are currently required to carry AIS; and (ii) some vessels that carry AIS cheat by turning off transponders, falsifying positional data, or transmitting improper identification data. Data analytics can play a major role in correcting AIS noncompliance. Newly developed algorithms can process data from thousands of ships to flag events when AIS has been switched off at sea. Other "despoofing" algorithms use diagnostic behaviors to determine the true purpose of misrepresented vessels (e.g., circular tracks to identify purse seine fishing) and correct falsified tracks (*4*, *9*). About 28 satellites capable of receiving AIS messages are in low-Earth orbit, with the launch of ~60 more low-cost micro- and nanosatellites planned in coming years (*4*). Such additions are a major step toward continuous global AIS coverage.

Although increased coverage and clever analytics can strengthen AIS, policy interventions are also required. First, the IMO should increase the strictness of its AIS regulation and require that all commercial fishing vessels ≥15 m, as well as all vessels >100 gross tonnes (regardless of industry and destination) be equipped with publicly accessible, tamper-resistant AIS systems. The 171 IMO member countries need then to collectively adopt these minimum IMO standards. Nations have codified the currently lax IMO AIS regulations with varying degrees of strictness (fig. S13 and table S4). For example, the European Union (EU) in 2014 mandated that all fishing vessels ≥15 m must carry AIS, and Mauritius and Ecuador require all fishing vessels to carry AIS. U.S. boats, however, are only required to carry AIS when fishing in the United States if they are ≥19.8 m and, when on the high seas, if they are ≥300 tons. Canadian fishing vessels are completely exempted from carrying AIS.

Second, each vessel carrying AIS should be required to obtain a unique IMO vessel identification number (*15*) that must be reported in all AIS transmissions and remain unchanged if a vessel reregisters or switches AIS hardware. Regional tuna management groups this year began to require IMO numbers for very large fishing vessels, but this remains optional for the many remaining vessels. In 2014, only 3.5% of self-identified fishing vessels reported a valid IMO number via AIS, making definitive vessel identification much more challenging and imprecise (*4*). Once assigned, vessel metadata need to be archived and shared in a regularly updated, publicly accessible system—for example, the UN Global Record of Fishing Vessels.

Finally, IMO member states and regional fisheries management organizations should

[1]University of California, Santa Barbara, CA 93106, USA. [2]SkyTruth, Shepherdstown, WV 25443, USA. [3]Google, Mountain View, CA 94043, USA. [4]Oceana, Washington, DC 20036, USA. [5]Dalhousie University, Halifax, NS, Canada B3H4R2. *E-mail: douglas.mccauley@lifesci.ucsb.edu

Published by AAAS

begin enforcing proper use of AIS. Simply having an AIS unit aboard a vessel, but failing to use it properly, can no longer be viewed as legal compliance. As noncompliance becomes better controlled, we also encourage that AIS data be more widely considered as admissible evidence in maritime judicial proceedings.

Evidence suggests that it is possible to equip all commercial fishing vessels in the world with AIS and enforce its use. About 75% of EU fishing vessels complied with 2014 AIS mandates within months (*9*). We estimated that 71% of large fishing vessels (>24 m) worldwide use AIS, and we observed a 17% increase in global AIS coverage for fishing vessels during 2014 (*4*). Closing remaining gaps among users resistant to compliance will be difficult but critically important.

Widespread implementation of publicly accessible AIS would effectively bring an end to the era of marine anonymity. There is growing awareness in marine and terrestrial sectors that benefits for human and environmental safety derived from observation technologies outweigh costs of renegotiating the boundaries of industrial privacy. Recognizing these values, the marine shipping industry has almost universally adopted AIS, as well as supplemental data-sharing systems.

Reforms under way to begin managing the ocean at vastly larger and ecologically meaningful scales will only matter if we can see and act on what is happening in these spaces. Transparency is an extremely important part of this process. Parallel closed-access tracking systems can and should be linked to AIS to improve our view of vessel activity, but closed-access systems allow only part of the picture to be seen by few actors and, consequently, have more limited value to science and transboundary biodiversity management. Unfortunately, current lack of legislative support for AIS has stunted this system into a service that best observes vessels that don't mind being seen. Although the policy shifts we call for require brave revisioning of the primacy of privacy on the oceans, failure to close loopholes will continue to foster illegal activities that steal income and biodiversity from developing nations, promote social injustice at sea, and undermine efforts to cooperatively manage the sustained vitality of our shared marine resources. ■

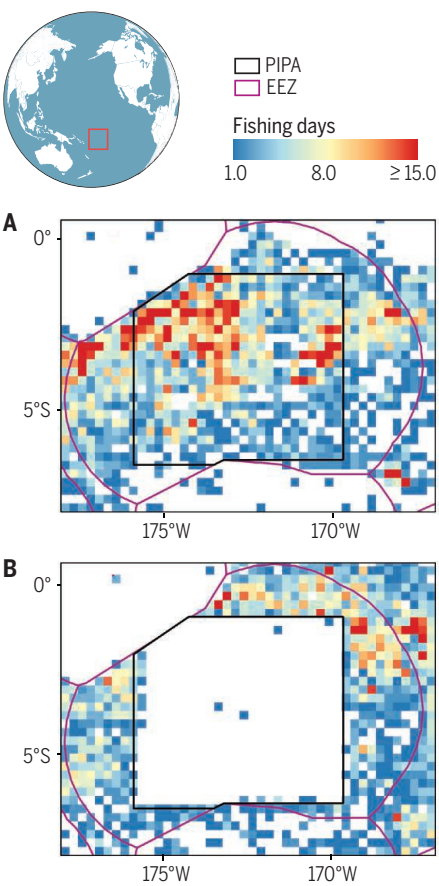

Observing marine protected areas from space. Summary of long-line and purse seine fishing as measured using S-AIS data in PIPA during the 6 months before (**A**) and 6 months after (**B**) it was closed to commercial fishing by the Kiribati government on 1 Jan 2015 (*4*).

REFERENCES AND NOTES

1. D. J. McCauley, *Nature* **515**, 29 (2014).
2. United Nations General Assembly, "Oceans and the law of the sea: Development of an international legally binding instrument under the United Nations Convention on the Law of the Sea on the conservation and sustainable use of marine biological diversity of areas beyond national jurisdiction" (A/69/922, 2015).
3. C. Pala, Tracking fishy behavior, from space. *The Atlantic* (16 November 2014).
4. Materials, methods, and data used in this paper are available as supplementary materials on *Science* Online.
5. International Maritime Organization (IMO), *International Convention for the Safety of Life at Sea* (SOLAS) (1184 UNTS 3, 2002).
6. D. J. McCauley *et al.*, *Science* **347**, 1255641 (2015).
7. J. Lubchenco, K. Grorud-Colvert, *Science*. **350**, 382 (2015).
8. Convention on Biological Diversity, Decision X/2, The Strategic Plan for Biodiversity 2011–2020 and the Aichi Biodiversity Targets (Nagoya, Japan, 2010).
9. F. Natale, M. Gibin, A. Alessandrini, M. Vespe, A. Paulrud, *PLOS ONE* **10**, e0130746 (2015).
10. B. B. Collette *et al.*, *Science*. **333**, 291 (2011).
11. N. K. Dulvy *et al.*, *Aquat. Conserv. Mar. Freshw. Ecosyst.* **18**, 459 (2008).
12. C. M. Brooks *et al.*, *Stan. Envtl. L.J.* **33**, 289 (2013).
13. E. Druel, K. M. Gjerde, *Mar. Policy* **49**, 90 (2014).
14. L. B. Crowder *et al.*, *Science* **313**, 617 (2006).
15. S. Flothmann *et al.*, *Science* **328**, 1235 (2010).

ACKNOWLEDGMENTS

We thank the Alfred P. Sloan Foundation, the Benioff Ocean Initiative, and NSERC for support; K. Gjerde, F. Joyce, P. DeSalles, A. Guerra, and B. S. Mitchell for comments/advice; and ORBCOMM and the Western and Central Pacific Fisheries Commission for data access. The views expressed in this article are those of the authors only and do not necessarily reflect the views of any affiliated institution or company.

SUPPLEMENTARY MATERIALS

www.sciencemag.org/content/351/6278/1148/suppl/DC1

10.1126/science.aad5686

MICROBIOLOGY

The invisible dimension of fungal diversity

Can microbial taxa be defined from environmental molecular sequences?

By **David Hibbett**

Taxonomy plays a central role in understanding the diversity of life, translating the products of biological exploration and discovery—specimens and observations—into systems of names that capture the relationships between species. Taxonomic names facilitate communication among scientists and the public and provide conceptual handles for complex phylogenetic hypotheses. However, taxonomy can be challenging, particularly for fungi and other microorganisms, which are morphologically simple and extremely diverse (*1*). Molecular environmental surveys have revealed previously unknown branches of the fungal tree of life (*2*–*5*) and illuminated biogeographic patterns across all groups of fungi (*6*, *7*). Yet the products of this research are not being translated into formal species names, in part because of the very rules designed to facilitate taxonomy.

Two recently recognized groups of fungi, Archaeorhizomycetes and Cryptomycota, illustrate the magnitude of ongoing molecular species discovery. Archaeorhizomycetes are root-associated soil fungi that have been found in more than 100 independent studies. When Menkis *et al.* (*3*) pooled environmental sequences of ribosomal internal transcribed spacer (ITS) genes, they found 50 lineages of Archaeorhizomycetes containing at least two independent sequences with 97% similarity, a standard cutoff for recognizing OTUs (operational taxonomic units, often equated with species). They also found 95 unique sequences (singletons). Thus, as many as 145 species of Archaeorhizomycetes have been discovered. But only two have been formally named, *Archaeorhizomyces finlayi* and *A. borealis*, based on the only live cultures obtained so far (see the figure).

Biology Department, Clark University, Worcester, MA 01610, USA. E-mail: dhibbett@clarku.edu

ILLUSTRATION: McCAULEY *ET AL.*, ADAPTED BY N. CARY/*SCIENCE*

Downloaded from on March 10, 2016

Published by AAAS

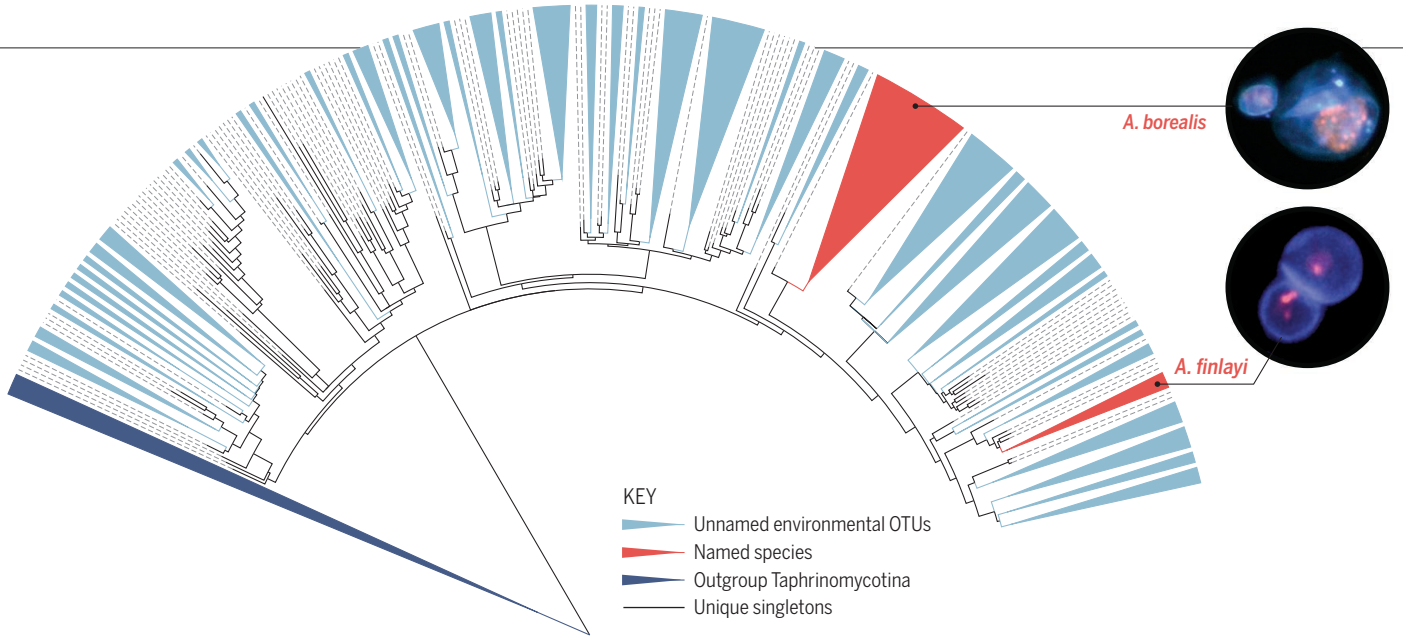

Visible and invisible diversity of Archaeorhizomycetes. Phylogenetic analysis of environmental DNA sequences resolves 50 species-level groups of Archaeorhizomycetes (*3*), but only two have been formally named. The existence of 95 unique singleton sequences suggests that there is much unsampled diversity. Archaeorhizomycetes is the most diverse class in the Taphrinomycotina, which include well-known plant pathogens and the model fission yeast. Tree topology from (*3*); micrographs by A. Rosling.

The aptly named Cryptomycota have also been detected repeatedly in molecular studies of soil, freshwater, and marine habitats (*4*, *5*). Phylogenetic analyses suggest that Cryptomycota make up an ancient clade of fungi. Cryptomycota cells have been visualized in environmental samples with fluorescent tags, but these observations are not linked to cultures or specimens (*4*). Lazarus and James analyzed 109 environmental sequences of Cryptomycota and resolved 12 strongly supported groups (*5*). However, they could only assign three sequences to a formally named taxon, the genus *Rozella*, which includes endoparasites of protists and other fungi.

Molecular ecological studies have investigated fungal distributions on global (*7*) and local (*8*) scales. In one recent global survey, Davison *et al.* (*6*) analyzed the distribution of arbuscular mycorrhizal fungi, which form symbioses with about 80% of plants, but do not produce mushrooms and cannot be grown in pure culture. Using 18*S* ribosomal RNA gene sequences, the authors detected 246 OTUs, of which 93% occurred on multiple continents and 34% on six continents. This level of endemism is surprisingly low for fungi that do not produce airborne spores (*6*). However, the results provide limited information about distributions of known taxa, because only 41 of the OTUs (17%) include sequences from named species.

In the largest study of fungal diversity to date, Tedersoo *et al.* (*7*) analyzed 1.4 million ITS sequences from 365 sites worldwide and recovered ~45,000 OTUs represented by at least two sequences, with a further ~36,000 singletons. Only about one-third of the nonsingleton OTUs matched any sequences in public databases at the 97% similarity cutoff. In other words, this study detected ~30,000 OTUs that could be new species—about 15 times the number of new fungal species descriptions published in journals and recorded in nomenclatural databases in the same year (*1*).

Environmental sequences have transformed understanding of the fungal tree of life, from its deepest roots to its finest branches. Why are these discoveries not being formalized in taxonomic names?

First, there are legitimate scientific concerns over the nature of evidence required to delimit species. Mycologists have selected ITS as the official barcode locus (*9*), but in some groups multiple species may have identical ITS sequences, whereas in other groups there may be multiple forms of ITS in a single genome. Single-cell genomics could provide multiple genes from individuals in environmental samples, but these technically demanding approaches are not yet widely applied in fungal ecology. Until they are, most studies will rely on single markers such as ITS, which can never reveal the patterns of gene flow that provide clues to the limits of reproductively isolated lineages.

Second, species names are no longer needed to test ecological or evolutionary hypotheses. Ecologists once relied on taxonomic resources to identify the species whose interactions they sought to explain; today, they use automated pipelines to cluster OTUs without reference to keys, vouchers, and monographs (*10*). Ecologists and evolutionary biologists do not need to undertake the tedious work of identification and formal taxon description to address the problems that motivate them. On the other hand, molecular ecological studies are providing unprecedented resources for taxonomists, who could use the new data to describe new species or enhance existing descriptions with expanded geographic ranges and new insights into ecological roles.

Unfortunately, the rules that govern biological nomenclature prohibit formal naming of fungi and other microbial taxa based on environmental sequences. Physical type specimens are required by the botanical and zoological codes of nomenclature, which collectively determine conditions for valid publication of names of fungi and protists, and the bacteriological code requires type cultures. Classical taxonomy is thus cut off, by its own nomenclatural rules, from the major modes of discovery for microbial organisms. Working models for purely sequence-based delimitation of fungal taxa do exist (*3*, *6*, *10*, *11*), but do not yet confer nomenclatural validity. Community standards for sequence-based taxon definition and revision of the codes of nomenclature are needed to make the products of molecular environmental surveys visible to scientific and lay communities. ■

ILLUSTRATION: K. SUTLIFF/*SCIENCE*

REFERENCES AND NOTES

1. Centre for Agriculture and Biosciences International, Species Fungorum; www.speciesfungorum.org.
2. A. Rosling *et al.*, *Science* **333**, 876 (2011).
3. A. Menkis *et al.*, *Fungal Biol.* **118**, 943 (2014).
4. M. D. M. Jones *et al.*, *Nature* **474**, 200 (2011).
5. K. L. Lazarus, T. Y. James, *Fungal Ecol.* **14**, 62 (2015).
6. J. Davison *et al.*, *Science* **349**, 970 (2015).
7. L. Tedersoo *et al.*, *Science* **346**, 1256688 (2014).
8. D. L. Taylor *et al.*, *Ecol. Monogr.* **84**, 3 (2014).
9. C. L. Schoch *et al.*, *Proc. Natl. Acad. Sci. U.S.A.* **109**, 6241 (2012).
10. U. Kõljalg *et al.*, *Mol. Ecol.* **22**, 5271 (2013).
11. C. de Vargas *et al.*, *Science* **348**, 1261605 (2015).
12. D. S. Hibbett *et al.*, *Fungal Biol. Rev.* **25**, 38 (2011).

ACKNOWLEDGMENTS

I thank T. James, P. Kirk, M. Öpik, J. Davison, and A. Rosling for images and comments.

10.1126/science.aae0380

Published by AAAS

QUANTUM OPTICS

The time is right for multiphoton entangled states

A chip-based microresonator enables time-bin entanglement

By **Anna C. Peacock**[1] *and* **Michael J. Steel**[2]

In photonics, fundamental advances depend critically on continual improvements in device coupling, transmission losses, and material functionality. These requirements are especially critical in quantum photonics—the manipulation of quantum properties of light—where every photon is precious. A stunning example of how improved capabilities can facilitate basic discovery occurred in late 2015, when a few percent improvement in the efficiency of single-photon detectors enabled a definitive loophole-free demonstration of quantum nonlocality (*1*). On page 1176 of this issue, Reimer *et al.* (*2*) now show how a highly nonlinear optical glass can enable the on-chip generation of biphoton as well as multiphoton entangled qubits.

The authors studied the well-known problem of generating individual pairs of photons by spontaneous four-wave mixing (SFWM). In this intrinsically quantum process, two photons from a bright optical source propagating in a nonlinear material at pump pulse frequency ν_p may spontaneously decay into a new pair of photons, which lie at matching frequencies offset by a frequency $\Delta\nu$ below and above ν_p to satisfy energy conservation. The process occurs randomly, and typically the pump power is chosen so that the probability of a pair event is a few percent per pump pulse. Photon pairs of this type may be engineered to show strong correlations in time, frequency, and other parameters, and so are useful sources for many quantum optics experiments (*3*, *4*).

Following the work of a number of groups (*5*, *6*), Reimer *et al.* generated their photon pairs using an optical microring resonator (a device that confines the light within a circulating cavity; see the figure, panel B). Photon generation is strongly enhanced at frequencies satisfying the resonance condition of the ring, resulting in a comb made up of pairs of lines corresponding to the signal and idler waves (panel C). The output quantum state is a frequency-entangled superposition of photon pair states at all of the resonant lines; the entanglement guarantees that when the photons are detected with a spectrally resolved measurement system (panel D), they always appear at matching lines on either side of the pump (panel E).

Correlated frequency combs of photon pairs have been demonstrated in a number of resonator systems in recent years (*5*, *6*). Here the important advance is that Reimer *et al.* used a ring with a very high quality factor ($Q \approx 235{,}000$) made in a high-refractive index glass known as Hydex. This material is not widely available but has extraordinary properties that are ideal for broadband comb generation. Specifically, it exhibits low linear losses (required for high fidelity), weak material dispersion (so that the resonance positions are near-equally spaced), and high nonlinearity (which enhances the SFWM efficiency). Thus, Reimer *et al.* generated correlated pairs across dozens of lines spanning three telecommunications bands, the broadest quantum frequency comb to date.

The first key result is the demonstration of time-bin entanglement in this system. The authors pumped the device with a pair of pulses separated in time and with a tunable phase difference (see the figure, panel A). With a low-power pump source, pair generation events in both pulses are unlikely, so the main contribution to the state (apart from vacuum) is a superposition where both photons of a pair are emitted in "early" or "late" slots, or time bins (see the figure, panels C and E). Because each slot of the time-bin pair is itself a frequency-entangled superposition over all of the allowed comb lines, the entire state is quite complex. By varying the relative phase of the pump pulses and measuring interference between the early and late bins in an asymmetric Franson interferometer (*7*), Reimer *et al.* were able to demonstrate the entanglement with high visibility—a result they confirmed with full quantum state tomography.

The high efficiency of the nonlinear process in this experiment has allowed the authors to demonstrate a four-photon time-bin state by extracting two pairs on different resonance line pairs simultaneously at useful rates (see the figure, panel E). At this stage, the two pairs are restricted to a product state, so that the degree of entanglement is the same as in the indi-

[1]*Optoelectronics Research Centre, University of Southampton, Southampton SO17 1BJ, UK.* [2]*Department of Physics and Astronomy, Macquarie University, NSW 2109, Australia. E-mail: acp@orc.soton.ac.uk; michael.steel@mq.edu.au*

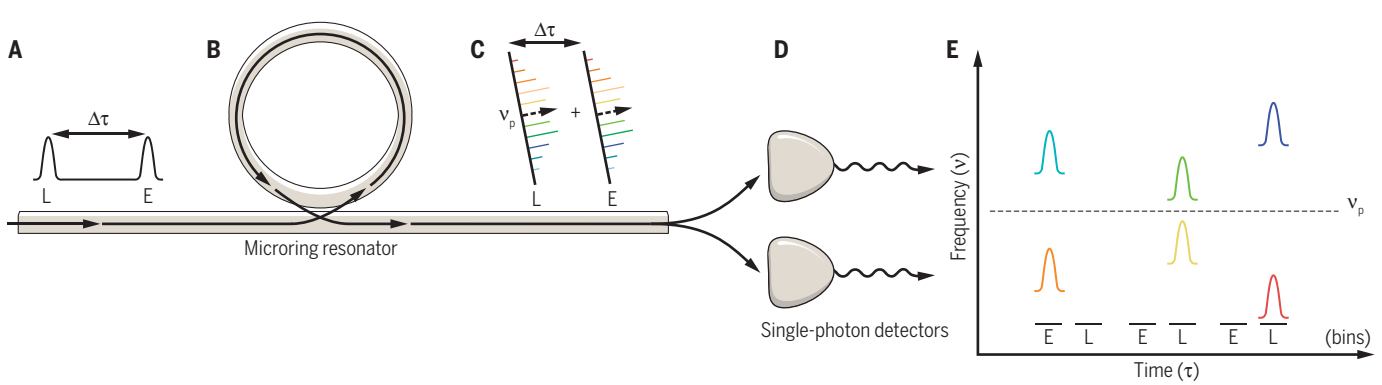

Entangled combs. Reimer *et al.* sent early (E) and late (L) pulses (**A**) spaced by a time $\Delta\tau$ through a waveguide-coupled ring resonator (**B**) to generate entangled frequency combs. The combs, centered around the pump frequency ν_p, were in a coherent superposition of the early or late time bin (**C**). Photon pairs were measured with single-photon detectors (**D**) at a range of different frequencies (colors) determined by the comb lines, with the arriving pairs correlated in both frequency and time of arrival (**E**).

ILLUSTRATION: P. HUEY/*SCIENCE*

Downloaded from on March 10, 2016

Published by AAAS

vidual pair states. However, as the authors suggest, additional excitation fields or the introduction of nondeterministic quantum logic gates could allow the outputs to reach full four-photon entanglement.

Time-bin entanglement offers several advantages over encoding quantum information in spatial or polarization modes. First, the number of time bins is in principle unlimited, so higher-dimensional Hilbert spaces holding qudits (*d*-dimensional states) rather than qubits (two-dimensional states) are easily accessible. Qudit states permit more flexible quantum processing, and time-bin representations allow this to occur in systems that support a single spatial mode, favored in waveguide systems, thereby complementing alternative representations such as optical vortex beams carrying angular momentum. Further, transport of these states in a single polarization mode protects against decoherence, with the other polarization state possibly being reserved as a quantum processing register (*8*, *9*). More generally, time- and frequency-domain representations of quantum information are well suited to routing of quantum signals, just as classical optical communications are routed by multiplexing in frequency and wavelength domains.

Quantum photonics is inevitably heading toward increasingly complex integrated photonic circuits, and the device demonstrated by Reimer *et al.* is compatible with both contemporary fiber and chip-scale architectures. However, in the past year, advances have been made to increase the number of integrated components on a single silicon-based photonic chip (*10, 11*). Thus, this raises a familiar tension between hybrid systems, where the device material and geometry can be individually optimized, versus monolithic platforms, which are generally considered to be more robust, compact, and stable. Time will tell whether the advantages of niche material systems such as this Hydex microring can challenge the dominance of silicon chips. ■

REFERENCES

1. B. Hensen *et al.*, *Nature* **526**, 682 (2015).
2. C. Reimer *et al.*, *Science* **351**, 1176 (2016).
3. A. Migdall, S. Polyakov, J. Fan, J. Bienfang, Eds., *Single-Photon Generation and Detection* (Academic Press, Waltham, MA, 2013).
4. A. S. Clark *et al.*, in *All-Optical Signal Processing*, S. Wabnitz, B. J. Eggleton, Eds. (Springer-Verlag, 2016), pp. 355–421.
5. D. Grassani *et al.*, *Optica* **2**, 88 (2015).
6. J. W. Silverstone *et al.*, *Nat. Commun.* **6**, 7948 (2015).
7. J. D. Franson, *Phys. Rev. Lett.* **62**, 2205 (1989).
8. P. C. Humphreys *et al.*, *Phys. Rev. Lett.* **111**, 150501 (2013).
9. C. Xiong *et al.*, *Optica* **2**, 724 (2015).
10. J. Carolan *et al.*, *Science* **349**, 711 (2015).
11. N. C. Harris *et al.*, http://arxiv.org/abs/1507.03406 (2015).

10.1126/science.aaf2919

ILLUSTRATION: V. ALTOUNIAN/*SCIENCE*

AUTISM

Unraveling a pathway to autism

A signaling pathway that controls protein synthesis may be a target for autism therapeutics

By **J. Peter H. Burbach**

Autism spectrum disorders (ASDs) are a heterogeneous group of neurodevelopmental disorders with shared symptoms in the area of communication and language, restricted interests, and stereotyped and social behaviors. Causes lie in perturbations of brain development, which can be manifold, but genetic factors are prominent among these. Genetic studies have pointed to hundreds of causative or susceptibility genes in ASD, making it difficult to find common underlying pathogenic mechanisms. Careful dissection of molecular and cellular mechanisms are needed to define the molecular targets that can translate into therapeutic strategies. On page 1199 of this issue, Bidinosti *et al.* (*1*) uncover defects in a molecular machinery of a genetic ASD mouse model. This allowed the authors to design specific chemical interventions that relieve cellular and behavioral autistic-like features. In addition, Yi *et al.* (*2*) report a channelopathy in neurons that may predispose to autism. The discoveries raise hope for developing new drugs that help patients with ASD.

Current thinking about pharmacological therapies for ASDs has been stimulated by two scientific milestones. One major advance has been the large number of genes associated with risk for autism (from human genetic studies). This has extended the clinical notion that ASDs include heterogeneous conditions ranging from severe intellectual disability to high-functioning forms (*3*). Furthermore, identified gene variants in ASDs all appear to be rare, and recurrence is very low (less than 1%) in sporadic cases. However, a number of syndromes with autistic-like features—in addition to fragile X and Rett syndromes—have been recognized. One of these is the Phelan-McDermid syndrome.

Considering the human genetics of ASDs, the spectrum of properties of proteins encoded by ASD genes can be aggregated in a number of molecular and cellular functions. Thus, protein synthesis and degradation, signal transduction, transcription, and synaptic transmission emerge as major cellular processes from which ASDs may originate (*3, 4*). These processes are not independent of each other. For example, transcription, translation, and degradation together control the quantity and quality of the total pool of proteins

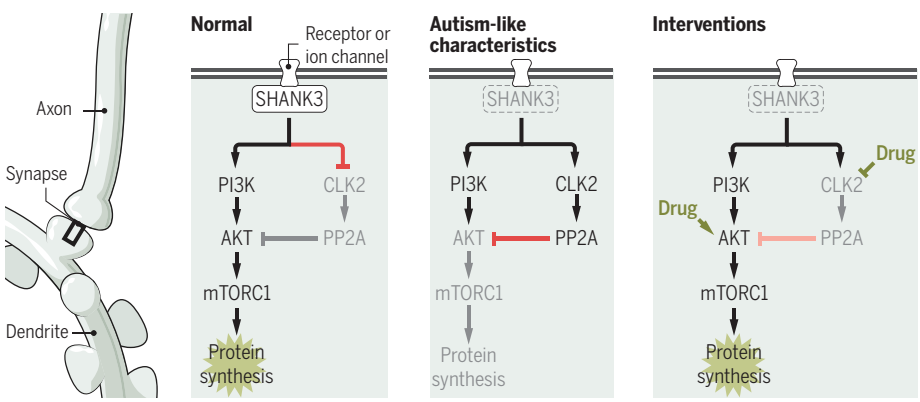

ASD pathway. In glutaminergic neurons, the AKT-mTORC1 pathway transduces signals from neurotransmitter and growth factor receptors and ion channels into several responses through scaffold proteins, including SHANK3. SHANK3 deficiency in a mouse model of ASD decreases the degradation of CLK2. This increases protein phosphatase 2A (PP2A) activity, which reduces AKT activity. As a consequence, protein synthesis decreases, leading to neuronal dysfunction. Drugs that activate AKT or inhibit CLK2 may adjust the AKT-mTORC1 pathway in ASDs. PI3K, phosphatidylinositol 3-kinase.

Brain Center Rudolf Magnus, Department of Translational Neuroscience, University Medical Center Utrecht, Netherlands. E-mail: j.p.h.burbach@umcutrecht.nl

Downloaded from on March 10, 2016

Published by AAAS

of the cell. Signal transduction couples extracellular chemical signals, such as neurotransmitters and growth factors, to intracellular responses including protein synthesis and degradation, and transcription. These are all essential activity-dependent pathways that remain highly dynamic in adult stages. At an integrated level, these cellular pathways are apparent in biological functions relevant for ASDs, in particular synaptogenesis, axon guidance, dendritic and spine morphology, and synaptic plasticity. This has led to the hypothesis that abnormal synaptic homeostasis could play a key role in the pathogenesis of ASDs (*3, 4*).

The other milestone in the field is the notion that neurodevelopmental defects are not necessarily permanent, but may be reversible. There has been a long-standing view that neurodevelopmental disorders are congenital inborn errors of brain development that leave the patient with irreversible defects. This traditional view was first challenged by the reactivation of a silenced gene encoding methyl CpG-binding protein 2 (MeCP2) in a mouse model of Rett syndrome (*5*). Induction of *Mecp2* expression dramatically reversed behavioral and electrophysiological abnormalities in developing and adult mice. Selective reversal of abnormalities was also observed in other ASD models. For example, phenotypes in mice lacking the gene encoding the protein tuberous sclerosis 1 (TSC1) could be reversed by the small molecule rapamycin. Rapamycin blocks mammalian/mechanistic target of rapamycin complex 1 (mTORC1), which controls protein synthesis. The TSC1-TSC2 complex controls mTORC1 activity (*6*). In mouse models of fragile X syndrome [mice that lack the gene encoding fragile X mental retardation protein 1 (FMRP1)], treatment with an antagonist of the metabotropic glutamate receptor 1/5 class (mGluR1/5) also reversed disease characteristics (*6*). Signaling by mGluR1/5 is coupled to synaptic response involving FMRP1. Moreover, insulin-like growth factor I has been successfully used to ameliorate autistic-like phenotypes in mouse models of Rett syndrome and Phelan-McDermid syndrome. *SHANK3* is the prime gene culprit causing the latter disorder. Interestingly, selective rescue of autistic-like phenotypes in a mouse model was established by reexpression of *Shank3* (*7*).

SHANK3 is a synaptic scaffolding protein in the postsynapse that connects receptors and ion channels in the membrane with intracellular signaling proteins and downstream processes (see the figure). Yi *et al.* propose that through direct interaction, SHANK3 may enrich hyperpolarization-activated cyclic nucleotide–gated channels at postsynaptic sites. *SHANK3* (haplo)deficiency severely impaired hyperpolarization-activation (I_h) current conductance, explaining increased input resistance, a neuronal phenotype in Phelan-McDermid syndrome. Bidinosti *et al.* generated cells with a genetic defect reminiscent of *SHANK3* variants seen in Phelan-McDermid syndrome and sporadic ASD, and encountered a deregulated pathway that has been implicated in other forms of ASD. The AKT-mTORC1 signaling pathway is a hub for many cellular processes and is down-regulated as a consequence of *Shank3* deletion in mice. This is opposite of the effect of several other ASD gene mutations on the AKT-mTORC1 pathway. Apparently, an imbalance in this pathway in either direction can elicit autistic-like features. Bidinosti *et al.* discovered that the down-regulation involves a cascade of events tracing back to an increase in Cdc2-like kinase (CLK2); this is attributed to reduced CLK2 degradation by the ubiquitin-proteosome pathway. How mutated *Shank3* affects ubiquitination remains unclear. This may result from a loss-of-function of SHANK3 protein, or perhaps a gain-of-function of other SHANK3 isoforms as a consequence of genetic interference. An intriguing speculation is that it relates to I_h-channel impairment.

The findings of Bidinosti *et al.* suggest that small molecules that activate AKT or inhibit CLK2 may be used to adjust the activity of a critical signaling pathway in ASDs. Indeed, Bidinosti *et al.* reversed abnormalities at the molecular level (AKT phosphorylation) and cellular level (density of dendritic spines; miniature excitatory postsynaptic currents) with such compounds in *Shank3*-deficient neurons, and also reversed abnormal social behaviors in *Shank3*-deficient mice. These are important proofs of principle for drug targets to be taken further in the direction of drug development.

Previously, mGluR1/5 antagonists that successfully rescued phenotypes in genetic animal models of fragile X syndrome had disappointing results in patients with the disorder (*8*). Other candidate compounds are in queue to take this translational route, like compounds related to the mTORC1-inhibitor rapamycin. Bidinosti *et al.* add new targets to intervene with the pathogenesis of ASDs. The decade to come will show whether this finding can reach patients. ■

REFERENCES

1. M. Bidinosti *et al.*, *Science* **351**, 1199 (2016).
2. F. Yi *et al.*, *Science* 10.1126/science.aaf2669 (2016).
3. T. Bourgeron, *Nat. Rev. Neurosci.* **16**, 551 (2015).
4. M. Sahin, M. Sur, *Science* **350**, aab3897 (2015).
5. J. Guy, J. Gan, J. Selfridge, S. Cobb, A. Bird, *Science* **315**, 1143 (2007).
6. D. Ehninger, W. Li, K. Fox, M. P. Stryker, A. J. Silva, *Neuron* **60**, 950 (2008).
7. Y. Mei *et al.*, *Nature* 10.1038/nature16971 (2016).
8. E. Berry-Kravis *et al.*, *Sci. Transl. Med.* **8**, 321ra5 (2016).

10.1126/science.aaf5097

MICROBIOLOGY

Feeding on plastic

A bacterium completely degrades poly(ethylene terephthalate)

By **Uwe T. Bornscheuer**

An estimated 311 million tons of plastics are produced annually worldwide; 90% of these are derived from petrol. A considerable portion of these plastics is used for packaging (such as drinking bottles), but only ~14% is collected for recycling (*1*). Most plastics degrade extremely slowly, thus constituting a major environmental hazard (*2*), especially in the oceans, where microplastics are a matter of major concern (*3*). One potential solution for this problem is the synthesis of degradable plastics from renewable resources (*4*). This approach provides hope for the future but does not help to get rid of the plastics already in the environment. On page 1196 of this issue, Yoshida *et al.* (*5*) address this problem by reporting an organism that can fully degrade a widely used plastic.

"...if the terephthalic acid could be isolated and reused, this could provide huge savings in the production of new polymer without the need for petrol-based starting materials."

Poly(ethylene terephthalate) (PET) is a widely used, colorless polymer with an annual worldwide production of more than 50 million tons. Although this polyester is made from two simple monomers joined via ester bonds (see the figure), its enzymatic or biological degradation has turned out to be very challenging. Until recently, no organisms were known to be able to decompose it. Yoshida *et al.* now describe a

Institute of Biochemistry, Department of Biotechnology and Enzyme Catalysis, Greifswald University, 17489 Greifswald, Germany. E-mail: uwe.bornscheuer@uni-greifswald.de

Downloaded from on March 10, 2016

Published by AAAS

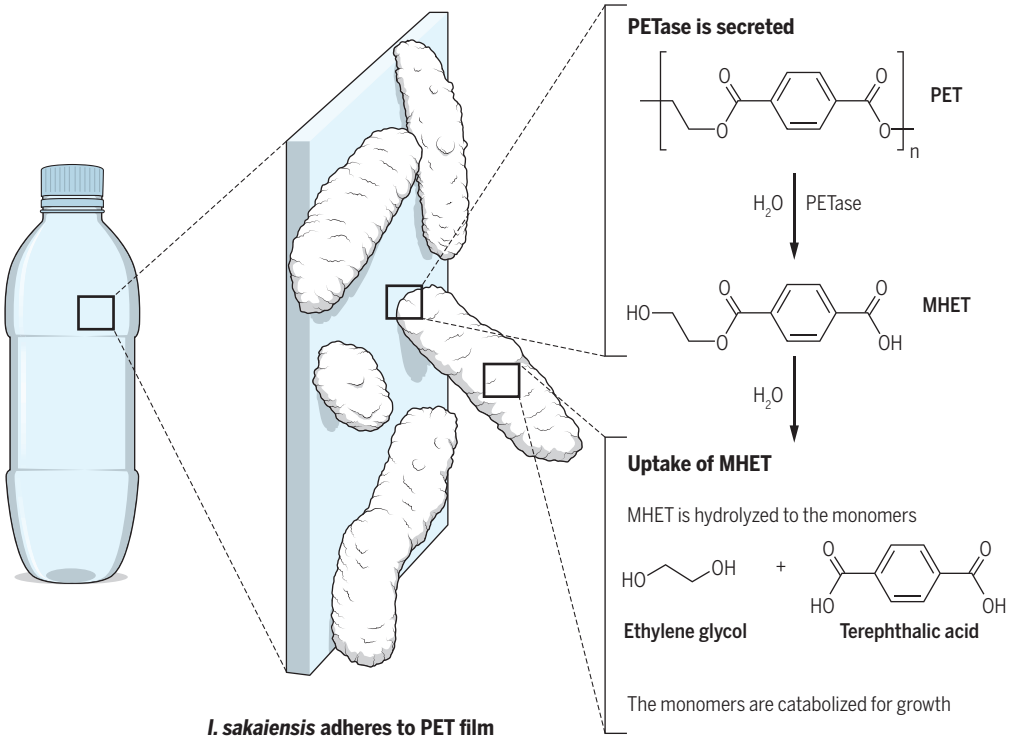

Delicious plastic. The *I. sakaiensis* bacterium discovered by Yoshida *et al.* (*5*) can attach to PET. It produces two hydrolytic enzymes (PETase and MHETase) that catalyze the degradation of the PET fibers to form the starting monomers. The monomers are then catabolized by the bacterium as its sole carbon source.

bacterium, *Ideonella sakaiensis*, that completely degrades and assimilates PET as its sole carbon source.

The authors identified this strain by screening 250 environmental samples at a PET bottle recycling site. Initially, they discovered an entire microbial consortium, but subsequent experiments confirmed that the *I. sakaiensis* strain—a Gram-negative, aerobic beta-proteobacteria—is the sole microorganism responsible for degrading PET.

Using genetic and biochemical analyses, the authors identified two key enzymes involved in PET hydrolysis. First, the bacterium adheres to the PET material and secretes a PETase, which generates the intermediate mono(2-hydroxyethyl) terephthalic acid (MHET). MHET is taken up by the cell and then hydrolyzed by the second enzyme, the intracellular MHET hydrolase, to furnish the two starting monomers (see the figure). The organism produces these monomers from PET to facilitate its growth.

The degradation process is relatively slow; complete degradation of a small PET film took 6 weeks. Nevertheless, the discovery may have important implications for PET recycling. It also raises questions about the principles of enzyme evolution.

So far, only a few hydrolytic enzymes have been known to cleave the ester bonds in PET when used as isolated enzymes: a hydrolase from *Thermobifida fusca* and cutinases (*6*). The PETase shows only 51% sequence homology to its closest known relative, the hydrolase enzyme from *T. fusca*, and its substrate spectrum is remarkably different from all of them. The MHETase belongs to the tannase enzyme family but is not active on typical aromatic esters converted by tannases. It thus seems that both enzymes—PETase and MHETase—are unique and play a distinct role in the *I. sakaiensis* strain. Yoshida *et al*. further show that the genes encoding the two hydrolases are upregulated in the presence of PET, implying that the dedicated role of the enzymes is the degradation of the polymer.

Human-made PET has been present in the natural environment for about 70 years. Did both hydrolytic enzymes evolve during that relatively short period to enable the bacterium to access a novel carbon source and hence provide an advantage for survival? Examples for such rapid natural evolution are scarce, but one prominent case is an atrazine chlorohydrolase. Atrazine is a herbicide widely used since the 1950s. The atrazine chlorohydrolase is now able to cleave the C-Cl bond evolved from a melamine deaminase, which is active on a C-N bond. The two enzymes differ by only nine amino acid mutations; atrazine chlorohydrolase has lost the deaminase activity (*7*).

In this context, one often-discussed aspect (*8*) is how novel (promiscuous) enzyme activities evolve and, hence, how natural adaption of enzymes takes place. Answering this evolutionary question will require three-dimensional structures of the PETase and the MHETase proteins, as well as sufficient data about phylogenetically related enzymes.

Another important question is how the *I. sakaiensis* cells can access the PET polymer fibers in the smooth plastic surface. Specific proteins such as carbohydrate-binding modules (CBM) are crucial for the degradation of cellulose: By lifting fibers from the cellulose surface, these proteins make the fibers accessible for glycosidases and other hydrolytic enzymes (*9*). It remains to be shown whether similar proteins are present in *I. sakaiensis* or whether CBM-like enzymes can be developed to assist PET degradation.

The assimilation of PET by *I. sakaiensis* bacteria may be advantageous for removing this plastic material from the environment. However, if the terephthalic acid could be isolated and reused, this could provide huge savings in the production of new polymer without the need for petrol-based starting materials. To establish such a process, it may be possible to integrate the PETase/MHETase pair into common production strains via metabolic engineering or the use of enzyme cascade systems (*10*). Further research in this area will hopefully provide concepts and solutions for the degradation and recycling of other degradation-resistant plastic materials that are currently used and disposed. ■

ILLUSTRATION: P. HUEY/*SCIENCE*

REFERENCES AND NOTES

1. D. E. MacArthur, D. Waughray, M. R. Stuchtey, *The New Plastics Economy, Rethinking the Future of Plastics*; www3.weforum.org/docs/WEF_The_New_Plastics_Economy.pdf, January 2016.
2. C. M. Rochman *et al.*, *Nature* **494**, 169 (2013).
3. K. L. Law, R. C. Thompson, *Science* **345**, 144 (2014).
4. H. Chung *et al.*, *Curr. Opin. Biotechnol.* **36**, 73 (2015).
5. S. Yoshida *et al.*, *Science* **351**, 1196 (2016).
6. R. Wei *et al.*, *Biotechnol. Bioeng.* 10.1002/bit.25941 (2016).
7. J. L. Seffernick *et al.*, *J. Bacteriol.* **183**, 2405 (2001).
8. U. Bergthorsson, D. I. Andersson, J. R. Roth, *Proc. Natl. Acad. Sci. U.S.A.* **104**, 17004 (2007).
9. U. Bornscheuer, K. Buchholz, J. Seibel, *Angew. Chem. Int. Ed.* **53**, 10876 (2014).
10. J. Muschiol *et al.*, *Chem. Comm.* **51**, 5798 (2015).

ACKNOWLEDGMENTS

Supported by Deutsche Forschungsgemeinschaft grant no. Bo1862/16-1.

10.1126/science.aaf2853

Published by AAAS

PHYSICS

To see the world in a grain of spins

A universal simulator is developed that can model the workings of any classical spin system

By **Stephanie Wehner**

Grappling with our desire to understand nature, we construct models of the specific systems that we wish to study. Unsurprisingly, such models are generally highly tailored to the system of interest. But are all these models really that distinct? Or, could there be a universal model that can somehow describe the behavior of any system we could think of? On page 1180 of this issue, De las Cuevas and Cubitt (*1*) venture out to weave ideas from physics and computer science in an attempt to answer this question for all classical spin models.

Although spin models affect many areas of science, they have their origin in condensed-matter physics, where quantum-mechanical spin is a property of particles. In oversimplified terms, we may think of spin as a direction for each particle that is either "up" or "down." A particular model will describe how such spins can interact with each other. A possible interaction between two spins, for example, may indicate that if one spin changes its state to "up," the other spin will become "down." We usually consider systems in which the spins are arranged in some geometry, such as on a line, a two-dimensional (2D) plane, or in three dimensions (3D). For example, one model may specify that we can only have interactions between nearby spins, whereas other models may include long-range interactions between distant spins.

We could write down a daunting number of such models. However, when we zoom out and focus on the macroscopic behavior to which all these spins together give rise, then simplifications can arise. It has long been known that models can be grouped into certain classes (*2*), and for all models within the same class, even unrelated materials behave in a very similar fashion in the vicinity of a phase transition (a point at which a material changes its macroscopic behavior dramatically, such as the transition of water from a liquid to ice).

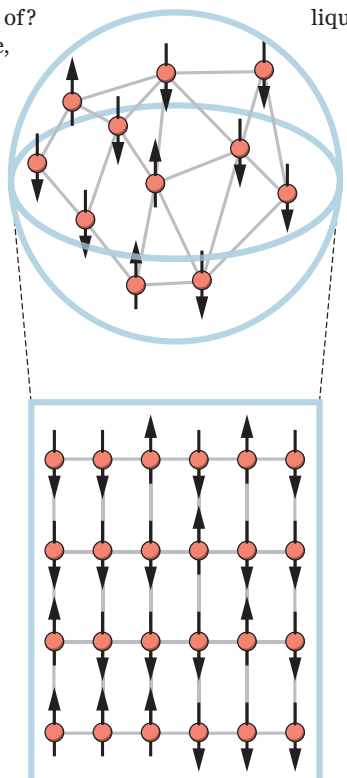

A universal spin simulator. A complicated spin model in 3D can be mapped onto the simpler 2D Ising model with fields, which De las Cuevas and Cubitt find to be a universal simulator for all classical spin models.

In contrast, De las Cuevas and Cubitt zoom into the microscopic regime, where such known simplifications do not apply. Intriguingly, they find simple models that are universal simulators. A model is termed a universal simulator if we can tune its parameters to simulate the entire physical behavior of all other classical spin models, even at the microscopic scale. Though at first glance a universal simulator might be expected to be very complicated, it turns out that one of the simplest and most well-studied models, known as the 2D Ising model (*3*) (with fields), does the trick. Perhaps surprisingly, this means that even though in the 2D Ising model spins are arranged on a 2D plane, it can thus be used to simulate the physics of any model in 3D, even one with long-range interactions. Stashed away in the low-energy sector of the universal model rests the entire physics of the one we wish to simulate (see the figure).

Unsurprisingly, the 2D simulation requires more spins than the original 3D one, but that number of additional spins remains manageable. Furthermore, De las Cuevas and Cubitt map the original model onto the universal simulator explicitly and efficiently. This makes the simulation useful, allowing us to apply techniques known for the simpler universal model to study the more complex one that we would actually want to simulate.

The possibility of realizing such a simulation is appealing for our ability to probe the physics of certain models experimentally. It may be the case that a 2D model may be easier to realize than a 3D one. Indeed, we could think of an experiment realizing a universal model with tunable parameters as a universal spin simulator that can reproduce the physics of any classical spin model. Just as a universal classical computer (*4*) can be programmed to run any algorithm, the universal spin simulator can be programmed to simulate any classical spin model.

Crucially, the universal spin simulator goes beyond the use of a computer to perform simulations as a means to do calculations. To draw a rough analogy, we could use a computer simulation to try and calculate how a magnet behaves, but this is quite different from actually creating something that behaves like one. It may be tempting to conclude that the relation between universal spin models and the universal classical computer stops here—that the brief encounter between physics and computer science merely inspired the idea of universal simulation. But, that would be incorrect. To establish their result, De las Cuevas and Cubitt not only need ideas from physics, but make use of technical results developed in computer science, starting with an encoding of the computer science question of whether a formula can be transformed into a Hamiltonian (the quantum-mechanical description of the system). We thus see quantum information at work—the long-standing affair between physics and computer science, which continues to shed new light on our understanding of nature. ■

QuTech, Delft University of Technology, Delft 2628 CJ, Netherlands. E-mail: s.d.c.wehner@tudelft.nl

REFERENCES

1. G. De las Cuevas, T. S. Cubitt, *Science* **351**, 1180 (2016).
2. L. P. Kadanoff, *From Order to Chaos. Essays: Critical, Chaotic and Otherwise*, Section B, World Scientific Series on Nonlinear Science (World Scientific, 1993).
3. B. M. McCoy, T. T. Wu, *The Two-Dimensional Ising Model* (Dover, 2014).
4. S. Arora, B. Barak, *Computational Complexity: A Modern Approach* (Cambridge Univ. Press, 2009).

10.1126/science.aaf0748

ILLUSTRATION: P. HUEY/*SCIENCE*

Downloaded from on March 10, 2016

Published by AAAS

Misguided metrics underestimate the intelligence of early learners.

The Importance of Being Little
What Preschoolers Really Need from Grownups
Erika Christakis
Viking, 2016. 400 pp.

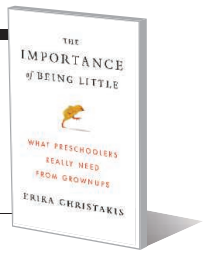

CHILD DEVELOPMENT

The preschool paradox

It's time to rethink our approach to early education

By **Kathy Hirsh-Pasek**[1,2]* *and* **Roberta Michnick Golinkoff**[3]

The Little Prince opens with a 6-year-old narrator who proudly drew a boa constrictor that had swallowed an elephant (*1*). Disheartened that adults think his masterpiece is a picture of a hat, he quips, "Grown-ups never understand anything by themselves."

In her new book, *The Importance of Being Little*, Erika Christakis comes to the same conclusion. Her "preschool paradox" suggests a misalignment between what we offer young children and what they really need. If children have "limitless capacity to learn in all environments," she writes, "why should we settle for unimaginative goals … like being able to identify triangles and squares, or recalling the names of colors and seasons?"

This superbly written book takes us inside the culture of current U.S. preschools and eloquently exposes parental fears that without academic "strategies" and "toolkits," their little Einsteins might fall woefully behind. Society's response has been to trade emotional grounding and strong language skills known to support learning for assembly-line schooling that teaches children isolated factoids.

Supported by a rich scientific literature, Christakis illustrates why a "factory model" of education that turns teaching into "carnival barking" will not serve children well. In these contexts, learning is shallow. A child can be trained to answer "four" when a teacher asks "What is three plus one?" but rote memorization does not mean the child understands what "four" means. So, too, our laser focus on letter identification and letter-sound correspondence as the sine qua non of early reading masks the fact that language and general knowledge skills are the foundation for reading readiness (*2*, *3*). Christakis argues that we must endorse an early education model that has strong learning goals but also encourages a "flexibility of mind, not [merely] a command of facts."

The Importance of Being Little is not a scientific book per se, and Christakis's arguments for constructivist, child-centered preschools and home environments are not new. However, her years of well-honed experience and breadth of knowledge about the underlying science lend weight to the growing belief that we must resuscitate childhood and encourage learning through discovery—à la Reggio Emilia—and that we must design preschools that nurture the development of close adult-child relationships and creativity.

Although the book speaks to how we might attain high-quality preschool education, it also challenges scientists to confront why findings in child development are often ignored in educational practice.

First, despite the fact that education and psychology are closely related, experts in these fields often fail to consult one another. Research in the relatively new science of learning is designed to rectify this gap.

Second, scientists typically look for gaps within, rather than consensus across, the literature. This can cause the appearance of disagreement even where none exists. Scientists largely agree on what needs to be learned and on how children best learn. For example, nearly all would contend that a narrow focus on reading and mathematics to the exclusion of emotion regulation, critical thinking, and grit is a mistake. All would also likely agree that learning is optimized when children are active participants in inquiry and the material is integrated and contextualized, rather than spoon-fed and compartmentalized.

There is also large consensus about what foundational knowledge is required for children to master particular topic areas (*4*). Learning math, for example, requires attention to geometric shapes and patterns, as well as an understanding of the number line—components that are scantly covered in preschool classrooms. Focusing on areas of consensus across a well-established literature allows scientists to develop broad principles of learning that can be used in preschools of varying educational philosophies.

Lastly, scientists often recoil when contacted by journalists rather than providing "edible science" that is accessible, digestible, and usable. It is no wonder then that educators and the public know little about areas of scientific consensus. Such a gap leaves the public vulnerable to inaccurate claims like "Your baby can read" and promises of "brain-based" education.

The Importance of Being Little invites readers to sample the science of learning and helps close the gap between what we know and what we do. Scientists in particular might see the book as a call to action to ensure better alignment between psychological scientists and educators. In the end, books like this bring us all closer to seeing why a drawing of a snake that swallows an elephant is not a hat.

[1]*Department of Psychology, Temple University, Philadelphia, PA 19122, USA.* [2]*The Brookings Institution, Washington, DC 20036, USA.* [3]*Departments of Psychology and Linguistics and Cognitive Science, University of Delaware, Newark, DE 19716, USA.* **Corresponding author. E-mail: khirshpa@temple.edu*

REFERENCES

1. A. Saint-Exupery, *The Little Prince* (Harcourt, New York, 1943).
2. D. Dickinson, R. M. Golinkoff, K. Hirsh-Pasek, *Educational Researcher* **4**, 305 (2010).
3. S. B. Neuman, E. H. Newman, J. Dwyer, *Reading Research Quarterly* **46**, 249 (2011).
4. R. Golinkoff, K. Hirsh-Pasek, *Becoming Brilliant: What Science Tells Us About Raising Successful Children* (APA Press, New York, 2016).

10.1126/science.aaf1173

PHOTO: FAMVELD/ISTOCKPHOTO

Downloaded from on March 10, 2016

Published by AAAS

GRADUATE EDUCATION

Getting into grad school

Who benefits from the Ph.D. admissions process and who falls through the cracks?

By **Sian Beilock**

Inside Graduate Admissions
Merit, Diversity, and Faculty Gatekeeping
Julie R. Posselt
Harvard University Press, 2016. 262 pp.

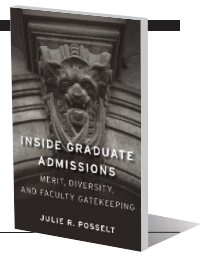

During graduate school, a professor I worked with asked me an odd question: Was I a slow reader? She was in the midst of reviewing applications for a new crop of Ph.D. students and, in reasoning about their potential success, had remembered that, although I had gotten a fairly high quantitative score on the Graduate Record Examination (GRE), my verbal score was not as impressive. Rather than use my case to conclude that the GRE was a poor predictor of success, she was looking for a reason to categorize me as an exception to the rule.

It turns out that my former professor is not alone. In *Inside Graduate Admissions: Merit, Diversity, and Faculty Gatekeeping*, Julie Posselt shows how the process of offering admission at selective Ph.D. programs is chock-full of assumptions that are seldom made explicit or challenged. Over the course of 2 years, Posselt sat through admissions processes in 10 top Ph.D. programs, and her experience provides a firsthand look into admissions decisions in disciplines from astrophysics to classics to economics.

Many more highly qualified candidates apply to prominent Ph.D. programs than there are slots. Faculty are therefore constantly looking for reasons to reject applicants—whether it's an odd recommendation letter, uncertain research interests, or less-than-stellar standardized test scores. At first glance, these rejection criteria don't seem objectionable, but Posselt astutely points out that, when faculty follow a model of risk aversion, they tend to gravitate toward applicants similar to themselves. It's perceived as risky to take a chance on a student from a nonelite educational background or one with different training. The result is often a failure to realize the Ph.D. diversity that most faculty and universities strive to achieve.

The reviewer is Vice Provost for Academic Initiatives at the University of Chicago, Chicago, IL 60637, USA.
E-mail: beilock@uchicago.edu

This risk aversion is perhaps nowhere more apparent than in how faculty treat GRE scores. Although ample evidence demonstrates that the GRE is not an especially good predictor of graduate school success, the appeal of this simple metric is real. Posselt points out that, because average GRE scores differ as a function of racial and other group factors, relying heavily on GREs in the initial judgment of candidates—as many departments do—fundamentally alters the makeup of applicants given most attention in later admissions rounds.

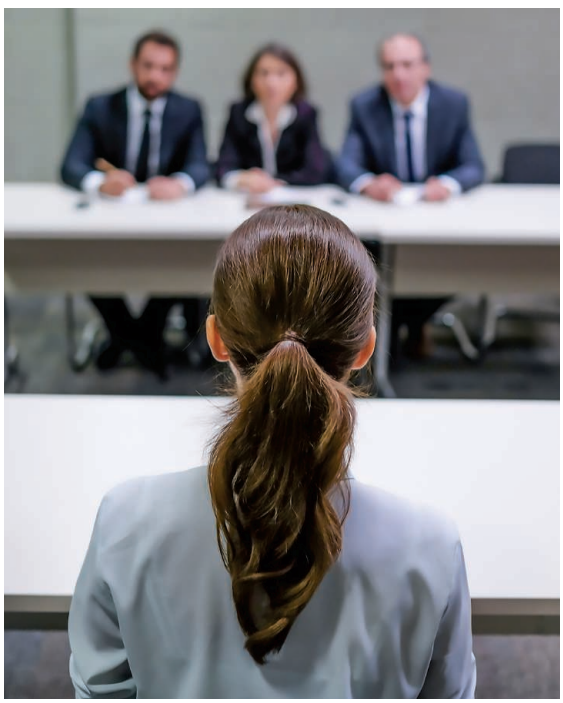

Admitting on "merit" can mean different things to different faculty.

Even more striking is that faculty rely on GRE scores in an inconsistent manner. Although we are quick to use GRE scores as a potential indicator of success for domestic students, faculty often discount the typically high scores of applicants from China, in the belief that they carry little predictive power. Of course, high and low scores can be found among applicants of all backgrounds, but faculty may unconsciously follow their own biases in ways that can stymie the goals of both quality and diversity.

Posselt offers some concrete suggestions to improve the admissions process. She suggests that departments should revisit their admissions routines and make explicit the practices used to judge applicants. Who is being cut out of the pool if a department triages prospective students based solely on GRE scores and undergraduate grade point average? Do the indicators that faculty use to predict success pan out when looking at students 3, 4, or 10 years later? These questions seem like obvious ones to ask, yet they are rarely posed in a systematic way.

Posselt also argues that Ph.D. outreach and recruitment need to be rethought. Whether departments draw from already established undergraduate summer programs at their universities or build connections with institutions that could serve as pipelines for a diverse student body, universities can do more to ensure more equitable admissions outcomes.

Finally, from my own experiences leading UChicagoGRAD (the University of Chicago's new initiative to support graduate students and postdocs to be leaders in their chosen careers), it is clear that the labor market for individuals with doctorates is changing and that the admissions process needs to change, too. When an individual with a Ph.D. goes into the academy, she often advances her adviser's work. This is the outcome many faculty aim for when making admissions decisions. However, it is also important to recognize that when an individual with a Ph.D. goes into government, industry, or the nonprofit world, he serves as a conduit for the transmission of knowledge from the academy into other sectors. We must therefore strive to admit students who are interested in diverse career paths, which will mean actively countering our inclination to admit only those students who will end up just like us.

Whether you make admissions decisions or are just curious about higher education, Posselt's book will push you to think about Ph.D. admissions in new ways. You may disagree with some of her arguments, but if you have ever sat around an admissions table, many of the episodes she recounts will likely resonate with you.

10.1126/science.aaf2200

PHOTO: EMRE OGAN/ISTOCKPHOTO

Downloaded from on March 10, 2016

Published by AAAS

LETTERS

Edited by **Jennifer Sills**

Streamlining China's protected areas

CHINA IS A mega-diverse country, harboring more than 30,000 vascular plant species and about 2340 terrestrial vertebrate species, about half of which are found exclusively in China (*1*). The conservation of this unique flora and fauna strongly depends on China's protected areas. Currently, 2729 nature reserves form the backbone of the country's protected area network. However, in December 2015, the central government started to redesignate some nature reserves as centrally controlled National Parks. This process was piloted by Sanjiangyuan Nature Reserve in Qinghai Province. Another eight national park pilots are planned in Beijing, Jilin, Heilongjiang, Zhejiang, Fujian, Hubei, Hunan, and Yunnan Provinces (*2*), with many local governments expressing a keen interest in the initiative (*3*). The overall goals of national parks are to realize "one protected area with one title, one regulation, and one management agency" and to promote the development of a coherent national park management system (*4*, *5*).

Sanjiangyuan Nature Reserve in Qinghai Province.

These objectives are extremely important, as the management of China's existing protected area network currently falls to many separate local administrations, which are associated with nine different ministries and state-level authorities. This leads to a substantial replication of administrative efforts, a fragmentation of invaluable conservation expertise, and incoherent guidance and awareness of best-practice examples. It has also resulted in the creation of partly contradictory conservation laws and regulations (*6*). Furthermore, current structures arguably underpin bad management practices such as the release of alien, potentially invasive species at protected area tourist hotspots, or the creation of tourism infrastructure threatening the spatial integrity and conservation targets of many protected areas (*7*). Protected areas are also generally established according to their individual functions, without due consideration of their wider role within the national protected area network.

The ongoing national park initiative does not explicitly address reforming the existing protected area management system and lacks strong top-down steering required to optimize the conservation performance of the protected area network. We nonetheless believe that this initiative should be used as an opportunity to establish a unified protected area management agency at the central government level that will eventually support an integrated management of the entire national protected area network. Designating one agency entrusted with full powers will alleviate the current management confusion, increase administrative effectiveness, and improve the crucial conservation effectiveness and performance of China's protected area network.

Junsheng Li,[1]* Wei Wang,[1]* Jan Christoph Axmacher,[2] Yuanyuan Zhang,[1] Yanpeng Zhu[1]

[1]Biodiversity Research Center, Chinese Research Academy of Environmental Sciences, Chaoyang District, Beijing, 100012, China. [2]UCL Department of Geography, University College London, London, WC1E 6BT, UK.

*Corresponding author. E-mail: lijsh@craes.org.cn (J.L.); wang.wei@craes.org.cn (W.W.)

REFERENCES

1. J. Liu *et al.*, *Science* **300**, 1240 (2003).
2. The Central People's Government of China, "China identified nine provinces to explore the national park pilots" (2015); www.gov.cn/xinwen/2015-06/08/content_2875563.htm [in Chinese].
3. Z. Lü, *Biodivers. Sci.* **22**, 421 (2014) [in Chinese].
4. The Central Committee of the Communist Party of China, "Decision on 'Major Issues Concerning Comprehensively Deepening Reforms'" (2013); www.scio.gov.cn/zxbd/tt/Document/1350709/1350709.htm [in Chinese].
5. The Central Committee of the Communist Party of China, State Council, "Integrated Reform Plan for Promoting Ecological Progress" (2015); www.gov.cn/guowuyuan/2015-09/21/content_2936327.htm [in Chinese].
6. J. Qiu, *Nature* **471**, 19 (2011).
7. L. Zhong *et al.*, *Biol. Conserv.* **181**, 219 (2015).

Social cost of carbon: Global duty

IN THEIR LETTER "Social cost of carbon: Domestic duty" (5 February, p. 569), A. Fraas *et al.* argue that regulations to limit greenhouse gas emissions in the United States should be evaluated in the light of the domestic benefits they provide instead of global benefits, as recommended by the Interagency Group on the Social Cost of Carbon (2010) (*1*). This idea, which has already been put into practice by some (*2*), may seem reasonable. However, climate change is a special case. No matter where a ton of carbon is emitted, it has the same impact on the atmosphere, and it ultimately leads to the same damages from climate change. As a consequence, if the United States avoids emissions, other countries will also benefit, just as the United States will benefit from other countries reducing emissions. If every country adhered to Fraas *et al.*'s proposal to focus only on its domestic benefits, all countries would end up worse off. This was demonstrated at the beginning of climate change economics (*3*).

This situation is similar to the prisoner's dilemma (*4*), in which prisoners in separate rooms are given the opportunity to betray each other in exchange for a reduced sentence. Betrayal offers a greater reward than cooperation, unless both prisoners cooperate. Given the rules of the scenario, all rational self-interested prisoners would betray one another, leading to an outcome worse than if they had cooperated. In the case of climate change, we are in a better position than the prisoners in one way: We can talk to each other and decide to cooperate. In fact, we did so already. In Paris, last December, 195 countries decided to hold "the increase in the global average temperature to well below 2°C above pre-industrial levels and to pursue efforts to limit the temperature increase to 1.5°C above pre-industrial levels, recognizing that this would significantly reduce the risks and impacts

PHOTO: WEI WANG

Downloaded from on March 10, 2016

Published by AAAS

of climate change" (*5*). Meeting this goal will not be possible if every country focuses only on its domestic benefits. The Interagency Group on the Social Cost of Carbon is right to recommend using global benefits to evaluate mitigation projects and regulations, and every country that is not doing so should follow the lead.

Céline Guivarch,[1] Aurélie Méjean,[2] Antonin Pottier,[3] Marc Fleurbaey[4]

[1]Ecole des Ponts ParisTech, CIRED, Nogent-sur-Marne, 94130, France. [2]CNRS, CIRED, Nogent-sur-Marne, 94130, France. [3]MINES ParisTech, PSL Research University, CERNA—Centre for Industrial Economics, i3, CNRS UMR 9217, Paris, 75006, France. [4]Woodrow Wilson School of Public and International Affairs-University Center for Human Values, Princeton University, Princeton, NJ 08544, USA.

*Corresponding author. E-mail: guivarch@centre-cired.fr

REFERENCES

1. Interagency Working Group on Social Cost of Carbon, Technical Support Document: Social Cost of Carbon for Regulatory Impact Analysis Under Executive Order 12866 (White House, Washington, DC, 2013); http://1.usa.gov/18ftAsH.
2. P. Watkiss, C. Hope, *Wiley Interdiscip. Rev. Clim. Change* **2**, 886 (2011).
3. W. D. Nordhaus, Z. Yang, *Am. Econ. Rev.* **86**, 741 (1996).
4. A. W. Tucker, "A two-person dilemma" (Stanford University, 1950), reproduced in *Readings in Games and Information*, E. Rasmusen, Ed. (Wiley-Blackwell, Oxford, 2001).
5. Paris Agreement, as contained in the report of the Conference of the Parties on its 21st session, FCCC/CP/2015/10/Add.1; http://unfccc.int/meetings/paris_nov_2015/items/9445.php.

Reforming China's science awards

YOUYOU TU won the Nobel Prize, yet she failed to be nominated for China's own State Science and Technology (S&T) Awards. This has triggered a fierce debate on the S&T Award evaluation system in China. S&T awards are determined by bureaucrats and social circles ("guanxi") (*1*). Because the system lacks transparency and allows no input from citizens or scientists, it is prone to opaque operations and influence by cronyism, favoritism, and bureaucracy. This has contaminated the science culture in China. Scientists feel obligated to develop "guanxi" networks instead of focusing on scientific discovery. A large portion of the country's science budget was estimated to have been wasted on networking dinners instead of invested in research labs (*1*, *2*). Such priorities lead to scientific corruption and fraud (*3*). If nothing changes, talented scientists and scientific breakthroughs will continue to be suppressed.

It is time for China to reform its S&T evaluation system. It should depend on merit, transparency, peer reviews, and objective measures. True participation by the science community should be institutionalized. The government should detach itself from the process. Decision-makers should consult with international academic circles and nongovernmental organizations. This new system is feasible with the availability of the Internet and social media. Making these changes will set an example for other countries that suffer from issues similar to China's.

Guoyou Qi,[1] Xuemei Xie,[2]* Kevin Zhu[3]

[1]School of Business, East China University of Science and Technology, Shanghai, 200237, China. [2]School of Management, Shanghai University, Shanghai, 200444, China. [3]Rady School of Management, University of California, San Diego, CA 92093-0553, USA.

*Corresponding author. E-mail: xxm1030@126.com

REFERENCES

1. Y. G. Shi, Y. Rao, *Science* **329**, 1128 (2010).
2. Y. Xie, C. Zhang, Q. Lai, *Proc. Natl. Acad. Sci. U.S.A.* **111**, 9437 (2014).
3. C. Cao, N. Li, X. Li, L. Liu, *Science* **341**, 460 (2013).

TECHNICAL COMMENT ABSTRACTS

Comment on "Math at home adds up to achievement in school"

Michael C. Frank

Berkowitz *et al.* (Reports, 9 October 2015, p. 196) described a randomized field experiment testing whether a math app designed to increase parent-child interaction could also bring academic benefits. A reanalysis of the data suggests that this well-designed trial failed to find strong evidence for the efficacy of the intervention. In particular, there was no significant effect of the intervention on math performance.

Full text at http://dx.doi.org/10.1126/science.aad8008

Response to Comment on "Math at home adds up to achievement in school"

Talia Berkowitz, Marjorie W. Schaeffer, Christopher S. Rozek, Erin A. Maloney, Susan C. Levine, Sian L. Beilock

Frank presents an alternative interpretation of our data, yet reports largely similar results to those in our original Report. A critical difference centers on how to interpret and test interaction effects. Frank finds no mistakes in our analyses. We stand by our original conclusions of meaningful effects of the Bedtime Learning Together (BLT) math app on children's math achievement.

Full text at http://dx.doi.org/10.1126/science.aad8555

Published by AAAS

TECHNICAL COMMENT

EDUCATION

Comment on "Math at home adds up to achievement in school"

Michael C. Frank*

Berkowitz *et al*. (Reports, 9 October 2015, p. 196) described a randomized field experiment testing whether a math app designed to increase parent-child interaction could also bring academic benefits. A reanalysis of the data suggests that this well-designed trial failed to find strong evidence for the efficacy of the intervention. In particular, there was no significant effect of the intervention on math performance.

Can electronic apps increase parent-child interaction around academic subjects like math and in turn help improve children's school outcomes? Berkowitz *et al.* (*1*) reported a randomized field experiment testing this hypothesis. Children were randomly assigned to math and reading app groups, and their learning outcomes were reassessed at the end of the school year. The study had a strong design, including a large sample size, objective measures of app usage, standardized outcome measures, and a well-matched control group. Unfortunately, a reanalysis of Berkowitz *et al.*'s data—which they provided as part of their Report, in a commendable show of open practices—suggests that their results provide limited support for the effectiveness of the intervention.

First, the intervention resulted in no significant improvement in math performance for the experimental group compared with the control group (Fig. 1). A longitudinal mixed-effects regression predicting math performance as a function of condition, time, and their interaction (including random intercepts for each student and classroom and random slopes for each classroom) (*2*) showed no significant condition-by-time interaction for either grade-level equivalent scores or raw scores (β_{GE} = 0.07, SE = 0.10, t = 0.73, P = 0.47; $\beta_{raw\text{-}W}$ = 1.00, SE = 1.74, t = 0.58, P = 0.56). Thus, the intervention was not successful overall.

Second, although greater use of the math app by families was related to greater growth in children's math performance, causal interpretation of this result is difficult because of endogeneity issues. Parents who used the app more might also have greater interest in math learning more generally, and both children's math gains and their app usage could plausibly reflect those underlying differences (rather than gains being a causal effect of random assignment). Further, this relationship did not reach statistical significance in all analyses. For example, when app usage is added to the longitudinal analysis described above, the three-way app usage by condition-by-time interaction was significant when computed on grade-level equivalent scores but only marginal using raw scores (β_{GE} = 0.14, SE = 0.06, t = 2.19, P = 0.03; $\beta_{raw\text{-}W}$ = 1.87, SE = 1.11, t = 1.68, P = 0.09).

Third, the authors report that the math app intervention was especially effective for those children

Department of Psychology, Stanford University, Stanford, CA, USA.
*Corresponding author. E-mail: mcfrank@stanford.edu

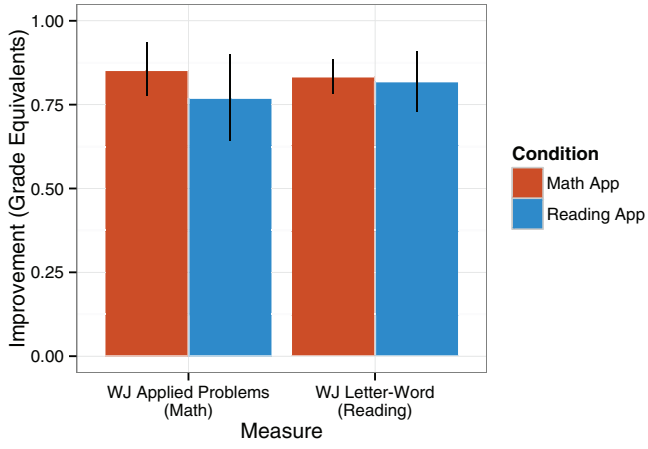

Fig. 1. Student improvement (grade-level equivalents), plotted by intervention condition and measure. Error bars show 95% confidence intervals computed by nonparametric bootstrap. The groups did not differ significantly on either measure in simple pairwise tests: $t(498)$ = 1.06, P = 0.29 for math; $t(507)$ = 0.27, P = 0.79 for reading.

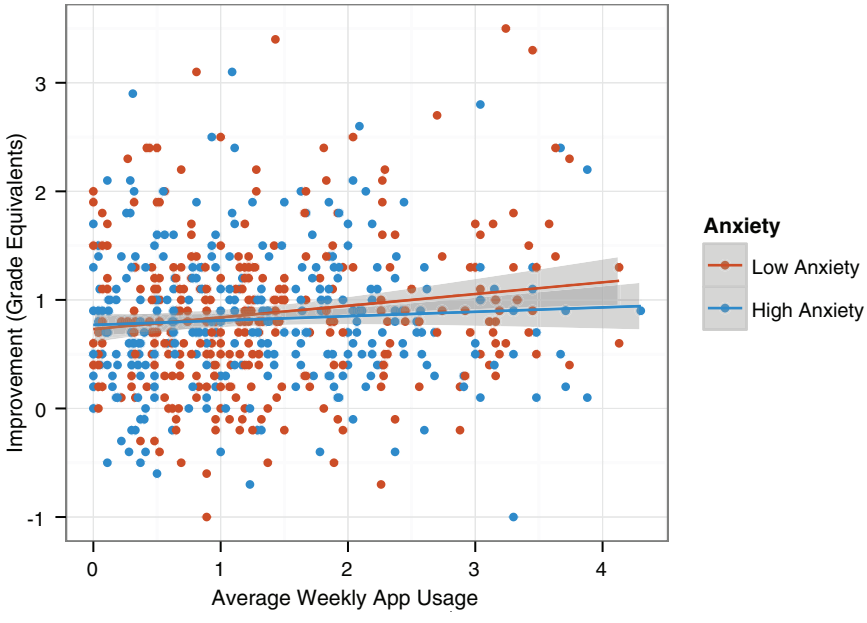

Fig. 2. Student math improvement (grade-level equivalents) for children in the math intervention condition, plotted by average weekly app usage and split by parent math anxiety. Dots show individual students, lines show the best fitting linear trend, and shaded areas show 95% confidence intervals.

Downloaded from on March 10, 2016

whose parents were anxious about math, and especially for moderate app users. These descriptive claims are not supported by the data, however (Fig. 2). On average, children of highly math-anxious parents tended numerically to learn slightly less in both the intervention and control conditions. In addition, a statistical test of the claim that an intervention is especially effective for a subgroup requires a test for an interaction rather than a comparison of separate significance tests, the analysis that was performed in the original report (*3*, *4*). But when math anxiety is added to the basic longitudinal model described above, the three-way interaction (time by condition by math anxiety) was not significant for either measure (ts ≤ 1.28, Ps ≥ 0.20). There were additionally no four-way interactions (time by condition by math anxiety by app usage) when app usage was added (ts ≤ 0.82, Ps ≥ 0.41).

Finally, although some analyses of the original data do show statistically significant support for aspects of the intervention, these analyses rely on a variety of decisions that were not specified a priori. Hence, the findings run a heightened risk of being false positives (*5*, *6*). These decisions include (i) the discretization of continuous variables into two (math anxiety) or three (app usage) categorical bins, a practice that is also known to reduce statistical power (*7*), and (ii) the specification of primary analytic models to subsets of the data rather than the full data set (e.g., only the high-anxiety group or only a matched subset of families).

Although the authors may not have chosen to report statistical tests on the basis of the tests having produced significant results, their analysis strategy was nevertheless data-dependent. Consider the scenario in which the intervention as a whole had yielded a positive effect; in that case, the simple analysis in Fig. 1 would almost certainly have been a centerpiece of the report. This analytic situation, known as the "garden of forking paths," leads to an inflation of type 1 error, just as if analyses were actively selected (*6*). Preregistration of analytic hypotheses before data collection is currently the strongest method for protecting against this problem.

In sum, Berkowitz *et al*. report a well-designed study that shows at best weak support for an app-based intervention. This result, although disappointing, is nevertheless extremely informative for parents and policy-makers interested in the potential of app-based interventions.

REFERENCES AND NOTES

1. T. Berkowitz *et al*., *Science* **350**, 196–198 (2015).
2. D. J. Barr, R. Levy, C. Scheepers, H. J. Tily, *J. Mem. Lang.* **68**, 255–278 (2013).
3. S. Nieuwenhuis, B. U. Forstmann, E. J. Wagenmakers, *Nat. Neurosci.* **14**, 1105–1107 (2011).
4. A. Gelman, H. Stern, *Am. Stat.* **60**, 328–331 (2006).
5. E. J. Wagenmakers, R. Wetzels, D. Borsboom, H. L. J. van der Maas, R. A. Kievit, *Pers. Psychol. Sci.* **7**, 632–638 (2012).
6. A. Gelman, E. Loken, *Am. Sci.* **102**, 460 (2014).
7. P. Royston, D. G. Altman, W. Sauerbrei, *Stat. Med.* **25**, 127–141 (2006).

ACKNOWLEDGMENTS

The supplementary materials contain additional data and computer code. Thanks to Berkowitz *et al*. for posting raw data and providing feedback on a draft of this reanalysis. Thanks also to J. Haushofer and the members of the Language and Cognition laboratory at Stanford for valuable feedback.

SUPPLEMENTARY MATERIALS

www.sciencemag.org/content/351/6278/aad8008/suppl/DC1
Methods
Data File

3 November 2015; accepted 21 January 2016
10.1126/science.aad8008

TECHNICAL RESPONSE

EDUCATION

Response to Comment on "Math at home adds up to achievement in school"

Talia Berkowitz, Marjorie W. Schaeffer, Christopher S. Rozek, Erin A. Maloney, Susan C. Levine,* Sian L. Beilock*

Frank presents an alternative interpretation of our data, yet reports largely similar results to those in our original Report. A critical difference centers on how to interpret and test interaction effects. Frank finds no mistakes in our analyses. We stand by our original conclusions of meaningful effects of the Bedtime Learning Together (BLT) math app on children's math achievement.

The Bedtime Learning Together (BLT) math app provides a structured way for parents to increase math engagement with their children. Families were randomized at the classroom level to receive either a math or reading app. We hypothesized that the math app would increase children's math learning over the school year. Logically, we only predicted that the math app would improve students' math achievement if used. Based on our previous research showing that (i) high-math-anxious parents and teachers negatively affect children's math achievement (*1*, *2*), (ii) people with high math anxiety avoid math (*3*), and (iii) talking about math with children enhances math achievement (*4*–*8*), we also hypothesized that the math app would be most effective for children with high-math-anxious parents. The data support our hypotheses.

Frank raises issues with our data analysis (*9*). He argues that some of our analyses are "data-dependent"—that is, driven by our obtained results rather than by theory. This claim is unfounded because our previous work in this area directly leads to the a priori hypotheses that we posited.

Frank then goes on to reanalyze our data using tests that are less statistically powerful, and in our view less appropriate, than in the original Report and finds weaker yet similar results. We have a philosophical disagreement with Frank about the most appropriate analyses to employ. As we lay out below and in the original Report, we view our analyses as most appropriate for informing our hypotheses.

In our analyses, we wanted to assess whether the math app was specifically impactful for children of high-math-anxious parents. Thus, we split children into groups based on their parents' math anxiety levels. Our intent-to-treat (ITT) analysis confirms a significant effect of app group, with children in the math group outperforming those in the reading group when parents are high-math-anxious $[\hat{\beta}_{21} = 5.25, t = 1.99, P = 0.048]$ but not when parents are low-math-anxious $[\hat{\beta}_{31} = -0.61, t = -0.27, P = 0.79]$. Even though comparing the coefficients of intent-to-treat effects for children of high- and low-math-anxious parents (i.e., the interaction between parent-math-anxiety and app condition) is a low-powered test, especially in field trials (*10*, *11*), we see a marginally significant difference between the coefficients estimating the effects of the math app for these two groups of children at $P = 0.06$ (significant at $P = 0.03$ using a one-tailed test given our a priori hypothesis). In field trials like ours, not testing for preplanned contrasts because of a nonsignificant interaction term can lead to unnecessarily missing heterogeneous treatment effects and, as a result, to misleading conclusions, both practically and theoretically (*10*, *11*).

The ITT analysis underestimates the effect of using the app because it does not take app use into account (*12*). We can obtain an unbiased estimate of the effect of app use by using randomization as an instrumental variable (IV) to identify the effect of actual app use (*12*). We conducted an IV analysis on end-of-year math achievement (controlling for beginning-of-year math achievement), which estimates the effect of dosage on those whose dosage was induced by randomization. As in the ITT analysis, we obtained a significant effect of math app use on children of high-math-anxious parents (*13*) (Model S6). This analysis suggests that there is a causal effect of math app usage on end-of-year math achievement for the children of high-math-anxious parents and that this effect is negligibly influenced by selection bias, in contrast to Frank's speculation.

In our other main analysis, we show that the more times parents and their children used the app, the higher children's math achievement at school-year's end (controlling for beginning-of-year math achievement), but only for children in the math group—a group by use interaction

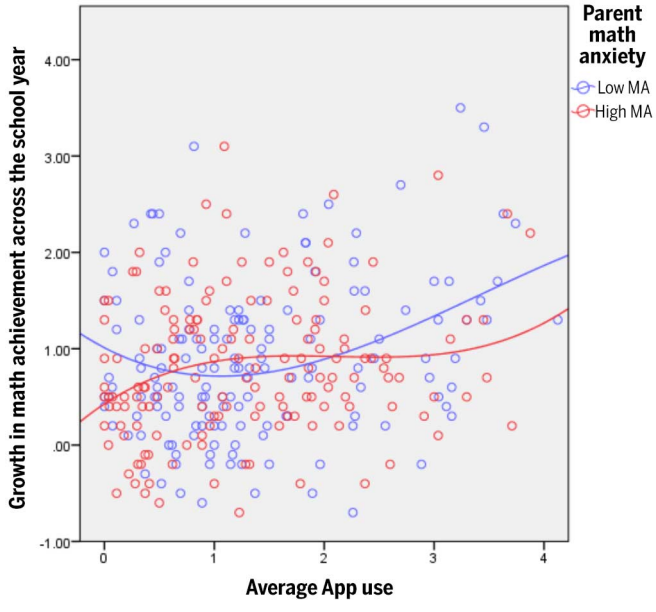

Fig. 1. The nonlinear relation between app usage and growth in math achievement across the school year (grade-equivalent change) in the math app group. As stated in the original Report, we use grade-equivalent change scores for illustrative purposes only; all analyses are conducted on W scores (a Rasch-scale score with equal intervals and thus the most appropriate outcome for our analyses). Beyond 3.29 average app uses per week, one is looking at 16 out of 310 families that fall more than 2 SD above the mean of app use. One should be cautious about conclusions regarding group differences in growth in math achievement across the school year based on this small number of families.

University of Chicago, Chicago, IL, USA.
*Corresponding author. E-mail: s-levine@uchicago.edu (S.C.L.); beilock@uchicago.edu (S.L.B.)

Downloaded from on March 10, 2016

$[\hat{\beta}_{21} = 4.03, t = 2.83, P = 0.005]$ (*13*) (Model S1). This interaction is for children matched within schools, which is most appropriate for comparing the math and reading groups. However, when using the entire sample, the interaction holds $[\hat{\beta}_{21} = 2.55, t = 2.25, P = 0.03]$.

Conducting the above analysis using change scores, as Frank does, is a weaker-powered and less appropriate test than using end-of-year achievement as an outcome, controlling for beginning-of-year achievement as we do in our model (*14*). Further, we view the choice to examine only children who attend a school with classrooms in both conditions as the most conservative test of our hypothesis, given the possibility of school-level differences. For example, if students in the math group came from schools with stronger math instruction than students in the reading group, we might see a large advantage for the math group in terms of math growth over the school year, due to a selection bias instead of randomization to condition. Using a combination of lower-powered tests that do not control for school-level effects contributed to the marginally significant effect that Frank obtained. The statistical tests we report, which we consider more appropriate, show a significant effect of app usage in the math group but not in the reading group. We note that, although app use analyses do not equivocally rule out selection bias, showing strong effects of app use for the math but not the reading group does control for at least one family of endogeneity effects (e.g., parents' propensity to use an app with their children).

Finally, by binning app usage as a secondary analysis, we explored how usage amounts that were understandable in real-word terms related to math growth (e.g., once-a-week app use versus very little). As seen in Berkowitz *et al.*'s figure 2 (*13*) and Fig. 1 below, once-a-week app usage helps close the gap in math achievement growth between children with high- and low-math-anxious parents (although achievement is higher among children of low-math-anxious parents when app usage is highest). We note that the cubic pattern, the best fit for our data (Fig. 1), looks quite similar to the pattern highlighted in our binned data. For reference, there is a significant app use (cubic term of the continuous variable) by parent-math-anxiety interaction on children's end-of-year math achievement (controlling for beginning-of-year math achievement) $[\hat{\beta} = -1.21, t = 3.75, P < 0.001]$.

In sum, we view our data-analytic strategy as appropriate and as providing support for the efficacy of the BLT math app for promoting children's math achievement. We welcome debate about data analysis and hope that this discussion benefits the scientific community.

REFERENCES

1. E. A. Maloney, G. Ramirez, E. A. Gunderson, S. C. Levine, S. L. Beilock, *Psychol. Sci.* **26**, 1480–1488 (2015).
2. S. L. Beilock, E. A. Gunderson, G. Ramirez, S. C. Levine, *Proc. Natl. Acad. Sci. U.S.A.* **107**, 1860–1863 (2010).
3. R. Hembree, *J. Res. Math. Educ.* **21**, 33–46 (1990).
4. S. C. Levine, L. W. Suriyakham, M. L. Rowe, J. Huttenlocher, E. A. Gunderson, *Dev. Psychol.* **46**, 1309–1319 (2010).
5. E. A. Gunderson, S. C. Levine, *Dev. Sci.* **14**, 1021–1032 (2011).
6. S. C. Levine, K. R. Ratliff, J. Huttenlocher, J. Cannon, *J. Dev. Psychol.* **48**, 530–542 (2012).
7. S. M. Pruden, S. C. Levine, J. Huttenlocher, *Dev. Sci.* **14**, 1417–1430 (2011).
8. B. N. Verdine, C. M. Irwin, R. M. Golinkoff, K. Hirsh-Pasek *J. Exp. Child Psychol.* **126**, 37–51 (2014).
9. M. C. Frank, *Science* **351**, 1161 (2016).
10. C. F. Manski, *Social Choice with Partial Knowledge of Treatment Response* (Princeton University Press, 2005).
11. G. H. McClelland, C. M. Judd, *Psychol. Bull.* **114**, 376–390 (1993).
12. J. D. Angrist, G. W. Imbens, D. B. Rubin, *J. Am. Stat. Assoc.* **91**, 444–455 (1996).
13. T. Berkowitz *et al.*, *Science* **350**, 196–198 (2015).
14. G. J. P. Van Breukelen, *J. Clin. Epidemiol.* **59**, 920–925 (2006).

19 November 2015; accepted 21 January 2016
10.1126/science.aad8555

RESEARCH ARTICLE SUMMARY

BACTERIAL PILI

Architecture of the type IVa pilus machine

Yi-Wei Chang, Lee A. Rettberg, Anke Treuner-Lange, Janet Iwasa, Lotte Søgaard-Andersen, Grant J. Jensen*

INTRODUCTION: Type IVa pili are bacterial cell surface structures that perform critical functions in motility, surface adhesion, virulence, and biofilm formation. Type IVa pili are anchored in the cell envelope and pull cells forward through cycles of extension, adhesion to surfaces, and retraction, all powered by the type IVa pilus machine (T4PM). Although the structures and connectivities of the 10 core T4PM proteins and minor pilins have already been determined, the overall architecture of the T4PM and its extension and retraction mechanisms have not.

RATIONALE: To elucidate the architecture of the intact T4PM, we directly imaged T4PMs within intact *Myxococcus xanthus* cells by cryo–electron tomography. Mutants that either lacked T4PM components or contained individual T4PM proteins fused to a tag were then imaged. Difference maps revealed the locations of all components of the T4PM machine. Hypothetical models were then built by fitting the known atomic structures of the components together in their relative positions.

RESULTS: Both piliated and nonpiliated T4PMs are multilayered structures that span the entire cell envelope. T4PMs include an outer membrane pore, three interconnected periplasmic ring structures and another in the cytoplasm, a cytoplasmic disc and dome, and a periplasmic stem. The PilQ secretin forms the outer membrane pore; TsaP forms a periplasmic ring around PilQ; periplasmic domains of PilQ together with PilP constitute the mid-periplasmic ring; and the globular domains of PilO and PilN constitute the lower periplasmic ring and connect via coiled coils across the inner membrane to PilM, which forms the cytoplasmic ring. The cytoplasmic domains of the inner membrane protein PilC form the cytoplasmic dome on the T4PM axis inside the PilM ring. The short stem in the nonpiliated state is composed of minor pilins and PilA, the major subunit of the pilus. In the piliated state, the pilus extends from the cell exterior through the PilQ pore and the periplasmic rings to PilC in the inner membrane. In the piliated structure, the hexameric adenosine triphosphatases (ATPases) PilB and PilT bind in a mutually exclusive manner to the base of the T4PM, where they appear as the cytoplasmic disc during extensions and retractions, respectively.

ON OUR WEB SITE

Read the full article at http://dx.doi.org/10.1126/science.aad2001

Next, we asked whether the known atomic structures of the proteins could be fit within the map where our imaging results indicated, while still satisfying all known constraints of size, connectivities, and interfaces. This successful effort resulted in "pseudo-atomic" working models of both states of the T4PM. The models suggest that through ATP hydrolysis, PilB rotates PilC, incrementally moving it into positions that facilitate incorporation of new PilA subunits one by one from the inner membrane onto the base of the growing helical pilus. Pilus retraction is driven by replacement of PilB with PilT, which rotates PilC into positions that promote PilA departure from the base of the pilus back into the membrane.

CONCLUSION: We determined the architecture of the T4PM in the piliated and nonpiliated states and mapped all known components onto this architecture, producing a complete structural map of the T4PM. The results illustrate how the structure and function of macromolecular complexes that defy purification and traditional structural approaches can nonetheless be interrogated through cryo–electron tomography of intact cells and model building. ■

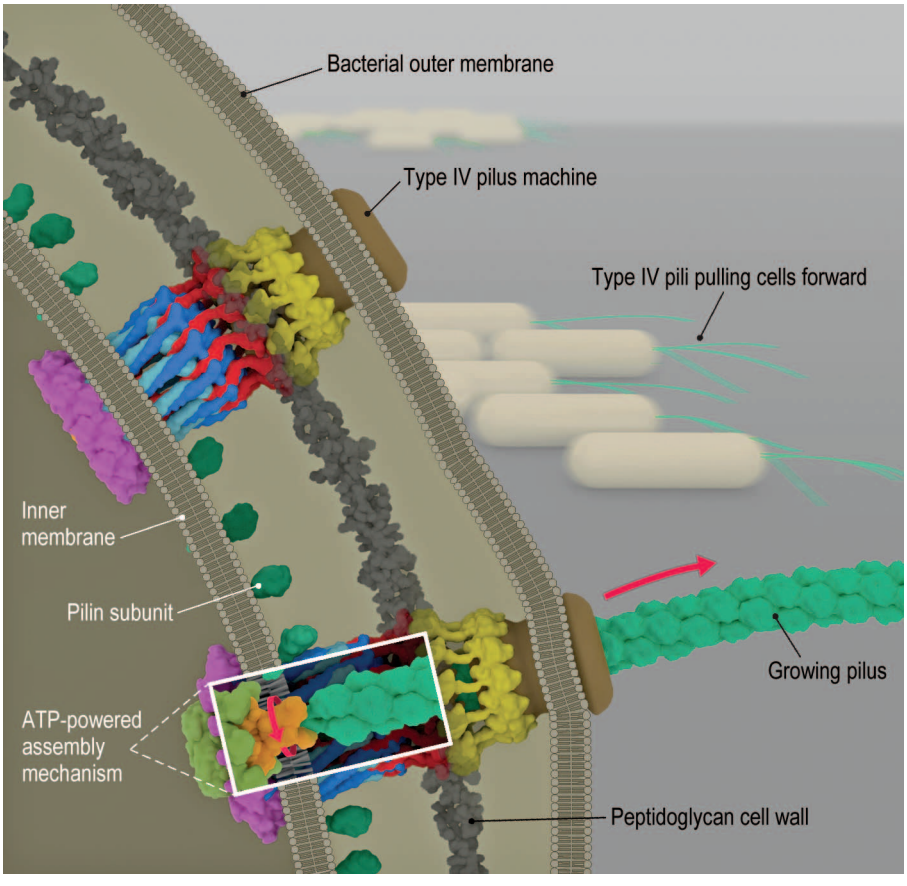

Bacterial type IVa pilus machine (T4PM). Two T4PMs are depicted on the left, spanning the envelope of a Gram-negative bacterial cell. T4PMs extend and retract pili to pull cells forward. The structural data presented here support the hypothesis that ATP hydrolysis in the cytoplasm causes an adapter protein in the inner membrane to rotate, facilitating the transfer of pilin subunits from the inner membrane onto the growing pilus. The process is reversed during retraction.

The list of author affiliations is available in the full article online.
*Corresponding author. E-mail: jensen@caltech.edu
Cite this article as Y.-W. Chang *et al.*, *Science* 351, aad2001 (2016). DOI: 10.1126/science.aad2001

Downloaded from on March 10, 2016

RESEARCH ARTICLE

BACTERIAL PILI

Architecture of the type IVa pilus machine

Yi-Wei Chang,[1,2] Lee A. Rettberg,[2] Anke Treuner-Lange,[3] Janet Iwasa,[4] Lotte Søgaard-Andersen,[3] Grant J. Jensen[1,2]*

Type IVa pili are filamentous cell surface structures observed in many bacteria. They pull cells forward by extending, adhering to surfaces, and then retracting. We used cryo–electron tomography of intact *Myxococcus xanthus* cells to visualize type IVa pili and the protein machine that assembles and retracts them (the type IVa pilus machine, or T4PM) in situ, in both the piliated and nonpiliated states, at a resolution of 3 to 4 nanometers. We found that T4PM comprises an outer membrane pore, four interconnected ring structures in the periplasm and cytoplasm, a cytoplasmic disc and dome, and a periplasmic stem. By systematically imaging mutants lacking defined T4PM proteins or with individual proteins fused to tags, we mapped the locations of all 10 T4PM core components and the minor pilins, thereby providing insights into pilus assembly, structure, and function.

Type IVa pilus machines (T4PMs) are part of a superfamily of bacterial and archaeal multiprotein assemblies that also include type IVb pilus machines, type II secretion systems (T2SS), DNA uptake systems, and archaeal flagella (*1*, *2*). T4PMs are involved in cell motility (*3*), host adhesion (*4*), predation (*5*), DNA uptake (*6*), biofilm formation (*7*, *8*), and protein secretion (*9*). T4PMs consist of an extracellular pilus fiber (T4P) and a cell envelope–spanning complex that we refer to here as the basal body. A key feature of T4Ps is their ability to undergo cycles of extension and retraction (*10*, *11*). Powered by a T4P-assembly adenosine triphosphatase (ATPase), the basal body extracts pilin monomers from the inner membrane (IM) and appends them onto the base of the helical pilus fiber, pushing the fiber outward. The fiber has a diameter of ~6 nm, can extend up to several micrometers in length, and can adhere to specific surfaces (*12*). Subsequently, the basal body, powered by a T4P-disassembly ATPase, extracts monomers from the pilus base back into the membrane (*13*). T4PMs retract at rates up to 1 μm/s and generate forces as high as 150 pN to pull the cell forward (*14*, *15*), making T4PMs the strongest molecular motors known. T4Ps have been identified as important virulence factors in several human pathogens, including *Neisseria gonorrhoeae*, *N. meningitidis*, and *Pseudomonas aeruginosa* (*16*).

T4PMs exhibit a multilayered structure spanning the cell envelope of *M. xanthus*

To determine the structure of the T4PM in vivo, we used cryo–electron tomography (also known as electron cryotomography) to image the cell poles of *Myxococcus xanthus*, a ubiquitous rod-shaped soil-residing predatory bacterium (Fig. 1A). (Examples of a tilt series and a cryotomogram are shown in movies S1 and S2, respectively). T4Ps with diameters of ~6 nm were easily recognized on the cell surface with their basal bodies spanning the cell envelope (Fig. 1B, white arrows). Basal bodies exhibited three layers of densities in the periplasm and a fourth in the cytoplasm (Fig. 1C). In the vicinity of piliated T4PMs, we also observed "empty" nonpiliated basal bodies with similar structures but without long fibers attached (Fig. 1B, black arrow, and Fig. 1D).

To reveal details, we generated subtomogram averages of the piliated T4PM and nonpiliated basal bodies with local resolution between ~2.5 nm and 4.5 nm (Fig. 1F and fig. S1, A and B). We later determined that a Δ*pilB* mutant (which lacks the PilB T4P-assembly ATPase and cannot assemble T4P) produced better-quality images of the empty basal body (likely due to the basal bodies being stalled in a "pilus preassembly" state and therefore more structurally homogeneous than in the wild type; see below), so we used the average from this strain for subsequent structural interpretation (Fig. 1G).

We found that the structure of the piliated T4PM basal body comprises an outer membrane (OM)–spanning pore including a ring immediately below the OM, two distinct rings in the periplasm, another ring in the cytoplasm surrounding a disc-like structure, and a long stem originating at the IM and passing through the periplasmic rings and OM pore (Fig. 1F). The structure of the empty basal body shows several similar structural features, including an OM pore with a ring immediately below the OM, two periplasmic rings, and a cytoplasmic ring, as well as a gate density in the OM pore, connections between the OM pore and the mid-periplasmic ring, connections between the lower periplasmic ring and the IM, a much shorter stem, and no cytoplasmic disc (Fig. 1G). In the absence of the cytoplasmic disc, a cytoplasmic dome is also apparent. Aligning the averages of piliated and empty basal bodies with the IM reveals clear conformational changes upon piliation (movie S3). Going from the nonpiliated to the piliated state, the OM pore is ~2 nm farther away from the mid-periplasmic ring (13.9 to 15.7 nm). Also, the diameter of the cytoplasmic ring in the piliated state is greater by ~4 nm (18.4 versus 14.4 nm), possibly because of its association with the cytoplasmic disc (Fig. 1, E and H).

Mapping components in the molecular envelope by imaging T4PM mutants

Ten highly conserved proteins are known to constitute the T4PM (*16*, *17*). PilA, the major pilin protein, contains an N-terminal hydrophobic α helix and alternates between being anchored individually in the IM or bundled with other PilA N-terminal α helices to form the central pilus core (*18*). The remaining nine proteins are divided into three subgroups according to their location and function: the OM pore complex (PilQ and TsaP); the alignment complex (PilM, PilN, PilO, and PilP); and the motor complex (PilB, PilT, and PilC) (*19*). To systematically localize each component within the basal body, we imaged a series of *M. xanthus* mutants with individual T4PM proteins either missing or fused to a superfolder green fluorescent protein (sfGFP) (*20*) tag. Difference maps between the resulting subtomogram averages of the T4PM mutants and the wild-type structures were then calculated (Fig. 2). Combined with information already available about the accumulation, subcellular localization, and incorporation of individual T4PM proteins into the T4PM basal bodies of these mutants (fig. S2) and their connectivities and structures (fig. S3) (*17*, *18*, *21*–*40*), these maps allowed us to pinpoint each component within the T4PM (Figs. 2 and 3A).

PilQ

A previous study showed that knocking out *pilP* accelerates degradation of PilM, PilN, and PilO and causes mislocalization of PilC, whereas PilQ and TsaP remain stable and at the cell pole, forming a rudimentary T4PM basal body consisting only of PilQ and TsaP (fig. S2) (*21*). This suggests that PilP is crucial for stabilizing and linking other components to the OM pore complex. We therefore first imaged the Δ*pilP* mutant to obtain the structure of the OM pore complex (PilQ and TsaP) alone (Fig. 2, B1). The average showed a cylindrical channel in the OM with a clear gate and a large periplasmic vestibule. The overall structure is reminiscent of single-particle reconstructions of secretin channel complexes in T4PM, T2SS, and type III secretion systems (T3SS) (*41*–*44*) (fig. S4). Superposing the highly conserved gate and periplasmic vestibule regions, our in vivo structure was seen to be markedly longer in the transmembrane region than the structures generated from single-particle analyses, probably because the detergent

[1]California Institute of Technology, Pasadena, CA 91125, USA. [2]Howard Hughes Medical Institute, Pasadena, CA 91125, USA. [3]Max Planck Institute for Terrestrial Microbiology, 35043 Marburg, Germany. [4]University of Utah, Salt Lake City, UT 84112, USA.
*Corresponding author. E-mail: jensen@caltech.edu

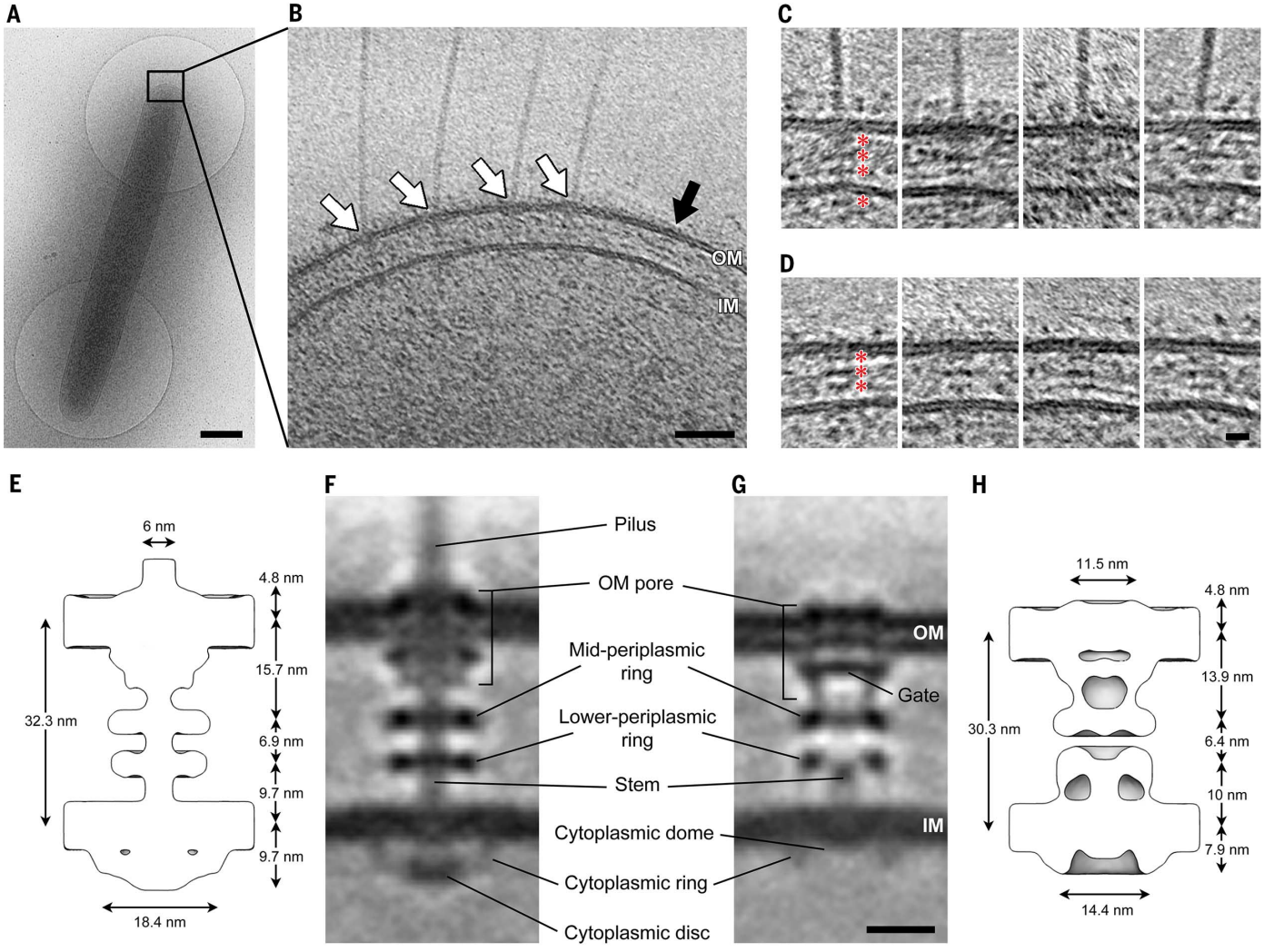

Fig. 1. Visualizing the T4PM in intact *M. xanthus* cells. (**A**) A frozen-hydrated *M. xanthus* cell on an EM grid. (**B**) Slice through tomogram of the cell pole. White arrows, piliated T4PM basal bodies; black arrow, an empty T4PM basal body. Outer and inner membranes (OM and IM) are indicated. (**C** and **D**) Examples of slices through subtomograms containing piliated and empty T4PM basal body structures, respectively. Red asterisks denote periplasmic and cytoplasmic density layers. (**E** and **H**) Schematic envelopes of the subtomogram averages of wild-type piliated (E) and Δ*pilB* empty (H) T4PM basal bodies, showing their molecular dimensions. (**F** and **G**) Slices through subtomogram averages of wild-type piliated (F) and Δ*pilB* empty (G) T4PM basal bodies, with annotations of structural features. Scale bars, 500 nm (A), 50 nm (B), 5 nm [(C) and (D)], 10 nm [(F) and (G)].

solubilization used in the single-particle reconstructions fails to support this structure. By comparing the Δ*pilP* mutant structure to that of the wild-type empty basal body (Fig. 2, B2), and noting that the single-particle reconstructions contained no TsaP, we infer that PilQ forms the OM channel as well as part of the mid-periplasmic ring (Fig. 2, B3).

PilP

Because PilP is known to interact directly with PilQ (*21*, *26*) and the Δ*pilP* structure shows a decrease in density of the mid-periplasmic ring (Fig. 2, B2), we hypothesized that PilP is part of the mid-periplasmic ring. To confirm this, we imaged a mutant in which PilP is fused to sfGFP, giving rise to an active fusion protein (fig. S2). Consistently, in this strain, additional densities appeared at the periphery of the mid-periplasmic ring (Fig. 2, C1 to C5).

TsaP

Single-particle EM reconstructions have shown that TsaP forms a ring-like structure surrounding the PilQ channel, but only top views were obtained (*17*). To localize TsaP in the OM pore complex in three dimensions, we imaged a Δ*tsaP* mutant (Fig. 2, D1 and D3). In the Δ*tsaP* mutant, all other T4PM proteins accumulate and are incorporated into the T4PM basal body as in the wild type (fig. S2) (*17*). Difference maps pinpointed TsaP's location to the upper periplasmic region of the OM pore complex just beneath the OM in both the piliated and empty basal bodies [Fig. 2, D2 (white arrow), D4 (white arrow), and D5]. Lack of TsaP caused disengagement of the OM channel from the mid-periplasmic ring in the empty basal body (Fig. 2, D3, black arrow; note that the extensive systematic differences in Fig. 2, D4, reveal a global shift of the periplasmic rings and IM), making the overall length of the complex similar to that of the piliated basal body. In a previous study, lack of TsaP resulted in accumulation of pilus fibers in the periplasm in *N. gonorrhoeae* and formation of fewer pili in *M. xanthus*, suggesting a role for TsaP in correct PilQ channel function (*17*). Consistently, during our imaging, we observed that in the Δ*tsaP* mutant, about one-tenth as many pili were found on cell poles relative to wild-type cells (table S1).

PilO and PilN

Because knocking out *pilO* disrupts the entire alignment complex and causes mislocalization of

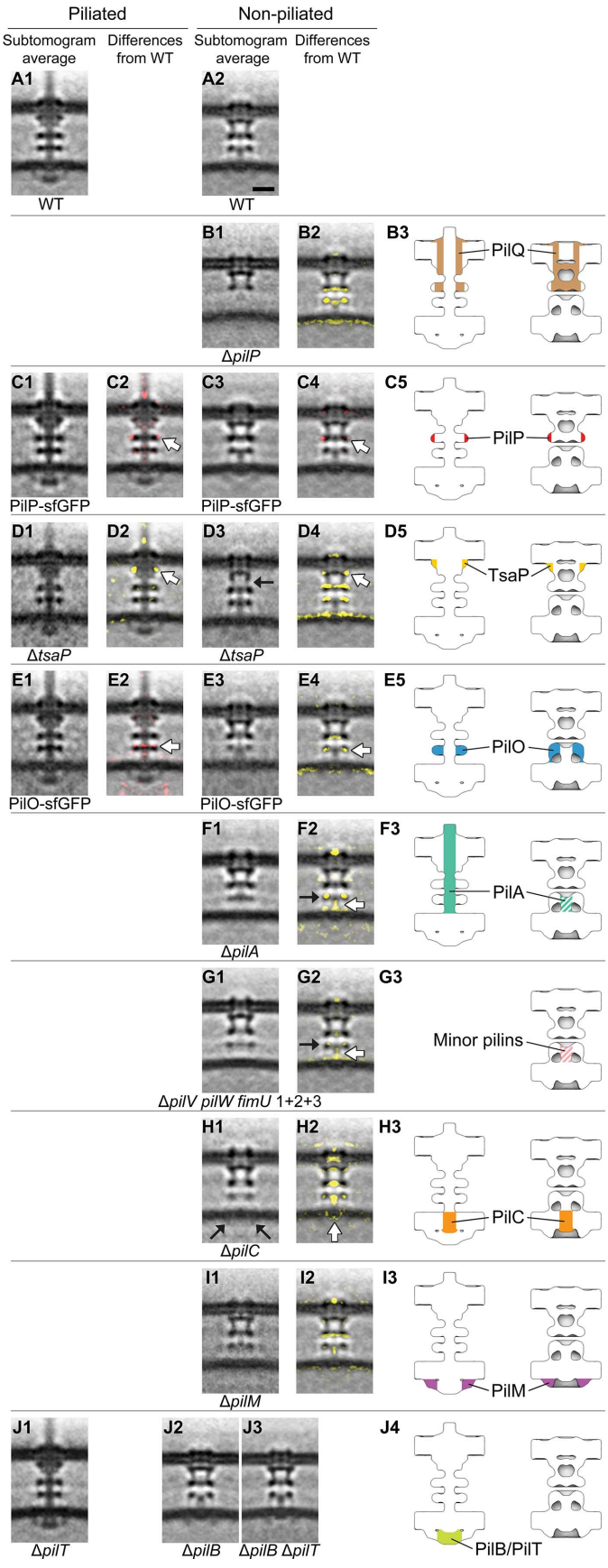

Fig. 2. Mapping T4PM components. First and third columns: Central slices of subtomogram averages of piliated and empty T4PM basal bodies, respectively, from different *M. xanthus* strains. Second and fourth columns: Differences in the T4PM mutant structures versus the wild type (red and yellow colors respectively denote addition and omission of densities, with opacities of 10%, 20%, 30%, 40%, and 50% corresponding to density differences of 1, 1.5, 2, 2.5, and 3 standard deviations, respectively, overlaid on the wild-type subtomogram averages). White arrows indicate the component locations identified by the difference maps. Fifth column: Schematic representations of piliated (left) and empty (right) T4PM basal bodies showing each identified component location. Scale bar in A2, 10 nm (applies to columns 1 through 4).

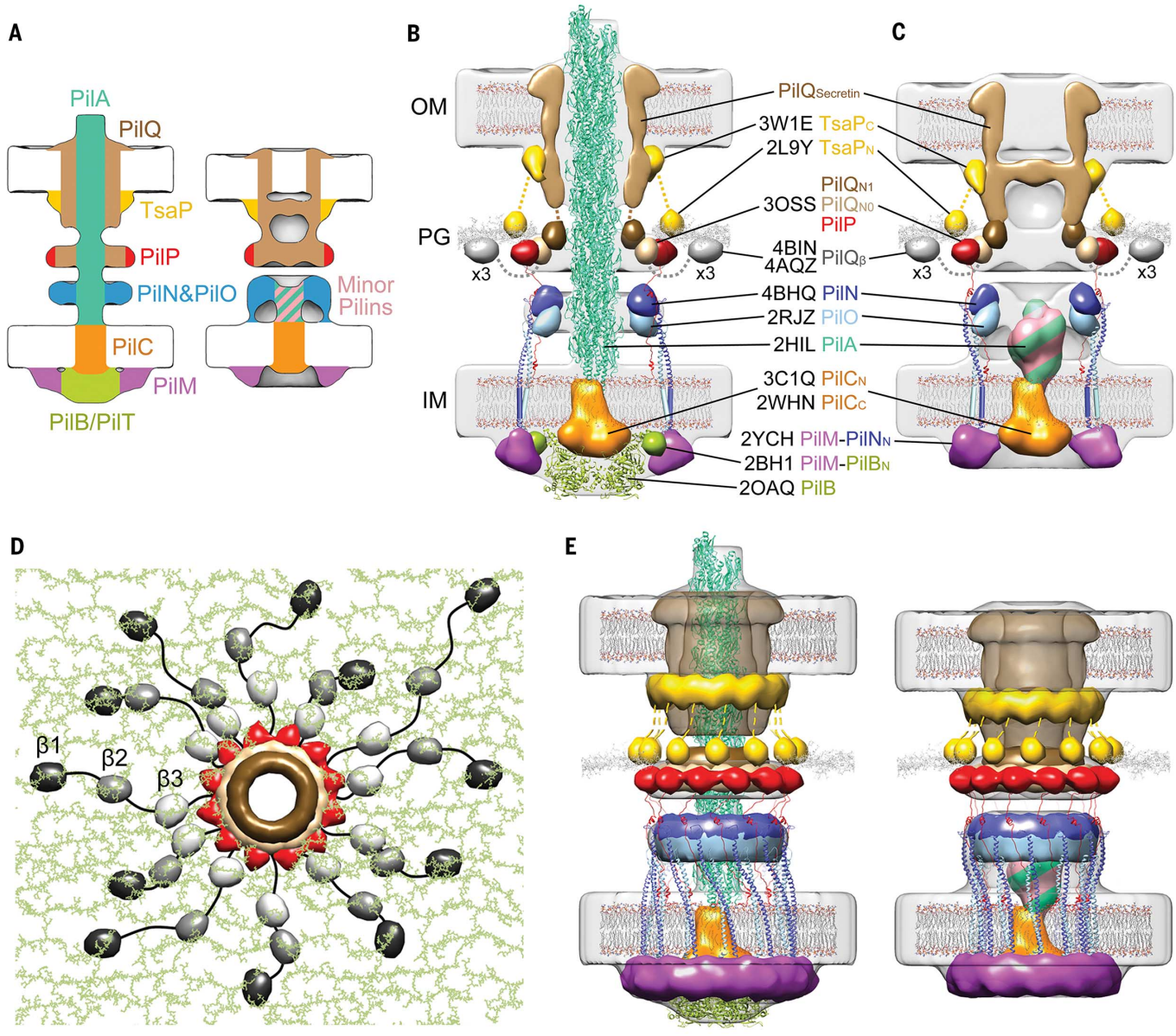

Fig. 3. Architectural models of the T4PM. (**A**) Summary schematics showing the component locations identified in the piliated and empty T4PM basal body structures. (**B** and **C**) Central slices of the architectural models of piliated and empty T4PM basal bodies, respectively, in which atomic models of T4PM components are placed in the in vivo envelopes according to the component maps in (A) and previously reported constraints and filtered to 3-nm resolution. (The process of how each component was placed is detailed in Movie 1 and the supplementary materials.) Models of each component are colored as in (A), with the transmembrane segments of PilN and PilO shown as cylinders; "x3" indicates three AMIN domains per PilQ monomer, only one of which is shown. Note that the empty T4PM basal body is shown with five PilA major pilin subunits in the short stem; however, the short stem likely also contains minor pilins. (**D**) Top view of the PilP HR domains and the PilQ N0 and N1 domains in the architectural model [colored as in (B) and (C)], with PG model (colored green) as background; 36 AMIN (β) domain models from 12 PilQ proteins are randomly placed on PG and connected by long flexible linkers (black) with lengths within 20 nm between β1 and β2 domains (70 residues), 12 nm between β2 and β3 domains (40 residues), and 12 nm between β3 and N0 domains (40 residues). (**E**) Overall architectural models of piliated (left) and empty (right) T4PM basal bodies. For clarity, the PilQ AMIN domains displayed in (D) are not shown.

PilC, leaving only PilQ and TsaP in the basal body (fig. S2) (*21*), we imaged a mutant with an active PilO-sfGFP fusion protein to map the location of PilO (fig. S2). In the piliated structure, we observed additional density in the lower periplasmic ring (Fig. 2, E1 and E2), but in the empty basal body structure, we observed decreased density in this ring (Fig. 2, E3 and E4). Both results suggest that PilO localizes to the lower periplasmic ring (Fig. 2, E5), because the sfGFP tag likely added density to the ring in the piliated form but perturbed the ring in the empty basal body. As with *pilO*, a Δ*pilN* mutant also disrupts the entire alignment complex and also causes mislocalization of PilC, leaving only PilQ and TsaP in the basal body (fig. S2) (*21*). So far, we have been unable to generate a functional PilN protein fused to a tag. Therefore, the same method could not be used to localize PilN in the T4PM basal body. Nonetheless, the two structural homologs PilO and PilN interact directly (*21*, *30*), likely forming heterodimers (*30*). Therefore, we assume that PilN is also located in the lower periplasmic ring.

PilA and minor pilins

In the wild-type piliated basal body structure, we observed a rod-like stem structure that passes up

from the IM through the lower periplasmic ring, mid-periplasmic ring, and OM pore. This stem has the same diameter as the PilA helical polymer (*18*) (~6 nm) and is directly connected to the pilus outside of the cell. Also, this long stem is missing in the empty basal body structure. These observations suggest that the stem is the part of the pilus fiber located in the periplasm and is associated with the basal body. In the empty basal body, a short stem is also present between the lower periplasmic ring and the IM. To investigate whether this remaining short stem is formed by PilA or by other T4PM components, we first imaged a Δ*pilA* mutant that lacks the major pilin PilA. As expected (*45*), no T4P formed in this mutant.

In agreement with the observation that the T4PM assembles in a Δ*pilA* mutant (fig. S2) (*21*), we were able to identify empty basal body structures in the cells and generate an average of the Δ*pilA* mutant, which clearly lacked any stem [Fig. 2, F1 and F2 (white arrow)]. Because the minor pilins in *P. aeruginosa* were recently suggested to form a complex that primes pilus assembly (*46*) and the four minor pseudopilins in the T2SS are thought to prime pseudopilus formation by the major pseudopilin (*47*, *48*), we generated mutants lacking as many as nine of the 10 minor pilins encoded in the *M. xanthus* genome (fig. S5A). Lack of nine of the minor pilins abolished T4P-dependent motility, and T4P did not assemble; however, all 10 core components of the T4PM accumulated at wild-type levels in total cell extracts (fig. S5, B to D). Consistently, when we imaged the mutant deleted for nine of the minor pilin genes, we did not detect T4P (table S1). We did, however, detect empty basal body structures, and they clearly lacked the short stem [Fig. 2, G1 and G2 (white arrow)].

On the basis of these observations, we conclude that the extended stem is made of the major pilin PilA (Fig. 2, F3) and that the short stem is composed of an assembly-priming complex consisting of minor pilins and PilA (Fig. 2, F3 and G3). In the PilA and minor pilin mutants, the structure of the lower periplasmic ring was perturbed and the short stem was absent (Fig. 2, F2 and G2, black arrows). Because it is unlikely for PilA to withdraw its hydrophobic α helix from the IM or pilus fiber to participate in the lower periplasmic ring, the simultaneous changes of the short stem and the lower periplasmic ring suggest a structural/functional linkage between them (see below).

PilC, PilM, PilB, and PilT

The T4PM components PilC, PilM, PilB, and PilT all have folded cytoplasmic domains and are therefore the candidates for the cytoplasmic ring, disc, and dome. Within the set of single-gene knockouts of these four proteins, only empty basal bodies were found on the Δ*pilC*, Δ*pilM*, and Δ*pilB* cells, as expected (Fig. 2, H1, I1, and J2), and only piliated T4PM basal bodies were found on the Δ*pilT* cells (Fig. 2, J1). In these four mutants, all the remaining T4PM proteins accumulated (fig. S2). Because the cytoplasmic ring was missing in the Δ*pilM* mutant (Fig. 2, I1) but appeared unperturbed in the Δ*pilC*, Δ*pilB*, and Δ*pilT* mutants, we conclude that the ring is composed of PilM (Fig. 2, I3). Because the ring and dome were retained in the Δ*pilB* mutant but not the disc, the disc must be PilB (Fig. 2, J2 and J4). The fact that the cytoplasmic disc had a size corresponding to that of a hexameric secretion or traffic ATPase (*37*–*40*) also strengthens this conclusion (see below). The cytoplasmic dome and disc were both missing in the Δ*pilC* mutant (Fig. 2, H2), but the cytoplasmic ring was still present (Fig. 2, H1, black arrows), which suggests that the dome is composed of PilC and that the PilB disc does not localize in its absence (Fig. 2, H3). Notably, the short stem structure was also missing in the Δ*pilC* structure, revealing that PilC is required to stabilize it.

With the identification of the ring as PilM, the dome as PilC, and the disc as PilB, it follows that (i) the PilM ring assembles in the absence of the PilC dome or PilB disc, (ii) the PilC dome and PilB disc both require the PilM ring, and (iii) the PilC dome assembles without the PilB disc, but the PilB disc requires the PilC dome. These interdependencies match previous observations (fig. S2) except in one regard: Earlier immunofluorescence experiments demonstrated that PilC can be incorporated into the T4PM independently of PilM (*21*) (fig. S2). Our observation that in the Δ*pilM* mutant all cytoplasmic densities and the short stem are missing in averages (Fig. 2, I2) clarifies that the PilM cytoplasmic ring is important for consistent incorporation of the other cytoplasmic proteins and formation of the short stem.

After the cytoplasmic ring, dome, and disc had been assigned to PilM, PilC, and PilB, respectively, no additional cytoplasmic density was available to interpret as PilT. The most likely explanation is that PilT occupies the same location as PilB. When generating subtomogram averages, because we could not tell whether any particular pilus was in the extension or retraction state, we averaged all identified particles. The fact that the Δ*pilT* mutant displayed more T4Ps than wild-type cells in our images (table S1) confirmed that the T4Ps were actively extending and retracting in our wild-type sample. Hence, the wild-type piliated structure was an average of both PilB- and PilT-bound states. The Δ*pilT* piliated structure (Fig. 2, J1), however, showed no clear addition or loss of cytoplasmic densities relative to the wild type (fig. S1, B and D), which suggests that the differences between PilB- and PilT-bound particles are not visible at this resolution. We conclude that both PilB and PilT form cytoplasmic disc structures (Fig. 2, J4) and bind to the basal body in a mutually exclusive manner.

To test this idea, we generated a Δ*pilB* Δ*pilT* double mutant. As expected, this mutant lacked T4P-dependent motility and all other T4PM proteins accumulated as in the wild type (fig. S6). When we imaged the Δ*pilB* Δ*pilT* double mutant (Fig. 2, J3), no clear differences were observed on its empty basal body relative to that of Δ*pilB* and wild-type strains (Fig. 2, A2 and J2), confirming our assignment of both PilB and PilT ATPases to the same cytoplasmic disc. The ATPase density was located ~2 nm away from the IM, preventing any direct interaction between the ATPases and pilin subunits. We therefore conclude that PilC, which forms the cytoplasmic dome structure, lies between the ATPases and the stem and transduces force generated by ATP hydrolysis into pilus extension and retraction. In agreement with this model, the N-terminal cytoplasmic domain of PilC was recently shown to interact directly with PilB, and the C-terminal cytoplasmic domain was suggested to interact with PilT (*49*).

Placing available component structures into the overall molecular envelope

Because atomic structures are available for homologs of >90% of the domains of the T4PM, we next sought to test the plausibility of our component maps by trying to place these structures into the overall molecular envelope in a way that would satisfy the maps and all known constraints, including domain sizes, structures, and connectivities (see supplementary materials, in particular figs. S7 to S11, and for details, and Movie 1 for a presentation of the process in three dimensions). Remarkably, in this process, the sizes and shapes of all domains analyzed fitted well into the molecular envelopes and resulted in a hypothetical working model of the piliated and nonpiliated basal bodies (fig. S12). Because the 2- to 4-nm resolution of the subtomogram averages was not high enough to reveal the orientation of each component within the EM envelope, we next generated models with most components filtered to 3-nm resolution (Fig. 3, B to E). The process of positioning and connecting the domains in the context of a full hypothetical structural model nonetheless revealed important relationships that rationalize numerous previous observations and suggest insights into T4PM assembly, structure, and function, as described below and shown in Movie 2.

Overall architecture and assembly

All T4PM components except the pilus and PilC appear to form rings. Each of the OM, peptidoglycan (PG), and IM cell envelope layers is negotiated or engaged by a proteinaceous ring, and there is an additional "floating" lower periplasmic ring. Each ring is linked to the rings above and below to create an integrated but flexible structure spanning the entire cell envelope. The subtomogram averages of assembled T4PM subcomplexes in different mutants provide snapshots of the assembly pathway and support the sequence [PilQ, TsaP] → [PilP, PilN, PilO] → [PilM, PilC, PilA, minor pilins] → [PilB, PilT] (fig. S13). The coiled-coil domains of PilN and PilO form a cage-like compartment above and within the IM. Although the exact number of subunit monomers in each ring remains unknown, the 1:1 connectivities between PilQ-PilP, PilP-PilN-PilO, and PilN-PilM suggest that all the rings have the same stoichiometry. We found that 12 copies of the ring components fit best into the EM density, in agreement with observations of secretin channels of T4PM and T2SS in multiple species (*41*, *42*, *50*). The entire basal body is therefore robustly anchored to the PG by ~12 TsaP N-terminal LysM domains and ~36 PilQ AMIN domains arranged irregularly (for

instance, as in Fig. 3D). PilQ in turn links to PilP, which links to the PilN-PilO ring, which links to PilM, which binds PilB (and PilT). Unless one of these known connectivities is only transitory in vivo, the only components free to rotate are PilC and potentially the pilus.

Pilus assembly and disassembly by a rotating PilC

The structure of the pilus can be thought of as either a 3-start left-handed helix or a 1-start or 4-start right-handed helix. Because no substantial pilus rotation has been observed during pilus retraction or extension, three different assembly structures or mechanisms can be imagined (*18*): (i) a fixed structure with three active sites adding pilins at each of the three sites needed to extend a 3-start helix; (ii) a fixed structure with four active sites adding pilins at each of the four sites needed to extend a 4-start helix; or (iii) a rotating structure with one or a few active sites adding pilins one at a time as it rotates around the axis of the fiber, extending the fiber as a 1-start helix (*3*, *51*). As described above, the OM pore complex, alignment complex, and PilM-ATPase complexes are all directly or indirectly linked and anchored to the PG. The only T4PM component able to rotate is PilC. We found that the space inside the PilM-PilN-PilO "cage" can accommodate no more than one PilC dimer. It is unlikely that a PilC dimer would have three or four active sites for interacting with different PilA molecules; therefore, our models point to a 1-start assembly mechanism in which PilC rotates as it assembles the helical pilus fiber. It is also known that *N. gonorrhoeae* T4Ps extend and retract in increments smaller than the length of one helical turn (*52*), which is most easily explained by a mechanism with more than one step per turn, corresponding to the 1-start assembly mechanism. Another reason to favor models that involve rotation of some component such as PilC is that the homologous archaeal flagellar motor clearly begins to rotate its flagellar filament once this filament has been assembled (*53*).

In our architectural model of the piliated basal body, the PilC dimer rests on top of (and is presumed to interact with) two opposing PilB subunits in the ATPase hexamer, and the six NTDs of PilB in the ATPase hexamer are clamped in place by interacting with every second PilM subunit in the cytoplasmic ring (fig. S12A). We therefore propose that ATP hydrolysis by the pairs of opposing PilB subunits that contact the PilC dimer causes PilB NTD movements that rotate the asymmetrical PilC dimer. We predict the rotation of PilC to have two consequences: (i) It "scoops" new PilA subunits one at a time out of the membrane and onto the base of the pilus, and (ii) PilC is transferred to the next pair of opposing PilB subunits. The transmembrane segments of PilC likely mate with the tapered tip of the helical pilus fiber in such a way as to extend and anchor the pilus to the basal body, thereby creating a complete binding pocket for the hydrophobic tail of the next PilA subunit to be incorporated. Once a new PilA subunit is incorporated, PilB drives PilC around a fraction of a turn, pushing the pilus up a fraction of the length of a pilin subunit and recreating the binding pocket in the next available position.

One problem with this model is that the hexameric nature of PilB would predict elementary turns of 60° or 120°; neither would result in the exactly 3.6 subunits per turn needed to extend the pilus without any rotation. Perhaps the process does involve some slight rotations or Brownian motions of the proteins that would cause small slips in register. Pilus retraction would be accomplished by a switch from PilB to PilT. Thus, although the exact structure of the PilC dimer and its orientation in the T4PM remain uncertain, the architecture alone implies that both PilB and PilT act as ratchets biasing the assembly or disassembly process: While PilB holds the PilC-tip pocket on the next empty position of the pilus fiber until it is filled, and then quickly rotates to prevent subsequent dissociation, PilT holds the PilC-tip pocket on the last subunit of the tip until it dissociates back into the membrane, after which it quickly rotates to prevent reassociation.

The PilN-PilO and PilM rings likely sense pilus retraction signals and guide ATPase selection

Previous studies have shown that pilus retraction is induced by adding pilin-binding substrates (*54*) or pulling on the pilus directly (*52*). Recent studies with antibodies showed that tension induces conformational changes in the pilus itself (*55*), which could propagate into the basal body. Substrate binding may also induce similar conformational changes. Our results point to a model in which the alignment complex is an IM-crossing transmission module: Pilus retraction signals carried by the pilus itself into the basal body could be sensed in the periplasm by the PilN-PilO ring and then transmitted via the coiled-coil domains through the IM to modulate the conformation of the PilM ring, which in turn governs which ATPase is bound. This model rationalizes the recent report that conformational changes are required in the coiled-coil domains of PilN-PilO during the transition between T4P extension and retraction, which suggests that the alignment complex is not simply a static connector between IM and OM components, but instead plays a critical role in T4P dynamics (*56*).

The power of combined structural approaches to dissect complicated molecular machines

Solving the structures of large macromolecular machines is challenging. Traditional structural methods such as x-ray crystallography, nuclear magnetic resonance spectroscopy, and single-particle cryo–electron microscopy can deliver near-atomic resolution, but they all rely on purified samples. Many important biological structures such as flagellar motors (*57*), chemoreceptor arrays (*58*), and the T4PM studied here, however, may never be purifiable in a native state; we found that even the PilQ (fig. S4), PilC (fig. S10), and PilM-PilN-PilO (fig. S14) subcomplexes lose their native structure when purified. As a result, only structures of isolated subunits and small subcomplexes have been determined. Cryo–electron tomography can reveal at least the architectures of these large machines in situ, as our work has shown. When there is sufficient additional information about the structures and connectivities of the components, working models can be built that provide a path toward structural understanding, where both the structural relationships and the new mechanistic insights they suggest can then be tested.

REFERENCES AND NOTES

1. K. V. Korotkov, M. Sandkvist, W. G. J. Hol, The type II secretion system: Biogenesis, molecular architecture and mechanism. *Nat. Rev. Microbiol.* **10**, 336–351 (2012). pmid: 22466878
2. K. F. Jarrell, S.-V. Albers, The archaellum: An old motility structure with a new name. *Trends Microbiol.* **20**, 307–312 (2012). doi: 10.1016/j.tim.2012.04.007; pmid: 22613456
3. J. S. Mattick, Type IV pili and twitching motility. *Annu. Rev. Microbiol.* **56**, 289–314 (2002). doi: 10.1146/annurev.micro.56.012302.160938; pmid: 12142488
4. L. Craig, M. E. Pique, J. A. Tainer, Type IV pilus structure and bacterial pathogenicity. *Nat. Rev. Microbiol.* **2**, 363–378 (2004). doi: 10.1038/nrmicro885; pmid: 15100690
5. K. J. Evans, C. Lambert, R. E. Sockett, Predation by Bdellovibrio bacteriovorus HD100 requires type IV pili. *J. Bacteriol.* **189**, 4850–4859 (2007). doi: 10.1128/JB.01942-06; pmid: 17416646
6. I. Chen, D. Dubnau, DNA uptake during bacterial transformation. *Nat. Rev. Microbiol.* **2**, 241–249 (2004). doi: 10.1038/nrmicro844; pmid: 15083159
7. M. Klausen, A. Aaes-Jørgensen, S. Molin, T. Tolker-Nielsen, Involvement of bacterial migration in the development of complex multicellular structures in *Pseudomonas aeruginosa* biofilms. *Mol. Microbiol.* **50**, 61–68 (2003). doi: 10.1046/j.1365-2958.2003.03677.x; pmid: 14507363
8. G. A. O'Toole, R. Kolter, Flagellar and twitching motility are necessary for *Pseudomonas aeruginosa* biofilm development. *Mol. Microbiol.* **30**, 295–304 (1998). doi: 10.1046/j.1365-2958.1998.01062.x; pmid: 9791175
9. A. J. Hager *et al*., Type IV pili-mediated secretion modulates *Francisella* virulence. *Mol. Microbiol.* **62**, 227–237 (2006). doi: 10.1111/j.1365-2958.2006.05365.x; pmid: 16987180
10. A. J. Merz, M. So, M. P. Sheetz, Pilus retraction powers bacterial twitching motility. *Nature* **407**, 98–102 (2000). doi: 10.1038/35024105; pmid: 10993081
11. J. M. Skerker, H. C. Berg, Direct observation of extension and retraction of type IV pili. *Proc. Natl. Acad. Sci. U.S.A.* **98**, 6901–6904 (2001). doi: 10.1073/pnas.121171698; pmid: 11381130
12. L. Craig, J. Li, Type IV pili: Paradoxes in form and function. *Curr. Opin. Struct. Biol.* **18**, 267–277 (2008). doi: 10.1016/j.sbi.2007.12.009; pmid: 18249533
13. P. C. Morand *et al*., Type IV pilus retraction in pathogenic *Neisseria* is regulated by the PilC proteins. *EMBO J.* **23**, 2009–2017 (2004). doi: 10.1038/sj.emboj.7600200; pmid: 15103324
14. B. Maier *et al*., Single pilus motor forces exceed 100 pN. *Proc. Natl. Acad. Sci. U.S.A.* **99**, 16012–16017 (2002). doi: 10.1073/pnas.242523299; pmid: 12446837
15. M. Clausen, V. Jakovljevic, L. Søgaard-Andersen, B. Maier, High-force generation is a conserved property of type IV pilus systems. *J. Bacteriol.* **191**, 4633–4638 (2009). doi: 10.1128/JB.00396-09; pmid: 19429611
16. V. Pelicic, Type IV pili: E pluribus unum? *Mol. Microbiol.* **68**, 827–837 (2008). doi: 10.1111/j.1365-2958.2008.06197.x; pmid: 18399938
17. K. Siewering *et al*., Peptidoglycan-binding protein TsaP functions in surface assembly of type IV pili. *Proc. Natl. Acad. Sci. U.S.A.* **111**, E953–E961 (2014). doi: 10.1073/pnas.1322889111; pmid: 24556993
18. L. Craig *et al*., Type IV pilus structure by cryo-electron microscopy and crystallography: Implications for pilus assembly and functions. *Mol. Cell* **23**, 651–662 (2006). doi: 10.1016/j.molcel.2006.07.004; pmid: 16949362
19. L. L. Burrows, *Pseudomonas aeruginosa* twitching motility: Type IV pili in action. *Annu. Rev. Microbiol.* **66**, 493–520 (2012). doi: 10.1146/annurev-micro-092611-150055; pmid: 22746331
20. J.-D. Pédelacq, S. Cabantous, T. Tran, T. C. Terwilliger, G. S. Waldo, Engineering and characterization of a superfolder

green fluorescent protein. *Nat. Biotechnol.* **24**, 79–88 (2006). doi: 10.1038/nbt1172; pmid: 16369541
21. C. Friedrich, I. Bulyha, L. Søgaard-Andersen, Outside-in assembly pathway of the type IV pilus system in *Myxococcus xanthus*. *J. Bacteriol.* **196**, 378–390 (2014). doi: 10.1128/JB.01094-13; pmid: 24187092
22. I. Bulyha *et al*., Regulation of the type IV pili molecular machine by dynamic localization of two motor proteins. *Mol. Microbiol.* **74**, 691–706 (2009). doi: 10.1111/j.1365-2958.2009.06891.x; pmid: 19775250
23. M. Georgiadou, M. Castagnini, G. Karimova, D. Ladant, V. Pelicic, Large-scale study of the interactions between proteins involved in type IV pilus biology in *Neisseria meningitidis*: Characterization of a subcomplex involved in pilus assembly. *Mol. Microbiol.* **84**, 857–873 (2012). doi: 10.1111/j.1365-2958.2012.08062.x; pmid: 22486968
24. C. Li, R. A. Wallace, W. P. Black, Y. Z. Li, Z. Yang, Type IV pilus proteins form an integrated structure extending from the cytoplasm to the outer membrane. *PLOS ONE* **8**, e70144 (2013). doi: 10.1371/journal.pone.0070144; pmid: 23922942
25. S. Tammam *et al*., PilMNOPQ from the *Pseudomonas aeruginosa* type IV pilus system form a transenvelope protein interaction network that interacts with PilA. *J. Bacteriol.* **195**, 2126–2135 (2013). doi: 10.1128/JB.00032-13; pmid: 23457250
26. S. V. Balasingham *et al*., Interactions between the lipoprotein PilP and the secretin PilQ in *Neisseria meningitidis*. *J. Bacteriol.* **189**, 5716–5727 (2007). doi: 10.1128/JB.00060-07; pmid: 17526700
27. M. Ayers *et al*., PilM/N/O/P proteins form an inner membrane complex that affects the stability of the *Pseudomonas aeruginosa* type IV pilus secretin. *J. Mol. Biol.* **394**, 128–142 (2009). doi: 10.1016/j.jmb.2009.09.034; pmid: 19857645
28. S. Tammam *et al*., Characterization of the PilN, PilO and PilP type IVa pilus subcomplex. *Mol. Microbiol.* **82**, 1496–1514 (2011). doi: 10.1111/j.1365-2958.2011.07903.x; pmid: 22053789
29. S. Gu *et al*., Solution structure of homology region (HR) domain of type II secretion system. *J. Biol. Chem.* **287**, 9072–9080 (2012). doi: 10.1074/jbc.M111.300624; pmid: 22253442
30. L. M. Sampaleanu *et al*., Periplasmic domains of *Pseudomonas aeruginosa* PilN and PilO form a stable heterodimeric complex. *J. Mol. Biol.* **394**, 143–159 (2009). doi: 10.1016/j.jmb.2009.09.037; pmid: 19857646
31. V. Karuppiah, J. P. Derrick, Structure of the PilM-PilN inner membrane type IV pilus biogenesis complex from *Thermus thermophilus*. *J. Biol. Chem.* **286**, 24434–24442 (2011). doi: 10.1074/jbc.M111.243535; pmid: 21596754
32. K. V. Korotkov *et al*., Structural and functional studies on the interaction of GspC and GspD in the type II secretion system. *PLOS Pathog.* **7**, e1002228 (2011). doi: 10.1371/journal.ppat.1002228; pmid: 21931548
33. V. Karuppiah, R. F. Collins, A. Thistlethwaite, Y. Gao, J. P. Derrick, Structure and assembly of an inner membrane platform for initiation of type IV pilus biogenesis. *Proc. Natl. Acad. Sci. U.S.A.* **110**, E4638–E4647 (2013). doi: 10.1073/pnas.1312313110; pmid: 24218553
34. V. Karuppiah, D. Hassan, M. Saleem, J. P. Derrick, Structure and oligomerization of the PilC type IV pilus biogenesis protein from *Thermus thermophilus*. *Proteins* **78**, 2049–2057 (2010). pmid: 20455262
35. J. Abendroth *et al*., The three-dimensional structure of the cytoplasmic domains of EpsF from the type 2 secretion system of *Vibrio cholerae*. *J. Struct. Biol.* **166**, 303–315 (2009). doi: 10.1016/j.jsb.2009.03.009; pmid: 19324092
36. J. Abendroth, P. Murphy, M. Sandkvist, M. Bagdasarian, W. G. J. Hol, The X-ray structure of the type II secretion system complex formed by the N-terminal domain of EpsE and the cytoplasmic domain of EpsL of *Vibrio cholerae*. *J. Mol. Biol.* **348**, 845–855 (2005). doi: 10.1016/j.jmb.2005.02.061; pmid: 15843017
37. A. Yamagata, J. A. Tainer, Hexameric structures of the archaeal secretion ATPase GspE and implications for a universal secretion mechanism. *EMBO J.* **26**, 878–890 (2007). doi: 10.1038/sj.emboj.7601544; pmid: 17255937
38. A. M. Misic, K. A. Satyshur, K. T. Forest, *P. aeruginosa* PilT structures with and without nucleotide reveal a dynamic type IV pilus retraction motor. *J. Mol. Biol.* **400**, 1011–1021 (2010). doi: 10.1016/j.jmb.2010.05.066; pmid: 20595000
39. K. A. Satyshur *et al*., Crystal structures of the pilus retraction motor PilT suggest large domain movements and subunit cooperation drive motility. *Structure* **15**, 363–376 (2007). doi: 10.1016/j.str.2007.01.018; pmid: 17355871
40. C. Lu *et al*., Hexamers of the type II secretion ATPase GspE from *Vibrio cholerae* with increased ATPase activity. *Structure* **21**, 1707–1717 (2013). doi: 10.1016/j.str.2013.06.027; pmid: 23954505
41. J.-L. Berry *et al*., Structure and assembly of a trans-periplasmic channel for type IV pili in *Neisseria meningitidis*. *PLOS Pathog.* **8**, e1002923 (2012). doi: 10.1371/journal.ppat.1002923; pmid: 23028322
42. S. L. Reichow, K. V. Korotkov, W. G. J. Hol, T. Gonen, Structure of the cholera toxin secretion channel in its closed state. *Nat. Struct. Mol. Biol.* **17**, 1226–1232 (2010). doi: 10.1038/nsmb.1910; pmid: 20852644
43. J. Kowal *et al*., Structure of the dodecameric *Yersinia enterocolitica* secretin YscC and its trypsin-resistant core. *Structure* **21**, 2152–2161 (2013). doi: 10.1016/j.str.2013.09.012; pmid: 24207124
44. T. Tosi *et al*., Structural similarity of secretins from type II and type III secretion systems. *Structure* **22**, 1348–1355 (2014). doi: 10.1016/j.str.2014.07.005; pmid: 25156426
45. S. S. Wu, D. Kaiser, Genetic and functional evidence that Type IV pili are required for social gliding motility in *Myxococcus xanthus*. *Mol. Microbiol.* **18**, 547–558 (1995). doi: 10.1111/j.1365-2958.1995.mmi_18030547.x; pmid: 8748037
46. Y. Nguyen *et al*., *Pseudomonas aeruginosa* minor pilins prime type IVa pilus assembly and promote surface display of the PilY1 adhesin. *J. Biol. Chem.* **290**, 601–611 (2015). doi: 10.1074/jbc.M114.616904; pmid: 25389296
47. N. Sauvonnet, G. Vignon, A. P. Pugsley, P. Gounon, Pilus formation and protein secretion by the same machinery in *Escherichia coli*. *EMBO J.* **19**, 2221–2228 (2000). doi: 10.1093/emboj/19.10.2221; pmid: 10811613
48. D. A. Cisneros, P. J. Bond, A. P. Pugsley, M. Campos, O. Francetic, Minor pseudopilin self-assembly primes type II secretion pseudopilus elongation. *EMBO J.* **31**, 1041–1053 (2012). doi: 10.1038/emboj.2011.454; pmid: 22157749
49. H. K. Takhar, K. Kemp, M. Kim, P. L. Howell, L. L. Burrows, The platform protein is essential for type IV pilus biogenesis. *J. Biol. Chem.* **288**, 9721–9728 (2013). doi: 10.1074/jbc.M113.453506
50. M. Chami *et al*., Structural insights into the secretin PulD and its trypsin-resistant core. *J. Biol. Chem.* **280**, 37732–37741 (2005). doi: 10.1074/jbc.M504463200; pmid: 16129681
51. D. Nunn, Bacterial type II protein export and pilus biogenesis: More than just homologies? *Trends Cell Biol.* **9**, 402–408 (1999). doi: 10.1016/S0962-8924(99)01634-7; pmid: 10481178
52. M. Clausen, M. Koomey, B. Maier, Dynamics of type IV pili is controlled by switching between multiple states. *Biophys. J.* **96**, 1169–1177 (2009). doi: 10.1016/j.bpj.2008.10.017; pmid: 19186152
53. S.-V. Albers, K. F. Jarrell, The archaellum: How Archaea swim. *Front. Microbiol.* **6**, 23 (2015). doi: 10.3389/fmicb.2015.00023; pmid: 25699024
54. Y. Li *et al*., Extracellular polysaccharides mediate pilus retraction during social motility of *Myxococcus xanthus*. *Proc. Natl. Acad. Sci. U.S.A.* **100**, 5443–5448 (2003). pmid: 12704238
55. N. Biais, D. L. Higashi, J. Brujić, M. So, M. P. Sheetz, Force-dependent polymorphism in type IV pili reveals hidden epitopes. *Proc. Natl. Acad. Sci. U.S.A.* **107**, 11358–11363 (2010). doi: 10.1073/pnas.0911328107; pmid: 20534431
56. T. L. Leighton, N. Dayalani, L. M. Sampaleanu, P. L. Howell, L. L. Burrows, Novel role for PilNO in type IV pilus retraction revealed by alignment subcomplex mutations. *J. Bacteriol.* **197**, 2229–2238 (2015). doi: 10.1128/JB.00220-15
57. S. Chen *et al*., Structural diversity of bacterial flagellar motors. *EMBO J.* **30**, 2972–2981 (2011). doi: 10.1038/emboj.2011.186; pmid: 21673657
58. A. Briegel *et al*., New insights into bacterial chemoreceptor array structure and assembly from electron cryotomography. *Biochemistry* **53**, 1575–1585 (2014). doi: 10.1021/bi5000614

ACKNOWLEDGMENTS

We thank C. Oikonomou and D. Ortega for discussions. Supported by NIH grant R01 GM094800B (G.J.J.), the Howard Hughes Medical Institute, the Max Planck Society, and the Deutsche Forschungsgemeinschaft within the framework of the Collaborative Research Center (SFB) 987 "Microbial Diversity in Environmental Signal Response." The 18 subtomogram averages of T4PMs reported in this study have been deposited in the Electron Microscopy Data Bank with accession numbers EMD-3247 (wild type, piliated); EMD-3248 (wild type, empty); EMD-3249 (Δ*pilP*, empty); EMD-3250 (PilP-sfGFP, piliated); EMD-3251 (PilP-sfGFP, empty); EMD-3252 (Δ*tsaP*, piliated); EMD-3253 (Δ*tsaP*, empty); EMD-3254 (PilO-sfGFP, piliated); EMD-3255 (PilO-sfGFP, empty); EMD-3256 (Δ*pilC*, empty); EMD-3257 (Δ*pilA*, empty); EMD-3258 (Δ*pilV pilW fimU* 1+2+3, empty); EMD-3259 (Δ*pilT*, piliated); EMD-3260 (Δ*pilB*, empty); EMD-3261 (Δ*pilB* Δ*pilT*, empty); EMD-3262 (Δ*pilM*, empty); EMD-3263 ($\Delta pilQ_{\beta1\text{-}\beta2}$, piliated); and EMD-3264 ($\Delta pilQ_{\beta1\text{-}\beta2}$, empty). The coordinates of the hypothetical T4PM working models have been deposited in the Protein Data Bank with accession numbers 3JC8 (piliated) and 3JC9 (empty), respectively. Author contributions: Y.-W.C. collected the cryo–electron tomography data, which were analyzed by Y.-W.C. and L.A.R.; Y.-W.C. built the T4PM models and generated the movie describing the modeling process; A.T.-L. and L.S.-A. provided the *M. xanthus* strains and characterized their motility and T4PM component accumulation and localization; J.I. produced the animation of T4PM dynamics; and Y.-W.C., L.S.-A., and G.J.J. wrote the paper.

SUPPLEMENTARY MATERIALS

www.sciencemag.org/content/351/6278/aad2001/suppl/DC1
Materials and Methods
Figs. S1 to S14
Tables S1 to S5
Movies S1 to S3
References (59–98)

10 August 2015; accepted 13 January 2016
10.1126/science.aad2001

EXTENDED PDF FORMAT
SPONSORED BY

www.rndsystems.com

Architecture of the type IVa pilus machine

Yi-Wei Chang *et al.*

Science **351**, (2016);
DOI: 10.1126/science.aad2001

This copy is for your personal, non-commercial use only.

If you wish to distribute this article to others, you can order high-quality copies for your colleagues, clients, or customers by clicking here.

Permission to republish or repurpose articles or portions of articles can be obtained by following the guidelines here.

The following resources related to this article are available online at www.sciencemag.org (this information is current as of March 10, 2016):

Updated information and services, including high-resolution figures, can be found in the online version of this article at:
/content/351/6278/aad2001.full.html

Supporting Online Material can be found at:
/content/suppl/2016/03/09/351.6278.aad2001.DC1.html

This article **cites 98 articles**, 41 of which can be accessed free:
/content/351/6278/aad2001.full.html#ref-list-1

This article appears in the following **subject collections:**
Biochemistry
/cgi/collection/biochem

Downloaded from on March 10, 2016

Science (print ISSN 0036-8075; online ISSN 1095-9203) is published weekly, except the last week in December, by the American Association for the Advancement of Science, 1200 New York Avenue NW, Washington, DC 20005. Copyright 2016 by the American Association for the Advancement of Science; all rights reserved. The title *Science* is a registered trademark of AAAS.

RESEARCH ARTICLES

HEART DISEASE

Rare variant in scavenger receptor BI raises HDL cholesterol and increases risk of coronary heart disease

Paolo Zanoni,[1]* Sumeet A. Khetarpal,[1]* Daniel B. Larach,[1]* William F. Hancock-Cerutti,[1,2] John S. Millar,[1] Marina Cuchel,[1] Stephanie DerOhannessian,[1] Anatol Kontush,[2] Praveen Surendran,[3] Danish Saleheen,[3,4,5] Stella Trompet,[6,7] J. Wouter Jukema,[7,8] Anton De Craen,[6] Panos Deloukas,[9] Naveed Sattar,[10] Ian Ford,[11] Chris Packard,[12] Abdullah al Shafi Majumder,[13] Dewan S. Alam,[14] Emanuele Di Angelantonio,[3] Goncalo Abecasis,[15] Rajiv Chowdhury,[3] Jeanette Erdmann,[16] Børge G. Nordestgaard,[17] Sune F. Nielsen,[17] Anne Tybjærg-Hansen,[18] Ruth Frikke Schmidt,[19] Kari Kuulasmaa,[20] Dajiang J. Liu,[21] Markus Perola,[20,22] Stefan Blankenberg,[23,24] Veikko Salomaa,[20] Satu Männistö,[20] Philippe Amouyel,[25] Dominique Arveiler,[26] Jean Ferrieres,[27] Martina Müller-Nurasyid,[28,29] Marco Ferrario,[30] Frank Kee,[31] Cristen J. Willer,[32] Nilesh Samani,[33,34] Heribert Schunkert,[35] Adam S. Butterworth,[3] Joanna M. M. Howson,[3] Gina M. Peloso,[36] Nathan O. Stitziel,[37] John Danesh,[3,9] Sekar Kathiresan,[36] Daniel J. Rader,[1]† CHD Exome+ Consortium,‡ CARDIoGRAM Exome Consortium, Global Lipids Genetics Consortium

Scavenger receptor BI (SR-BI) is the major receptor for high-density lipoprotein (HDL) cholesterol (HDL-C). In humans, high amounts of HDL-C in plasma are associated with a lower risk of coronary heart disease (CHD). Mice that have depleted *Scarb1* (SR-BI knockout mice) have markedly elevated HDL-C levels but, paradoxically, increased atherosclerosis. The impact of SR-BI on HDL metabolism and CHD risk in humans remains unclear. Through targeted sequencing of coding regions of lipid-modifying genes in 328 individuals with extremely high plasma HDL-C levels, we identified a homozygote for a loss-of-function variant, in which leucine replaces proline 376 (P376L), in *SCARB1*, the gene encoding SR-BI. The P376L variant impairs posttranslational processing of SR-BI and abrogates selective HDL cholesterol uptake in transfected cells, in hepatocyte-like cells derived from induced pluripotent stem cells from the homozygous subject, and in mice. Large population-based studies revealed that subjects who are heterozygous carriers of the P376L variant have significantly increased levels of plasma HDL-C. P376L carriers have a profound HDL-related phenotype and an increased risk of CHD (odds ratio = 1.79, which is statistically significant).

The strong inverse association between amounts of high-density lipoprotein (HDL) cholesterol (HDL-C) and coronary heart disease (CHD) risk has generated interest in a potential causal relationship between HDL metabolism and CHD. However, clinical trials with drugs that raise HDL-C levels, niacin and cholesteryl ester transfer protein (CETP) inhibitors, have produced disappointing results (*1*). Furthermore, recent studies of human genetic variants that are associated with HDL-C levels have generally failed to show association with CHD (*2*, *3*). Most notably, a loss-of-function variant in *LIPG*, a gene encoding an endothelial lipase that, in the heterozygous state, raises HDL-C by ~5 mg/dl, was found to have no association with CHD (*4*). Although these previous studies suggest that higher HDL-C levels may not be causally protective against CHD, we reasoned that additional human genetic analyses might provide mechanistic insight into the complex relationship between HDL and CHD.

The scavenger receptor class BI (SR-BI), encoded by the gene *SCARB1*, was discovered to be an HDL receptor two decades ago (*5*). SR-BI promotes the selective uptake of HDL cholesteryl esters (HDL-CEs) into cells, particularly hepatocytes and steroidogenic cells (*5*, *6*). In mice, overexpression of SR-BI in the liver reduces levels of HDL-C (*7*–*10*), and genetic deletion of SR-BI results in higher HDL-C levels (*11*–*13*). Remarkably, these genetic manipulations in mice have effects on atherosclerosis opposite to those predicted by human epidemiological data: Overexpression reduces atherosclerosis despite the lower HDL-C levels (*14*–*16*), and gene deletion increases atherosclerosis despite the higher HDL-C levels (*17*–*20*). One potential explanation relates to the flux of cholesterol from macrophages through the reverse cholesterol transport (RCT) pathway; SR-BI overexpression increases macrophage RCT, and SR-BI knockout reduces macrophage RCT (*21*). The human relevance of these observations has been unclear.

Identification of SCARB1 P376L homozygote and association with extremely high HDL-C

We hypothesized that humans with extremely high levels of HDL-C may harbor loss-of-function variants in *SCARB1* and undertook a targeted resequencing discovery experiment in 328 participants with very high HDL-C (>95th percentile, mean HDL-C of 106.8 mg/dl) and a control group of 398 subjects with low HDL-C (<25th percentile, mean HDL-C of 30.4 mg/dl). In this cohort, we sequenced the exons of ~990 genes located within 300 kb of each of the 95 loci with significant associations ($P < 5 \times 10^{-8}$) with plasma lipid levels identified by the Global Lipids Genetics Consortium as of 2010 (*22*). Among the high HDL-C subjects, we identified a homozygote for *SCARB1* P376L (g.125284671 G>A, c.1127 C>T, p.P376L, rs74830677), a 67-year-old female with an HDL-C of 152 mg/dl, and confirmed this finding by Sanger sequencing. This subject harbored no mutations in other high HDL-C genes such as *CETP* and *LIPG*. In addition to this homozygote, four P376L heterozygotes were identified by targeted sequencing in the high HDL-C group; no heterozygotes were found in the low HDL-C group (P = 0.008, Fisher's exact test).

To identify additional P376L carriers, we genotyped an expanded cohort of very high versus low HDL-C subjects. Among 524 additional subjects with very high HDL-C (mean HDL-C 95.0 mg/dl), we identified 11 heterozygotes for P376L; whereas among 758 subjects with low HDL-C (mean HDL-C 33.5 mg/dl), we identified 3 heterozygotes. In total, our combined sequencing and genotyping for discovery of the P376L variant showed that this variant is significantly overrepresented in subjects with high HDL-C [minor allele frequency (MAF) = 0.010 in high HDL-C versus 0.0013 in low HDL-C controls, P = 0.000127, Fisher's exact test, Table 1].

Because this variant is present on the exome array, we expanded our analysis to the Global Lipid Genetics Consortium exome array data in >300,000 individuals. The P376L variant was very rare in this population (MAF of ~0.0003). It was significantly associated with higher HDL-C levels with a relatively large effect size (beta = 8.4 mg/dl; $P = 1.4 \times 10^{-15}$). Notably, this variant was not associated with plasma levels of low-density lipoprotein cholesterol (LDL-C) or triglycerides (TGs) (table S1). Thus, we conclude that *SCARB1* P376L is associated specifically with elevated HDL-C levels.

HDL-related phenotypes of SCARB1 P376L homozygote and heterozygotes

We next recruited the P376L homozygote, eight heterozygous carriers, and both high HDL-C and normal HDL-C noncarrier controls for deep phenotyping of HDL metabolism and related traits. All of the P376L study participants were of

Downloaded from on March 10, 2016

European ancestry, almost exclusively of Ashkenazi Jewish descent. Clinical characteristics and lipid profiles of the subjects are reported in Table 2. Fast protein liquid chromatography (FPLC) analysis of plasma lipoproteins confirmed the increase in large HDL particles in the homozygote (Fig. 1A). Cholesterol and apolipoprotein A-I (apoA-I) levels in HDL were significantly increased in the homozygote and heterozygotes compared with controls, but HDL apoA-II levels were not elevated (Table 2 and Fig. 1B). There were no differences between P376L carriers and controls in the absolute amount of HDL free cholesterol or the ratio of free-to-esterified cholesterol in their HDL (Fig. 1C). P376L heterozygotes had a 2.8-fold increase and the homozygote a 6.1-fold increase in large HDL-2b particles compared with noncarrier controls (Fig. 1D). There was more apoA-I (Fig. 1E and fig. S2) and apoC-III (Fig. 1F) in large HDL particles in the homozygote and heterozygous carriers. Cholesterol efflux capacity was similar in carriers and controls (Fig. 1G). In contrast to the infertility phenotype of *Scarb1*-deficient female mice (*18*), the P376L homozygote had two healthy children and reported no fertility impairment. We also did not observe the steroidogenic or platelet phenotypes reported in *Scarb1*-deficient mice (see supplementary materials).

SCARB1 P376L results in complete loss of function of SR-BI

Given the profound HDL phenotype of the P376L carriers, we sought to understand the impact of the variant on SR-BI function. We generated induced pluripotent stem cells (iPSCs) using peripheral blood mononuclear cells from the P376L homozygote and a noncarrier control. We next differentiated these cells into hepatocyte-like cells (HLCs) to study HDL metabolism in the setting of endogenous cellular *SCARB1* expression. HLCs differentiated through this protocol recapitulate phenotypes of cultured primary hepatocytes such as albumin and VLDL (very low density lipoprotein) secretion (*23*–*26*). The cell lines from the control donor and the P376L homozygous subject demonstrated expression of hepatocyte-specific genes *ALB* (albumin) and *AFP* (alpha-fetoprotein) and exhibited comparable *SCARB1* gene expression (fig. S3). Compared with control iPSC hepatocyte lines, those from the P376L homozygote demonstrated a profound reduction in selective cholesterol uptake from HDL in vitro (Fig. 2A). Similar results were observed in experiments with COS7 cells transfected with plasmids expressing wild-type (WT) or the P376L variant of *SCARB1* (fig. S3, A and B), along with defective binding to HDL in vitro at 4°C (fig. S4, C and D).

To evaluate the physiological impact of the P376L variant on HDL-C levels and catabolism in vivo, we used adeno-associated virus (AAV) vectors to direct hepatic overexpression of WT SR-BI or the P376L variant in mice with depleted *Scarb1* [*Scarb1* knockout (KO) mice]. The two groups of mice demonstrated similar hepatic expression levels of *Scarb1* mRNA (fig. S5A) and SR-BI protein (fig. S5B). Mice expressing WT *Scarb1* demonstrated a robust 73% decrease in HDL-C. In contrast, mice expressing the P376L variant had no reduction in HDL-C; their HDL-C levels were comparable to those in the control AAV-null injected mice (Fig. 2B). Although the clearance of ^{125}I-labeled HDL protein was not different among the three groups, the clearance of [^{3}H]HDL-CE was much slower in mice expressing the P376L variant compared with those expressing WT SR-BI and was comparable to that in the control mice (Fig. 2, C and D). Selective HDL-CE clearance from plasma was increased by WT SR-BI but was undetectable in the P376L-expressing mice (Fig. 2E and fig. S5C), as was hepatic uptake of [^{3}H]CE at 24 hours (fig. S5D). This indicates that the P376L sequence variant results in complete loss of the canonical function of SR-BI—namely, selective uptake of HDL-CE.

We hypothesized that the markedly reduced HDL-CE uptake could be because of aberrant processing of the P376L SR-BI protein, which leads to impaired cell surface localization. To test this, we isolated cell surface proteins from COS7 cells transfected with WT and P376L SR-BI using biotinylation and found markedly reduced cell surface SR-BI in the P376L transfected cell lysates after streptavidin cell surface protein pull-down assays (fig. S4E). Given that SR-BI undergoes N-glycosylation in the endoplasmic reticulum concomitant with proper folding, we hypothesized that altered posttranslational modification may underlie its reduced cell surface localization (*27*–*29*). We measured the molecular weights of SR-BI forms after endoglycosidase-H (Endo-H) treatment of transfected COS7 (fig. S4E) and iPSC-derived HLC

Table 1. Association of *SCARB1* P376L with HDL-C in high versus low HDL-C cohorts. Carriers of the P376L variant were ascertained from the Penn High HDL Study through two approaches, targeted sequencing of the *SCARB1* gene in a total of 726 subjects (328 high HDL-C and 398 low HDL-C subjects) and genotyping on the exome array (Illumina) in an additional 1282 subjects (524 high HDL-C subjects and 758 low HDL-C subjects). The association of the P376L variant with the high HDL-C cohort from both approaches individually and combined together was tested using Fisher's exact test. *N*, number of participants; NonC, noncarriers; Het, heterozygotes; Hom, homozygotes.

Discovery cohort	High HDL-C (>95th percentile) (*N*)				Low HDL-C (<25th percentile) (*N*)				Association (*P*)
	Total	NonC	Het	Hom	Total	NonC	Het	Hom	
Targeted sequencing of *SCARB1*	328	323	4	1	398	398	0	0	0.008398
Exome array genotyping	524	513	11	0	758	755	3	0	0.005296
Combined	852	836	15	1	1156	1153	3	0	0.000127

[1]Departments of Genetics and Medicine, Division of Translational Medicine and Human Genetics, Perelman School of Medicine, University of Pennsylvania, Philadelphia, PA 19104, USA. [2]INSERM UMR 1166 ICAN, Université Pierre et Marie Curie Paris 6, Hôpital de la Pitié, Paris, France. [3]Cardiovascular Epidemiology Unit, Department of Public Health and Primary Care, University of Cambridge, Cambridge, UK. [4]Department of Biostatistics and Epidemiology, Perelman School of Medicine, University of Pennsylvania, Philadelphia, PA 19104, USA. [5]Centre for Non-Communicable Diseases, Karachi, Pakistan. [6]Department of Gerontology and Geriatrics, Leiden University Medical Center, Leiden, Netherlands. [7]Department of Cardiology, Leiden University Medical Center, Leiden, Netherlands. [8]The Interuniversity Cardiology Institute of the Netherlands, Utrecht, Netherlands. [9]Wellcome Trust Sanger Institute, Genome Campus, Hinxton, UK. [10]Institute of Cardiovascular and Medical Sciences, British Heart Foundation, Glasgow Cardiovascular Research Centre, University of Glasgow, Glasgow, UK. [11]Robertson Center for Biostatistics, University of Glasgow, Glasgow, UK. [12]Glasgow Clinical Research Facility, Western Infirmary, Glasgow, UK. [13]National Institute of Cardiovascular Diseases, Sher-e-Bangla Nagar, Dhaka, Bangladesh. [14]International Centre for Diarrhoeal Disease Research, Mohakhali, Dhaka, Bangladesh. [15]Center for Statistical Genetics, Department of Biostatistics, University of Michigan School of Public Health, Ann Arbor, MI 48109, USA. [16]Institute for Integrative and Experimental Genomics, University of Lübeck, Lübeck 23562, Germany. [17]Department of Clinical Biochemistry, Herlev Hospital, Copenhagen University Hospital, Herlev, Denmark. [18]Copenhagen University Hospital, University of Copenhagen, Copenhagen, Denmark. [19]Department of Clinical Biochemistry, Rigshospitalet, Copenhagen University Hospitals, Copenhagen, Denmark. [20]Department of Health, National Institute for Health and Welfare, Helsinki, Finland. [21]Department of Public Health Sciences, College of Medicine, Pennsylvania State University, Hershey, PA 17033, USA. [22]Institute of Molecular Medicine FIMM, University of Helsinki, Helsinki, Finland. [23]Department of General and Interventional Cardiology, University Heart Center Hamburg, Hamburg, Germany. [24]University Medical Center Hamburg-Eppendorf, Hamburg, Germany. [25]Department of Epidemiology and Public Health, Institut Pasteur de Lille, Lille, France. [26]Department of Epidemiology and Public Health, University of Strasbourg, Strasbourg, France. [27]Department of Epidemiology, Toulouse University-CHU Toulouse, Toulouse, France. [28]Institute of Genetic Epidemiology, Helmholtz Zentrum München–German Research Center for Environmental Health, Neuherberg, Germany. [29]Department of Medicine I, Ludwig-Maximilians-University Munich, Munich, Germany. [30]Research Centre in Epidemiology and Preventive Medicine, Department of Clinical and Experimental Medicine, University of Insubria, Varese, Italy. [31]UKCRC Centre of Excellence for Public Health, Queens University, Belfast, Northern Ireland. [32]Department of Computational Medicine and Bioinformatics, Department of Human Genetics, and Department of Internal Medicine, University of Michigan, Ann Arbor, MI 48109, USA. [33]Department of Cardiovascular Sciences, University of Leicester, Leicester, UK. [34]National Institute for Health Research (NIHR) Leicester Cardiovascular Biomedical Research Unit, Glenfield Hotel, Leicester, UK. [35]Deutsches Herzzentrum München, Technische Universität München, Munich, Germany. [36]Broad Institute and Center for Human Genetic Research, Massachusetts General Hospital, Boston, MA 02114, USA. [37]Department of Medicine, Division of Cardiology, Department of Genetics, and the McDonnell Genome Institute, Washington University School of Medicine, St. Louis, MO 63110, USA.

*These authors contributed equally to this work. **†Corresponding author. E-mail: rader@mail.med.upenn.edu** ‡For each consortium and study, authors and affiliations are listed in the supplementary materials.

lysates, as well as mouse liver lysates expressing WT or mutant SR-BI (Fig. 2, F and G). Higher-molecular-weight forms represent N-glycosylation modified Endo-H–resistant and partially sensitive forms at the cell surface after modification by alpha-mannosidase II in the Golgi apparatus (*28*). In the iPSC-derived differentiated HCLs from the P376L homozygote (Fig. 2F), we found much less total cellular SR-BI in the mutant cell lines relative to that of WT cells, despite comparable *SCARB1* gene expression (fig. S3C). After Endo-H treatment, the SR-BI from *SCARB1* WT cell and liver lysates across models was predominantly the partially sensitive form, along with small amounts of the fully resistant form. In contrast, the SR-BI from cell and tissue lysates across P376L-expressing groups was all the immature, fully Endo-H–sensitive form (Fig. 2, F and G, and fig. S4F). Together, these data

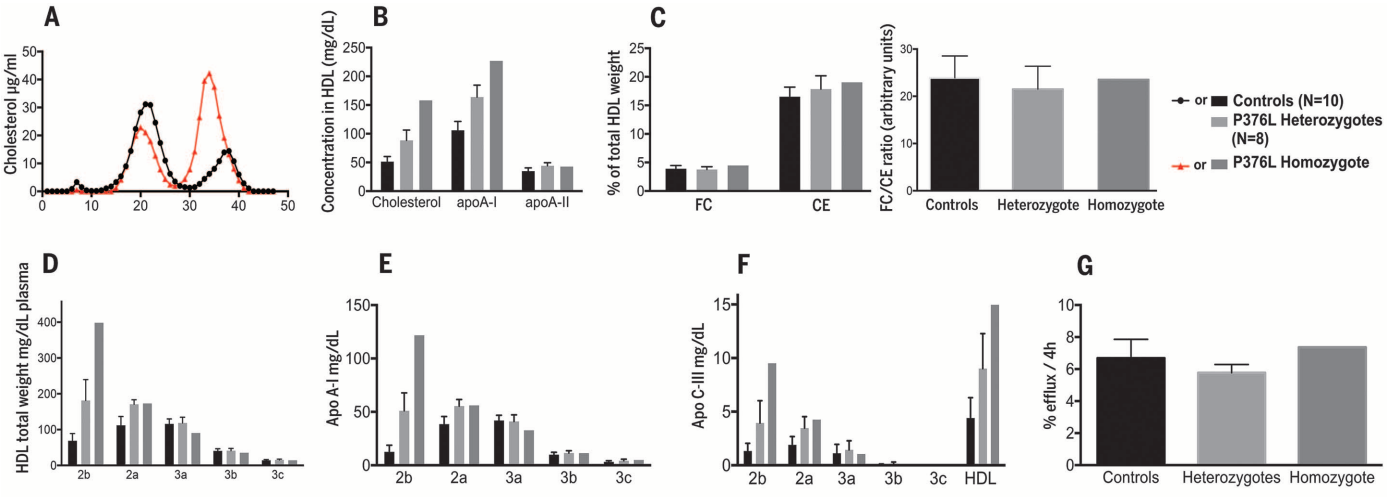

Fig. 1. HDL composition and functionality in a *SCARB1* P376L homozygote, heterozygous carriers, and controls. (**A**) FPLC fractionation of plasma lipoproteins from the P376L homozygote subject (red) and from a control with normal HDL-C. (**B**) Cholesterol, apoA-I, and apoA-II content in total HDL. (**C**) Free cholesterol (FC) and esterified cholesterol (CE) in total HDL (left) and the FC/CE ratio in total HDL (right). (**D**) HDL subclass concentrations after separation by density-gradient ultracentrifugation. (**E**) ApoA-I content in the same HDL subclasses. (**F**) ApoC-III content in the same HDL subclasses. (**G**) Cholesterol efflux capacity from macrophages of the THP-1 cell line. All data are reported as means ± SD.

Table 2. Characteristics of *SCARB1* P376L carriers and controls recruited for deep phenotyping. Demographic, plasma lipid, and apolipoprotein traits measured from one P376L homozygote, eight heterozygotes, and noncarrier controls from subjects identified from sequencing or genotyping of the Penn High HDL Study cohort for deep phenotyping. Lipid measurements from plasma were performed using an autoanalyzer. Where applicable, data are presented as means ± SD. Numbers correspond to groups for comparison. Group 1, normal HDL-C controls; group 2, high HDL-C controls; group 3, *SCARB1* P376L heterozygotes. Tested: ANOVA or chi-square. Groups: Comparison between groups by number with Tukey's multiple comparison. *Significant at $P < 0.05$. **Significant at $P < 0.05$ by chi-square but not ANOVA. Dash indicates no significant comparison. BMI, body mass index; PTA, phosphotungstate precipitation method; VLDL, very low density lipoprotein; Lp(a), lipoprotein a.

Measure	Group			P376L Hom	Significance	
	1	2	3		Tested	Groups
Number of subjects	11	10	8	1		-
Age (years)	61.6 (9.7)	64.2 (12.5)	67.5 (15.3)	65	n.s.	-
Sex (M/F)	6/5	5/5	6/2	0/1	n.s.**	-
BMI (kg/m^2)	26.4 (2)	22.9 (1.3)	25.6 (3.9)	21	*	1/2
TC (mg/dl)	185.8 (22.3)	215.8 (29.9)	228 (33.2)	280	*	1/3
Glucose (mg/dl)	93.5 (2.9)	91.6 (7.0)	98.8 (5.3)	86	n.s.	-
LDL-C (mg/dl)	109.1 (17.3)	97.4 (21.6)	116.6 (27.1)	109	n.s.	-
HDL-C (PTA) (mg/dl)	51 (11.4)	110.1 (19.8)	86.9 (19.9)	152	*	1/2, 1/3, 2/3
TG (mg/dl)	121.2 (35)	71.5 (32.3)	99.5 (23.7)	57	*	1/2
Alcohol >1/day (n)	4	4	2	0	n.s.**	-
VLDL-C (mg/dl)	26.9 (8.8)	19 (6.2)	23.1 (9.2)	13	n.s.	-
Lp(a) (mg/dl)	22.3 (18.8)	19 (22.7)	15.9 (21.2)	17	n.s.	-
apoA-I (mg/dl)	172.2 (33.3)	241.7 (41.2)	229.6 (36.1)	327	*	1/2, 1/3
apoA-II (mg/dl)	40.5 (7)	49.5 (11.5)	46.6 (5.5)	45	n.s.	-
apoB (mg/dl)	99.7 (13.4)	82.8 (17.1)	95.9 (18.2)	92	n.s.	-
apoC-II (mg/dl)	4.32 (1.55)	6.09 (2.69)	4.49 (2.17)	5.3	n.s.	-
apoC-III (mg/dl)	11.4 (4.3)	15.5 (6.9)	13.7 (2.7)	16.1	n.s.	-
apoE (mg/dl)	4.52 (0.89)	6.03 (1.86)	4.94 (1.12)	6.4	*	1/2

are consistent with a model in which the P376L sequence variant alters the endogenous posttranslational N-glycosylation of SR-BI to prevent either transit from the ER to the Golgi or further posttranslational modifications in the Golgi, which ultimately result in reduced cell surface expression.

SCARB1 P376L is associated with increased risk of CHD in humans

Despite a profound increase in HDL-C, SR-BI deficiency in mice causes accelerated atherosclerosis (*17*–*20*). The relationship of reduced SR-BI function to atherosclerotic cardiovascular disease in humans has not been established. The P376L homozygous subject did not have clinical CHD, but her carotid intimal-medial thickness (cIMT) was 0.789 mm (left-right average), which is in the >75th percentile for females of her age; in addition, she had detectable plaque throughout the left internal carotid artery and at the bifurcation of her right internal carotid artery. cIMT measurements were not significantly different in the P376L heterozygotes compared with both groups of controls (fig. S8), but because of small sample size, the statistical power is limited.

To achieve greater statistical power to address this question, we performed a meta-analysis of large exome array genotyping studies of CHD cases and healthy controls to determine the relationship of the P376L variant with risk of CHD (Table 3). Among 16 sample sets from two consortia [the CARDIoGRAM Exome Consortium and the CHD Exome+ Consortium], we tested the association between P376L carrier status and CHD in 137,995 individuals. Across 49,846 CHD cases and 88,149 CHD controls, we found that P376L carriers had a significantly higher risk of CHD compared with noncarriers [odds ratio for disease among carriers = 1.79; $P = 0.018$] (Table 3). Thus, carriers of this *SCARB1* P376L variant have significantly increased HDL-C levels and a significantly increased risk of CHD.

Discussion

Studies of mice have provided important insights into the effects of SR-BI on HDL metabolism, RCT, and atherosclerosis. These studies revealed that overexpression of SR-BI reduces HDL-C (*7*–*10*) and reduces atherosclerosis (*14*–*16*), whereas gene deletion of SR-BI increases HDL-C (*11*–*13*) and accelerates atherosclerosis (*17*–*20*). The clinical relevance of these findings has remained uncertain, however. Studies of injected labeled HDL-CE in humans suggested that the majority of the HDL-CE was transported to the liver via

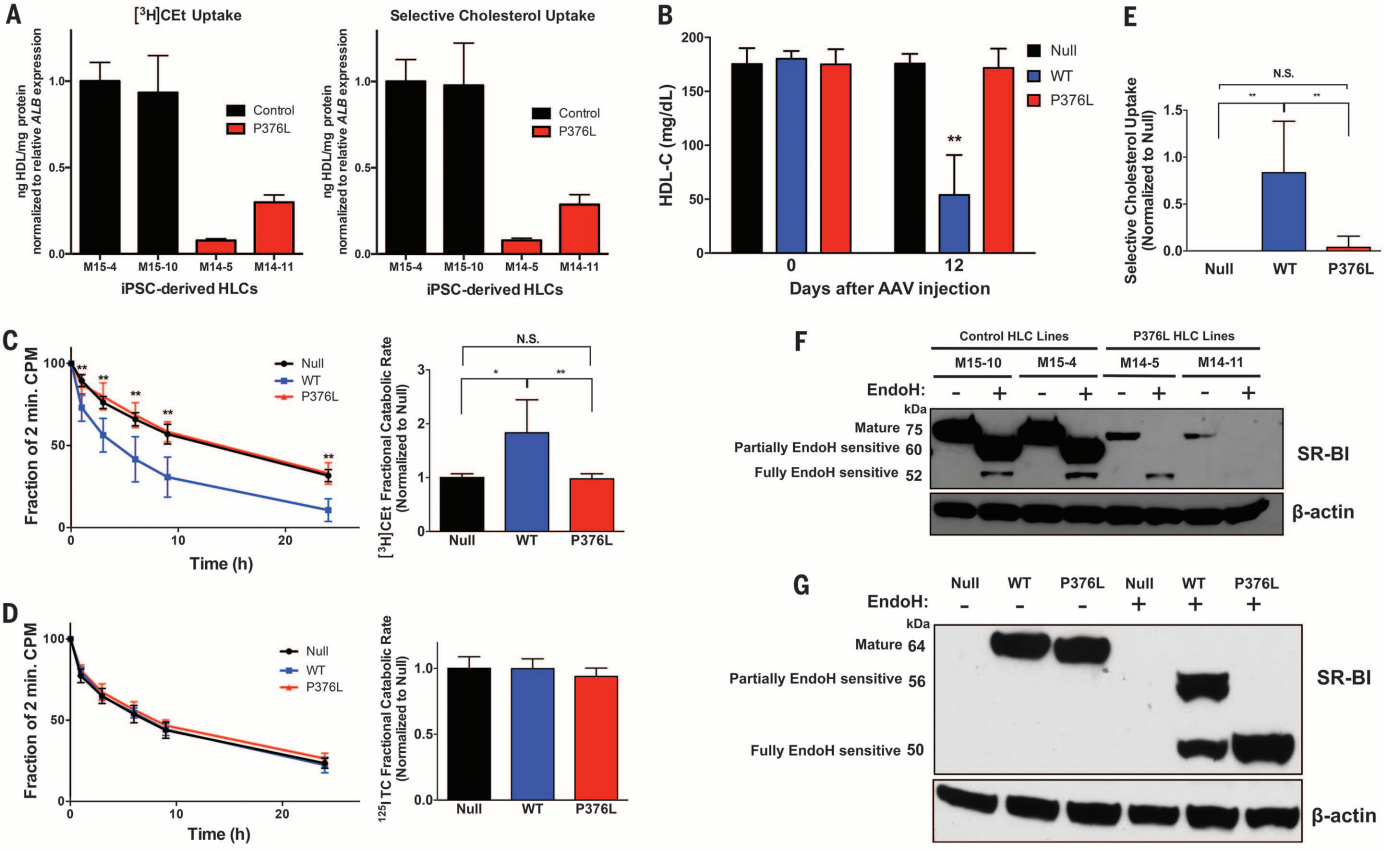

Fig. 2. *SCARB1* P376L is a null variant in vitro and in vivo. (**A**) [^{3}H]Cholesterol ether (CEt) uptake (left) and selective cholesterol uptake from HDL (right) in iPSC-derived HLCs from the P376L homozygote versus a noncarrier control. Cells were incubated with [^{3}H]CEt and ^{125}I-labeled tyramine cellobiose (TC) dual-labeled human HDL. All values are normalized to relative *ALB* gene expression in each cell line. All data represent mean values for wells of respective cell lines ± SD. (**B**) Plasma HDL cholesterol levels before and 12 days after AAV administration to *Scarb1* KO mice. (**C**) [^{3}H]Cholesterol ether (CEt) clearance (left) and fractional catabolic rate (right) from plasma of *Scarb1* KO mice injected with null or SR-BI AAVs after administration of [^{3}H]CE/^{125}I-labeled TC dual-labeled human HDL. (**D**) ^{125}I-labeled TC clearance (left) and fractional catabolic rate (right) from plasma after administration of dual-labeled HDL. (**E**) Selective cholesterol uptake in mice expressing null, SR-BI WT, or P376L measured by relative differences in ^{3}H- and ^{125}I-labeled fractional catabolic rates. (**F**) Sensitivity to Endo-H in P376L homozygous versus noncarrier iPSC-derived HLCs. Cell lysates of each genotype were treated with Endo-H to remove complex N-linked glycans from mature forms of proteins and then immunoblotted for SR-BI. Molecular weights of different forms of SR-BI after Endo-H treatment are given on the left. (**G**) SR-BI Endo-H sensitivity from liver lysates from mice expressing null, SR-BI WT, or SR-BI P376L AAV. Lysates were treated with Endo-H, followed by immunoblotting for SR-BI. Molecular weights of different forms of SR-BI after Endo-H treatment are given on the left. (A) Mean values for wells of respective cell lines ± SD; [(B) to (E)] means ± SD for each of the three groups. *$P < 0.05$; ** $P < 0.01$; ***$P <$ 0.001 by analysis of variance (ANOVA) [(B) and (C)]; plasma clearance, unpaired *t* test (E).

Table 3. Meta-analysis of association of *SCARB1* P376L variant with CHD. CHD cases and healthy controls across the CARDIoGRAM Exome Consortium and CHD Exome+ Consortium were genotyped for the *SCARB1* P376L variant by using the exome array. BioVU, Vanderbilt University Medical Center Biorepository; BHF, British Heart Foundation; GoDARTS-CAD, Genetics of Diabetes and Audit Research Tayside Study; MHI, Montreal Heart Institute; North German, German North Coronary Artery Disease Study; Ottawa, Ottawa Heart Study; PAS, Premature Atherosclerosis Study—Academic Medical Center—Amsterdam; Penn, University of Pennsylvania CHD Cohort; South German, German South Coronary Artery Disease Study; WHI-EA, Women's Health Initiative—European American Cohort; CCHS, Copenhagen City Heart Study; CIHDS/CGPS, Copenhagen Ischemic Heart Disease Study/Copenhagen General Population Study; EPIC-CVD, European Prospective Investigation into Cancer and Nutrition—Cardiovascular Disease Study; MORGAM, MOnica Risk, Genetics, Archiving and Monograph Project; PROSPER, Prospective Study of Pravastatin in the Elderly at Risk Study; WOSCOPS, West of Scotland Coronary Prevention Study. The association of the P376L variant with CHD cases was determined using a Mantel-Haenszel fixed-effects meta-analysis; results were odds ratio = 1.79; $P = 0.018$.

Consortium or study cohort	P376L carriers		Total		Frequency	
	Cases	Controls	CHD cases	Controls	Cases	Controls
CARDIoGRAM Exome Consortium						
BioVU	6	10	4587	16546	0.0013	0.0006
BHF	1	0	2833	5912	0.0004	0
GoDARTS-CAD	1	0	1568	2772	0.0006	0
MHI	0	4	2483	8085	0	0.0005
North German	0	1	4464	2886	0	0.0004
Ottawa	0	1	1024	2267	0	0.0004
PAS	1	1	728	808	0.0014	0.0012
Penn	3	0	683	156	0.0044	0
South German	4	0	5255	2921	0.0008	0
WHI-EA	8	29	2860	14929	0.0028	0.0019
CHD Exome+ Consortium						
CCHS	1	1	2020	6087	0.0003	0.0001
CIHDS/CGPS	4	3	8079	10367	0.0003	0.0001
EPIC-CVD	4	2	9810	10970	0.0002	0.0001
MORGAM	0	0	2153	2118	0	0
PROSPER	1	0	640	638	0.0008	0
WOSCOPS	0	0	659	687	0	0
Total	34	52	49846	88149	0.00068	0.00059

CETP-mediated exchange to apoB-containing lipoproteins rather than by direct uptake from HDL by the liver (*30*), which brings into question the importance of hepatic SR-BI in human physiology. Common genetic variants near the *SCARB1* locus were found to be significantly associated with plasma HDL-C levels, which suggests that SR-BI may play a role in HDL metabolism in humans (*22*, *31*). A family with a rare *SCARB1* variant in which serine replaces proline 297 (P297S) was reported in which the heterozygous carriers of the variant had modestly elevated HDL-C levels (*31*). However, the variant retains substantial SR-BI activity, no homozygotes were identified, the apparent effect on HDL-C was modest, and there was insufficient power to address its effects on atherosclerosis.

Through sequencing of subjects with extremely high plasma levels of HDL-C, we identified a homozygote for a P376L variant in SR-BI. Our complementary approaches consistently demonstrated that this variant confers virtually complete loss of function of SR-BI. Our results demonstrate many similarities in the consequences of SR-BI deficiency on HDL composition between mice and humans, including a shift toward large, buoyant HDL particles and a significant increase in apoA-I, but not apoA-II, in plasma and HDL (*12*, *32*, *33*). The homozygote is a woman who had two healthy children without fertility issues or delivery complications, which suggests that, in humans, SR-BI deficiency may not impair reproductive function in the same manner as it does in mice (*18*, *34*). In mice, SR-BI–mediated CE uptake from HDL is a critical process underlying steroid hormone synthesis in adrenal and gonadal tissues, and SR-BI deficiency alters adrenal cholesterol content, impairs adrenal glucocorticoid response under stress, and can lead to fasting-induced hypoglycemia (*6*, *35*, *36*). We did not observe any differences in fasting glucose, serum cortisol, adrenocorticotropic hormone, or female gonadal hormones in P376L heterozygous subjects versus controls, and we saw only a modest increase in testosterone in male P376L heterozygotes relative to noncarriers. We postulate that differences in expression or capacity for up-regulation of apoB-containing lipoprotein receptors relative to SR-BI between mouse models and humans in steroidogenic tissues may account, at least partially, for the lack of recapitulation of some of the phenotypes of SR-BI deficiency in mice. We also observed no differences in platelet levels, cholesterol content, and activation from the P376L carriers, despite reports of thrombocytopenia and altered platelet activity in *Scarb1* KO mice (*31*). These results suggest a relatively different contribution of SR-BI to platelet function between mice and humans. Note that the phenotypes of human *SCARB1* P376L homozygote (elevated HDL-C and large HDL particles but relatively normal steroidogenesis, reproductive viability, and platelet function) are comparable to those observed in mice lacking PDZ domain containing 1 (PDZK1), an adaptor protein for SR-BI (*37*).

Perhaps the most important finding of our study is that, despite the elevation in HDL-C, P376L carriers exhibit increased risk of CHD, as do *Scarb1* KO mice. Our results are consistent with a growing theme in HDL biology that steady-state concentrations of HDL-C are not causally protective against CHD and that HDL function and cholesterol flux may be more important than absolute levels. Using an in vivo assay of macrophage RCT, we previously showed that *Scarb1* KO mice have impaired macrophage RCT even though they have elevated HDL-C levels (*21*). Our results suggest that reduced hepatic SR-BI function in humans causes impaired RCT, which leads to increased risk of CHD despite elevation in HDL-C levels. However, SR-BI is also expressed in vascular cell types, including endothelial cells, vascular smooth muscle cells, and macrophages, where it could have protective effects against atherosclerosis as well (*38*, *39*). Our results are also consistent with the previously suggested concept (*39*) that up-regulation or enhancement of SR-BI

could be a novel therapeutic approach to reducing CHD risk in the general population.

REFERENCES AND NOTES

1. D. J. Rader, A. R. Tall, *Nat. Med.* **18**, 1344–1346 (2012).
2. C. L. Haase *et al.*, *J. Clin. Endocrinol. Metab.* **97**, E248–E256 (2012).
3. R. Frikke-Schmidt *et al.*, *JAMA* **299**, 2524–2532 (2008).
4. B. F. Voight *et al.*, *Lancet* **380**, 572–580 (2012).
5. S. Acton *et al.*, *Science* **271**, 518–520 (1996).
6. M. Hoekstra, T. J. Van Berkel, M. Van Eck, *World J. Gastroenterol.* **16**, 5916–5924 (2010).
7. N. Wang, T. Arai, Y. Ji, F. Rinninger, A. R. Tall, *J. Biol. Chem.* **273**, 32920–32926 (1998).
8. Y. Ueda *et al.*, *J. Biol. Chem.* **274**, 7165–7171 (1999).
9. K. F. Kozarsky *et al.*, *Nature* **387**, 414–417 (1997).
10. Y. Ji *et al.*, *J. Biol. Chem.* **274**, 33398–33402 (1999).
11. M. L. Varban *et al.*, *Proc. Natl. Acad. Sci. U.S.A.* **95**, 4619–4624 (1998).
12. A. Rigotti *et al.*, *Proc. Natl. Acad. Sci. U.S.A.* **94**, 12610–12615 (1997).
13. M. Brundert *et al.*, *Arterioscler. Thromb. Vasc. Biol.* **25**, 143–148 (2005).
14. Y. Ueda *et al.*, *J. Biol. Chem.* **275**, 20368–20373 (2000).
15. K. F. Kozarsky, M. H. Donahee, J. M. Glick, M. Krieger, D. J. Rader, *Arterioscler. Thromb. Vasc. Biol.* **20**, 721–727 (2000).
16. T. Arai, N. Wang, M. Bezouevski, C. Welch, A. R. Tall, *J. Biol. Chem.* **274**, 2366–2371 (1999).
17. M. Van Eck *et al.*, *J. Biol. Chem.* **278**, 23699–23705 (2003).
18. B. Trigatti *et al.*, *Proc. Natl. Acad. Sci. U.S.A.* **96**, 9322–9327 (1999).
19. D. Huszar *et al.*, *Arterioscler. Thromb. Vasc. Biol.* **20**, 1068–1073 (2000).
20. A. Braun *et al.*, *Circ. Res.* **90**, 270–276 (2002).
21. Y. Zhang *et al.*, *J. Clin. Invest.* **115**, 2870–2874 (2005).
22. T. M. Teslovich *et al.*, *Nature* **466**, 707–713 (2010).
23. A. Ghodsizadeh *et al.*, *Stem Cell Rev.* **6**, 622–632 (2010).
24. M. A. Cayo *et al.*, *Hepatology* **56**, 2163–2171 (2012).
25. S. K. Mallanna, S. A. Duncan, *Curr. Protocol Stem Cell Biol.* **26** (Unit 1G), 4 (2013).
26. K. Si-Tayeb *et al.*, *Hepatology* **51**, 297–305 (2010).
27. J. Babitt *et al.*, *J. Biol. Chem.* **272**, 13242–13249 (1997).
28. M. Viñals, S. Xu, E. Vasile, M. Krieger, *J. Biol. Chem.* **278**, 5325–5332 (2003).
29. D. Calvo, D. Gómez-Coronado, M. A. Lasunción, M. A. Vega, *Arterioscler. Thromb. Vasc. Biol.* **17**, 2341–2349 (1997).
30. C. C. Schwartz, J. M. VandenBroek, P. S. Cooper, *J. Lipid Res.* **45**, 1594–1607 (2004).
31. M. Vergeer *et al.*, *N. Engl. J. Med.* **364**, 136–145 (2011).
32. R. B. Hildebrand *et al.*, *Arterioscler. Thromb. Vasc. Biol.* **30**, 1439–1445 (2010).
33. L. Lagrost *et al.*, *Arterioscler. Thromb.* **13**, 815–825 (1993).
34. H. E. Miettinen, H. Rayburn, M. Krieger, *J. Clin. Invest.* **108**, 1717–1722 (2001).
35. M. Hoekstra *et al.*, *J. Lipid Res.* **49**, 738–745 (2008).
36. M. Hoekstra *et al.*, *J. Lipid Res.* **50**, 1039–1046 (2009).
37. O. Kocher *et al.*, *J. Biol. Chem.* **278**, 52820–52825 (2003).
38. C. Mineo, P. W. Shaul, *Curr. Opin. Lipidol.* **23**, 487–493 (2012).
39. A. Rigotti, H. E. Miettinen, M. Krieger, *Endocr. Rev.* **24**, 357–387 (2003).

ACKNOWLEDGMENTS

We appreciate the participation and support of participants of the deep clinical phenotyping studies. We thank E. Mohler for assistance in interpretation of cIMT results and J. Billheimer and E. Pashos for helpful discussions. We also acknowledge J. Tabita-Martinez for expert assistance with clinical phenotyping studies. This work was supported in part by an award from the National Center for Research Resources (grant TL1RR024133) and National Center for Advancing Translational Sciences of the NIH (grant TL1R000138) to support patient recruitment. D.B.L. was supported by a fellowship from the Doris Duke Charitable Foundation. S.K. has financial relationships with Novartis, Aegerion, Bristol-Myers Squibb, Sanofi, AstraZeneca, Alnylam, Eli Lilly, Leerink Partners, Merck, Catabasis, Regeneron Genetic Center, San Therapeutics, and Celera. H.S. has financial relationships with MSD Sharp and Dohme, Sanofi-Aventis, and Amgen. S.B. has financial relationships with Boehringer Ingelheim, Bayer, Novartis, Roche, and Thermo Fisher. N.S has financial relationships with Amgen, Sanofi, Astrazeneca, and MSD Sharp and Dohme. A.K. has a financial relationship with Amgen. J.D. has a financial relationship with Novartis. A.T.-H. has financial relationships with Eli Lilly and LGC Genomics. Sequencing data have been deposited in GenBank (SRX1458096). Genotyping data have been deposited in the Gene Expression Omnibus (GSE76065).

SUPPLEMENTARY MATERIALS

www.sciencemag.org/content/351/6278/1166/suppl/DC1
Materials and Methods
Supplementary Text
Figs. S1 to S7
Table S1
References (*40*–*76*)
Consortia and Study Author Lists

1 September 2015; accepted 7 January 2016
10.1126/science.aad3517

CHEMICAL PHYSICS

Wavelike charge density fluctuations and van der Waals interactions at the nanoscale

Alberto Ambrosetti,[1,2] Nicola Ferri,[1] Robert A. DiStasio Jr.,[3]* Alexandre Tkatchenko[1,4]*

Recent experiments on noncovalent interactions at the nanoscale have challenged the basic assumptions of commonly used particle- or fragment-based models for describing van der Waals (vdW) or dispersion forces. We demonstrate that a qualitatively correct description of the vdW interactions between polarizable nanostructures over a wide range of finite distances can only be attained by accounting for the wavelike nature of charge density fluctuations. By considering a diverse set of materials and biological systems with markedly different dimensionalities, topologies, and polarizabilities, we find a visible enhancement in the nonlocality of the charge density response in the range of 10 to 20 nanometers. These collective wavelike fluctuations are responsible for the emergence of nontrivial modifications of the power laws that govern noncovalent interactions at the nanoscale.

The assembly of complex nanostructures and biological systems from simpler building blocks is often driven by noncovalent van der Waals (vdW) or dispersion interactions that arise from electrodynamic correlations between instantaneous charge fluctuations in matter (*1*, *2*). The influence of vdW forces extends well beyond binding energies and encompasses the structural (*3*, *4*), mechanical (*5*, *6*), spectroscopic (*7*), and even electronic (*8*) signatures of condensed matter. A common way to characterize vdW interactions is by power laws in the distance D between two or more objects (e.g., atoms, molecules, nanostructures, surfaces, or solids); the most familiar is arguably the Lennard-Jones potential, which is characterized by a short-range repulsive wall with a D^{-12} dependence and a long-range attractive tail with a D^{-6} dependence. Even a slight variation in these power laws can have a profound impact on observed properties and therefore demands an accurate, physically sound theoretical description.

Thus far, both our conceptual understanding of vdW interactions and the quantitative models widely used for describing these quantum mechanical phenomena are primarily rooted in low-order intermolecular perturbation theory (IPT), wherein vdW binding originates from the interactions between transient local multipoles (*9*), and macroscopic Lifshitz theory (*10*). Although IPT-based approaches have had enormous success in describing vdW binding in (small) gas-phase molecular systems (*11*, *12*), recent advanced experimental techniques have produced several findings that are challenging the basic assumptions of IPT and macroscopic approaches for nanostructured materials, and are strongly indicative that even our qualitative understanding of these interactions is incomplete and needs to be substantially revised (*13*). Examples of such experimental observations include (i) ultra–long-range vdW interactions extending up to tens of nanometers into heterogeneous dielectric interfaces (*14*, *15*), (ii) complete screening of the vdW interaction between an atomic force microscope (AFM) tip and a SiO_2 surface by the presence of one or more layers of graphene adsorbed on the surface (*16*), (iii) superlinear sticking power laws for the self-assembly of metallic clusters on carbon nanotubes with increasing surface area (*17*), and (iv) nonlinear increases in the vdW attraction between homologous molecules and an Au(111) surface as a function of molecular size (*18*). Satisfactory theoretical explanations for these experimental findings either require ad hoc modifications to IPT [(iii) and (iv)] or are inherently outside the domain of applicability of IPT [(i) and (ii)].

To address these issues, we note that the spatial extent of the instantaneous charge density fluctuations responsible for vdW interactions depends rather sensitively on the nature and character of the occupied-to-virtual transitions of the

[1]Fritz-Haber-Institut der Max-Planck-Gesellschaft, D-14195 Berlin, Germany. [2]Dipartimento di Fisica e Astronomia, Università degli Studi di Padova, 35131 Padova, Italy. [3]Department of Chemistry and Chemical Biology, Cornell University, Ithaca, NY 14853, USA. [4]Physics and Materials Science Research Unit, University of Luxembourg, L-1511 Luxembourg.
*Corresponding author. E-mail: distasio@cornell.edu (R.A.D.); alexandre.tkatchenko@uni.lu (A.T.)

Downloaded from on March 10, 2016

valence electrons in a given molecule or material. In this regard, the inherent delocalization characteristic of low-dimensional metallic systems leads to a remarkably slow decay in the interaction energies between metallic chains and layers as a function of their separation (*19*–*21*), which represents a substantial modification of the "conventional" asymptotic behavior of the vdW interaction energy that dominates the binding at very large distances (e.g., beyond 10 to 20 nm in bilayer graphene) (*22*). Moreover, Misquitta *et al.* (*23*, *24*) demonstrated that upon closure of the band gap, semiconducting nanowires may also exhibit unconventional power laws as a function of the interwire distance D, namely $\sim D^{-2}$ at intermediate separations, followed by asymptotic convergence to the pairwise-additive D^{-5} limit for large interwire separations.

Here, we revise and extend these seminal asymptotic results to the finite distance regime between nanostructures, because interactions at such distances (as opposed to asymptotic separations) determine the structural, mechanical, spectroscopic, and (opto)electronic properties at the nanoscale. By considering a series of relevant zero-, one-, and two-dimensional systems that include proteins, carbyne-like wires, nanotubes, graphenic layers, and MoS_2, we show that a qualitatively correct description of vdW interactions between nonmetallic nanostructures can only be attained by accounting for the wavelike nature of charge density fluctuations in such systems. In doing so, our analysis extends well beyond the low-order particle- or fragment-based IPT paradigm and provides further insight into the roles played by dimensionality, topology, and polarizability in determining the magnitude of these fundamental forces at the nanoscale.

The many-body dispersion approach

In systems where electrons are well described by a localized representation of the occupied space (e.g., systems with finite band gaps), collective charge density fluctuations stem from the dynamically correlated motions of local dipolar excitations. Accordingly, we project the valence electronic response in a given nucleo-electronic system onto a set of N interacting atomic response functions, as outlined by the many-body dispersion (MBD) approach (*25*). This scheme has been applied with great success to the computation of polarizabilities (*26*) and dispersion interactions in weakly bound systems (*27*, *28*), and has recently been extended to arbitrary nonmetallic molecules, solids, and nanostructures through the use of spatially distributed polarizabilities (*25*, *29*). The advantage of the MBD method resides in an efficient and accurate quantum mechanical parameterization of the valence electronic response in terms of coupled atomic dipolar fluctuations (*30*, *31*), allowing for a chemically accurate treatment of molecules and extended systems when used in conjunction with state-of-the-art exchange-correlation (XC) functionals in density functional theory (*3*, *4*, *7*, *29*, *32*–*35*).

Within the MBD framework, the long-range correlation energy $E_{\mathrm{vdW}}^{\mathrm{LR}}$ is computed via the adiabatic connection fluctuation-dissipation theorem (*30*, *36*) as

$$E_{\mathrm{vdW}}^{\mathrm{LR}} = -\frac{1}{2\pi}\int_0^\infty d\omega \int_0^1 d\lambda\ [\mathrm{Tr}(\chi_\lambda - \chi_0)v] \qquad (1)$$

in which χ_0 is the bare response function for a system of noninteracting atoms and χ_λ is the interacting response function "dressed" by the rescaled and range-separated (*25*, *29*) Coulomb interaction, λv. [We adopt the atomic units convention of $m_e = \hbar = e = 1/(4\pi\varepsilon_0) = 1$, where m_e is the mass of the electron, $\hbar$ is the Planck constant divided by 2π, e is the elementary charge, and ε_0 is the permittivity of free space.] Within the dipole approximation, the energy expression in Eq. 1 can be computed exactly and is equivalent to diagonalization of the coupled dipolar Hamiltonian (*30*),

$$\hat{H}_{\mathrm{MBD}} = -\frac{1}{2}\sum_{p=1}^{N}\nabla_{\mathbf{d}_p}^2 + \frac{1}{2}\sum_{p=1}^{N}\omega_p^2\mathbf{d}_p^2 + \sum_{p>q}^{N}\omega_p\omega_q\sqrt{\alpha_p^0\alpha_q^0}\mathbf{d}_p\mathbf{T}_{pq}\mathbf{d}_q \qquad (2)$$

in which each atom p is characterized by a static dipole polarizability α_p^0 and a characteristic excitation frequency ω_p, and $\mathbf{d}_p$ represents the mass-weighted displacement of atom p from its equilibrium position $\mathbf{R}_p$. The first two terms in this Hamiltonian correspond to the single-particle kinetic and potential energies, respectively; the last term describes the coupling between atoms p and q via the dipole-dipole interaction tensor $\mathbf{T}_{pq} = \nabla_{\mathbf{R}_p} \otimes \nabla_{\mathbf{R}_q} v(R_{pq})$, where $v(R_{pq})$ is the Coulomb interaction at the interatomic distance $R_{pq} = |\mathbf{R}_p - \mathbf{R}_q|$ (*30*). $E_{\mathrm{vdW}}^{\mathrm{LR}}$ is then computed as the energetic difference between the eigenfrequencies of the collective modes of the fully interacting system, $\overline{\omega}_i$, and the characteristic excitation frequencies of the isolated atoms, ω_p.

Dipole waves in one-dimensional carbyne wires

We begin our investigation into the nature of vdW interactions at the nanoscale with a detailed analysis of the collective charge density fluctuations sustained in a linear one-dimensional (1D) carbyne-like atomic wire comprising 2000 atoms (and subject to periodic boundary conditions). From Fig. 1A, we first note that such finite atomic wires are characterized by a set of very-low-energy collective eigenmodes (albeit with nonzero energy eigenvalues). In this regard, the minimum energy (gap) observed in these modes approaches the independent atom value of $\omega_C = 0.43$ Ha (Hartree units) at large C-C distances $d_{C\text{-}C}$, but decreases to approximately 1/20th of this value at $d_{C\text{-}C} = 1.2$ Å, the C-C bond length in acetylene. Because of charge conservation, the quantity $\overline{\alpha}_i^0\overline{\omega}_i^2$ (where $\overline{\alpha}_i^0$ and $\overline{\omega}_i^2$ denote the static dipole polarizability and resonant frequency of the ith eigenmode, respectively) must be equivalent for every MBD eigenmode, as initially set by the independent atomic value of $\alpha_C^0\omega_C^2$. Hence, the lowest-energy eigenmode can be characterized by a substantially increased polarizability (i.e., up to ~400 times that of a single C atom), which is strongly indicative of a marked delocalization of the charge density fluctuations over the entire wire. In this case, the low dimensionality and particular topology of this nanostructure is crucial for sustaining coherent delocalized fluctuations along the length of the wire. As depicted in Fig. 1, B and C, these fluctuations result from strongly enhanced (head-to-tail) dipole-dipole coupling along the longitudinal axis of the atomic wire, which leads to substantial anisotropy in the associated polarizability tensor (*37*).

To further expand on these observations, we analyzed the low-energy spectrum of the collective MBD eigenmodes in this low-dimensional nanostructure. As illustrated in Fig. 1, B and C, these modes correspond to coherent dipolar fluctuations aligned along the entire wire with negligible components orthogonal to the longitudinal axis. Consistent with a normal mode analysis of a dipolar-coupled system with this underlying topology, the higher-energy modes correspond to polarization waves with an increasing number of nodes. At the highest energies (i.e., beyond the shoulder in the spectrum of Fig. 1A), these eigenmodes have sizable transverse components and therefore make a negligible contribution to the coherent dipolar fluctuations along the wire.

Upon compression of the carbyne wire (i.e., by varying $d_{C\text{-}C}$ from 3.0 to 1.2 Å), the gap in the eigenvalue spectrum becomes visibly reduced and is accompanied by a corresponding increase in the slope of the dispersion curves (Fig. 1A). A gapless metallic dispersion (*21*) is thus approached, but never reached, in the MBD model—a fact that we attribute to the intrinsic charge confinement of the valence atomic responses. A flat dispersion (approached only in the limit $d_{C\text{-}C} \to \infty$) would indicate a localization of the system response; with every eigenmode degenerate in energy, single-atom dipolar fluctuations would occur along the wire and result in a decorrelation of the atomic susceptibilities. Conversely, we observe from Fig. 1A that intrawire interactions can also induce nontrivial dispersion in the eigenvalue spectrum despite the absence of explicitly delocalized electrons, implying a marked nonlocality in the collective dipolar response within the MBD model. This collective behavior stems from a subtle interplay between the kinetic and potential energy operators in the MBD Hamiltonian (see. Eq. 2). Upon compression of the carbyne wire, the kinetic energy term increases relative to the potential energy terms, leading to large-amplitude oscillatory motions induced by the presence of many-body kinetic energy contributions. In addition, an analysis of the exact two-atom MBD solution reveals an underlying dependence of $E_{\mathrm{vdW}}^{\mathrm{LR}}$ on the quantity $\alpha_C d_{C\text{-}C}^{-3}$; as such, the effect of varying the interatomic distance is expected to be qualitatively equivalent to an inversely proportional modification of the polarizability.

vdW interactions between carbyne wires

The analysis presented above already provides strong evidence of the importance of wavelike charge density fluctuations in accounting for vdW interactions in low-dimensional nonmetallic nanostructures. To investigate this aspect further, we

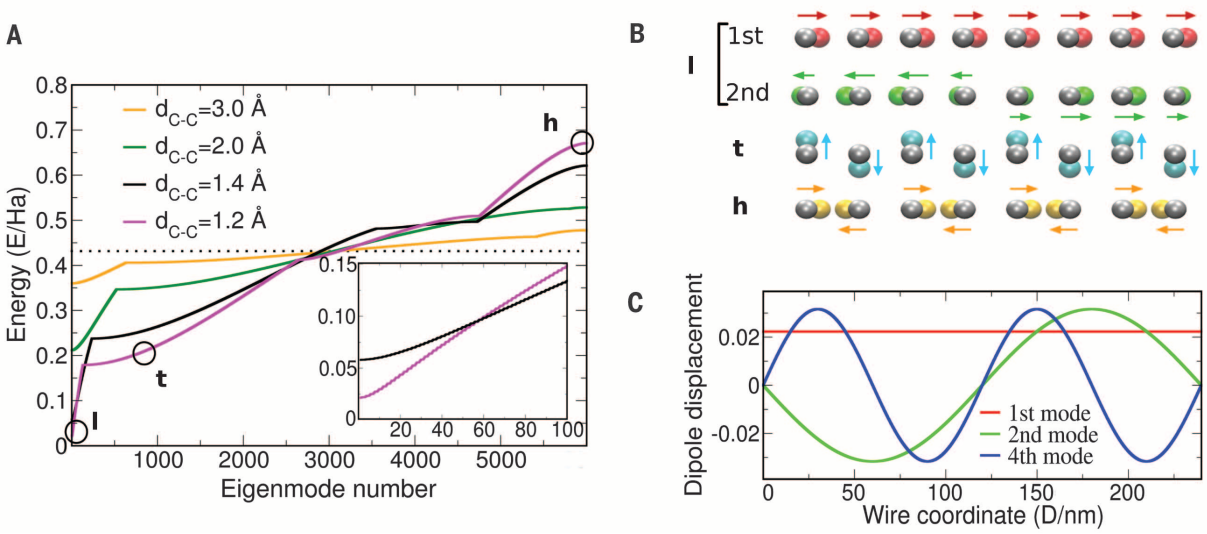

Fig. 1. Charge density fluctuations in carbyne wires. (**A**) Energy eigenvalue spectrum corresponding to the 3*N* collective eigenmodes of the many-body dispersion (MBD) model (*25*, *29*) plotted in ascending order for 1D carbyne-like atomic wires comprising N = 2000 C atoms (subject to periodic boundary conditions) and values of the interatomic C-C distance $d_{C\text{-}C}$ ranging from 1.2 Å (the C-C bond length in acetylene) to 3.0 Å. For reference, the independent atom value of ω_C = 0.43 Ha is denoted by the dotted line. The inset shows a more detailed view of the low-energy portion of the spectrum, with the same units. (**B**) Schematic illustration of several representative low-energy (**l**), transverse (**t**), and high-energy (**h**) collective MBD eigenmodes, as indicated in (A). The colored spheres represent dipole displacements with respect to the equilibrium atomic positions (depicted in gray). (**C**) Longitudinal dipole displacements of several low-energy collective MBD eigenmodes (in arbitrary units) with respect to the wire coordinate for $d_{C\text{-}C}$ = 1.2 Å. Because of the inversion symmetry of this system, every eigenmode is doubly degenerate except for the lowest-energy longitudinal mode (depicted in red). Consistent with a normal mode analysis of a dipolar-coupled system with this underlying topology, the number of nodes present in a given MBD eigenmode is directly correlated with its relative location in the energy eigenvalue spectrum.

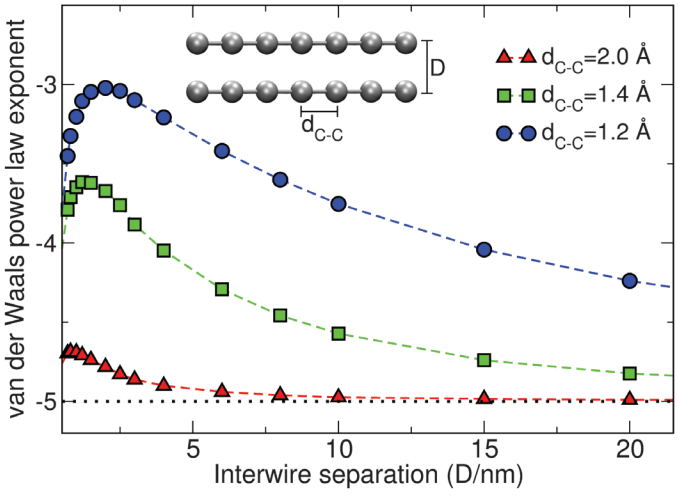

Fig. 2. Power laws for interwire vdW interactions. Interwire interaction energy power-law exponents (*46*) for two parallel 1D carbyne-like atomic wires as a function of the interwire separation D and several values of $d_{C\text{-}C}$ computed using the MBD model. Over a range of relevant nanoscale distances, there are strong deviations from the well-known asymptotic power law of D^{-5}, as predicted by widely used pairwise-additive vdW models (denoted by the dotted line).

now consider the case of two mutually interacting parallel carbyne-like wires. In Fig. 2, the resulting vdW power-law exponents are plotted as a function of the interwire separation D (for several values of $d_{C\text{-}C}$); they exhibit strong deviations from the asymptotic D^{-5} behavior predicted by widely used vdW approaches based on pairwise additivity. This macroscopic effect goes beyond a simple renormalization of Hamaker constants and results from a theoretical account of both intra- and interwire many-body vdW interactions on an equal footing. As seen in Fig. 2, these modifications to the vdW interaction energy power laws become even more pronounced upon compression of the carbyne wire, reaching ~D^{-3} for interwire separations between 1 and 3 nm (with $d_{C\text{-}C}$ = 1.2 Å), but still not converging to the pairwise-additive asymptote at interwire separations exceeding 20 nm.

Such power-law modifications are particularly relevant at the nanoscale and can be understood as resulting from long-range electrodynamic coupling between the collective longitudinal modes (dipole waves) delocalized along the entirety of each carbyne-like wire. These wavelike charge density fluctuations are simply absent in localized particle- or fragment-based models for vdW interactions, despite being crucial for an accurate theoretical description of these fundamental interactions in low-dimensional nonmetallic nanostructures. These findings resemble the results obtained with approximate many-body models of metallic chains that explicitly account for the delocalized wavelike nature of metallic electrons (*5*, *21*, *23*, *38*), which implies that a collective dipolar response with markedly nonlocal character can also be used to predict the emergence of wavelike dynamical electron correlation in nonmetallic systems.

To better understand the influence of these fluctuations on the vdW interaction between carbyne wires, we now consider an analytical model for this interaction in more detail. At sufficiently large D, the interwire Coulomb interaction in the continuum approximation is given by $w_{12} = 2K_0(qD)$, where K_0 is a modified (or hyperbolic) Bessel function of the second kind and q is the magnitude of the wave vector parallel to the longitudinal wire axis (*21*). Within the random-phase approximation, one can account for the effects of the interwire coupling on χ_1, the response function of a single wire, via $\chi_1^2 w_{12}^2 = 1$, which predicts a splitting of $\overline{\omega}(q)$ into eigenfrequencies that correspond to coupled dipolar fluctuations that are either aligned ($\overline{\omega}_+$) or anti-aligned ($\overline{\omega}_-$) with respect to the two parallel wires [i.e., $\overline{\omega}_\pm(q) = \overline{\omega}(q)\sqrt{1 \pm \overline{\alpha}^0(q)\mathbf{T}(q)}$, wherein $\mathbf{T}(q)$ is the interwire dipole-dipole interaction derived from w_{12}]. Neglecting the higher-energy transverse eigenmodes that provide smaller contributions

to the interwire interaction, the interaction energy between carbyne-like wires of length L can then be computed in the nonretarded regime as

$$E^{\mathrm{LR}}_{\mathrm{vdW},12} = \frac{L}{4\pi}\int dq[\overline{\omega}_{+}(q) + \overline{\omega}_{-}(q) - 2\overline{\omega}(q)] \quad (3)$$

which in turn can be expanded to second order in the interaction at large D, yielding

$$E^{\mathrm{LR}}_{\mathrm{vdW},12} \approx -\frac{(\alpha^0_{\mathrm{C}}\omega^2_{\mathrm{C}})^2 L}{4\pi d^2_{\mathrm{C\text{-}C}}}\int dq \frac{K^2_0(qD)q^4}{\overline{\omega}^3(q)} \quad (4)$$

A q-space decomposition of the integrand in Eq. 4 is provided in Fig. 3 and illustrates that the power law governing the interwire interaction energy has a nontrivial dependence on D that originates from a summation over individual reciprocal-space contributions, each of which corresponds to a normal mode of the system with a different characteristic decay rate. This observation is in stark contrast to the determination of the interwire interaction energy from approximate particle- or fragment-based pairwise approaches, in which each contribution has the same D^{-5} power-law decay. As such, this analysis is also strongly indicative that the complex power-law exponents displayed in Fig. 2 can only be correctly described by models that allow for delocalized wavelike fluctuations of the charge density. In this regard, even state-of-the-art nonlocal XC functionals (*39*, *40*), which describe long-range electron correlation effects in a pairwise-additive fashion, would completely miss the interaction energy profiles in Fig. 2.

To gain a more detailed understanding of the power-law exponents displayed in Fig. 2, we note that the asymptotic behavior of the interwire interaction energy is largely influenced by $\overline{\omega}(q)$, the single-wire dispersion appearing in the integrand of Eq. 4. In fact, a first estimate of the decay rate of $E^{\mathrm{LR}}_{\mathrm{vdW},12}$ can be obtained by fitting the dispersion law with a single exponent—that is, as $\overline{\omega}(q) \propto q^{\delta}$—which directly leads to the finding that $E^{\mathrm{LR}}_{\mathrm{vdW},12} \propto D^{-5+3\delta}$ upon variable substitution of $q' = q/D$. Physically speaking, the quantity $K_0(qD)$ governs the interwire interaction by introducing a momentum cutoff at $q \approx 1/D$, and the resultant integration over the infinitesimal contributions $q^4/\overline{\omega}^3(q)$ up to this momentum cutoff controls the scaling of $E^{\mathrm{LR}}_{\mathrm{vdW},12}$ with respect to D. In particular, a linear plasmon dispersion leads (up to logarithmic corrections) to a D^{-2} decay (*21*) in metallic wires, whereas the slightly sublinear dispersion observed here for $d_{\mathrm{C\text{-}C}}$ = 1.2 Å (see the inset in Fig. 1A after the initial energetic gap) is consistent with a $\sim D^{-2.8}$ power law and is in qualitative agreement with the numerical evidence provided by the MBD model in Fig. 2. Despite this initial deviation from D^{-5}, the power law at large distances again tends toward the pairwise-additive asymptote, although deviations still persist at interwire separations greater than 20 nm. A direct account of this phenomenon follows from Fig. 3: Because of the decay of $K_0(qD)$ with respect to the quantity qD, only very small values of q will contribute to the interwire interaction energy at large D (see Eq. 4). In fact, only those wave vectors near the gap [in which $\omega(q) \approx$ constant] will be of relevance in recovering the asymptotic D^{-5} limit. Hence, the pairwise-additive limit can only be approached in the presence of a flat dispersion, wherein the localization of the system response to single-atom dipolar fluctuations occurring along the individual wires would actually validate the fundamental particle- or fragment-based assumption that the vdW interaction energy can be described as a summation over induced atomic dipole contributions.

Note that the results of the above analysis are quite general and are not simply intrinsic properties of the MBD coupled dipolar Hamiltonian (Eq. 2). The same conclusions are observed when the qualitatively different tight binding (TB) model (*23*) is used for the single wire response. Within this approach, the individual atomic wires are described by a two-site nearest-neighbor interaction that can be tuned (by manipulating the β_1 and β_2 free-parameter space) to reproduce both the metallic (symmetric interactions via $\beta_2/\beta_1 = 1$) and insulating (asymmetric/single-sided interactions via $\beta_2/\beta_1 = 0$) limits. A second-order perturbative treatment of the interwire interaction energy leads to power-law exponents that describe these two respective limits—that is, $\sim D^{-2}$ for metallic nanowires and $\sim D^{-5}$ for insulating nanowires with flat energy bands—as depicted in Fig. 4. By analogy to the MBD model, the TB response becomes markedly nonlocal in the metallic limit, the regime in which the largest deviations from the pairwise-additive $\sim D^{-5}$ power law are expected. Conversely, a substantial localization of the response is recovered in the insulating limit, in which the pairwise-additive approximation becomes asymptotically valid. Comparisons between the power-law exponents provided in Figs. 2 and 4 demonstrate semiquantitative agreement between the qualitatively different MBD and TB models, which is strongly indicative of the universality of the influence of wavelike charge density fluctuations on vdW interactions between nanostructures.

vdW interactions between complex nanostructures

Although the results above were obtained for model 1D carbyne-like wires, our calculations suggest that collective charge density fluctuations will also strongly influence the behavior of strained

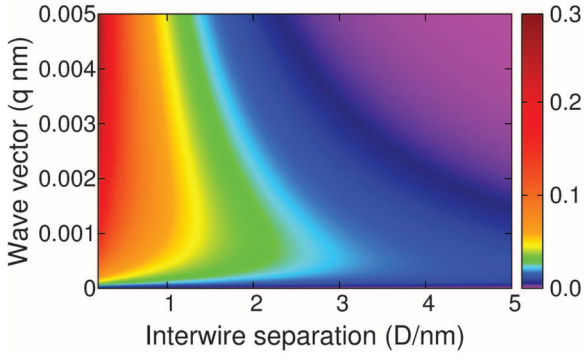

Fig. 3. Analytical model for interwire vdW interactions. A reciprocal-space decomposition analysis of the integrand $K^2_0(qD)q^4/\overline{\omega}^3(q)$, which is required for computing the second-order interwire interaction energy in Eq. 4. Assuming linear dispersion, the decay rate of the integrand with respect to D exhibits a nontrivial dependence on the momentum q (in nm^{-1}), which is responsible for the observed power laws. At large D, only small q contributions substantially influence $E^{\mathrm{LR}}_{\mathrm{vdW},12}$, so that D effectively determines the scale of relevant momenta. In this plot, the integrand has been rescaled by the constant $\overline{\omega}(0)^3$ and the corresponding color scale is provided in atomic units.

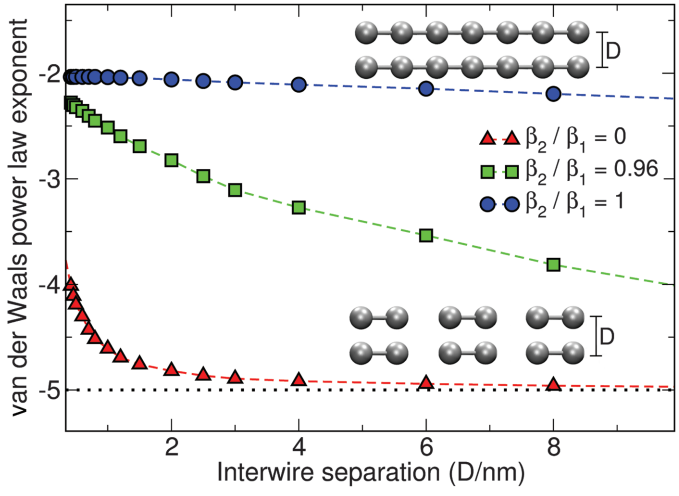

Fig. 4. The tight-binding model for interwire vdW interactions. Interwire interaction energy power-law exponents (*46*) are shown for two parallel 1D carbyne-like atomic wires as a function of the interwire separation D computed using the tight-binding (TB) model (*23*, *46*). With $d_{\mathrm{C\text{-}C}}$ = 2.0 Å, the two limiting cases of insulating ($\beta_2/\beta_1 = 0$) and metallic ($\beta_2/\beta_1 = 1$) nanowires were considered, along with an intermediate case ($\beta_2/\beta_1 = 0.96$). As previously observed with the qualitatively different MBD model (see Fig. 2), there are strong deviations from the asymptotic D^{-5} power law (denoted by the dotted line) over a wide range of relevant nanoscale distances.

hydrocarbon polymers and inorganic wires made from polarizable elements such as phosphorus, silicon, or germanium. To further elucidate the roles of dimensionality, topology, and polarizability on determining vdW interaction power laws across distances relevant at the nanoscale, we carried out a study of layered two-dimensional (2D) materials, including graphenic sheets of varying polarizability as well as bilayer MoS_2. Although a smaller reduction in the power-law exponent is expected in bilayer graphene because of its higher dimensionality, a $D^{-3.5}$ decay was found for interlayer distances of 0.6 to 3.0 nm, with convergence to the conventional D^{-4} power law only achieved for interlayer distances well beyond 10 nm (Fig. 5). In general, the interlayer interaction power-law exponents for bilayer graphene were intermediate between D^{-3} and the pairwise-additive D^{-4} asymptote, which are induced by gapless π states and are expected to be valid in the case of finite-gap doped graphene (*41*, *42*). Increasing the polarization response of the graphenic sheets to effectively model highly polarizable 2D materials leads to substantial delocalization in the system response; for $\alpha_C^0 = 50$ bohr^3, the power law exhibited an extended plateau between $D^{-2.5}$ and D^{-3} at interlayer separations from 1.5 nm to well beyond 10 nm—distances that are again quite relevant to interactions at the nanoscale.

As a final set of examples, we extend our observations regarding the crucial importance of many-body vdW interactions (*43*) to the description of complex nanostructures such as carbon nanotubes and biological systems. As Fig. 6 demonstrates, the decay rate of the MBD interaction energy between a nanowire and the 1MC5 protein (human glutathione-dependent formaldehyde dehydrogenase) is much slower than the prediction of the pairwise-additive approximation. In addition, the ratio between the MBD and pairwise interaction energies, $\Delta E_{vdW}^{LR}/\Delta E_{vdW}^{LR(2)}$, is quite large and grows as a function of the wire-protein separation, demonstrating a nontrivial coupling between delocalized charge density fluctuations sustained across the protein and along the wire.

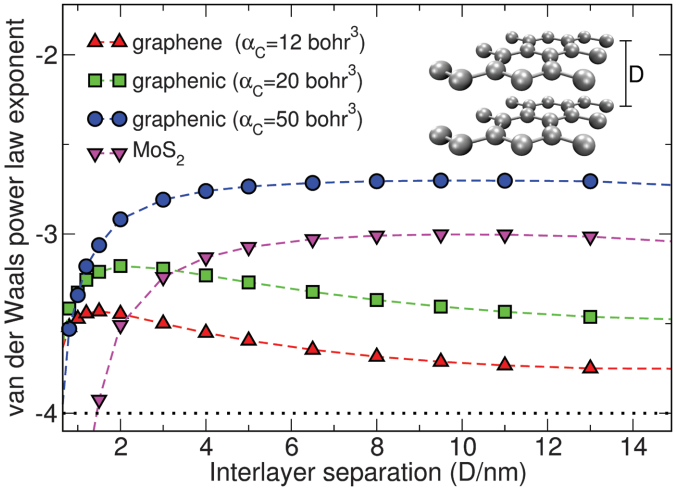

Fig. 5. Power laws for interlayer vdW interactions. Interlayer interaction energy power-law exponents (*46*) for two parallel 2D graphenic layers and MoS_2 as a function of the interlayer separation D computed using the MBD model. To investigate the behavior of these power laws in highly polarizable 2D materials, we considered several values of α_C^0 for the graphenic layers, ranging from 12 bohr^3 (the static atomic dipole polarizability of a C atom) to 50 bohr^3. As found above for the case of interacting parallel 1D nanowires over a range of relevant nanoscale distances, there are substantial deviations from the asymptotic D^{-4} power law predicted by pairwise-additive vdW approaches (denoted by the dotted line).

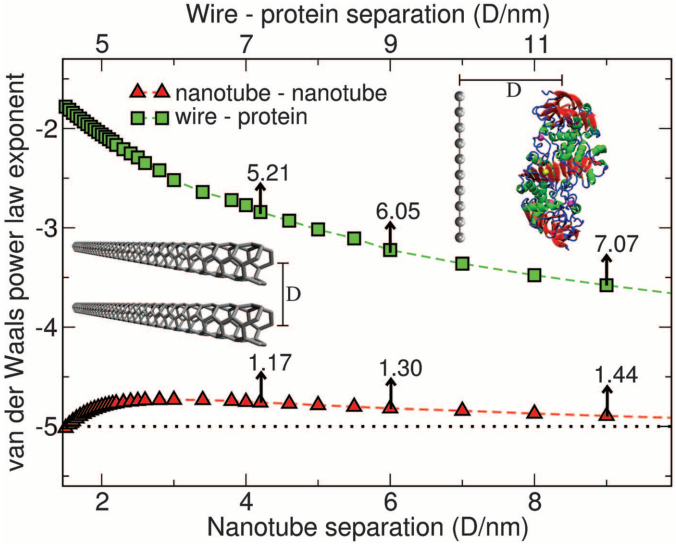

Fig. 6. Power laws for vdW interactions between complex nanostructures. Interaction energy power-law exponents (*46*) computed using the MBD model for two parallel (3,3) carbon nanotubes and a wire-protein nanostructure (depicted in insets) as a function of the respective center-of-mass separations D. As observed above for interacting 1D nanowires and 2D layered materials, we report substantial deviations in the decay rate of the MBD interaction energy in such nanostructures when compared against the pairwise-additive asymptote of D^{-5} (denoted by the dotted line). The ratio of the MBD and pairwise (*12*) interaction energies $\Delta E_{vdW}^{LR}/\Delta E_{vdW}^{LR(2)}$ are provided for select values of D; the growth of this ratio with D is another indication of the nontrivial coupling between delocalized charge density fluctuations sustained across these nanostructures.

Outlook

Our analysis demonstrates the possibilities for engineering the vdW interaction energy power laws in low-dimensional nanostructures by modifying their underlying dimensionality, topology, and response properties. Moreover, our findings suggest that complex power laws could also play an important role in numerous low-dimensional biologically relevant systems, including phospholipid aggregates and bilayers (*44*) or even the subnanometer spatula-shaped structures that determine the peculiar pedal adhesion in the gecko (*45*). Our study provides strong evidence that the ubiquitous vdW forces between polarizable nonmetallic nanostructures can be more completely understood in terms of collective interactions between wavelike charge density fluctuations, rather than simply a summation over pairwise interactions between instantaneous particle- or fragment-like dipolar fluctuations.

In a manner analogous to metallic systems, the marked nonlocality of the valence electronic response in low-dimensional polarizable nanostructures is reflected in the emergence of collective modes that span the entire system. It is these delocalized wavelike charge density fluctuations that are responsible for the nontrivial interaction energy power laws observed herein that substantially deviate from the predictions of standard pairwise-additive vdW approximations. As such, these wavelike fluctuations govern the magnitude of vdW interactions at large, but finite, distances of relevance at the nanoscale. Our findings reveal a smooth transition from a system consisting of independent atoms to the collective fully interacting limit, thereby providing a potential pathway for tuning the fundamental noncovalent vdW interactions responsible for the assembly of complex polarizable nanostructures.

REFERENCES AND NOTES

1. V. A. Parsegian, *Van der Waals Forces: A Handbook for Biologists, Chemists, Engineers, and Physicists* (Cambridge Univ. Press, 2006).
2. J. F. Dobson, *Int. J. Quantum Chem.* **114**, 1157–1161 (2014).
3. A. Tkatchenko, *Adv. Funct. Mater.* **25**, 2054–2061 (2015).
4. A. M. Reilly, A. Tkatchenko, *Chem. Sci.* **6**, 3289–3301 (2015).

5. Y. V. Shtogun, L. M. Woods, . *J. Phys. Chem. Lett.* **1**, 1356–1362 (2010).
6. W. Gao, A. Tkatchenko, *Phys. Rev. Lett.* **114**, 096101 (2015).
7. A. M. Reilly, A. Tkatchenko, *Phys. Rev. Lett.* **113**, 055701 (2014).
8. N. Ferri, R. A. DiStasio Jr., A. Ambrosetti, R. Car, A. Tkatchenko, *Phys. Rev. Lett.* **114**, 176802 (2015).
9. A. J. Stone, *The Theory of Intermolecular Forces* (Oxford Univ. Press, ed. 2, 2013).
10. E. M. Lifshitz, *Sov. Phys. JETP* **2**, 73 (1956).
11. S. Grimme, *WIREs Comput. Mol. Sci.* **1**, 211–228 (2011).
12. A. Tkatchenko, M. Scheffler, *Phys. Rev. Lett.* **102**, 073005 (2009).
13. C. A. Silvera Batista, R. G. Larson, N. A. Kotov, *Science* **350**, 1242477 (2015).
14. P. Loskill *et al.*, *Adv. Colloid Interface Sci.* **179–182**, 107–113 (2012).
15. P. Loskill *et al.*, *J. R. Soc. Interface* **10**, 20120587 (2013).
16. S. Tsoi *et al.*, *ACS Nano* **8**, 12410–12417 (2014).
17. G. A. Rance, D. H. Marsh, S. J. Bourne, T. J. Reade, A. N. Khlobystov, *ACS Nano* **4**, 4920–4928 (2010).
18. C. Wagner *et al.*, *Nat. Commun.* **5**, 5568 (2014).
19. D. B. Chang, R. L. Cooper, J. E. Drummond, A. C. Young, *Phys. Lett. A* **37**, 311–312 (1971).
20. M. Boström, B. E. Sernelius, *Phys. Rev. B* **61**, 2204–2210 (2000).
21. J. F. Dobson, A. White, A. Rubio, *Phys. Rev. Lett.* **96**, 073201 (2006).
22. J. F. Dobson, T. Gould, G. Vignale, *Phys. Rev. X* **4**, 021040 (2014).
23. A. J. Misquitta, J. Spencer, A. J. Stone, A. Alavi, *Phys. Rev. B* **82**, 075312 (2010).
24. A. J. Misquitta, R. Maezono, N. D. Drummond, A. J. Stone, R. J. Needs, *Phys. Rev. B* **89**, 045140 (2014).
25. A. Tkatchenko, R. A. DiStasio Jr., R. Car, M. Scheffler, *Phys. Rev. Lett.* **108**, 236402 (2012).
26. J. Applequist, K. R. Sundberg, M. L. Olson, L. C. Weiss, *J. Chem. Phys.* **70**, 1240 (1979).
27. W. L. Bade, *J. Chem. Phys.* **27**, 1280 (1957).
28. A. G. Donchev, *J. Chem. Phys.* **125**, 074713 (2006).
29. A. Ambrosetti, A. M. Reilly, R. A. DiStasio Jr., A. Tkatchenko, *J. Chem. Phys.* **140**, 18A508 (2014).
30. A. Tkatchenko, A. Ambrosetti, R. A. DiStasio Jr., *J. Chem. Phys.* **138**, 074106 (2013).
31. A. P. Jones, J. Crain, V. P. Sokhan, T. W. Whitfield, G. J. Martyna, *Phys. Rev. B* **87**, 144103 (2013).
32. A. M. Reilly, A. Tkatchenko, *J. Phys. Chem. Lett.* **4**, 1028–1033 (2013).
33. A. Ambrosetti, D. Alfè, R. A. DiStasio Jr., A. Tkatchenko, *J. Phys. Chem. Lett.* **5**, 849–855 (2014).
34. R. A. DiStasio Jr., O. A. von Lilienfeld, A. Tkatchenko, *Proc. Natl. Acad. Sci. U.S.A.* **109**, 14791–14795 (2012).
35. R. A. DiStasio Jr., V. V. Gobre, A. Tkatchenko, *J. Phys. Condens. Matter* **26**, 213202 (2014).
36. J. F. Dobson, J. Wang, B. P. Dinte, K. McLennan, H. M. Le, *Int. J. Quantum Chem.* **101**, 579–598 (2005).
37. V. V. Gobre, A. Tkatchenko, *Nat. Commun.* **4**, 2341 (2013).
38. R.-F. Liu, J. G. Ángyán, J. F. Dobson, *J. Chem. Phys.* **134**, 114106 (2011).
39. M. Dion, H. Rydberg, E. Schröder, D. C. Langreth, B. I. Lundqvist, *Phys. Rev. Lett.* **92**, 246401 (2004).
40. K. Berland *et al.*, *Rep. Prog. Phys.* **78**, 066501 (2015).
41. J. Dai, J. Yuan, P. Giannozzi, *Appl. Phys. Lett.* **95**, 232105 (2009).
42. P. A. Denis, *Chem. Phys. Lett.* **508**, 95–101 (2011).
43. J. Tao, J. P. Perdew, *J. Chem. Phys.* **141**, 141101 (2014).
44. L. J. Lis, M. McAlister, N. Fuller, R. P. Rand, V. A. Parsegian, *Biophys. J.* **37**, 667–672 (1982).
45. K. Autumn *et al.*, *Nature* **405**, 681–685 (2000).
46. See supplementary materials on *Science* Online.

ACKNOWLEDGMENTS

Supported by a startup grant from Cornell University (R.A.D.), European Research Council Starting Grant VDW-CMAT, and DFG/SFB-951 HIOS project A10. A.A. thanks F. Toigo and P. L. Silvestrelli for useful discussions. This research used resources of the Argonne Leadership Computing Facility at Argonne National Laboratory, which is supported by the Office of Science of the U.S. Department of Energy under contract DE-AC02-06CH11357.

SUPPLEMENTARY MATERIALS

www.sciencemag.org/content/351/6278/1171/suppl/DC1
Theoretical Methods
Supplementary Text
Tables S1 to S3

10 December 2015; accepted 31 January 2016
10.1126/science.aae0509

REPORTS

QUANTUM OPTICS

Generation of multiphoton entangled quantum states by means of integrated frequency combs

Christian Reimer,[1]* Michael Kues,[1]*† Piotr Roztocki,[1] Benjamin Wetzel,[1,2] Fabio Grazioso,[1] Brent E. Little,[3] Sai T. Chu,[4] Tudor Johnston,[1] Yaron Bromberg,[5]‡ Lucia Caspani,[6]§ David J. Moss,[7]|| Roberto Morandotti[1,8]†

Complex optical photon states with entanglement shared among several modes are critical to improving our fundamental understanding of quantum mechanics and have applications for quantum information processing, imaging, and microscopy. We demonstrate that optical integrated Kerr frequency combs can be used to generate several bi- and multiphoton entangled qubits, with direct applications for quantum communication and computation. Our method is compatible with contemporary fiber and quantum memory infrastructures and with chip-scale semiconductor technology, enabling compact, low-cost, and scalable implementations. The exploitation of integrated Kerr frequency combs, with their ability to generate multiple, customizable, and complex quantum states, can provide a scalable, practical, and compact platform for quantum technologies.

Multi-entangled states of light hold answers to fundamental questions in quantum physics and are the cornerstone of a range of applications, including quantum communications (*1*), computation (*2*–*4*), and sensing and imaging with a resolution beyond the classical limit (*5*). Thus, the controllable realization of multiple quantum states in a compact platform would enable a practical and powerful implementation of quantum technologies. Although applications of frequency combs have been mostly classical thus far, their distinctive architecture, based on multiple interacting modes and the phase characteristics of the underlying nonlinear processes, has the potential to offer new and powerful ways to achieve the generation of multiple, customizable, and complex states of nonclassical light. The quantum properties of frequency combs have recently begun to be investigated, revealing their potential for the generation of large quantum states (*6*–*8*). However, the continuous-variable nonclassical states (squeezed vacuum) that have been demonstrated with this approach have not yet achieved the quality (amount of squeezing) required for optical quantum computation (*9*). For the generation of single photons and continuous- and discrete-variable quantum states (qubits), a wide variety of second- and third-order nonlinear sources, optical fibers, and gases, as well as single quantum emitters, have been exploited (*10*, *11*). Recent progress has focused on transferring both classical frequency combs (*12*) and quantum sources (*13*) to integrated optical platforms. Such integrated approaches provide the advantages of compact, scalable, mass-producible, and low-cost devices (*14*). Demonstrated integrated devices include sources of heralded single photons (*15*–*17*) and entangled photon pairs (*18*), in principle allowing implementations of quantum algorithms (*19*, *20*). Here we show the parallel generation of bi- and multiphoton entangled states in a compact, integrated quantum frequency comb source.

Our quantum frequency comb is generated in a CMOS (complementary metal-oxide semiconductor)–compatible, high-refractive-index glass in a four-port microring resonator architecture [details on device fabrication and characteristics are presented in (*21*)]. The weak and anomalous dispersion of our device enables broadband phase matching for spontaneous four-wave mixing (SFWM), thereby generating a broad frequency

[1]Institut National de la Recherche Scientifique–Énergie Matériaux Télécommunications, 1650 Boulevard Lionel-Boulet, Varennes, Québec J3X 1S2, Canada. [2]Department of Physics and Astronomy, University of Sussex, Falmer, Brighton BN1 9RH, UK. [3]State Key Laboratory of Transient Optics and Photonics, Xi'an Institute of Optics and Precision Mechanics, Chinese Academy of Science, Xi'an, China. [4]Department of Physics and Materials Science, City University of Hong Kong, Tat Chee Avenue, Hong Kong, China. [5]Department of Applied Physics, Yale University, New Haven, CT 06520, USA. [6]School of Engineering and Physical Sciences, Heriot-Watt University, Edinburgh EH14 4AS, UK. [7]School of Electrical and Computer Engineering, RMIT University, Melbourne, Victoria 3001, Australia. [8]Institute of Fundamental and Frontier Sciences, University of Electronic Science and Technology of China, Chengdu 610054, China. *These authors contributed equally to this work. **†Corresponding author. E-mail: michael.kues@emt.inrs.ca (M.K.); morandotti@emt.inrs.ca (R.M.)** ‡Present address: Racah Institute of Physics, The Hebrew University of Jerusalem, Jerusalem 91904, Israel. §Present address: Institute of Photonics, Department of Physics, University of Strathclyde, Glasgow G4 0NW, UK. ||Present address: Center for Micro-Photonics, Swinburne University of Technology, Hawthorn, Victoria 3122,Australia.

Downloaded from on March 10, 2016

comb of photons emitted at the cavity resonances. The ring resonator's characteristics, with a high quality (Q) factor of around 240,000 (803 MHz linewidth and 200 GHz free spectral range; fig. S1), lead to high field enhancement and allow for low-power operation, while simultaneously enabling the direct generation of bright and narrow-bandwidth photons, without the need for spectral filtering of the photons (*22*, *23*). The device is pumped with a passive mode-locked fiber laser (repetition rate, 16.8 MHz), which is spectrally filtered to excite a single ring resonance at 1556.2 nm (192.65 THz) with a pulse duration of 570 ps coupled into the resonator. The pulses are directly filtered by the resonator, resulting in a perfect match between the spectral bandwidth of the pump pulses and the excited resonator mode. This in turn leads to the generation of pure single-mode photons in each resonance (*13*), confirmed by single-photon autocorrelation measurements [fig. S2 and (*21*)].

Using a high-resolution tunable C-band wavelength filter and a grating-based spectrum analyser, the single-photon spectrum was characterized at the output of the resonator (*21*). Figure 1 shows the measured single-photon count rate and the calculated photon-pair production rate per pulse as a function of wavelength. A very broad frequency comb of photons is emitted, covering the full S, C, and L bands defined by the International Telecommunication Union (wavelengths ranging from 1470 to 1620 nm). The SFWM process generates a spectrum that is symmetric in frequency, whereas the spectral asymmetry in the measured photon counts can be explained by Raman scattering, which could be further reduced by cooling the chip (*24*). As a result of the broad phase-matching condition, achieved through the close-to-zero waveguide dispersion, the emitted comb exhibits a flat and broadband spectrum with uniform pair production rates, ranging from 0.02 to 0.04 pairs per pulse, over the full measured comb.

To demonstrate an entangled quantum frequency comb, we chose time-bin entanglement, which, among several intrinsic advantages, is particularly suitable for information processing and transmission (*25*) because of its robustness (e.g., with respect to polarization fluctuations); it thus can be preserved even over long propagation distances in standard fiber networks (*26*).

Starting from the single-mode photon pairs, we generated time-bin–entangled qubits by passing the pulsed pump laser through a stabilized unbalanced fiber interferometer with a 11.4-ns delay (longer than the pulse duration of the laser), thereby producing double pulses of equal power with a defined relative phase difference. The temporal separation of the two pulses can be arbitrarily chosen, as long as it is larger than the temporal duration of the single photons; this approach thus offers considerable flexibility. The double pulses were then coupled into the integrated microring resonator (Fig. 2), where an average pump power of 0.6 mW was chosen so that the probability of creating a photon pair from both pulses simultaneously was low enough to be negligible.

This pump configuration transforms the originally single-mode photon pairs into entangled states, where the photons are in a superposition of two temporal modes. In particular, the entangled state $|\psi_{\text{time-bin}}\rangle = \frac{1}{\sqrt{2}}(|S_s, S_i\rangle + |L_s, L_i\rangle)$ is generated, where the signal (s) and idler (i) photons are in a quantum superposition of the short (S) and long (L) time bins (*21*). Most importantly, these entangled qubits are generated over all the microring resonances, thus leading to a quantum frequency comb of time-bin–entangled photon pairs.

To characterize the degree of entanglement, the generated signal and idler photons were each passed individually through a different fiber interferometer with an imbalance identical to

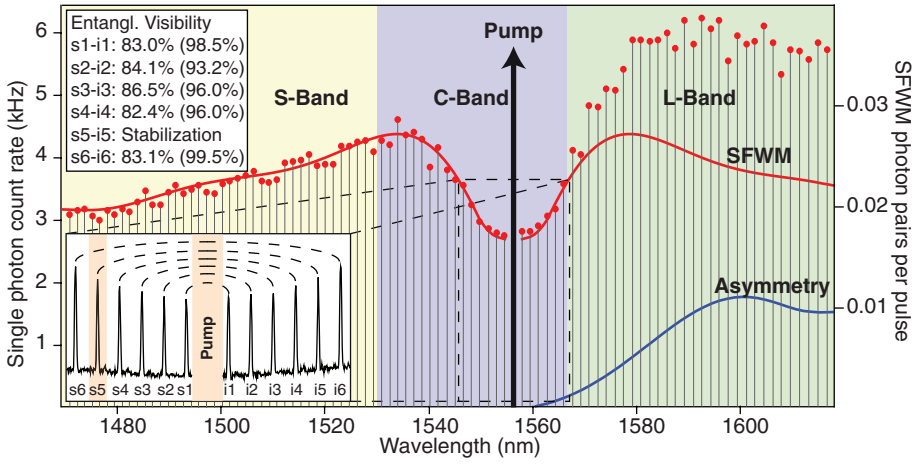

Fig. 1. Measured single-photon spectrum of the integrated quantum frequency comb. Single-photon spectrum (red circles) emitted by the microring resonator, measured using a grating-based spectrum analyzer and a high-resolution digital tunable filter in the C band (bottom inset). The S, C, and L bands are indicated. The red curve shows the symmetric contribution generated through SFWM, whereas the blue curve shows the spectral asymmetry, which can be explained by Raman scattering. The channels used in the entanglement measurements are shown in the bottom inset; the measured raw entanglement visibilities (with background-corrected values in parentheses) for the individual channel pairs are shown in the top inset.

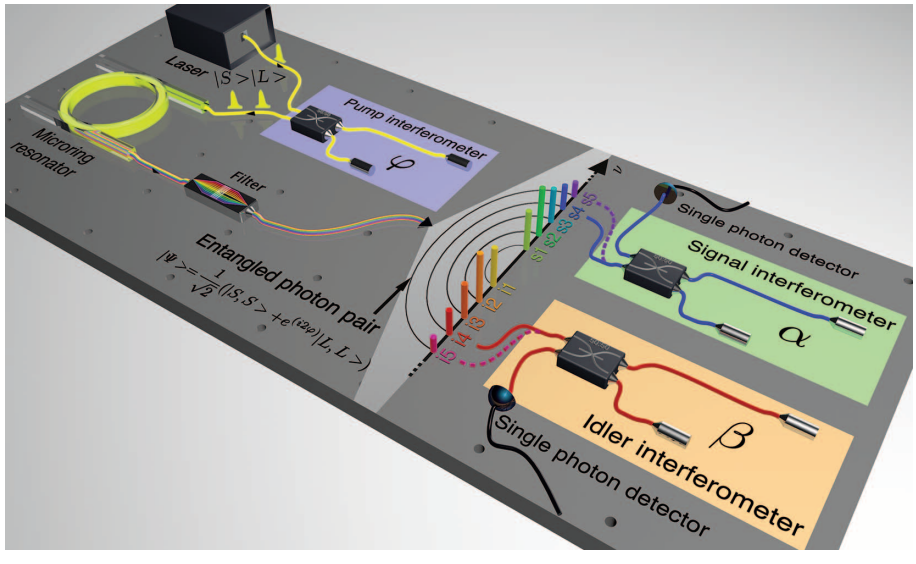

Fig. 2. Quantum frequency comb. A pulsed laser is passed through an unbalanced fiber Michelson interferometer, generating double pulses with a phase difference φ. The pulses are fed into the microring resonator, exciting one microring resonance and generating time-bin–entangled photon pairs on a frequency comb through SFWM. For the purposes of analysis [entanglement verification (Fig. 3, A to D) or quantum state tomography (Fig. 4, A and B)], each photon of the spectrally filtered photon pair is individually passed through an interferometer with the temporal imbalance equal to the time-bin separation and then detected with a single-photon detector. For the four-photon measurements (Fig. 3E and Fig. 4, C to D), four frequency modes that are symmetric to the excitation field are collected, passed through the interferometers, and spectrally filtered before detection.

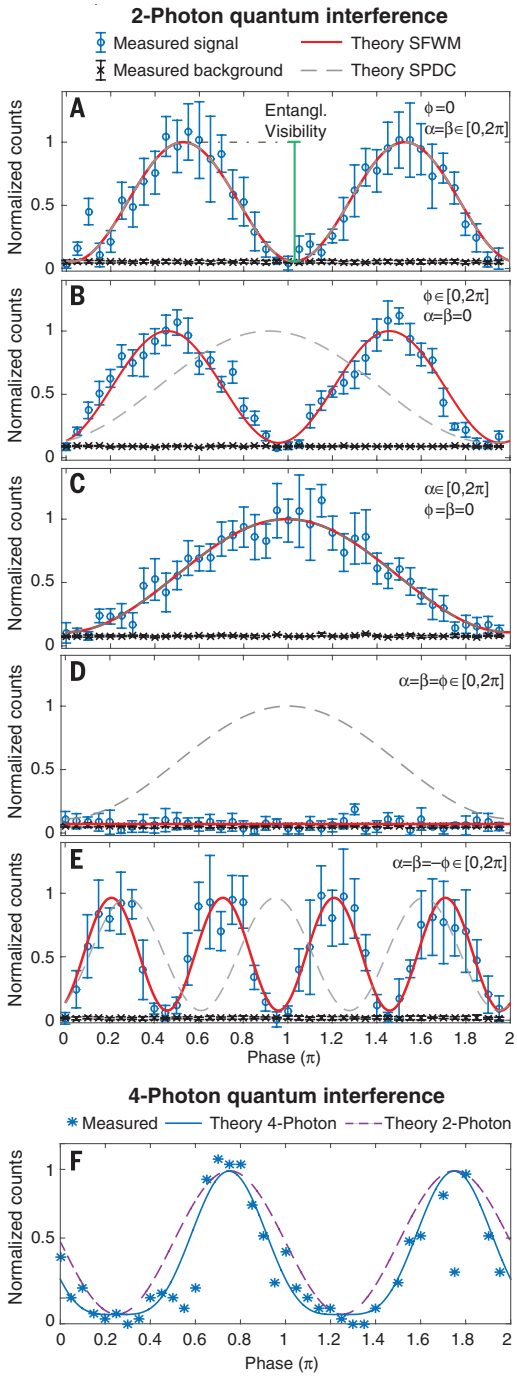

Fig. 3. Entanglement and phase control by means of SFWM. (**A** to **E**) To demonstrate the difference between the phase characteristics of SPDC and SFWM, five different quantum interference measurements were performed. Three interferometer phases were adjusted: φ, α, and β, being the phases of the pump, signal, and idler interferometers, respectively (conditions are specified in each panel). The error bars represent the standard deviation of seven measurements. (**F**) Four-photon entanglement measurement with all photon phases tuned simultaneously, showing clear four-photon quantum interference with a visibility of 89%. The solid line indicates the expected function; the dashed line shows the cosine interference in the two-photon case.

that used for the pump laser (Fig. 2). This setup allowed the measurement of the quantum interference between the signal and idler photons. For the resonances closest to the excitation frequency, we measured a photon coincidence rate of 340 Hz, which gives an estimated pair production rate of 302 kHz per channel (0.018 pairs per double pulse), accounting for system and detection losses of 14.75 dB (*21*). We selected five different frequency channel pairs within the C band (marked in Fig. 1) and recorded quantum interference with raw visibilities above 82.4%, which, being greater than $\frac{1}{\sqrt{2}} \approx 71\%$ (Fig. 1, top inset, and Fig. 3), confirm entanglement through the violation of the Clauser-Horne-Shimony-Holt (Bell-like) inequality (*27*). After subtracting the measured background (Fig. 3), the visibility was found to be above 93.2% on all channel pairs (Fig. 1, top inset).

In addition to confirming time-bin entanglement, the quantum interference also reveals the phase characteristic of the nonlinear generation process. This phase dependency has been well described in theory (*28*) and has been exploited, for example, in optical squeezing (*29*). Here we show that this phase dependency is also manifested at the single-photon level, with a clear difference between second- and third-order nonlinear interactions. When spontaneous parametric down-conversion (SPDC) in second-order nonlinear media is used to generate the entangled photon pairs, quantum interference is expected to be proportional to $1 - V\cos(\alpha + \beta + \varphi)$ (*26*), where V is the fringe visibility, φ is the pump interferometer phase, and α and β are the phases for the signal and idler interferometers, respectively. In contrast, for photons generated through SFWM (as in this work), quantum interference is expected to be of the form $1 - V\cos(\alpha + \beta - 2\varphi)$ for degenerate SFWM or $1 - V\cos(\alpha + \beta - \varphi_1 - \varphi_2)$ for nondegenerate SFWM, where φ_1 and φ_2 are the phases of the two pump fields (*21*). As shown in Fig. 3, we confirmed this important difference in phase dependency between SPDC and SFWM through five separate quantum interference measurements, where the phases of the interferometers are either tuned separately or simultaneously in a symmetric and an antisymmetric way. The expected behavior for SPDC and SFWM is plotted in Fig. 3, A to E, with dashed and solid lines, respectively. The measurements confirm the difference between the two processes, which can be explained through the additional photon involved in SFWM. In the generation of entangled photon pairs, the phase of the excitation photon (or photons) can be used to adjust the quantum state. If a single photon is involved (as in second-order processes), only the phase of this photon can be used as a control parameter. In third-order nonlinear processes, however, two photons generate the quantum state, enabling an additional control parameter (the relative phase between the two photons). Although in this study only a single excitation field was used to demonstrate the effect, exploiting two distinct nondegenerate pump fields could lead to an additional degree of freedom for the generation of all-optical reconfigurable quantum states.

The distinctive multimode characteristic of the frequency comb architecture presented here can be extended to create multiphoton entangled quantum states. By selecting two different signal-idler pairs, we can generate two-photon qubit states, given by $|\psi_1\rangle = \frac{1}{\sqrt{2}}(|S_{s1}, S_{i1}\rangle + e^{i2\varphi}|L_{s1}, L_{i1}\rangle)$ and $|\psi_2\rangle = \frac{1}{\sqrt{2}}(|S_{s2}, S_{i2}\rangle + e^{i2\varphi}|L_{s2}, L_{i2}\rangle)$. By post-selecting four-photon events with one photon on each frequency channel, these two states are multiplied, resulting in a four-photon time-bin–entangled state, given by $|\psi_{4\text{photon}}\rangle = |\psi_1\rangle \otimes |\psi_2\rangle = \frac{1}{2}(|S_{s1}, S_{i1}, S_{s2}, S_{i2}\rangle + e^{i2\varphi}|S_{s1}, S_{i1}, L_{s2}, L_{i2}\rangle + e^{i2\varphi}|L_{s1}, L_{i1}, S_{s2}, S_{i2},\rangle + e^{i4\varphi}|L_{s1}, L_{i1}, L_{s2}, L_{i2}\rangle)$. For the generation of a four-photon state, the coherence length of both photon pairs has to be the same and must be matched to the excitation field's coherence time. This requirement is intrinsically fulfilled through the resonant characteristics (equal resonance bandwidths) of the ring cavity, in combination with the excitation scheme described above. By setting the pump power to 1.5 mW, we measured a quadruple detection rate of 0.17 Hz, which corresponds to a calculated generation rate of 135 kHz, taking into account the system and detection losses of 14.75 dB. We then performed four-photon quantum interference measurements (Fig. 3F). Four-photon interference generally is not present for two completely independent

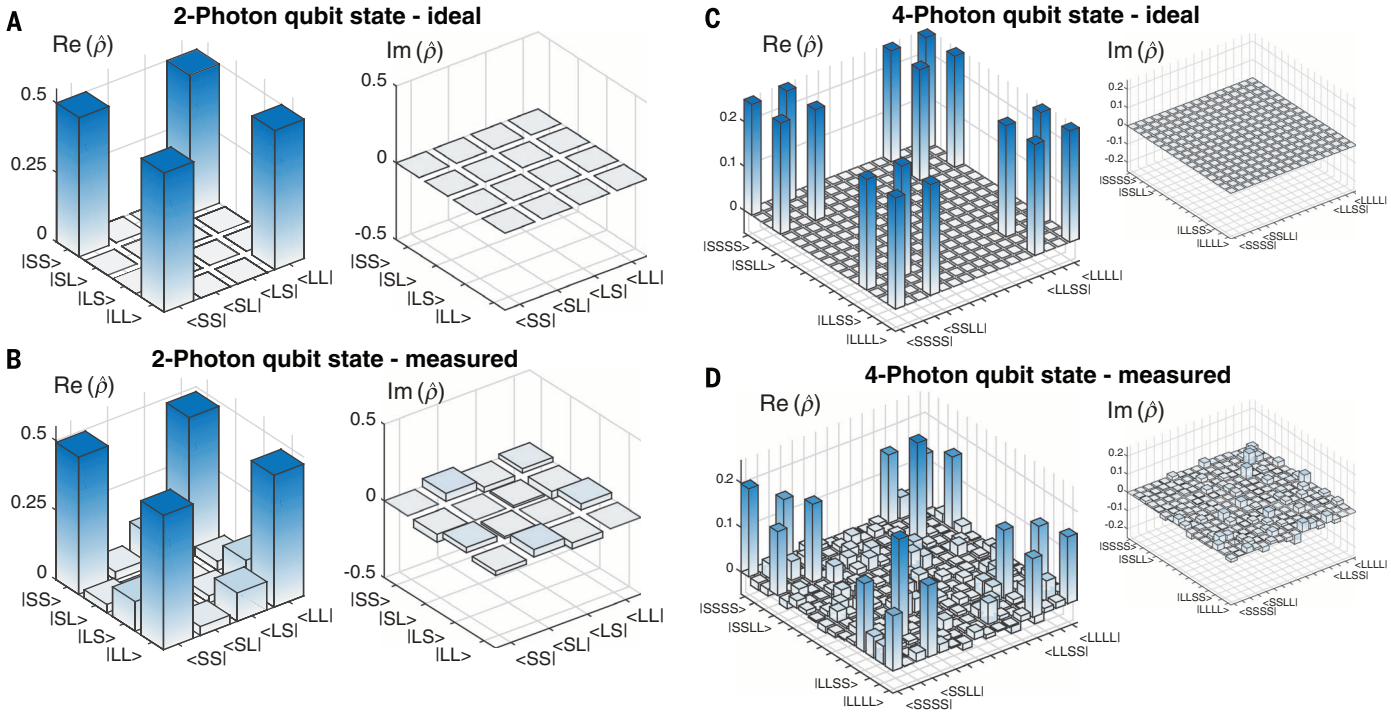

Fig. 4. Quantum state characterization by means of tomography. A quantum state can be fully described by its density matrix $\hat{\rho}$. The real (Re) and imaginary (Im) parts of the ideal density matrices of a two- and four-photon entangled qubit state are shown in (**A**) and (**C**), respectively, represented in the time-bin basis ($|SS\rangle$, $|SL\rangle$, $|LS\rangle$, $|LL\rangle$) and ($|SSSS\rangle$, $|SSSL\rangle$, ...$|LLLL\rangle$). The measured density matrix of the two-photon state (**B**) agrees very well with the ideal state, confirmed by a fidelity of 96%. The measured density matrix of the four-photon entangled qubit state (**D**) reaches a fidelity of 64%, which is comparable in quality to other nonintegrated four-photon states (*3*).

two-photon qubit states. The interference is expected to be proportional to $3 + \cos(4\alpha - 4\varphi) + 4\cos(2\alpha - 2\varphi)$, where α is the phase of all four entangled photons and φ is the pump interferometer phase (*21*). Our data follow the expected relation, having a visibility of 89% without compensation for background noise or losses. Furthermore, we repeated the four-photon measurement by selecting different combinations of four modes, always finding four-photon entanglement [fig. S3 and (*21*)].

Lastly, to fully characterize the entangled states, we performed quantum state tomography (*30*). This method measures the state density matrix, from which it is possible to extract important characteristics such as the fidelity, which describes how close the measured state is to the ideal entangled state (*21*). We first measured the two-photon qubits generated on comb lines that were symmetric with respect to the pump wavelength (Fig. 4, A and B) and found a fidelity of 96%, confirming that our generated quantum states are of high quality and very close to the ideal entangled state. For the four-photon entangled state (Fig. 4, C and D), we obtained a fidelity of 64% without compensation for background noise or interferometer imperfections, which is comparable to the fidelity measured for nonintegrated four-photon states used for practical applications (*3*).

Key characteristics of our quantum frequency comb include the intrinsic and simultaneous operation over many modes, the generation of high-purity photon pairs, the high-quality bi- and multiphoton entanglement shared among these modes, and the inherent compatibility with fiber technology. Because of these features, it has versatile and immediate applications in areas such as quantum communications and quantum computation. For example, our source can be implemented into both single-photon and entanglement-based quantum communication protocols. The broadband nature of the quantum comb is particularly attractive for multichannel applications, where the amount of transmitted data can be increased through the use of multiple, equally well-performing channels. We repeated the two-photon tomography measurement after adding 40 km of fiber and measured a fidelity of 87% [fig. S4 and (*21*)], demonstrating that the entanglement is preserved after long fiber propagation.

Furthermore, two-photon time-bin–entangled qubits have been used successfully for linear universal quantum computation (*4*, *25*), and the parallel generation and processing of multiple qubits can directly enhance such protocols where the information capacity scales with the number of comb lines used, as theoretically predicted (*25*). Even though the demonstrated multiphoton entangled states are separable, because they are generated as a product of biphoton Bell states, it is conceivable that—through the use of multiple excitation fields (*6*) or controlled phase gates (*31*)—nonseparable multiphoton cluster states could be constructed and used for measurement-based quantum computation (*3*).

Further device integration of the frequency comb will lead to more compact and stable systems with higher performances, resulting in better detection rates. All the components that were used in our setup, such as the laser, filters, interferometers, and detectors (connected via optical fibers), could be integrated on a single chip (*13*) to reduce size and losses (currently at 14.75 dB). An easily realized decrease in losses by 5 dB would increase the four-photon detection rate by a factor of 100, and an achievable loss reduction of 10 dB would increase it to the useful kilohertz range.

Our results indicate that integrated quantum frequency comb sources based on third-order nonlinearities can open up new venues for the generation and control of complex quantum states, thus providing a scalable and practical platform for optical quantum information processing.

REFERENCES AND NOTES

1. H. J. Kimble, *Nature* **453**, 1023–1030 (2008).
2. D. Deutsch, *Proc. R. Soc. A Math. Phys. Eng. Sci.* **400**, 97 (1985).
3. P. Walther *et al.*, *Nature* **434**, 169–176 (2005).
4. P. C. Humphreys *et al.*, *Phys. Rev. Lett.* **111**, 150501 (2013).
5. M. Kolobov, *Rev. Mod. Phys.* **71**, 1539–1589 (1999).
6. M. Chen, N. C. Menicucci, O. Pfister, *Phys. Rev. Lett.* **112**, 120505 (2014).
7. M. Pysher, Y. Miwa, R. Shahrokhshahi, R. Bloomer, O. Pfister, *Phys. Rev. Lett.* **107**, 030505 (2011).
8. J. Roslund, R. M. de Araújo, S. Jiang, C. Fabre, N. Treps, *Nat. Photonics* **8**, 109–112 (2013).
9. N. C. Menicucci, *Phys. Rev. Lett.* **112**, 120504 (2014).
10. M. D. Eisaman, J. Fan, A. Migdall, S. V. Polyakov, *Rev. Sci. Instrum.* **82**, 071101 (2011).
11. W. Wieczorek *et al.*, *IEEE J. Sel. Top. Quantum Electron.* **15**, 1704–1712 (2009).

12. T. J. Kippenberg, R. Holzwarth, S. A. Diddams, *Science* **332**, 555–559 (2011).
13. D. Bonneau, J. W. Silverstone, M. G. Thompson, in *Silicon Photonics III*, L. Pavesi, D. J. Lockwood, Eds. (Springer, ed. 3, 2016), pp. 41–82.
14. D. J. Moss, R. Morandotti, A. L. Gaeta, M. Lipson, *Nat. Photonics* **7**, 597–607 (2013).
15. S. Azzini *et al.*, *Opt. Express* **20**, 23100–23107 (2012).
16. C. Reimer *et al.*, *Nat. Commun.* **6**, 8236 (2015).
17. N. C. Harris *et al.*, *Phys. Rev. X* **4**, 041047 (2014).
18. D. Grassani *et al.*, *Optica* **2**, 88 (2015).
19. A. Politi, M. J. Cryan, J. G. Rarity, S. Yu, J. L. O'Brien, *Science* **320**, 646–649 (2008).
20. J. C. F. Matthews, A. Politi, A. Stefanov, J. L. O'Brien, *Nat. Photonics* **3**, 346–350 (2009).
21. Materials and methods are available as supplementary materials on *Science* Online.
22. Z. Ou, Y. Lu, *Phys. Rev. Lett.* **83**, 2556–2559 (1999).
23. C. Reimer *et al.*, *Opt. Express* **22**, 6535–6546 (2014).
24. A. S. Clark *et al.*, *Opt. Express* **20**, 16807 (2012).
25. T. Pittman, *Physics* **6**, 110 (2013).
26. J. Brendel, N. Gisen, W. Tittel, H. Zbinden, *Phys. Rev. Lett.* **82**, 2594–2597 (1999).
27. J. F. Clauser, M. A. Horne, A. Shimony, R. A. Holt, *Phys. Rev. Lett.* **23**, 880–884 (1969).
28. C. C. Gerry, P. L. Knight, *Introductory Quantum Optics* (Cambridge Univ. Press, 2005).
29. Z. Y. Ou, S. F. Pereira, H. J. Kimble, K. C. Peng, *Phys. Rev. Lett.* **68**, 3663–3666 (1992).
30. D. F. V. James, P. G. Kwiat, W. J. Munro, A. G. White, *Phys. Rev. A* **64**, 052312 (2001).
31. G. Vallone, E. Pomarico, P. Mataloni, F. De Martini, V. Berardi, *Phys. Rev. Lett.* **98**, 180502 (2007).

ACKNOWLEDGMENTS

This work was supported by the Natural Sciences and Engineering Research Council of Canada (NSERC) through the Steacie Memorial Fellowship and Discovery Grants programs and by the Australian Research Council Discovery Projects program. C.R. and P.R. acknowledge the support of a NSERC Vanier Canada Graduate Scholarship and a NSERC Alexander Graham Bell Canada Graduate Scholarship (Master's), respectively. M.K. acknowledges support from FRQNT (Fonds de Recherche du Québec–Nature et Technologies) through the MELS fellowship program (Merit Scholarship Program for Foreign Students; Ministère de l'Éducation, de l'Enseignement Supérieur et de la Recherche du Québec). M.K. also acknowledges funding from the European Union's Horizon 2020 research and innovation program under Marie Sklodowska-Curie grant agreement no. 656607. We acknowledge support from the People Programme (Marie Curie Actions) of the European Union's 7th Framework Programme for Research and Technological Development [B.W. under Research Executive Agency (REA) grant agreement no. 625466 and L.C. under REA grant agreement no. 627478]. F.G. acknowledges support from Mitacs through the Accelerate Program. S.T.C. acknowledges support from the CityU SRG-Fd (Strategic Research Grant for fundable Competitive Earmarked Research Grant) program #7004189. We thank R. Helsten for the mechanical design of the interferometer housing; P. Saggu for assisting in the measurement of the single-photon spectrum; L. La Volpe for assisting in the evaluation of the tomography measurement; J. Azaña, T. A. Denidni, S. O. Tatu, and L. Razzari for providing some of the required experimental equipment; and A. Tavares, A. Yurtsever, and M. A. Gauthier for helpful discussions. Special thanks go to QuantumOpus and N. Bertone of OptoElectronics Components for their help and for providing us with state-of-the-art photon detection equipment.

SUPPLEMENTARY MATERIALS

www.sciencemag.org/content/351/6278/1176/suppl/DC1
Materials and Methods
Supplementary Text
Figs. S1 to S4
References (*32*–*37*)

12 November 2015; accepted 5 February 2016
10.1126/science.aad8532

Downloaded from on March 10, 2016

SPIN MODELS

Simple universal models capture all classical spin physics

Gemma De las Cuevas[1]* and Toby S. Cubitt[2]

Spin models are used in many studies of complex systems because they exhibit rich macroscopic behavior despite their microscopic simplicity. Here, we prove that all the physics of every classical spin model is reproduced in the low-energy sector of certain "universal models," with at most polynomial overhead. This holds for classical models with discrete or continuous degrees of freedom. We prove necessary and sufficient conditions for a spin model to be universal and show that one of the simplest and most widely studied spin models, the two-dimensional Ising model with fields, is universal. Our results may facilitate physical simulations of Hamiltonians with complex interactions.

The description of systems with many interacting degrees of freedom is a ubiquitous problem across the natural and social sciences. Be it electrons in a material, neurons interacting through synapses, or speculative agents in a market, the challenge is to simplify the system so that it becomes tractable while capturing some of the relevant features of the real system. Spin models are one way of addressing this challenge. Originally introduced in condensed matter physics in order to study magnetic materials (*1*–*4*), they have permeated many other disciplines, including quantum gravity (*5*), error-correcting codes (*6*), percolation theory (*3*), graph theory (*7*), neural networks (*8*), protein folding (*9*), and trading models in stock markets (*10*).

Spin models are microscopically simple, yet their versatile interactions lead to a very wide variety of macroscopic behavior. Formally, a spin model is specified by a set of degrees of freedom, the "spins," and a cost function, or "Hamiltonian," H that specifies the interaction pattern as well as the type and strength of interactions among the spins. (In physics, the Hamiltonian specifies the energy of each possible spin configuration; in other contexts, this energy value may quantify a more abstract "cost" associated with a configuration.)

This definition encompasses a wide range of models, including attractive and/or repulsive interactions, regular and irregular interaction patterns, models in different spatial dimensions, models with different symmetries (for example, "conventional" spin models with global symmetries versus models with local symmetries, such as lattice gauge theories), many-body interactions [such as vertex models and edge models (*11*)], and more. We will use the word "model" to refer to a (generally infinite) family of spin Hamiltonians. Different Hamiltonians within the same model are typically related in some natural way. For example, the "two-dimensional (2D) Ising model with fields" is the family of Hamiltonians of the form

$$H_G(\sigma) = \sum_{\langle i,j \rangle} J_{ij}\sigma_i\sigma_j + \sum_i r_i\sigma_i \qquad (1)$$

where $\sigma = \sigma_1, \sigma_2, ..., \sigma_n$ is a configuration of Ising (two-level) spins $\sigma_i \in \{-1, 1\}$ on a 2D square lattice, $\langle i,j \rangle$ denotes neigbouring spins, and J_{ij} and r_i are real numbers specifying the coupling strengths and local fields, respectively.

Here, we show that there exist certain spin models, which we call universal, whose low-energy sector can reproduce the complete physics of any other classical spin model. What does it mean to "reproduce the complete physics"? Informally, we say that a spin model with Hamiltonian H simulates a target Hamiltonian H' if (i) the energy levels of H below a threshold Δ reproduce the energy levels of H'; (ii) there is a fixed subset P of the spins of H—which we call the "physical spins"—whose configuration for each energy level below Δ reproduces the spin configuration of the corresponding energy level of H'; and (iii) the partition function of H reproduces that of H'. From the partition function, one can derive all equilibrium thermodynamical properties of the system. A universal model is then a model that can simulate any other spin model.

We denote spin degrees of freedom—discrete or continuous—by a string of spin states $\sigma = \sigma_1, \sigma_2, ..., \sigma_n$. For q-level Ising spins (discrete degrees of freedom with a finite number q of distinct states), we can label the states arbitrarily by integers: $\sigma_i \in \{1, ..., q\}$. For continuous spins, a spin state is represented by a

[1]Max Planck Institute for Quantum Optics, Hans-Kopfermann-Strasse 1, 85748 Garching, Germany. [2]Department of Computer Science, University College London, Gower Street, London WC1E 6EA, UK.
*Corresponding author. E-mail: gemma.delascuevas@mpq.mpg.de

unit vector: $\sigma_i \in S^D$ (where S^D is the D-dimensional unit sphere; often $D = 2$ or 3). We write σ_R to refer to the configuration of a subset R of the spins. We can now define simulation more precisely.

Let $\sigma' = \sigma'_1, \sigma'_2, \ldots$ be the spin degrees of freedom of a target Hamiltonian H'. We say that a spin model with spin degrees of freedom $\sigma = \sigma_1, \sigma_2, \ldots$ can simulate H' if it satisfies all three of the following:

(i) For any $\Delta > \max_{\sigma'} H'(\sigma')$ and any $0 < \delta < 1$, there exists a Hamiltonian H in the model whose low-lying energy levels $E_\sigma = H(\sigma) < \Delta$ approximate the energy levels $E'_{\sigma'} = H'(\sigma')$ of H' to within additive error δ.

(ii) For every spin σ'_i in H', there exists a fixed subset P_i of the spins of H (independent of Δ) so that states of σ'_i are identified with specific configurations of σ_{P_i}, so that $|E'_{\sigma'} - E_\sigma| \leq \delta$ for any energy level $E_\sigma < \Delta$. We refer to the spins $P = \bigcup P_i$ in the simulation that correspond to the spins of the target model as the "physical spins."

(iii) The partition function $Z_H(\beta) = \sum_{\sigma'} e^{-\beta H(\sigma)}$ of H reproduces the partition function $Z_{H'}(\beta) = \sum_{\sigma'} e^{-\beta H'(\sigma')}$ of H' up to constant rescaling, to within arbitrarily small error: $Z_{H'}(\beta) = \gamma(1 + \delta)Z_H(\beta) + O(e^{-\Delta})$ for some known constant γ.

Rescaling of the partition function must necessarily be permitted in the definition of simulation because the universal model will in general have more degrees of freedom than will the target model. (The magnitude of the rescaling has no impact on the efficiency of the simulation, as long as the rescaling is a known, constant value.) For example, we may consider adding a single q-level spin to a system, which does not interact with anything else. Clearly, this new system simulates the original one (ignore the extra particle). However, its partition function is rescaled by a factor of q.

We say that a model is "universal" if, for any Hamiltonian $H' = \sum_{I=1}^{m} h_I$ on n spins composed of m separate k-body terms, H' can be simulated by some Hamiltonian H from the model specified by poly(m, 2^k, $1/\delta$) parameters and acting on poly(n, m, 2^k, $1/\delta$) spins, with the size of the set of physical spins scaling at most as $|P| = \text{poly}(1/\delta)$.

Our definition of simulation is very strong; it requires that the target model can be approximated with an arbitrarily large energy cut-off Δ and to arbitrarily good accuracy δ. In general, this accuracy is achieved at the expense of increasing the coupling strengths in the universal model. When both the universal model and the target Hamiltonian have discrete degrees of freedom (for example, the 2D Ising model with fields), the energy levels and configurations are reproduced exactly, $\delta = 0$.

The first property required for a universal spin model concerns the computational complexity of the ground state energy problem (GSE) of the model. In this problem, we are asked whether the ground state energy of the system is below some given value K. Recall that NP (nondeterministic polynomial time) is the class of Yes/No problems for which every Yes instance has a "certificate" or "proof" that can be verified in polynomial time, whereas all certificates are rejected in polynomial time if it is a No instance. A problem in NP is NP-complete if every other problem in NP can be efficiently transformed into it (a "polynomial-time reduction"). A canonical NP-complete problem is the Boolean satisfiability problem (SAT), which asks whether there is an assignment to the variables of a Boolean formula for which the formula evaluates to true (is "satisfiable").

It is a classic result that the GSE for some spin models is NP-complete (*12*). This can be seen by providing a polynomial-time reduction from SAT. That is, given a Boolean formula ϕ, one constructs a Hamiltonian H so that ϕ is satisfiable if and only if there is a spin configuration σ so that $H(\sigma) \leq K$, where H and K are determined by ϕ and the number of spins and parameters in H is at most polynomially larger than the number of Boolean variables. For universality, we will need a slightly stronger form of reduction: a "faithful" reduction from SAT. This should additionally preserve the structure of the solution, in the sense that every satisfying assignment of ϕ should be in one-to-one correspondence with a ground-state configuration of H, when the latter is restricted to a subset of spins P.

The second condition, which we call "closure," concerns combining different Hamiltonians from the same model. We say that a model is "closed" if for any pair of Hamiltonians $H_A^{(1)}$ and $H_B^{(2)}$ in the model acting on arbitrary sets of spins A, B (which could overlap), there is another Hamiltonian H in the model that simulates $H_A^{(1)} + H_B^{(2)}$. If the model places no constraints on the interaction pattern or coupling strengths (for example, if it is the set of Ising models on any graph), then it is trivially closed. Closure is nontrivial if the interaction pattern of the spins is restricted in some way (for example, to a lattice).

Our first main result is that a spin model is universal if and only if it is closed and its ground-state energy problem admits a faithful, polynomial-time reduction from SAT (supplementary text). Our second main result is that the 2D Ising model with fields (Eq. 1) satisfies these two conditions; hence, the 2D Ising model with fields is universal (supplementary text).

Closure allows large systems to be built up by combining basic building blocks, whereas the faithful SAT reduction guarantees that the model is sufficiently rich. More precisely, the SAT reduction allows us to encode universal computation into the ground state. We use this to isolate one bit of information about the spin configuration and localize it in a single "flag spin." To give energy E to a particular spin configuration σ, we make the state of the flag spin indicate whether or not the other spins are in the state σ (say, spin-up if they are, spin-down if not). Adding a term to the Hamiltonian that gives energy E to the spin-up state of the flag spin produces the desired energy level for the σ configuration. We do this for every energy level of each local interaction of the target Hamiltonian and then combine all the resulting Hamiltonian terms using closure.

To see how this works, we can consider the example of the Ising model with fields on an

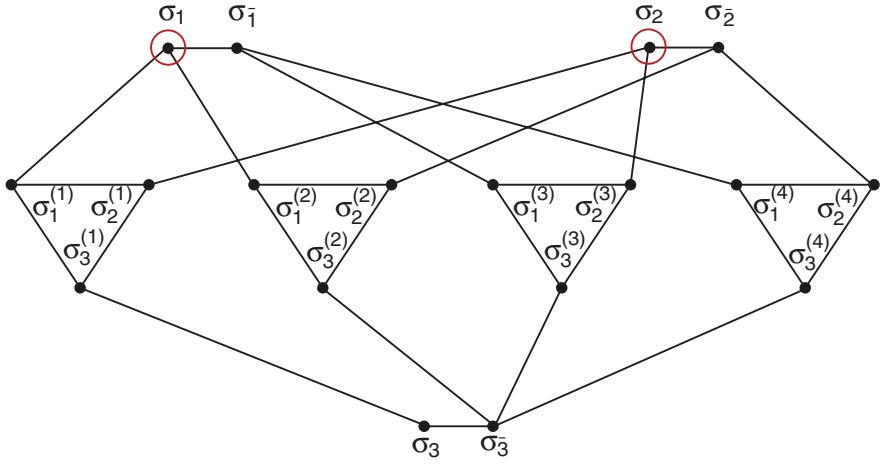

Fig. 1. Faithful reduction from SAT to the GSE of the Ising model. The Ising model with Hamiltonian H_{00} (Eq. 5) corresponding to formula ϕ_{00} (Eq. 2) is defined on the graph shown here. The spins marked in red are those belonging to the physical set P.

arbitrary graph. First, any Boolean expression can be rewritten in terms of a conjunction (Boolean AND, ∧) of clauses, in which each clause is the disjunction (Boolean OR, ∨) of three variables or their negations (Boolean NOT, ¬). For example, consider the Boolean function $\phi_{00}(x_1, x_2, x_3)$ = 1 if (x_1, x_2, x_3) = (0, 0, 1) or (0, 1, 0) or (1, 0, 0) or (1, 1, 0), and $\phi_{00}(x_1, x_2, x_3)$ = 0 otherwise. We can write this as

$$\phi_{00}(x_1, x_2, x_3) = (x_1 \vee x_2 \vee x_3) \wedge (x_1 \vee \neg x_2 \vee \neg x_3) \wedge (\neg x_1 \vee x_2 \vee \neg x_3) \wedge (\neg x_1 \vee \neg x_2 \vee \neg x_3) \quad (2)$$

Combining results from (*12*, *13*), we obtain a faithful reduction from any Boolean formula to the Ising model with fields (*14*). First, we identify each Boolean variable x_i (taking values 0/1) with an Ising spin $\sigma_i = 2x_i - 1$ (taking values −1/+1). We introduce an additional spin $\sigma_{\neg i}$ (whose state will be identified with $\neg x_i$) coupled to σ_i by an antiferromagnetic Ising interaction:

$$h_i = \frac{1}{2}\sigma_i\sigma_{\neg i} + \frac{1}{2} \quad (3)$$

For each clause c, we introduce three auxiliary spins $\sigma_1^{(c)}, \sigma_2^{(c)}, \sigma_3^{(c)}$, coupled to each other in a triangle of Ising interactions and local fields, and couple $\sigma_i^{(c)}$ to the spin corresponding to the literal (variable or its negation) appearing in the ith position of the clause. The Hamiltonian for the clause $(x_1 \vee x_2 \vee x_3)$ is

$$h_c = -\sum_{i=1}^{3}\sigma_i^{(c)} - \frac{1}{2}\sum_{i=1}^{3}\sigma_i + \frac{1}{2}\sum_{\substack{i,j=1 \\ i<j}}^{3}\sigma_i^{(c)}\sigma_j^{(c)} + \frac{1}{2}\sum_{i=1}^{3}\sigma_i\sigma_i^{(c)} + \frac{5}{2} \quad (4)$$

For a clause involving a negated variable $\neg x_i$, the second and the next-to-last term would contain $\sigma_{\neg i}$ instead of σ_i.

For example, the Hamiltonian for the formula ϕ_{00} from Eq. 2 is

$$H_{00} = \sum_{i=1}^{3} h_i + \sum_{c=1}^{4} h_c \quad (5)$$

where the second sum runs over the four clauses in Eq. 2 (Fig. 1). The four ground states of H_{00} have energy 0, and in any ground state, $\sigma_3 = 1$ only when (σ_1, σ_2) = (−1, −1); otherwise, $\sigma_3 = -1$. Thus, σ_3 acts as a "flag" for configuration (−1, −1) of the first two spins.

A flag spin b for a general spin configuration $(\sigma_1, \sigma_2, ..., \sigma_n)$ is constructed in the same way from the Boolean function

$$\phi(x_1, x_2, ..., x_n, b) = \begin{cases} 1 & b = 1 \text{ and } x_i = \dfrac{1+\sigma_i}{2} \text{ for all } i \\ 0 & \text{otherwise.} \end{cases} \quad (6)$$

We "penalize" configurations in which the flag spin is incorrect by multiplying the whole Hamiltonian by a large constant Δ.

Last, to reproduce one energy level of the target model, we add a local field E' to the corresponding flag spin, where E' is chosen to be the energy of the target model in this configuration. For example, to produce an energy level E' for the spin configuration (−1, −1), we use

$$H = \Delta H_{00} + E'\frac{\sigma_3 + 1}{2} \quad (7)$$

This Hamiltonian has exactly one energy level below Δ in which (σ_1, σ_2) = (−1, −1), and this level has energy E'.

This construction already shows that the Ising model with fields on an arbitrary graph (with real coupling strengths and fields) is universal. This is easier than the general case because closure is trivial (if H_1 and H_2 are both Ising Hamiltonians, then $H_1 + H_2$ is also an Ising Hamiltonian); the model includes arbitrary local field terms, which lets us simply add the second term in Eq. 7; and the construction automatically reproduces the partition function (with $\gamma = 1/576^m$ for a target Hamiltonian with m two-body terms). Nonetheless, the general proof (supplementary text) uses the same ideas, is also constructive, and similarly introduces only a polynomial overhead in the number of spins and interactions. The above proof can be extended to the 2D Ising model with fields (with inhomogeneous couplings and local fields), showing that the 2D Ising model with fields is universal. Full technical details, including precise expressions for the polynomial simulation overhead, are available in the supplementary text.

That the Ising model with fields is closed and has a faithful reduction from SAT shows that these conditions are necessary for universality: If a model is universal, one of the models it must be able to simulate is the Ising model.

We have focused so far on models with discrete spin degrees of freedom. For universal models with continuous spins, the requirement of a faithful reduction from SAT implies that the model is able to approximate energy distributions that are sharply peaked around a set of configurations that correspond to discrete Boolean values. Thus, the arguments for the discrete case essentially go through unchanged. (Such sharply peaked energy distributions seem somewhat artificial, so our results suggest that natural models with continuous degrees of freedom will typically not be universal.) To simulate target models with continuous spins, the idea is to discretize the continuous degrees of freedom sufficiently finely to give a good approximation and then simulate this discretized version. One can show that the overhead from this discretization scales favorably with the precision of the approximation (supplementary text).

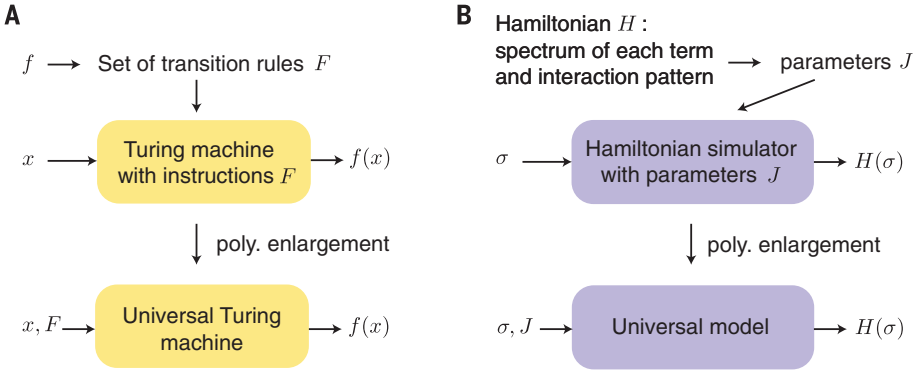

Fig. 2. Computation versus Hamiltonian simulation. (**A**) Any given Turing machine computes some function $f(x)$ of its input x. Knowing the transition rules of a specific Turing machine, we can choose the input to a Universal Turing machine in such a way that it simulates the original machine (at the expense of a polynomial overhead). (**B**) Similarly, any given spin Hamiltonian assigns an energy $H(\sigma)$ to each spin configuration σ. Knowing the energy levels of the individual terms of a specific Hamiltonian, we can choose the parameters of a universal model in such a way that it simulates the original Hamiltonian (at the expense of a polynomial enlargement of the model).

The role of universal models for classical spin Hamiltonians is analogous to that of universal Turing machines for classical computation (Fig. 2). Just as choosing the input to a universal Turing machine allows it to simulate any other computation, choosing the parameters of a universal model allows it to simulate any other Hamiltonian H'. Moreover, our proof is constructive: It provides the parameters needed for the universal model to simulate H'; indeed, these parameters can be computed efficiently from the description of H'.

The existence of universal models means that in different parts of its phase diagram, a universal model will reproduce every phase of every other spin model. In some sense, this can be viewed as an inversion of the usual renormalization group flow; by "fine-graining" the model and introducing additional short-range parameters, all models (including models in different universality classes) are revealed to be specific cases of the universal model (Fig. 3).

One might have assumed that the physics of a many-body system would have characteristics determined by the number of spatial dimensions, or the structure of the interaction pattern, or whether the interactions are two-body or many-body, or the symmetry of its interactions, or whether the local degrees of freedom are continuous or discrete. The existence of universal models implies that for

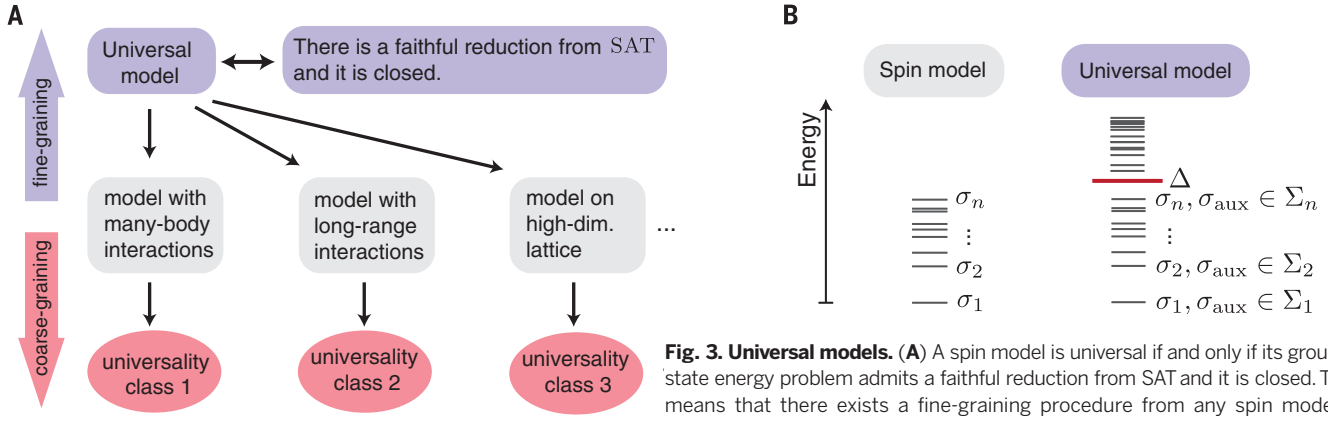

Fig. 3. Universal models. (**A**) A spin model is universal if and only if its ground-state energy problem admits a faithful reduction from SAT and it is closed. This means that there exists a fine-graining procedure from any spin model—including models with many-body interactions, long-range interactions, or defined on high-dimensional lattices—that transforms it to the low-energy sector of the universal model. On the other hand, coarse-graining different spin models leads to a classification into different universality classes. (**B**) For any spin Hamiltonian, the parameters of the universal model can be chosen so that its spectrum below a threshold Δ (red line) is identical to the entire spectrum of the target Hamiltonian. Moreover, the spin configuration of each energy level, σ_j, is reproduced in a subset of the spins of the universal model, and the spin configuration of the auxiliary spins, σ_{aux}, is in one of the allowed configurations Σ_j. The two partition functions are identical up to a rescaling and an exponentially small factor in Δ.

models with inhomogeneous couplings, none of these are the case. For example, there can be nothing specifically characteristic to the physics of spin systems in three spatial dimensions because all physical properties of a 3D system can be simulated in a 2D Ising model with inhomogeneous couplings. Another way of viewing this is that the inhomogeneity of the couplings in the universal model destroys all properties related to, for example, spatial dimension and symmetries. Similarly, in a sense there can be no physical properties specific to models with continuous degrees of freedom because these can be simulated to any desired precision by using Ising spins. Our result also implies and explains the recently found "completeness results" (*15*–*20*), in which a model is called "complete" if its partition function can equal (up to a factor) the partition function of any other model (*15*). Any universal model is complete by taking Δ to ∞ (supplementary text).

Simulating a target model by using a universal model necessarily incurs some overhead. In general, simulating the target model directly will usually be more efficient. However, sometimes one is interested in physically constructing a particular spin model. Indeed, in the quantum setting this is precisely the goal of "analog" or "physical" Hamiltonian simulation (*21*). Universal models are potentially interesting in this setting of physical simulation. Our results imply that one is free to choose a universal model with interactions that are easier to generate in a physical system (such as two-body, nearest-neighbor interactions), and that this will be sufficient to simulate any other spin model, even ones with interactions that are difficult to produce directly (such as long-range, many-body interactions). Examples of simulation of specific models are provided in the supplementary text. These constructions can be optimized for a specific pair of universal and target model. Finding optimal constructions in various physical settings is a remaining open problem.

It is not easy in general to determine whether the GSE of a model has a reduction from SAT, but for models with two-level spins, a complete classification is known (*22*, *23*). This could lead to a classification of all universal models with two-level spins. Another possibility is whether translationally invariant models can be universal. The NP-hardness of the GSE of certain translationally invariant models suggests that this may be a possibility (*24*).

Last, we may ask whether such (efficient) universal models exist for the simulation of quantum Hamiltonians, particularly given the potential applications to physical Hamiltonian simulation. The Quantum Merlin Arthur (QMA)–completeness of various important quantum Hamiltonians (*25*, *26*) and the ability to efficiently simulate Hamiltonian dynamics (*27*) could pave the way to quantum generalizations of our results.

REFERENCES AND NOTES

1. H. T. Diep, ed., *Frustrated Spin Systems* (World Scientific, 2004).
2. K. Binder, W. Knob, *Glassy Materials and Disordered Solids* (World Scientific, 2005).
3. H. Nishimori, G. Ortiz, *Elements of Phase Transitions and Critical Phenomena* (Oxford Univ. Press, 2011).
4. R. J. Baxter, *Exactly Solvable Models in Statistical Mechanics* (Academic Press Limited, 1982).
5. J. A. Ambjørn, K. N. Anagnostopoulos, R. Loll, I. Pushinka, *Nucl. Phys. B* **807**, 251–264 (2009).
6. H. Nishimori, *Statistical Physics of Spin Glasses and Information Processing: An Introduction* (Oxford Univ. Press, 2001).
7. B. Bollobás, *Modern Graph Theory* (Springer, 1998).
8. R. Rojas, *Neural Networks—A Systematic Introduction* (Springer-Verlag, 1996).
9. J. D. Bryngelson, P. G. Wolynes, *Proc. Natl. Acad. Sci. U.S.A.* **84**, 7524–7528 (1987).
10. S. N. Durlauf, *Proc. Natl. Acad. Sci. U.S.A.* **96**, 10582–10584 (1999).
11. G. De las Cuevas, *J. Phys. At. Mol. Opt. Phys.* **46**, 243001 (2013).
12. F. Barahona, *J. Phys. A* **15**, 3241–3253 (1982).
13. M. R. Garey, D. S. Johnson, *Computers and Intractability* (W. H. Freeman and Company, 1979).
14. M. Gu, A. Perales, *Phys. Rev. E Stat. Nonlin. Soft Matter Phys.* **86**, 011116 (2012).
15. M. Van den Nest, W. Dür, H. J. Briegel, *Phys. Rev. Lett.* **100**, 110501 (2008).
16. V. Karimipour, M. H. Zarei, *Phys. Rev. A* **86**, 052303 (2012).
17. G. De las Cuevas, W. Dür, M. Van den Nest, H. J. Briegel, *J. Stat. Mech.* **2009**, P07001 (2009).
18. G. De las Cuevas, W. Dür, H. J. Briegel, M. A. Martin-Delgado, *Phys. Rev. Lett.* **102**, 230502 (2009).
19. V. Karimipour, M. H. Zarei, *Phys. Rev. A* **85**, 032316 (2012).
20. Y. Xu, G. De las Cuevas, W. Dür, H. J. Briegel, M. A. Martin-Delgado, *J. Stat. Mech.* **2011**, P02013 (2011).
21. A. Trabesinger, *Nat. Phys.* **8**, 263 (2012).
22. N. Creignou, *J. Comput. Syst. Sci.* **51**, 511–522 (1995).
23. T. Schaefer, *STOC '78: Proceedings of the 10th Annual ACM Symposium on Theory of Computing*, pp. 216–226 (1978).
24. D. Gottesman, S. Irani, *Proceedings 50th Annual Symposium on Foundations of Computer Science*, pp. 95–104 (2009).
25. N. Schuch, F. Verstraete, *Nat. Phys.* **5**, 732–735 (2009).
26. A. M. Childs, D. Gosset, Z. Webb, in *Automata, Languages, and Programming* (Springer, 2014), pp. 308–319.
27. S. Lloyd, *Science* **273**, 1073–1078 (1996).

ACKNOWLEDGMENTS

We thank D. Pérez-García, W. Dür, and M. Van den Nest for discussions. G.D.L.C. acknowledges support from the Alexander von Humboldt foundation and Simulators and Interfaces with Quantum Systems (SIQS). T.S.C. is supported by the Royal Society. This work was made possible through the support of grant 48322 from the John Templeton Foundation. The opinions expressed in this publication are those of the authors and do not necessarily reflect the views of the John Templeton Foundation. The authors declare no competing financial interests.

SUPPLEMENTARY MATERIALS

www.sciencemag.org/content/351/6278/1180/suppl/DC1
Supplementary Text
Figs. S1 to S6
References (*28*–*38*)

13 April 2015; accepted 3 February 2016
10.1126/science.aab3326

TOPOLOGICAL MATTER

Quasiparticle interference of the Fermi arcs and surface-bulk connectivity of a Weyl semimetal

Hiroyuki Inoue,[1]* András Gyenis,[1]* Zhijun Wang,[1] Jian Li,[1] Seong Woo Oh,[1] Shan Jiang,[2] Ni Ni,[2] B. Andrei Bernevig,[1] Ali Yazdani[1]†

Weyl semimetals host topologically protected surface states, with arced Fermi surface contours that are predicted to propagate through the bulk when their momentum matches that of the surface projections of the bulk's Weyl nodes. We used spectroscopic mapping with a scanning tunneling microscope to visualize quasiparticle scattering and interference at the surface of the Weyl semimetal TaAs. Our measurements reveal 10 different scattering wave vectors, which can be understood and precisely reproduced with a theory that takes into account the shape, spin texture, and momentum-dependent propagation of the Fermi arc surface states into the bulk. Our findings provide evidence that Weyl nodes act as sinks for electron transport on the surface of these materials.

Understanding the exotic properties of quasiparticles at the boundaries of topological phases of electronic matter is at the forefront of condensed-matter physics research. Examples include helical Dirac fermions on the surface of time-reversal invariant topological insulators (*1*), which have been demonstrated to be immune to backscattering (*2*–*4*), or the emergent Majorana fermions at the edge of a topological superconductor (*5*–*7*). Topological properties of phases of matter are, however, not limited to gapped systems, and recent theoretical efforts have uncovered the possibility of topologically protected metallic phases. Topological Dirac semimetals (*8*, *9*)—three-dimensional analogs of graphene with band crossings protected by crystalline symmetry—have been recently realized experimentally (*10*–*12*). Breaking of the inversion or time-reversal symmetry splits the Dirac crossings of the band structure into Weyl points, which are singularities in the Berry curvature characterized by a Chern number or more colloquially monopole charge (*13*, *14*). These semimetals host bulk quasiparticles that are chiral Weyl fermions. The topologically protected boundary modes of Weyl semimetals are surface states with a disjointed two-dimensional Fermi surface (*15*, *16*). These so-called Fermi arcs connect surface projections of bulk Weyl points of opposing Chern numbers. A notable property of these Fermi arc states is that they can become delocalized into the bulk through the projected Weyl points. Ideally, in the absence of disorder, an electron on the Fermi arcs of one surface can sink through the bulk and appear on the arcs of the opposing surface.

Recent work has shown strong evidence that inversion symmetry–breaking transition-metal compounds (TaAs, TaP, NbAs, NbP) are Weyl semimetals (*17*–*21*). Angle-resolved photoemission spectroscopy (ARPES) measurements have confirmed that the surface electronic structure of these compounds has a disconnected arclike topology connecting the surface projection of 24 Weyl crossings in the bulk band structure. Here we used the scanning tunneling microscope (STM) to directly visualize the surface states of the Weyl semimetal TaAs and examine their scattering and quantum-interference properties. Our experimental approach follows similar STM studies that showed that the spin texture (and time-reversal symmetry) protects surface states on topological insulators from backscattering (*2*–*4*, *22*). In contrast to these previous studies, we find that the momentum-dependent delocalization of the Fermi arcs into the bulk, which is a unique property of these surface states, determines the coherent interference properties of these surfaces states. The surface-bulk connectivity examined here underlies several other novel electronic phenomena, such as nonlocal transport that can occur in Weyl semimetals (*23*–*27*). A recent magnetotransport study has observed quantum oscillations that may be associated with the nonlocal nature of transport, with electron orbits traversing through bulk Weyl nodes and surface states (*28*).

To probe the properties of the Weyl semimetal's Fermi arc states, we have carried out STM studies (at 40 K) of in situ cleaved surfaces of TaAs single crystals that show atomically ordered terraces and tunneling density of states spectra consistent with

[1]Joseph Henry Laboratories of Physics, Department of Physics, Princeton University, Princeton, NJ 08540, USA. [2]Department of Physics and Astronomy and California NanoSystems Institute, University of California at Los Angeles, Los Angeles, CA 90095, USA.
*These authors contributed equally to this work. †Corresponding author. E-mail: yazdani@princeton.edu

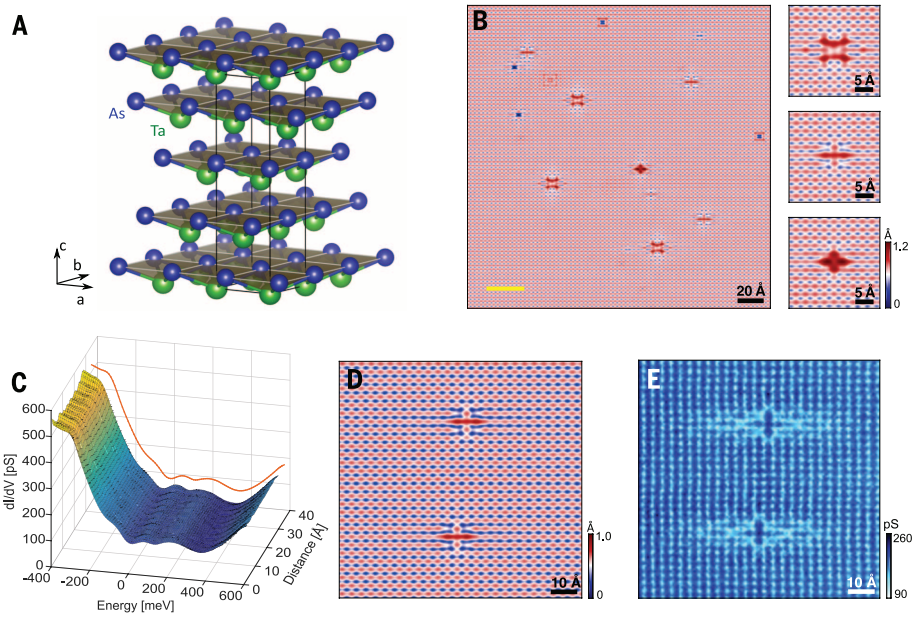

Fig. 1. STM topography and *dI/dV* spectroscopy of Weyl semimetal TaAs. (**A**) Illustration of the crystal structure of TaAs with (001) As termination. One unit cell contains four layers of As and Ta. The lattice parameters are $a = b = 3.43$ Å and $c = 11.64$ Å. (**B**) STM topographic image ($V_{bias} = 500$ mV, $I_{setpoint} = 100$ pA) of the cleaved (001) surface of TaAs. Magnified views on some of the pronounced impurities (right panels) show apparent C_{2v} symmetric deformation of the electronic structure. (**C**) Spatial variation of the differential conductance measurements along a line of 30 Å, shown as a yellow line in (B), was measured with lock-in techniques employing 3-mV excitations at 707 Hz. The orange curve shows the spatially averaged *dI/dV* spectra. An atomically periodic modulation of the spectra is visible. (**D**) Topographic image and (**E**) conductance map at 120 meV ($V_{bias} = -340$ mV, $I_{setpoint} = 80$ pA) on the same area, where the C_{2v} symmetric nature of the surface electronic states is clearly visible.

Downloaded from on March 10, 2016

a semimetal (Fig. 1). The analysis of the atomic step edge heights in STM topographs shows only one type of surface for the cleaved samples, which is likely terminated by As atoms [see below and (*29*)]. Although the surface atomic structure visualized in the STM images has fourfold symmetry, the underlying electronic structure of this compound only has C_{2v} symmetry, which is evident from its overall crystal structure shown in Fig. 1A. A C_{4v} nonsymmorphic symmetry is broken by the surface. The anisotropic local shape of electronic signatures caused by native surface defects shown in STM topography (Fig. 1, B and D), as well as the scattering of surface quasiparticles around such defects over long length scales displayed in STM conductance maps (Fig. 1E), both show a clear C_{2v} symmetry.

Detailed information about the electronic properties of the surface states can be obtained from measurements of the quasiparticle interference (QPI) patterns in large-area STM conductance maps. The Fourier transform of such STM conductance maps identifies scattering wave vectors q, which connect k_i and k_f states on the contours of constant-energy surface in momentum space (*30*). QPI measurements can be used not only to follow the evolution of the Fermi surface probed near the surface but also to determine whether some scattering wave vectors are forbidden as a result of discrete symmetries (*2*, *23*, *24*). Information on quasiparticle lifetime can also be extracted from QPI; however, such effects do not typically result in momentum-specific changes in the QPI, as we discuss here.

Experimentally, the detection of scattering wave vectors in QPI measurements is limited by instrumental resolution, which is determined by the stability of the instrument and the maximum averaging time possible during each map. In Fig. 2, we show QPI measurements on the TaAs surface obtained with a high-resolution, home-built STM instrument capable of averaging for up to 6 days while maintaining atomic register. The Fourier transform of these QPI measurements (Fig. 2) allows us to resolve the rich array of scattering wave vectors on this compound. Such high-resolution measurements are required to resolve the entire set of allowed scattering wave vectors in this compound. In Fig. 2, Q to S, we also show measurements of the QPI features as a function of energy along specific directions in q space, displaying continuous dispersion of these features with energy, as is typical of QPI features. Recent measurements on a related Weyl compound (NbP) at lower resolution have yielded a subset of QPI signals (3 out of 10 wave vectors) reported here (*31*).

QPI measurements from surface states of most materials can be understood by starting from a model of contours of constant energy in momentum space, consistent with ARPES-measured band structure, that can be used to calculate a joint density of states (JDOS) probability for scattering as a function of momentum difference q (*32*). If the Fermi surface is spin textured, as in the case of helical Dirac surface states or strongly spin-orbit–coupled systems, the experimental results can be compared with the spin-dependent scattering probability (SSP) maps that also take into account the influence of relative spin orientations of the initial and final states on the QPI measurements (*2*, *29*). Following such an approach, we use density functional theory (DFT) methods to calculate the surface states for TaAs. We reproduce both the shape (*17*, *20*, *21*) and spin texture (*33*–*35*) of the surface Fermi contours (Fig. 3A) recently measured with ARPES on this compound and calculate the SSP map near the chemical potential, which can then be compared to our experimental results at the same energy. In addition to the Fermi arcs, both ARPES measurements and the DFT calculations capturing them may include some features that are in fact caused by trivial surface states (*29*). This approach results in an SSP (Fig. 3B) that resembles the overall symmetry of the experimentally measured QPI pattern (Fig. 3F); however, it produces many more scattering wave vectors than seen experimentally (such as those in the middle of the QPI zone highlighted in Fig. 3B that are missing in Fig. 3F). This approach or a related one proposed recently (*36*) for understanding the data on NbP (*31*) also fails to capture the QPI data on TaAs at other energies (*29*).

An accurate model of our experimental results over a wide energy range can be achieved if we consider not only the shape, the density of states, and the spin texture of the Fermi arcs but also

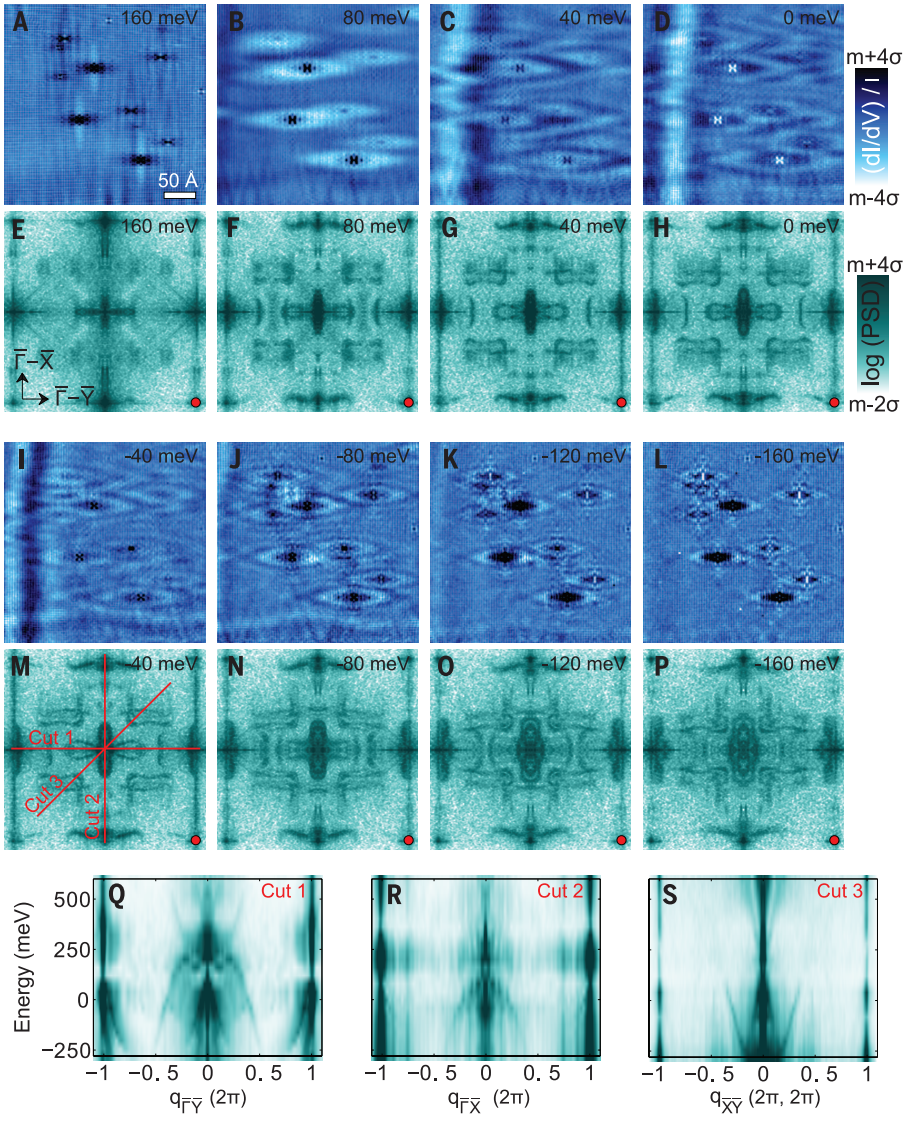

Fig. 2. Quasiparticle interference of TaAs surface states. (**A** to **D** and **I** to **L**) Spatially resolved *dI/dV* conductance maps at different energies obtained on the area shown in Fig. 1B (V_{bias} = 240 meV, $I_{setpoint}$ = 120 pA). (**E** to **H** and **M** to **P**) Symmetrized and drift-corrected Fourier transforms of the *dI/dV* maps (QPI maps). Red dot indicates the (2π, 2π) point in the reciprocal space in the unit of 1/*a*; PSD denotes power spectral density. In the color bar, *m* corresponds to the mean value of the map and σ to the standard deviation. (**Q** to **S**) Energy-momentum structure of the *dI/dV* maps (V_{bias} = 600 meV, $I_{setpoint}$ = 80 pA) along the high-symmetry directions shown in (M).

their momentum-dependent delocalization into the bulk of the sample. The key conceptual idea is that the QPI of the Fermi arcs is dominated by initial and final momentum states that do not strongly leak into the bulk. The degree of connectivity between Fermi arc surface states and the bulk is a property that depends on their momentum approaching the projection of Weyl points on the surface. It is also related to the atomic character of the Weyl nodes. Our DFT simulation of the TaAs electronic structure shows that the majority (~90%) of electronic states associated with the bulk Weyl nodes are based on Ta atomic orbitals (*29*). Consistent with this information, we also find from the DFT calculation that the electronic states close to the projected Weyl points on the surface arcs have a large component of such orbitals. This results in the slow decay of the Fermi arcs' spectral weight associated with Ta orbitals into the bulk, as compared to that associated with As orbitals (Fig. 3C) (*29*). This picture suggests that to understand the QPI data on TaAs, we should project out the Fermi arc states that are associated with Ta and focus only on states with the As-orbital characteristics, which have the weakest connectivity to the bulk states and hence can interfere coherently to produce the QPI patterns. The Ta orbitals in the first layer only weakly contribute to the QPI signal: An electron that scatters from the As site to a Ta site in the surface layer is more likely to sink into the bulk Weyl states (Fig. 3C). The presence of topologically trivial surface states [likely the inner bowtie feature in Fig. 3, A and D; see also (*29*)] does not alter the projection of bulk Weyl points at the surface, and all surface states at the Fermi level with these momenta would still be strongly delocalized into the bulk.

To confirm this idea, we consider a weighted Fermi arc contour for TaAs, in which we project the Fermi arc states onto the As orbitals at the topmost surface layer (Fig. 3D). This projection results in changes that are strongly dependent on the distance (in k space) from the Weyl point. Taking into account the delocalization into the bulk, we find strong fading of the innermost spoon-shaped Fermi arcs in the weighted Fermi surface, as compared to that shown in Fig. 3A. These short spoon-shaped sections of the Fermi arcs are close to their corresponding Weyl points, which are expected to act as sinks for electron propagation on the surface (because of their dominant Ta orbital character). In contrast, the prominent features of this weighted Fermi surface come from longer bowtie-shaped arcs at the Brillouin zone boundary, which lie far away from their corresponding Weyl point, with the least probability of sinking into the bulk (owing to their dominant As orbital character). An electron in the weighted Fermi arcs shown in Fig. 3D (or a similar one that also includes the As projection in the second layer; see the supplementary materials) is in a subset of states that do not efficiently propagate away into the bulk and remain near the surface.

Without any further computation, we can understand the various wave vectors seen in the QPI measurements by simply considering scattering around the weighted Fermi arc contours (Fig. 3D). Based on the length and orientation of the possible scattering wave vectors on the weighted Fermi surface, we identify 10 different groups of scattering wave vectors, Q_1 to Q_{10}, that are seen experimentally. More detailed calculations of SSP (Fig. 3E) near the chemical potential based on these weighted Fermi arcs also compare favorably to the experimentally measured QPI at the same energy (Fig. 3F). In making this comparison, we note that although the spin texture of the Fermi arcs and the absence of backscattering between time-reversed pairs of states play a role in the scattering data (a point to which we return below), the differences between JDOS and SSP for the Fermi arcs are relatively minor and not critical to understanding the QPI data [(*29*) and see below]. Contrasting results of the SSPs using weighted (Fig. 3E) and unweighted (Fig. 3B) Fermi arcs with the experimental data (Fig. 3F) demonstrates that at some momenta, the Fermi arc surface electrons have a strong probability of sinking into the bulk state and hence are not part of the QPI process. We further test this physical picture by a more exhaustive comparison of theoretical model calculations based on the weighted Fermi arcs and the experimental data over a wide range of energies (Fig. 4, A to L). As shown in this figure, our model SSP calculations for the weighted Fermi arc can reproduce the finer features of the large body of QPI data obtained in our studies. In addition, isolating the contribution from the As or Ta atomic sites to the QPI signal also can be used to confirm our theoretical identification of the major contribution of each atomic orbital to different sections of Fermi arcs [bowtie and spoon features dominated by As and Ta, respectively (*29*)]. The agreement between theory and QPI measurements demonstrates the importance of accounting for delocalization of the TaAs surface states caused by the Weyl nature of its band structure.

We now return to the role of spin texture in determining the scattering properties of the Fermi arcs. Focusing on some of the finer features of the QPI data, in particular, scattering wave vectors Q_3 and Q_9, and their comparison to the theory, we can also resolve the subtle influence of spin texture on the STM data. This comparison (Fig. 4, M to O) demonstrates that some of the duplicate features in the JDOS maps caused by scattering between arc states that have opposing spins are suppressed in the SSP maps. Although almost at the limit of our experimental resolution, the correspondence between the finer predicted features in the SSP based on our model and those in the experimental QPI data qualitatively confirms that spin does play a role, albeit minor, in

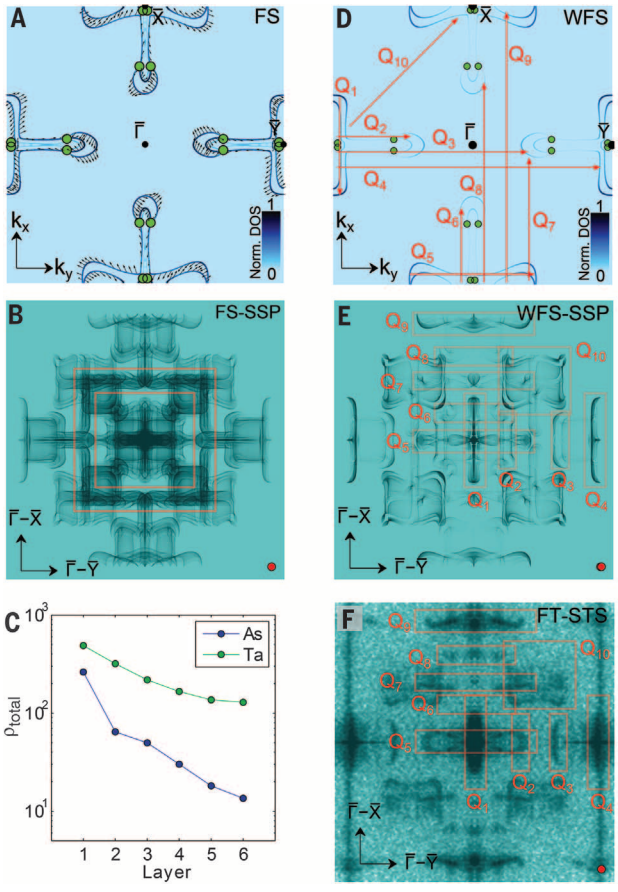

Fig. 3. Fermi arcs and quasiparticle interference. (**A**) DFT-calculated Fermi arc contour of constant energy in first Brillouin zone (BZ) at +40 meV calculated projecting the DFT-calculated spectral density to the top unit cell. Green dots indicate the projected positions of the Weyl nodes, and arrows show the direction of the spin on the Fermi arcs. The combination of time-reversal symmetry and C_{2v} symmetry implies vanishing out-of-plane component of the spin. FS, Fermi surface. (**B**) SSP derived from (A) marked by regions of strong scattering in the middle of the BZ, which is missing in the QPI data. (**C**) The integrated spectral density over the full BZ for As and Ta separately as a function of layer index shows the fast decay of As orbital states. (**D**) Weighted Fermi surface (WFS) calculated by projecting the electronic states only to the topmost As layer. The Q vectors indicate the scattering wave vectors expected. (**E**) SSP based on (D) with red boxes showing the scattering wave vectors mapped in (F). (**F**) QPI map at 40 meV (same as in Fig. 2G) and experimentally observed groups of Q vectors. FT-STS, Fourier transform–scanning tunneling spectroscopy.

our QPI measurements. There are a few special wave vectors that are strictly prohibited, owing to the presence of time-reversal or mirror symmetry (*23*, *24*). However, these signatures of protected scatterings are unfortunately obscured by many allowed overlapping wave vectors with similar lengths and are hard to resolve experimentally. Future experiments at higher resolution or on Weyl semimetal with simpler structures may better resolve this protection and other universal features of Fermi arcs that are predicted theoretically (*37*, *38*).

Our work reveals that the absences of, or restriction on, coherent scattering at certain wave vectors in both theory and experiments are not a consequence of a symmetry-related protection for the Fermi arc surface states, but rather follow from the topological connection between the surface and bulk states. This connection can also be seen in geometries in which the sample thickness is less than the bulk's scattering mean free path, where the top and bottom surface of a Weyl semimetal would be strongly linked through the Weyl points (*23*, *26*–*28*).

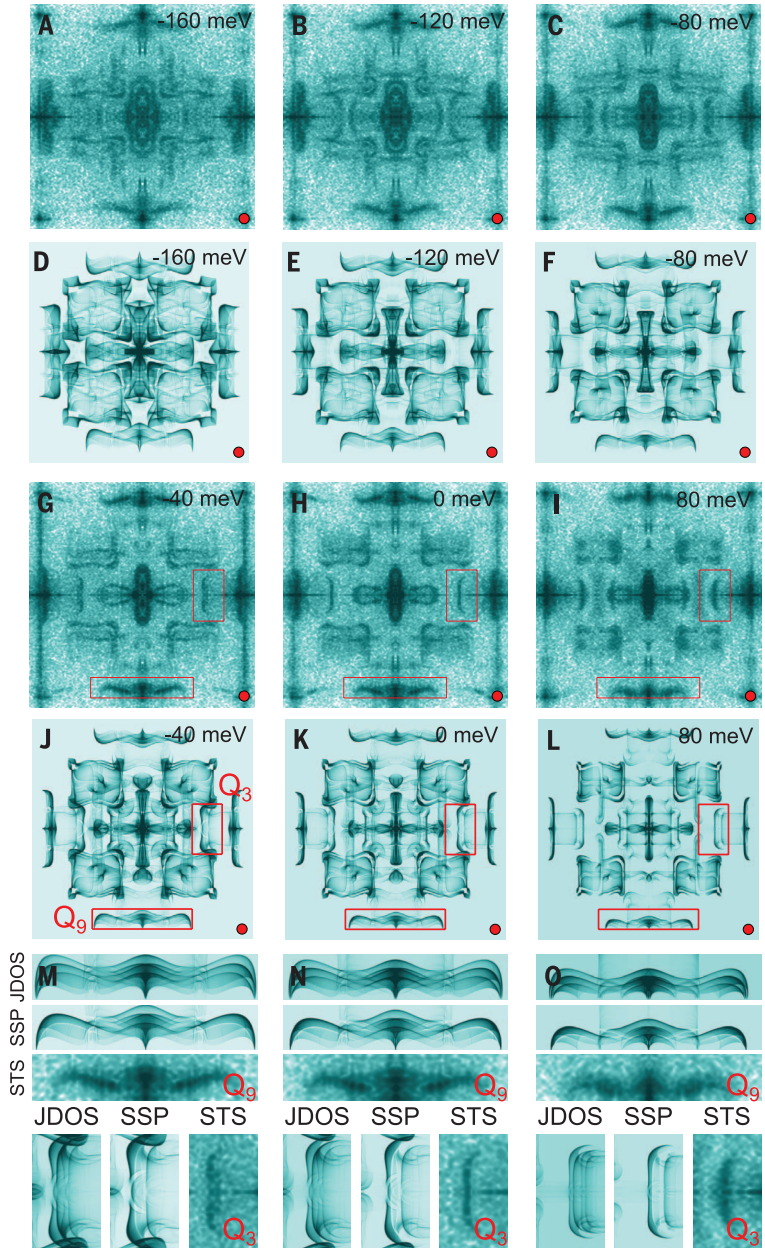

Fig. 4. Comparison of the FT-STS maps with the DFT calculation at various energies. (**A** to **C** and **G** to **I**) QPI maps (same as in Fig. 2) and (**D** to **F** and **J** to **L**) the corresponding SSP derived from the projection of the spectral density to the topmost As. The obtained data and the calculations are in agreement over a wide energy range. (**M** to **O**) Enlargement of the Q_9 and Q_3 vectors in the calculated JDOS, SSP, and QPI data at different energies. Whereas strong triple-arc structures are visible in JDOS, SSP shows a reduced number of arcs, which is consistent with the single arcs in the QPI data.

REFERENCES AND NOTES

1. J. E. Moore, *Nature* **464**, 194–198 (2010).
2. P. Roushan *et al.*, *Nature* **460**, 1106–1109 (2009).
3. Z. Alpichshev *et al.*, *Phys. Rev. Lett.* **104**, 016401 (2010).
4. T. Zhang *et al.*, *Phys. Rev. Lett.* **103**, 266803 (2009).
5. V. Mourik *et al.*, *Science* **336**, 1003–1007 (2012).
6. S. Nadj-Perge *et al.*, *Science* **346**, 602–607 (2014).
7. C. Beenakker, *Annu. Rev. Condens. Matter Phys.* **4**, 113–136 (2013).
8. S. M. Young *et al.*, *Phys. Rev. Lett.* **108**, 140405 (2012).
9. Z. Wang *et al.*, *Phys. Rev. B* **85**, 195320 (2012).
10. Z. K. Liu *et al.*, *Science* **343**, 864–867 (2014).
11. S. Borisenko *et al.*, *Phys. Rev. Lett.* **113**, 027603 (2014).
12. S. Jeon *et al.*, *Nat. Mater.* **13**, 851–856 (2014).
13. H. Nielsen, M. Ninomiya, *Phys. Lett. B* **130**, 389–396 (1983).
14. S. Murakami, *New J. Phys.* **9**, 356 (2007).
15. X. Wan, A. Turner, A. Vishwanath, S. Y. Savrasov, *Phys. Rev. B* **83**, 205101 (2011).
16. A. Burkov, M. Hook, L. Balents, *Phys. Rev. B* **84**, 235126 (2011).
17. H. M. Weng, C. Fang, Z. Fang, B. A. Bernevig, X. Dai, *Phys. Rev. X* **5**, 011029 (2015).
18. S.-M. Huang *et al.*, *Nat. Commun.* **6**, 7373 (2015).
19. B. Q. Lv *et al.*, *Phys. Rev. X* **5**, 031013 (2015).
20. L. X. Yang *et al.*, *Nat. Phys.* **11**, 728–732 (2015).
21. S. Y. Xu *et al.*, *Science* **349**, 613–617 (2015).
22. I. Drozdov *et al.*, *Nat. Phys.* **10**, 664–669 (2014).
23. P. Hosur, *Phys. Rev. B* **86**, 195102 (2012).
24. T. Ojanen, *Phys. Rev. B* **87**, 245112 (2013).
25. P. Hosur, X. L. Qi, *C. R. Phys.* **14**, 857–870 (2013).
26. A. C. Potter, I. Kimchi, A. Vishwanath, *Nat. Commun.* **5**, 5161 (2014).
27. Y. Baum, E. Berg, S. A. Parameswaran, A. Stern, *Phys. Rev. X* **5**, 041046 (2015).
28. J. W. Philip, Moll *et al.*, Chirality transfer dynamics in quantum orbits in the Dirac semi-metal Cd_3As_2 (2015); http://arxiv.org/abs/1505.02817.
29. Materials and methods are available as supplementary materials on *Science* Online.
30. L. Petersen *et al.*, *Phys. Rev. B* **57**, R6858–R6861 (1998).
31. H. Zheng *et al.*, *ACS Nano* **10**, 1378–1385 (2016).
32. J. E. Hoffman *et al.*, *Science* **297**, 1148–1151 (2002).
33. B. Q. Lv *et al.*, *Phys. Rev. Lett.* **115**, 217601 (2015).
34. S. Y. Xu *et al.*, Spin polarization and texture of the Fermi arcs in the Weyl Fermion semimetal TaAs (2015); http://arxiv.org/abs/1510.08430.
35. Y. Sun, S. C. Wu, B. H. Yan, *Phys. Rev. B* **92**, 115428 (2015).
36. G. Chang *et al.*, *Phys. Rev. Lett.* **116**, 066601 (2016).
37. S. Kourtis, J. Li, Z. Wang, A. Yazdani, B. A. Bernevig, *Phys. Rev. B* **93**, 041109 (2016).
38. A. K. Mitchell, L. Fritz, *Phys. Rev. B* **93**, 035137 (2016).

ACKNOWLEDGMENTS

Work at Princeton was supported by Army Research Office–Multidisciplinary University Research Initiative (ARO-MURI) program W911NF-12-1-0461, Gordon and Betty Moore Foundation as part of Emergent Phenomena in Quantum System initiative (GBMF4530), by NSF–Materials Research Science and Engineering Centers programs through the Princeton Center for Complex Materials DMR-1420541, NSF-DMR-1104612, NSF CAREER DMR-0952428, Packard Foundation, and Keck Foundation. This project was also made possible through use of the facilities at Princeton Nanoscale Microscopy Laboratory supported by grants through ARO-W911NF-1-0262, ONR-N00014-14-1-0330, ONR-N00014-13-10661, U.S. Department of Energy–Basic Energy Sciences (DOE-BES)Defense Advanced Research Projects Agency–U.S.Space and Naval Warfare Systems Command Meso program N6601-11-1-4110, LPS and ARO-W911NF-1-0606, and Eric and Wendy Schmidt Transformative Technology Fund at Princeton. Work at University of California–Los Angeles was supported by the DOE-BES (DE-SC0011978).

SUPPLEMENTARY MATERIALS

www.sciencemag.org/content/351/6278/1184/suppl/DC1
Materials and Methods
Supplementary Text
Figs. S1 to S8
References (*39*–*41*)

17 November 2015; accepted 3 February 2016
10.1126/science.aad8766

ZEOLITES

Accelerated crystallization of zeolites via hydroxyl free radicals

Guodong Feng,[1]* Peng Cheng,[1]* Wenfu Yan,[1] Mercedes Boronat,[2] Xu Li,[1] Ji-Hu Su,[3] Jianyu Wang,[1] Yi Li,[1] Avelino Corma,[2] Ruren Xu,[1] Jihong Yu[1]†

In the hydrothermal crystallization of zeolites from basic media, hydroxide ions (OH^-) catalyze the depolymerization of the aluminosilicate gel by breaking the Si,Al–O–Si,Al bonds and catalyze the polymerization of the aluminosilicate anions around the hydrated cation species by remaking the Si,Al–O–Si,Al bonds. We report that hydroxyl free radicals (•OH) are involved in the zeolite crystallization under hydrothermal conditions. The crystallization processes of zeolites—such as Na–A, Na–X, NaZ–21, and silicalite-1—can be accelerated with hydroxyl free radicals generated by ultraviolet irradiation or Fenton's reagent.

Zeolites are microporous crystalline aluminosilicates that are used as ion-exchangers in the detergent industry, catalysts in the petrochemical and chemical industry, and adsorbents in air separation through pressure swing adsorption (*1*, *2*). Zeolite materials are typically synthesized in a strong basic medium in which a high concentration of hydroxide ions (OH^-) assists in the mineralization of silicate and aluminate species in the reactant gels (*3*). The crystallization process can be described through the following steps: (i) polymerization, forming an amorphous gel via making Si,Al–O–Si,Al bonds; (ii) depolymerization, forming soluble aluminosilicates and silicates via breaking Si,Al–O–Si,Al bonds; and (iii) repolymerization, remaking Si,Al–O–Si,Al bonds around the hydrated cation species—that is, the structure-directing agents—via condensation reaction (*4*, *5*). These steps comprise the nucleation and crystal growth stage of the crystallization, which are catalyzed by OH^- involving multiple equilibria. However, the crystallization mechanism of zeolites is still unclear, and the understanding of their formation at a molecular level has not yet been achieved.

Under basic conditions, OH^- ions increase the coordination of tetrahedral silicon (Si) atoms to pentahedral or octahedral, which weaken and break the Si–O–Si bonds (*6*). Theoretical calculations show that the dissociation of the Si–O–Si bonds is more favorable when catalyzed by hydroxyl free radicals (•OH) (*7*, *8*); •OH species are highly active in organic synthesis (*9*), polymerization (*10*), and modification of proteins (*11*). Generation of •OH in solution can be achieved by means of, for example, electron pulse radiolysis, ultraviolet (UV) irradiation, Fenton reactions, chemical reactions, and high-voltage electrical discharge (*11*). We show that hydrothermal zeolite crystallization can be accelerated by introducing •OH via physical or chemical methods.

To investigate the effect of •OH on zeolite crystallization, we used a modified multiparallel reactor that allowed for UV irradiation and controlled heating (fig. S1). The hydrothermal syntheses conducted under UV irradiation are referred to as UV condition, and control syntheses conducted in the oven without the UV irradiation are referred to as dark condition. We initially studied the UV and dark-condition syntheses in the Na_2O–Al_2O_3–SiO_2–H_2O system at 298 K. Under UV conditions for 24 hours, the experimental and simulated x-ray diffraction (XRD) patterns of Na–X (SiO_2/$0.21Al_2O_3$/$9.36Na_2O$/$85H_2O$) (Fig. 1A), NaZ–21 (SiO_2/$0.32Al_2O_3$/$10.05Na_2O$/$85H_2O$) (Fig. 1B), and Na–A (SiO_2/$0.46Al_2O_3$/$4.4Na_2O$/$60H_2O$) (fig. S2A) and the scanning electron microscopy (SEM) images of the corresponding products (fig. S3) indicate that the products were already crystallized. Under dark conditions for 24 hours, the corresponding XRD patterns (Fig. 1, C and D, and fig. S2B) show that the materials were still primarily amorphous. These results demonstrate that the crystallization rate of zeolites was accelerated by UV irradiation.

The crystallization process of zeolite Na–A with the starting molar composition of SiO_2/$0.46Al_2O_3$/$4.4Na_2O$/$60H_2O$ was further investigated at 298 K under dark and UV conditions with different irradiances that varied the •OH concentration (reported as crystallization curves in Fig. 1E). Under dark conditions, long-range ordering of zeolite Na–A, as confirmed with XRD, began to be observed after 40 hours (fig. S4A). After 60 hours, highly crystalline zeolite Na–A was obtained, as confirmed with the SEM and high-resolution transmission electron microscopy (HRTEM) images (fig. S5). In contrast, the XRD patterns (fig. S4, B, C, and D) show that the long-range ordering of zeolite Na–A was already observed at 32, 20, and 16 hours, and highly crystalline zeolite Na-A was obtained at 52, 40, and 36 hours for irradiances of 2.0, 4.0, and 8.0 mW/cm^2, respectively, as shown in the SEM and TEM images (figs. S6 to S8).

Reducing the OH^- concentration could slow down the crystallization of zeolites. We further studied the crystallization behavior of the initial reaction mixture with a reduced Na_2O/SiO_2 molar ratio (3.08 versus 4.4) at 298 K. Under the dark conditions, the long-range ordering of zeolite Na–A was not observed until 45 hours, and the crystals have been well developed when the reaction time reached 55 hours (fig. S9A, XRD; fig. S10, SEM and TEM images), whereas long-range ordering was already observed at 40 hours when the Na_2O/SiO_2 ratio was 4.4 (fig. S4A). In contrast, when the initial reaction mixture was irradiated with a UV lamp, highly crystalline Na-A was formed at 40 hours (fig. S9B, XRD; fig. S11, SEM and TEM images). The results presented above clearly demonstrate that reducing OH^- decreases the crystallization rate of zeolite, whereas •OH can promote the crystallization at the same time. Consequently, the crystallization rate of zeolite Na–A under UV with a Na_2O/SiO_2 ratio of 3.08 is even faster than

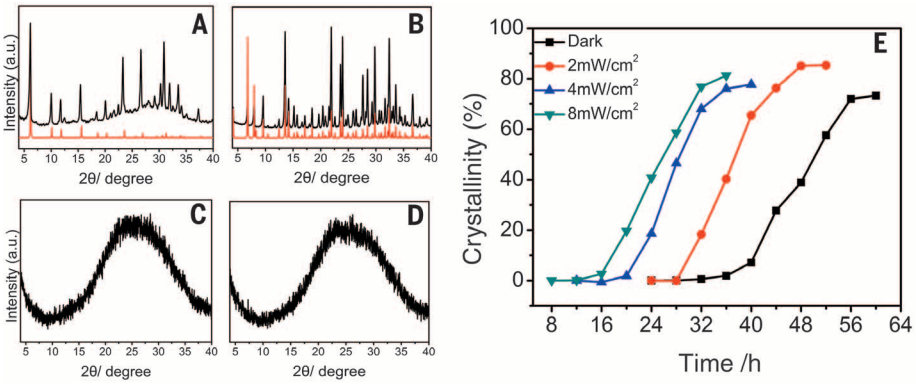

Fig. 1. Crystallization processes under UV irradiation and dark conditions at 298 K. (**A** to **D**) The experimental XRD patterns of Na–X and NaZ–21 synthesized under the UV conditions [(A) and (B), black, 4.0 mW/cm^2] and dark conditions [(C) and (D), black] for 24 hours, respectively. The corresponding simulated XRD patterns are plotted for comparison [(A) and (B), red]. (**E**) Crystallization curves of zeolite Na–A under dark conditions and under UV conditions with irradiance of 2.0, 4.0, and 8.0 mW/cm^2, with a Na_2O/SiO_2 ratio of 4.4.

[1]State Key Laboratory of Inorganic Synthesis and Preparative Chemistry, College of Chemistry, Jilin University, 2699 Qianjin Street, Changchun, 130012, China. [2]Instituto de Tecnologia Quimica, Universidad Politecnica de Valencia, Consejo Superior de Investigaciones Cientificas, Valencia, 46022, Spain. [3]Department of Modern Physics, University of Science and Technology of China, 96 Jinzhai Road, Hefei, 230026, China.
*These authors contributed equally to this work. †Corresponding author. E-mail: jihong@jlu.edu.cn

Downloaded from on March 10, 2016

that under dark with a Na_2O/SiO_2 ratio of 4.4. The accelerating effect on crystallization upon UV with the reduced alkalinity is further enhanced as compared with that upon UV with normal alkalinity.

Upon UV irradiation, water can generate •OH (*11*). We used electron paramagnetic resonance (EPR) to characterize •OH and the derived species formed in the zeolite reaction system. We added 5,5-dimethylpyrroline-*N*-oxide (DMPO) as the spin-trapping agent of •OH into the initial reaction mixture, and we recorded the EPR signals in situ after the reaction mixture was irradiated for 0, 30, and 90 s. For comparison, we also characterized the initial reaction mixture and the pure water under dark conditions. As anticipated, the EPR signals from •OH captured by the DMPO—a 1:2:2:1 quartet pattern, with a splitting of 1.5 mT characteristic of a DMPO-•OH adduct—were observed after irradiation for 90 s (Fig. 2A) and 30 s (Fig. 2B). The characterized hyperfine coupling constants (HFCs) were a_N = $a_{H\beta}$ = 1.5 mT. Because DMPO was also photolyzed, the EPR signals of oxidized DMPO radicals featured by a three-line spectrum were also observed. Sextet EPR signals (Fig. 2, A and B) with a_N = 1.59 mT and $a_{H\beta}$ = 4.5 mT were observed. None of these signals were observed in the spectrum of the initial reaction mixture without the UV irradiation (0 s) in the presence of DMPO (Fig. 2C), indicating that the new sextet EPR signals were not from the inorganic impurities of the initial reaction mixture but from the radicals generated by the UV irradiation.

Because of the large $a_{H\beta}$ value (4.5 mT), these sextet EPR signals cannot be attributed to the carbon (C)– and oxygen (O)–centered radicals. For the C-centered radical, the $a_{Hr\beta}$ is at the range of 1.8 to 2.8 mT, and for the O-centered radical, the $a_{H\beta}$ is at the range of 0.7 to 1.4 mT (*12*, *13*). In fact, the large HFCs of these sextet EPR signals are similar to that of the DMPO-•$P(O)(OC_2H_5)_2$ adduct (*12*). Because no phosphorous (P) species was involved in the initial reaction mixture, these signals might be attributed to the DMPO-•Si adduct. If this is so, then the slight change in the intensity

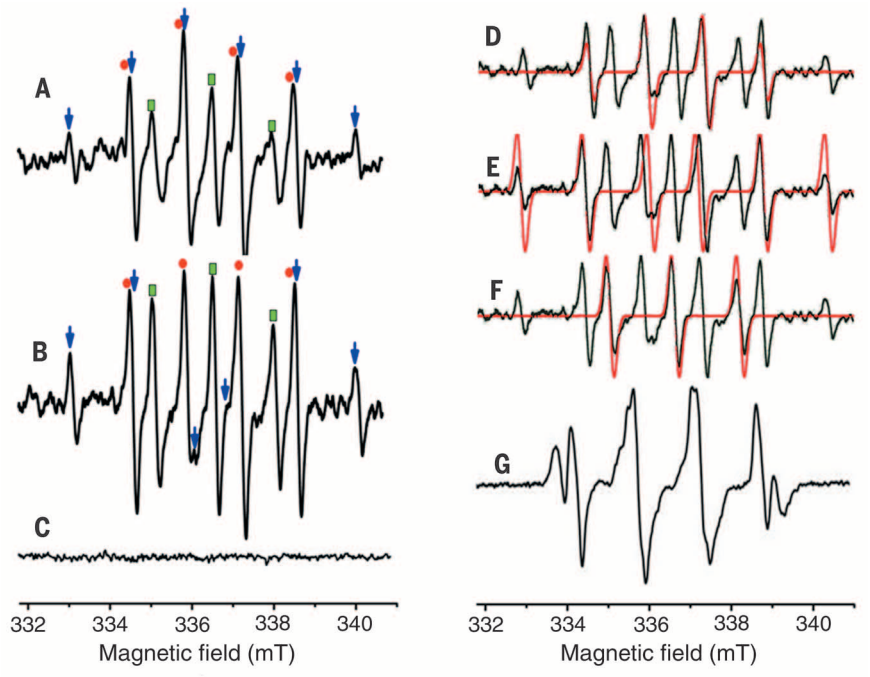

Fig. 2. Radicals' identification from UV irradiation. (**A** to **C**) EPR spectra of the initial reaction mixture containing DMPO under the UV irradiation for (A) 90 s, (B) 30 s, and (C) 0 s. (**D** to **F**) Comparison of the experimental and the simulated EPR spectra of (D) DMPO–•OH adduct, (E) DMPO–•Si adduct, and (F) oxidized DMPO radicals. (**G**) EPR spectra of the initial reaction mixture containing the spin-trapping agent of BMPO after 10 hours of dark incubation. The EPR signals are marked as following: red circles, hydroxyl free radicals; green rectangles, oxidized DMPO radicals; and blue arrows, silicon-based radicals.

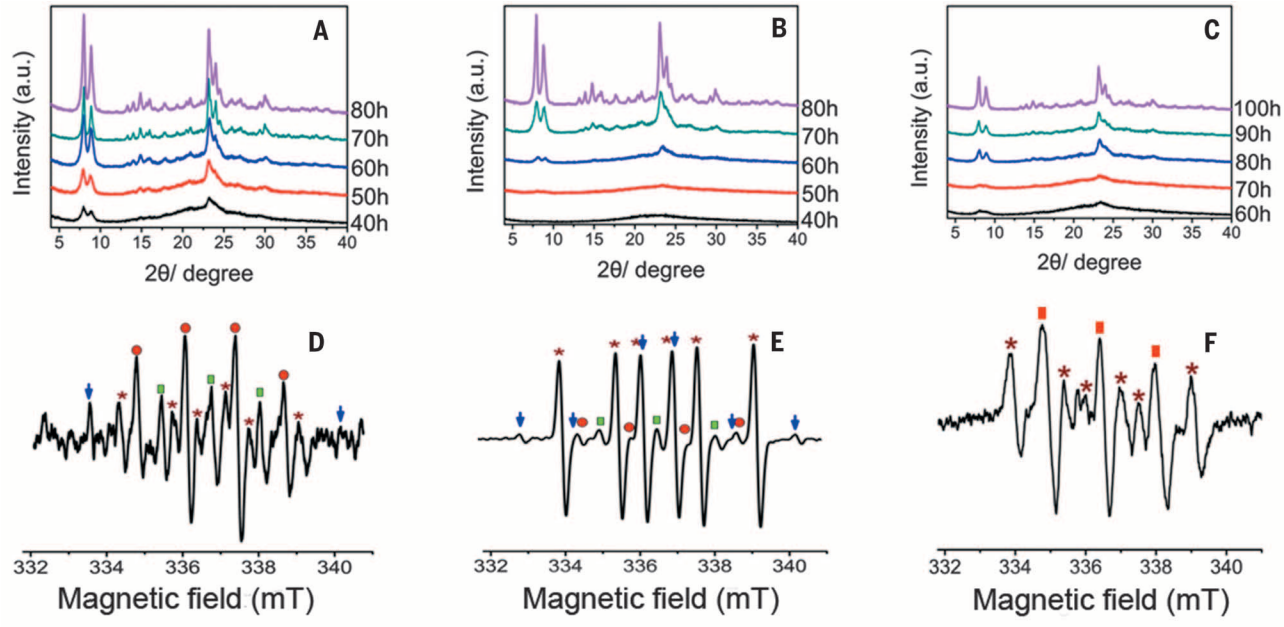

Fig. 3. Acceleration processes by Fenton's reagent. (**A** to **C**) Crystallization processes of silicalite-1 at 343 K under (A) Fenton conditions, (B) UV conditions (4.0 mW/cm^2), and (C) dark conditions. (**D** to **F**) EPR spectra of the TPAOH–TEOS–H_2O system under (D) Fenton conditions, (E) UV conditions (4.0 mW/cm^2), and (F) dark conditions. The EPR signals are marked as following: red circles, •OH; green rectangles, oxidized DMPO radicals; blue arrows, silicon-based radicals; asterisks, ethanol radicals; and red rectangles, oxidized BMPO radicals.

of these signals in the spectra after 30 and 90 s of irradiation indicated that these Si-based radicals were generated during the zeolite crystallization.

Previous studies show that fumed silica has an intrinsic population of planar three-membered-rings (3MRs) formed at high temperature and "frozen-in" by rapid quenching, which can undergo cleavage forming Si• and Si–O• radicals because of the strain in the Si–O–Si bonds (*14*–*16*). Aqueous alkaline silicate solutions also contain 3MRs, as confirmed by previous ^{29}Si–^{29}Si correlation spectroscopy nuclear magnetic resonance studies (*17*). Thus, the Si-based radicals in zeolite synthesis probably form through homolytic cleavage of the strained Si–O–Si bonds in planar 3MRs in the initial reaction mixture. The reason why no Si–O• radicals (another type of oxygen-centered radical) were observed might be caused by their high activity; they can easily react with water to form •OH. Shown in Fig. 2, D to F, is a comparison of the experimental and the simulated EPR spectra of DMPO–•OH adduct, DMPO–•Si adduct, and oxidized DMPO radicals, respectively, which confirms the assignment.

Considering that the concentration of radicals in the non–UV-irradiated initial reaction mixture and in the pure water might be too low to be detected by DMPO, we used a recently developed spin-trapping agent, 5-tert-butoxycarbonyl-5-methyl-1-pyrroline-*N*-oxide (BMPO), that allows a long-time accumulation of the EPR signals (*18*). We also observed •OH in the initial synthesis mixture under dark conditions for 10 hours (Fig. 2G). We recorded

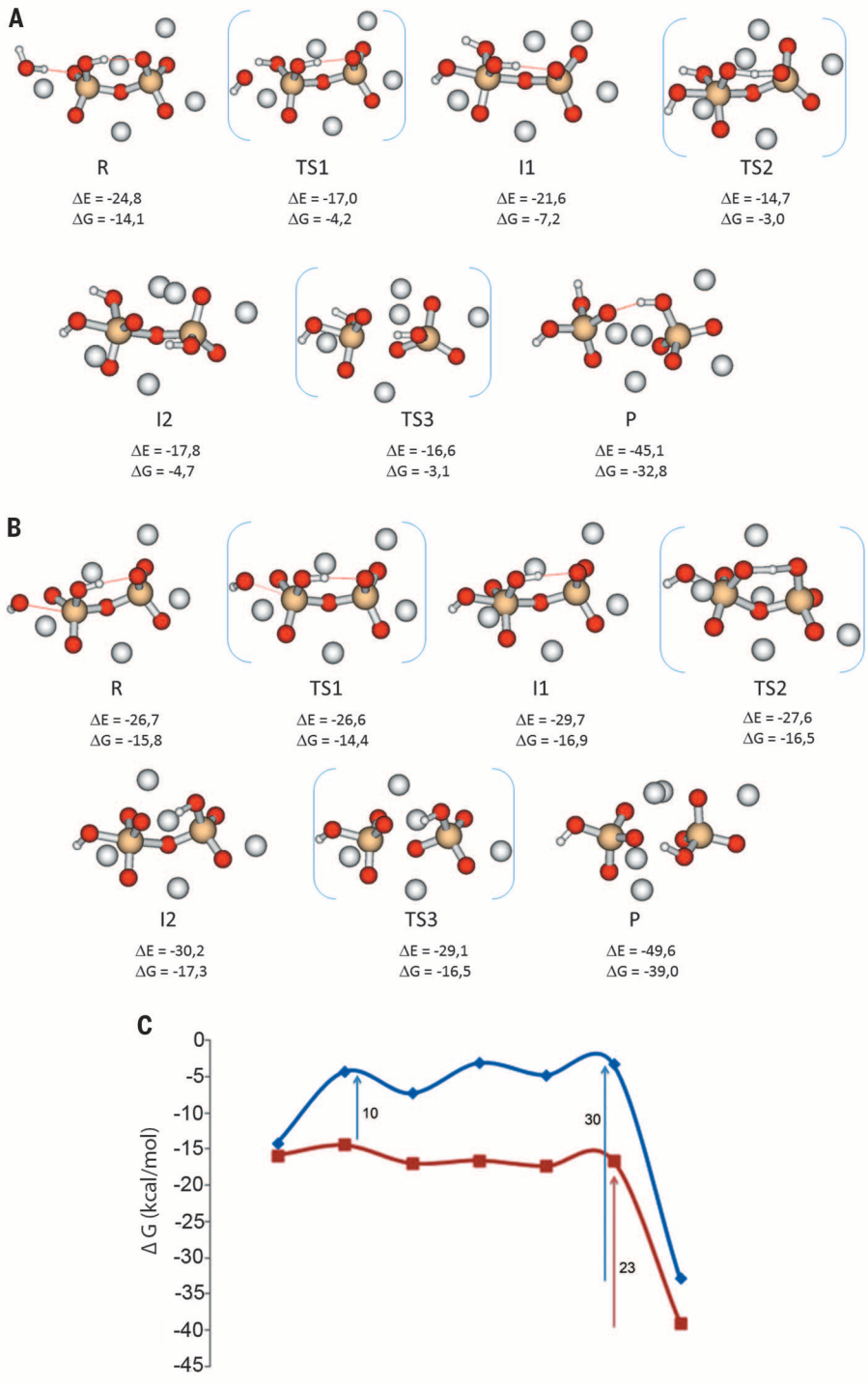

Fig. 4. Reaction of $[SiO_2(OH)–O–SiO_3]Na_5$ system and Gibbs free-energy calculation. (**A** and **B**) Reaction of $[SiO_2(OH)–O–SiO_3]Na_5$ system with (A) OH^- and (B) •OH. (**C**) Calculated Gibbs free-energy profiles for the reaction of $[SiO_2(OH)–O–SiO_3]Na_5$ model with OH^- (blue) and •OH (red). Electronic (ΔE) and Gibbs free energies (ΔG) are given in kilocalorie per mole.

the EPR signals that arose from •OH captured by BMPO, a characteristic 1:2:2:1 quartet pattern of a BMPO–•OH adduct (*18*). The complicated spectrum is due to the spectral overlapping of two isomers of BMPO (Fig. 3F, as well). Pure water under dark conditions did not give any EPR signals (fig. S12), suggesting that •OH came from the zeolite reaction system. The observation of •OH in the initial mixture under dark conditions suggests that in addition to OH^-, •OH was also involved in the zeolite crystallization as mineralizers. Although the reactivity of the •OH is much greater than that of OH^-, the concentration difference favors the OH^- mechanism.

The Fenton's reagent can also produce •OH, and we investigated the crystallization process for silicalite-1 in the reaction system tetrapropylammonium hydroxide (TPAOH)– tetraethyl orthosilicate (TEOS)–H_2O with the addition of the Fenton's reagent ($9TPAOH/25SiO_2/480H_2O/100EtOH/0.015H_2O_2/0.001FeSO_4{\bullet}18H_2O$, 343 K). The XRD patterns of the solid products (Fig. 3A) indicate that the long-rang ordering of silicalite-1 was already observed when the reaction time reached 40 hours, which is 10 hours shorter than that under UV conditions (Fig. 3B) and 20 hours shorter than that under dark conditions (Fig. 3C). The greater acceleration effect of the Fenton conditions than UV conditions indicates the higher concentration of •OH generated by the Fenton's reagent than by the UV irradiation. The SEM and TEM images of silicalite-1 recovered at the end of crystallization under Fenton conditions as compared with the dark and UV conditions are shown in fig. S13. The yields of silicalite-1 at different crystallization periods under Fenton and UV conditions, which are also remarkably improved as compared with the dark conditions, are given in fig. S14. The composition and N_2 adsorption data for all samples are included in table S1.

To identify the radicals in the crystallization of silicalite-1, we characterized the initial reaction mixtures at ambient temperature under Fenton, UV, and dark conditions by means of EPR spectroscopy (Fig. 3, D to F). Under dark conditions, signals from the BMPO–•$CH(CH_3)OH$ adduct (a_N = 1.51 mT, $a_{H\beta}$ = 2.1 mT) (Fig. 3F) imply the existence of alkane radicals, which may be formed from the reaction of •OH with the ethanol generated from the hydrolysis of TEOS. This reaction would consume the very limited •OH formed under the dark conditions. Under UV conditions (Fig. 3E), DMPO–•$CH(CH_3)OH$ (a_N = 1.59 mT, $a_{H\beta}$ = 2.27 mT), DMPO–•OH ($a_N = a_{H\beta}$ = 1.50 mT), DMPO–•Si (a_N = 1.59 mT, $a_{H\beta}$ = 4.5 mT), and oxidized DMPO radicals were observed and indicate that more •OH formed. The initial reaction mixture under the Fenton conditions (Fig. 3D) contained •OH ($a_N = a_{H\beta}$ = 1.50 mT), ethanol carbon radicals (a_N = 1.59 mT, $a_{H\beta}$ = 2.27 mT), Si-based radicals (a_N = 1.59 mT, $a_{H\beta}$ = 4.5 mT), and oxidized DMPO radicals.

Inhibiting •OH may slow down the zeolite crystallization. Because ethanol is an effective •OH scavenger, we crystallized silicalite-1 at 343 K under UV conditions by evaporating the ethanol in the mixture. We prepared two batches of the initial mixtures with the same molar composition; the batches were stirred overnight at ambient temperature under dark conditions in sealed and open quartz tubes, respectively. The weight loss of the initial mixture in the open quartz tube suggests that most of the ethanol hydrolyzed from TEOS was evaporated from the mixture. Subsequently, the quartz tubes were surely sealed and heated at 343 K for 48 hours under UV irradiation. As anticipated, the crystallization process was accelerated when the ethanol was removed, as indicated by the corresponding XRD patterns (fig. S15).

The zeolite crystallization is a two-step process, including nucleation and crystal growth. The sigmoidal crystallization curves shown in Fig. 1E show that the induction period under UV conditions is much shorter than that under dark conditions, which suggests that •OH generated by UV irradiation plays an important role in accelerating the nucleation stage during the crystallization. However, the slope of the crystallization curve for the UV conditions is similar to that for the dark conditions, implying similar crystal growth rates. To further confirm which stage was accelerated by •OH, we investigated the synthesis of zeolite Na–A at 298 K by means of UV pretreatment in the induction period for 18 hours, followed by crystallization under dark conditions. The XRD patterns of the products (fig. S16) show that the crystallization of the synthetic system under such conditions is similar to that under UV conditions, indicating that •OH mostly influences the nucleation stage but not the crystal growth stage.

Theoretical calculations provide more insight into how •OH accelerates the nucleation stage. Under the very basic conditions used in the synthesis, anionic $[Si_2O_{1+x}(OH)_{6-x}]^{x-}$ species stabilized by Na^+ cations will be preferentially formed via successive and clearly exothermic deprotonation steps (fig. S17). We first considered the depolymerization of the gel by breaking of the Si–O–Si bonds under very basic conditions and studied the attack of either OH^- or •OH to a highly deprotonated $[SiO_2(OH)–O–SiO_3]Na_5$ model of the gel. In the first case (Fig. 4A), water reacts with the dimeric silicon species, forming a pentacoordinated intermediate I1, this being the most energy-demanding step (Fig. 4C, blue line). A H transfer step converting intermediate I1 into I2 is necessary to have one OH group on each Si atom, which facilitates the rapid dissociation of the Si–O bond, generating the monomeric species P. Similar structures are involved in the reaction of the $[SiO_2(OH)–O–SiO_3]Na_5$ model with a •OH radical (Fig. 4B). However, all the activation energies obtained in the reaction with •OH (Fig. 4C, red line) are much lower, indicating that the presence of •OH in the reaction medium will considerably increase the rate of Si–O bond-breaking and depolymerization of the gel.

The second step in the nucleation process is the formation of new Si–O–Si bonds, which could be considered to be the reverse of the process investigated above, starting from products P and ending with reactants R. The high stability of the products when using the $[SiO_2(OH)–O–SiO_3]Na_5$ model of the gel results in very high activation energies: 30 kcal/mol in the presence of only OH^-, and somewhat lower—23 kcal/mol—when •OH is also present in the media.

In order to check the influence of decreased alkalinity on the mechanism, a monodeprotonated $[Si(OH)_2–O–Si(OH)_3]Na$ model was also considered. The theoretical results clearly prove the enhanced positive effect of •OH as compared with OH^- in breaking of the Si–O–Si bonds (activation barrier, 29 versus 4 kcal/mol) and promoting the formation of new Si–O–Si bonds (activation barrier, 17 versus 8 kcal/mol) in the gel with reduced alkalinity (figs. S18 and S19). This is consistent with our experimental results of the enhanced accelerating effect upon UV with reduced alkalinity.

The discovery that zeolite synthesis mechanism can be promoted through free radicals sheds a new light on zeolite crystallization and will open new perspectives for the synthesis of zeolite materials that are largely demanded in the chemical industry.

REFERENCES AND NOTES

1. Y. Li, J. Yu, *Chem. Rev.* **114**, 7268–7316 (2014).
2. J. Čejka, A. Corma, S. Zones, Eds., *Zeolites and Catalysis-Synthesis, Reactions and Applications* (Wiley-VCH Verlag GmbH & Co. KGaA, 2010).
3. C. S. Cundy, P. A. Cox, *Chem. Rev.* **103**, 663–702 (2003).
4. C. S. Cundy, P. A. Cox, *Micropor. Mesopor. Mater.* **82**, 1–78 (2005).
5. A. I. Lupulescu, J. D. Rimer, *Science* **344**, 729–732 (2014).
6. R. K. Iler, *The Chemistry of Silica: Solubility, Polymerization, Colloid and Surface Properties, and Biochemistry* (John Wiley & Sons, 1979).
7. Y. T. Xiao, A. C. Lasaga, *Geochim. Cosmochim. Acta* **60**, 2283–2295 (1996).
8. R. Konecny, *J. Phys. Chem. B* **105**, 6221–6226 (2001).
9. S. Z. Zard, *Radical Reactions in Organic Synthesis* (Oxford Univ. Press, 2003).
10. G. Moad, D. H. Solomon, *The Chemistry of Radical Polymerization* (Elsevier, 2006).
11. G. Xu, M. R. Chance, *Chem. Rev.* **107**, 3514–3543 (2007).
12. G. R. Buettner, *Free Radic. Biol. Med.* **3**, 259–303 (1987).
13. A. Angelo, M. Dante, in *Electron Paramagnetic Resonance: A Practitioner's Toolkit*, M. Brustolon, E. Giamello, Eds. (John Wiley & Sons, 2008), vol. 4, pp. 285–324.
14. D. L. Griscom, C. J. Brinker, C. S. Ashley, *J. Non-Cryst. Solids* **92**, 295–301 (1987).
15. H. Zhang *et al.*, *J. Am. Chem. Soc.* **134**, 15790–15804 (2012).
16. W. L. Warren, P. M. Lenahan, C. Jeffrey Brinker, *J. Non-Cryst. Solids* **136**, 151–162 (1991).
17. C. T. G. Knight, R. J. Balec, S. D. Kinrade, *Angew. Chem. Int. Ed. Engl.* **46**, 8148–8152 (2007).
18. C. H. Huang *et al.*, *Chem. Commun. (Camb.)* **49**, 6436–6438 (2013).

ACKNOWLEDGMENTS

This work was supported by the 973 Project (grants 2014CB931802 and 2013CB921802) and the National Natural Science Foundation of China (grants 21320102001, 91122029, and 21571075). A.C. thanks the Program Severo Ochoa for financial support and ERC-AdG-2014-671093—SynCatMatch. J.Y. designed and supervised the project; W.Y., A.C., and R.X. involved the design of the experiments; G.F., P.C., and J.W. performed the experiments; J.-H.S. performed the EPR analyses; M.B., X.L., and Y.L. contributed to the calculations; J.Y. and W.Y. analyzed the data; G.F. wrote the first draft; and J.Y. and W.Y. deeply revised the manuscript. A Chinese patent about the method for UV-assisted synthesis of zeolite materials has been applied for.

SUPPLEMENTARY MATERIALS

www.sciencemag.org/content/351/6278/1188/suppl/DC1
Materials and Methods
Figs. S1 to S19
Table S1
References (*19*–*22*)

24 December 2015; accepted 28 January 2016
10.1126/science.aaf1559

FUNGAL ENZYMES

Early-branching gut fungi possess a large, comprehensive array of biomass-degrading enzymes

Kevin V. Solomon,[1]* Charles H. Haitjema,[1] John K. Henske,[1] Sean P. Gilmore,[1] Diego Borges-Rivera,[2] Anna Lipzen,[3] Heather M. Brewer,[4,5] Samuel O. Purvine,[4,5] Aaron T. Wright,[4] Michael K. Theodorou,[6] Igor V. Grigoriev,[3] Aviv Regev,[2] Dawn A. Thompson,[2]† Michelle A. O'Malley[1]‡

The fungal kingdom is the source of almost all industrial enzymes in use for lignocellulose bioprocessing. We developed a systems-level approach that integrates transcriptomic sequencing, proteomics, phenotype, and biochemical studies of relatively unexplored basal fungi. Anaerobic gut fungi isolated from herbivores produce a large array of biomass-degrading enzymes that synergistically degrade crude, untreated plant biomass and are competitive with optimized commercial preparations from *Aspergillus* and *Trichoderma*. Compared to these model platforms, gut fungal enzymes are unbiased in substrate preference due to a wealth of xylan-degrading enzymes. These enzymes are universally catabolite-repressed and are further regulated by a rich landscape of noncoding regulatory RNAs. Additionally, we identified several promising sequence-divergent enzyme candidates for lignocellulosic bioprocessing.

Lignocellulosic biomass from plant matter is an abundant, renewable starting material for biofuel and industrial chemical production (*1*, *2*). Industrial-scale processes require fungal enzymes to convert biomass into fermentable sugars. However, to permit enzymatic degradation and sugar release (*3*), lignin must be removed from crude biomass via costly pretreatment processes (*1*). The need for multiple enzyme production processes increases this cost further, as genetically modified fungal platforms such as *Trichoderma reesei* and *Aspergillus nidulans* overproduce limited subsets of enzymes that are unable to independently digest even pretreated substrates completely to sugars (table S1) (*4*). Economical chemical production will require a versatile, unbiased platform to produce all of the enzymes needed to hydrolyze diverse lignocellulose feedstocks into fermentable sugars without pretreatment.

Microbes found in the digestive tract of large herbivores are attractive enzyme platforms for lignocellulose processing (*5*). Among these are Neocallimastigomycota (anaerobic gut fungi), the primary colonizers of biomass in ruminants and the earliest-branching nonparasitic fungi still living (*6*). Although Neocallimastigomycota account for ~8% of the gut microflora, they degrade up to 50% of the untreated biomass through invasive growth and enzyme secretion (*7*–*9*). Neocallimastigomycota contain a diverse repertoire of biomass-degrading enzymes (table S1) that degrade a range of feedstocks with equal efficiency (Fig. 1), making them rich untapped sources for previously unidentified lignocellulolytic enzymes. However, their strict anaerobic lifestyle, complex nutritional requirements, and culture recalcitrance have severely hindered early attempts at isolation, exploitation, and molecular characterization (*10*).

We isolated three previously uncharacterized cultures from the feces of different herbivorous mammals with varied diets. We used microscopy and ITS1 (internal transcribed spacer 1) sequencing (*11*) to verify that the isolates were distinct species, representing separate genera of Neocallimastigomycota (*Anaeromyces robustus*, *Neocallimastix californiae*, and *Piromyces finnis*). Each grew on C_3 and/or C_4 grasses at rates comparable to its growth on soluble substrates (Fig. 1A). *Anaeromyces* had a clear preference for glucose and grew more slowly on switch grass (~20% of the glucose growth rate). In contrast, the monocentric fungi, *Piromyces* and *Neocallimastix*, displayed limited substrate preference, with growth rates varying no more than 20% from the mean growth rate across all substrates. Similarly, these fungi had slight growth advantages on crude lignocellulose, growing up to 20% faster on reed canary grass (*Phalaris arundinacea*), an invasive species and bioenergy crop (*12*), when compared with glucose.

We collected and purified the biomass-degrading enzymes from fungal supernatants by exploiting the ability of many cellulases to bind to cellulose. We then tested the purified extracts for hydrolytic activity against several cellulosic substrates and analogs (fig. S1). Gut fungal secretions were active against all tested substrates, demonstrating cellulase, β-glucosidase, and hemicellulase activities comparable to those from engineered preparations of *Trichoderma* and *Aspergillus*. Neocallimastigomycota, and *Piromyces* in particular, displayed as much as a 300% increase in xylan-degradation activity when compared with commercial *Aspergillus* enzyme formulations (Fig. 1B). Gut fungi degrade cellulose at similar rates, demonstrating little preference for cellulose or hemicellulose (Fig. 1C), in agreement with their enzymatic distribution from genomic sequencing (table S1). This comprehensive array of biomass-degrading enzymes, and their inherent synergy, broadens the range of substrates that can be degraded effectively, making gut fungi better suited than later-diverging species to degrade diverse polymers found within crude plant biomass. More importantly, it is this synergy, and not enzyme diversity, that is responsible for the superior biomass-degradation abilities of *Piromyces*, making it an intriguing model system for further study.

Transcripts encoding biomass-degrading enzymes comprise ~2% of the gut fungal transcriptomes (data S1 to S3) containing diverse functions classified into distinct lignocellulolytic glycosyl hydrolase (GH) and other carbohydrate-active enzyme (CAZyme) domains (*13*) (Fig. 2A). The majority of these transcripts also encode noncatalytic dockerin domains thought to mediate self-assembly of an extracellular catalytic complex or cellulosome (Fig. 2, B and C) for synergistic degradation of lignocellulose (*14*). The hydrolytic capabilities of gut fungi on crude biomass are well explained by the functional expansions of many CAZyme families (table S1 and fig. S3). Neocallimastigomycota are rich in hemicellulases (notably GH10) and polysaccharide deacetylases, which allow gut fungi to remove hemicellulose and access the energy-rich cellulose core of plant biomass (*15*) in the absence of pretreatment. This process is greatly aided by pectin removal (*16*) with a number of polysaccharide lyases, carbohydrate esterases, and GH88s, allowing the anaerobic fungi to readily degrade an array of lignin-rich C_3 and C_4 bioenergy crops without pretreatment (Fig. 1A).

Functional annotations of the transcriptome were validated within *Piromyces*, *Anaeromyces*, and *Neocallimastix* via a proteomic survey (data S5 to S7). Proteins secreted from *Piromyces* in the presence of reed canary grass were isolated by cellulose precipitation (Fig. 2D and fig. S4) and individually mapped by mass spectrometry (MS) (*17*) to more than 50 cellulolytic transcripts including 25 GH families enriched in or specific to the anaerobic fungal lineage (e.g., GH9, GH45, GH48, GH10, and GH11). Also present was the full complement of endoglucanases, exoglucanases, and β-glucosidases needed to fully depolymerize cellulose (GH5, GH6, GH9, GH45, and GH48) and hemicellulases (GH10 and GH11) (table S2), with many transcripts containing dockerin domains for extracellular fungal cellulosome formation.

[1]Department of Chemical Engineering, University of California, Santa Barbara (UCSB), Santa Barbara, CA 93106, USA. [2]Broad Institute of MIT and Harvard, Cambridge, MA 02143, USA. [3]U.S. Department of Energy (DOE) Joint Genome Institute, 2800 Mitchell Drive, Walnut Creek, CA 94598, USA. [4]Earth and Biological Sciences Division, Pacific Northwest National Laboratory, Richland, WA 99352, USA. [5]Environmental Molecular Sciences Laboratory, Pacific Northwest National Laboratory, Richland, WA 99352, USA. [6]Animal Production, Welfare and Veterinary Sciences, Harper Adams University, Newport, Shropshire TF10 8NB, UK. *Present address: Department of Agricultural and Biological Engineering, Purdue University, West Lafayette, IN 47907, USA. †Present address: Ginkgo Bioworks, Boston, MA 02210, USA. ‡Corresponding author. E-mail: momalley@engineering.ucsb.edu

Downloaded from on March 10, 2016

A pervasive feature of gut fungal transcriptomes is long noncoding antisense transcripts (asRNA) (data S1 to S3). At least 11% of the *Piromyces* transcriptome is noncoding and complementary to putative targets involved in a range of catalytic and developmental pathways, including biomass degradation (Fig. 2A and fig. S2). asRNA is functionally enriched (hypergeometric test) in a number of gene ontology (GO) processes, such as the cellulose catabolic process (P = 0.02), ribosome biogenesis ($P = 10^{-11}$), RNA-dependent DNA replication ($P = 6 \times 10^{-6}$), and amino acid transmembrane transport (P = 0.003) (data S4). These results infer a role for asRNA regulation in fungal cellulose catabolism and suggest that noncoding asRNAs may be as critical for function in early-branching Neocallimastigomycota as they are in higher fungal lineages (*18*–*20*).

To assess how the activities of biomass-degrading enzymes are coordinated, we grew *Piromyces* cultures on lignocellulose and perturbed the system with a small pulse of glucose to induce catabolite repression, after which we collected RNA samples until the glucose was consumed (Fig. 3A). Three hundred seventy-four transcripts showed more than a twofold change in expression ($P \leq 0.01$), with a third of these transcripts containing cellulolytic domains (Fig. 3B). Among these regulated cellulolytic transcripts were all of the MS-validated proteins expressed under growth on reed canary grass (table S2), with the exception of GH45 and XylA. Transcripts associated with biomass degradation were almost exclusively repressed in response to glucose, as expected, and reflected activity trends from cellulose-isolated secretions (*21*). Expression levels of these transcripts returned to initial baselines once glucose was fully consumed (Fig. 3C and fig. S5). Cluster analysis revealed coordinated expression signatures of biomass degradation in the regulatory patterns of these transcripts (*22*).

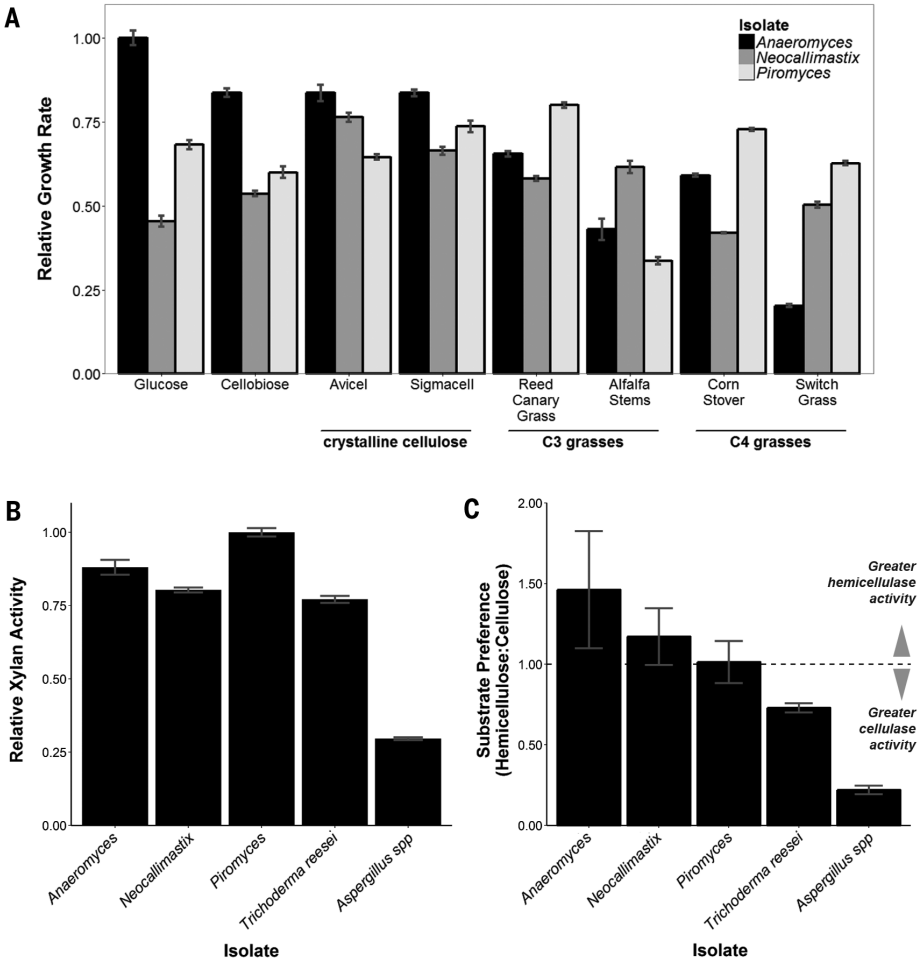

Fig. 1. Anaerobic fungi degrade crude biomass. (**A**) Relative growth of gut fungal isolates on crystalline cellulose and crude C_3 and C_4 bioenergy crops (see table S3 for specific growth rates). (**B**) Relative xylan activity of cellulose-precipitated gut fungal secretions and commercial *Trichoderma* [Celluclast (Sigma-Aldrich)] and *Aspergillus* [Viscozyme (Sigma-Aldrich)]. (**C**) Relative hemicellulose:cellulose [xylan versus carboxymethylcellulose (CMC)] activity of cellulose-precipitated gut fungal secretions and commercial preparations. For all panels, data represent mean ± SEM (error bars) of more than three samples.

Hierarchical cluster analysis revealed that glucose-regulated genes performing a common function grouped into 21 distinct clusters or regulons (Fig. 3B). Owing to the functional enrichment of these regulons, divergent transcripts of unknown function that co-regulate with biomass-degrading transcripts may be previously unidentified biomass-degrading enzymes for biotechnology. We identified 17 such candidates from *Piromyces* (table S4). Biomass-degrading regulons were either hemicellulose- and pectin-degrading and rapidly repressed within 40 min or contained a broad array of biomass-degrading enzymes that responded more slowly at 3.5 hours (Fig. 3B and data S8). The faster regulatory response of hemicellulases is conserved in higher fungi (*23*, *24*) and thought to be an adaptation to lignocellulose structure. Hemicellulose and pectin surround cellulose; thus, cellulases act only after the hemicellulases and pectinases remove this outer coating. Given a common regulatory input, coordinating this expression leads to quicker regulation of hemicellulases and pectinases than of cellulases, in agreement with observation. Candidate mediators of this response include conserved orthologs of the fungal master carbon regulator (CreABC); xylose-sensitive transcription factors (Xlr-1 and XlnR); and other conserved cellulolytic activators such as ACE1-2, ClbR, and Clr1-2 (table S5). In contrast, up-regulated clusters contained an array of metabolic and housekeeping genes consistent with logarithmic growth, along with protein expression genes (such as those encoding chaperonins and ribosomal RNA processing proteins) that probably mediated the cellular response to the sugar pulse (data S8).

To better understand the regulation of key biomass-degrading enzymes, we analyzed expression as a function of substrate. *Piromyces* showed substantial remodeling of the transcriptome as the carbon source was varied (~10% of all transcripts), reflecting changes in the biomass-degrading machinery and internal processes of gut fungal cultures (fig. S6 and data S9). Among these transcripts were 194 of the differentially regulated transcripts from the glucose perturbation experiment described above. Overall, a twofold change in the expression of biomass-degrading enzymes occurred during the switch from glucose to complex reed canary grass. This trend was mirrored in the activity of cellulose-precipitated secretions (Fig. 4A). Discernible changes in the composition of the biomass-degradation machinery also accompanied variations in expression level (fig. S7).

Gene set enrichment analysis (*25*) of the transcriptomes confirmed that the number and functional diversity of CAZyme domains increased as a function of substrate complexity (Fig. 4B), with insoluble substrates [filter paper, Avicel (Sigma-Aldrich), and reed canary grass] inducing fungal cellulosomes for enhanced degradation. Nonhemicellulosic substrates (cellobiose, filter paper, and Avicel) up-regulated unneeded hemicellulases such as GH10, suggesting a common regulatory network for diverse enzymes. Nonetheless, the additional enzymes necessary to degrade crude reed canary grass are independently regulated. Our

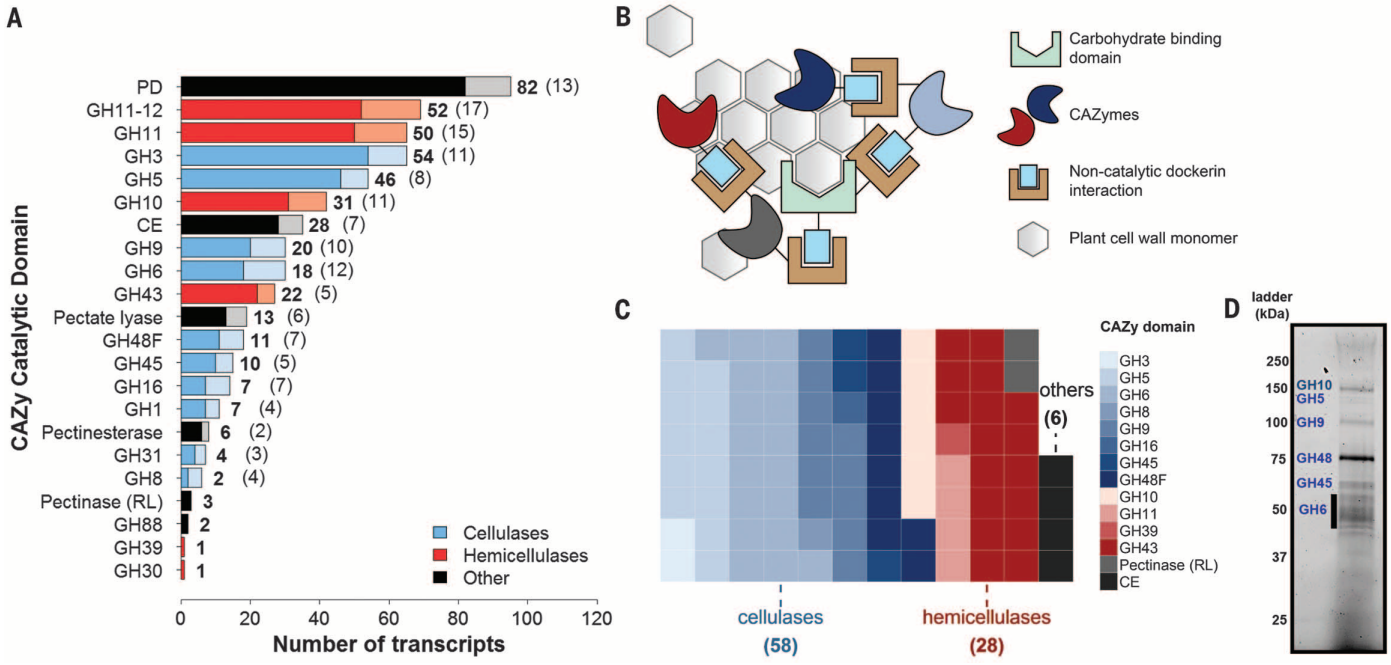

Fig. 2. Anaerobic fungi contain a wealth of biomass-degrading machinery. (**A**) Distribution of cellulolytic carbohydrate-active enzyme (CAZy) transcripts and their regulatory antisense transcripts in *Piromyces*. CAZymes are shown in bold, whereas antisense transcripts are indicated in parentheses and plotted in a lighter shade. In the key, "Other" refers to pectinases and accessory enzymes that separate cellulose and hemicellulose from other cell wall constituents. PD, polysaccharide deacetylase (acetylxylan esterase); CE, carbohydrate esterase (excluding pectinesterases); RL, rhamnogalacturonate lyase. (**B**) Proposed model for an extracellular catalytic complex for cellulose degradation. (**C**) CAZyme composition of the putative extracellular complex. Each square represents a single enzyme that encodes a CAZyme fused to at least one dockerin domain. (**D**) Identity of predominant secreted gut fungal CAZymes in the cellulose-precipitated fraction. Bands were excised and mapped to the transcriptome by tandem MS (fig. S4).

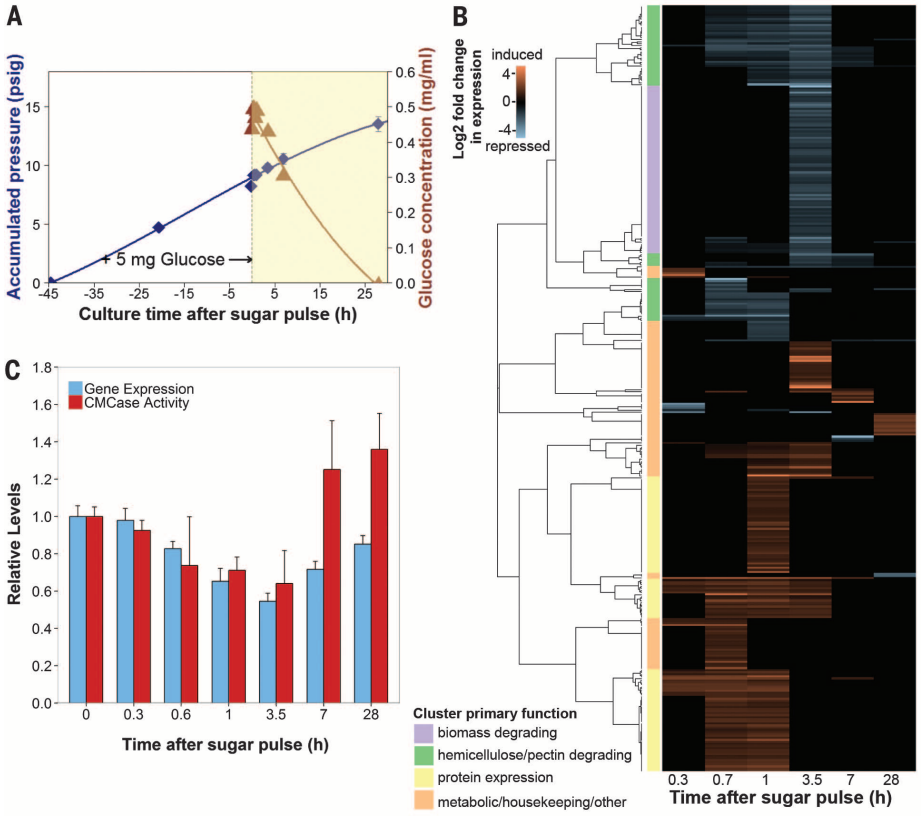

Fig. 3. Anaerobic fungal biomass-degrading machinery is catabolically repressed. (**A**) Glucose consumption in fungal cultures. Exponential cultures of *Piromyces* were pulsed with 5 mg of glucose, and mRNA and secretome samples were collected during glucose depletion (yellow region). Blue diamonds, accumulated pressure; brown triangles, glucose concentration. Error bars indicate SEM. (**B**) Cluster analysis of genes strongly regulated by glucose. Transcript abundance data were compared to uninduced samples at time $t = 0$ to calculate the $\log_2$ fold change in expression. Transcripts with large, significant regulation are displayed ($P \leq 0.01$, negative binomial distribution, ≥twofold change). Clusters were manually annotated based on the most common protein domains and/or BLAST (Basic Local Alignment Search Tool) hits. (**C**) Relative expression [fragments per kilobase of transcript per million mapped reads (FPKM)] of biomass-degrading enzymes (table S1) and their corresponding activity (cellulosome fraction) on CMC (*21*). Data represent the mean ± SEM (error bars) of at least two replicates.

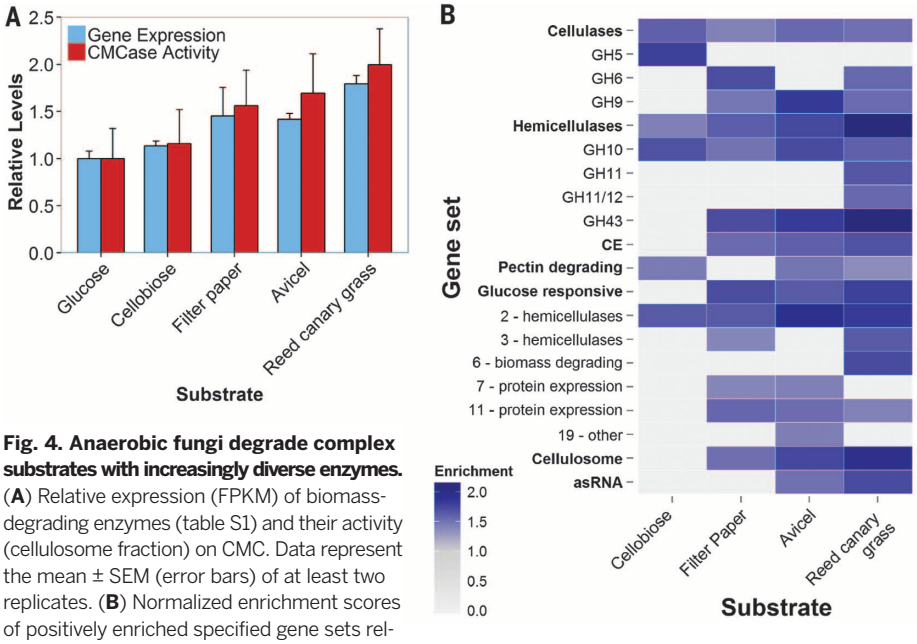

Fig. 4. Anaerobic fungi degrade complex substrates with increasingly diverse enzymes. (**A**) Relative expression (FPKM) of biomass-degrading enzymes (table S1) and their activity (cellulosome fraction) on CMC. Data represent the mean ± SEM (error bars) of at least two replicates. (**B**) Normalized enrichment scores of positively enriched specified gene sets relative to growth on glucose. Gene sets containing genes that are expressed more highly in a given substrate are indicated (FDR ≤ 10%; Kolmogorov-Smirnov distribution). Enrichment scores are directly proportional to expression level. Gene sets shown in bold were analyzed in aggregate and in subsets (unbolded sets below). asRNA, antisense RNA that targets CAZy domains (Fig. 2A); Cellulosome, dockerin tagged transcripts. Numbers in the "Glucose responsive" subset indicate clusters.

analyses also revealed shifts between enzyme types for similar reactions (e.g., GH5 to GH9 as a β-glucosidase) as a function of substrate, demonstrating a highly tailored catabolic response.

Among the gene sets we tested were clusters identified in the glucose perturbation experiment (Fig. 4B). Protein expression clusters (Fig. 3B) regulated by glucose were enriched on insoluble substrates, reaffirming their role in mediating expression of lignocellulolytic enzymes. Another regulon encoding diverse hemicellulases and a handful of cellulases (cluster 2: hemicellulases) was central to all growth phenotypes other than glucose. This enzyme prevalence, even on non-polymeric carbohydrates, suggests that enzymes play an integral role in the recognition of insoluble substrates (*26*): In the absence of glucose, these enzymes are expressed at low levels to partially solubilize available cellulosic materials that can be recognized to trigger a more specific catabolic response. Consistent with this hypothesis is the sixfold up-regulation ($P \sim 0.02$, negative binomial test) of the conserved transcription factor XlnR on reed canary grass and Avicel to better recognize solubilized sugars and induce fungal xylan degradation. This response is further regulated by asRNA targeting CAZyme domains, as evidenced by their functional enrichment on Avicel [$P = 0.003$, false discovery rate (FDR) = 0.03] and reed canary grass cultures ($P \sim 0$, FDR = 0.003). An independent analysis using a hypergeometric statistical test confirms that antisense transcripts targeting CAZyme domains (cellulose catabolic process GO annotation) are functionally enriched among the regulated transcripts ($P \approx 0.01$) (data S10). Identities of the expressed asRNA, however, are substrate-specific to modify the catabolic response through a number of mechanisms (*27*) to conserve cellular resources (table S6).

Overall, our results show that anaerobic gut fungi tailor their hydrolytic response to lignocellulose, implying a coordination in catalysis between all expressed enzymes that may inform industrial hydrolysis strategies. The clear transcriptional signatures of these biomass-degrading enzymes provide a route to identify hundreds of sequence-divergent enzyme candidates with commercial potential from anaerobic microbial communities (*28*).

REFERENCES AND NOTES

1. K. Sanderson, *Nature* **474**, S12–S14 (2011).
2. D. R. Dodds, R. A. Gross, *Science* **318**, 1250–1251 (2007).
3. A. Berlin *et al.*, *J. Biotechnol.* **125**, 198–209 (2006).
4. M. Schülein, *Methods Enzymol.* **160**, 234–242 (1988).
5. M. Hess *et al.*, *Science* **331**, 463–467 (2011).
6. M. J. Nicholson, M. K. Theodorou, J. L. Brookman, *Microbiology* **151**, 121–133 (2005).
7. C. G. Orpin, *J. Gen. Microbiol.* **99**, 107–117 (1977).
8. M. K. Theodorou *et al.*, *Proc. Nutr. Soc.* **55**, 913–926 (1996).
9. N. H. Youssef *et al.*, *Appl. Environ. Microbiol.* **79**, 4620–4634 (2013).
10. C. H. Haitjema, K. V. Solomon, J. K. Henske, M. K. Theodorou, M. A. O'Malley, *Biotechnol. Bioeng.* **111**, 1471–1482 (2014).
11. D. S. Tuckwell, M. J. Nicholson, C. S. McSweeney, M. K. Theodorou, J. L. Brookman, *Microbiology* **151**, 1557–1567 (2005).
12. S. Lavergne, J. Molofsky, *Crit. Rev. Plant Sci.* **23**, 415–429 (2004).
13. V. Lombard, H. Golaconda Ramulu, E. Drula, P. M. Coutinho, B. Henrissat, *Nucleic Acids Res.* **42**, D490–D495 (2014).
14. S. Raghothama *et al.*, *Nat. Struct. Mol. Biol.* **8**, 775–778 (2001).
15. M. E. Himmel *et al.*, *Science* **315**, 804–807 (2007).
16. V. Lionetti *et al.*, *Proc. Natl. Acad. Sci. U.S.A.* **107**, 616–621 (2010).
17. E. J. Finehout, K. H. Lee, *Electrophoresis* **24**, 3508–3516 (2003).
18. C. Kramer, J. J. Loros, J. C. Dunlap, S. K. Crosthwaite, *Nature* **421**, 948–952 (2003).
19. M. Yassour *et al.*, *Genome Biol.* **11**, R87 (2010).
20. M. E. Donaldson, B. J. Saville, *Mol. Microbiol.* **85**, 405–417 (2012).
21. B. C. King, M. K. Donnelly, G. C. Bergstrom, L. P. Walker, D. M. Gibson, *Biotechnol. Bioeng.* **102**, 1033–1044 (2009).
22. M. B. Eisen, P. T. Spellman, P. O. Brown, D. Botstein, *Proc. Natl. Acad. Sci. U.S.A.* **95**, 14863–14868 (1998).
23. U. Bakir, S. Yavascaoglu, F. Guvenc, A. Ersayin, *Enzyme Microb. Technol.* **29**, 328–334 (2001).
24. C. E. Todero Ritter, M. Camassola, D. Zampieri, M. M. Silveira, A. J. P. Dillon, *Enzyme Res.* **2013**, e240219 (2013).
25. A. Subramanian *et al.*, *Proc. Natl. Acad. Sci. U.S.A.* **102**, 15545–15550 (2005).
26. N. L. Glass, M. Schmoll, J. H. D. Cate, S. Coradetti, *Annu. Rev. Microbiol.* **67**, 477–498 (2013).
27. V. Pelechano, L. M. Steinmetz, *Nat. Rev. Genet.* **14**, 880–893 (2013).
28. K. V. Solomon, C. H. Haitjema, D. A. Thompson, M. A. O'Malley, *Curr. Opin. Biotechnol.* **28**, 103–110 (2014).
29. R. Edgar, M. Domrachev, A. E. Lash, *Nucleic Acids Res.* **30**, 207–210 (2002).

ACKNOWLEDGMENTS

We thank C. Ngan, C. Daum, E. Lindquist, and K. Barry for supervising library construction, transcriptome sequencing and analysis, and project management; K. Lee and L. Choe for proteomics support; P. Weimer for lignocellulosic substrates; and the Broad Institute core facilities for sequencing and computational assistance. Sequence and cluster descriptions are included in data S1 to S3, S8, and S9 in the supplementary materials. Raw sequence data and transcriptomic profiles reported in this study are deposited under BioProject accession no. PRJNA 291757 (www.ncbi.nlm.nih.gov/bioproject/291757). Expression data are deposited in the National Center for Biotechnology Information's Gene Expression Omnibus (GEO) (*29*) and are accessible through GEO Series accession no. GSE64834 (www.ncbi.nlm.nih.gov/geo/query/acc.cgi?acc=GSE64834). K.V.S., C.H.H., J.K.H., and M.A.O. are inventors on patent applications (UCSB 2014-075 and UCSB 2015-334), filed by The Reagents of the University of California, related to the production of anaerobic fungal enzymes. This work was supported by the Office of Science [Biological and Environmental Research (BER) program], DOE (grant DE-SC0010352); the U.S. Department of Agriculture (Award 2011-67017-20459); and the Institute for Collaborative Biotechnologies (grant W911NF-09-0001). A portion of this research was performed under the Joint Genome Institute (JGI)–Environmental Molecular Sciences Laboratory (EMSL) Collaborative Science Initiative and used resources at the DOE JGI and the EMSL, which are DOE Office of Science user facilities. Both facilities are sponsored by the Office of Science BER program and operated under contract nos. DE-AC02-05CH11231 (JGI) and DE-AC05-76RL01830 (EMSL). K.V.S., C.H.H., D.A.T., M.K.T., and M.A.O. planned the experiments. M.A.O., J.K.H., C.H.H., M.K.T., and K.V.S. isolated pure cultures of gut fungi. K.V.S., C.H.H., J.K.H., and M.A.O. performed growth and transcriptomic experiments. A.L. analyzed transcriptome sequencing. C.H.H., H.M.B., S.O.P., and A.T.W. performed proteomic analyses. S.P.G. performed enzyme characterization. K.V.S., D.B.-R., J.K.H., A.R., I.V.G., S.O.P., and S.P.G. facilitated bioinformatics analyses of the data sets. K.V.S., D.A.T., and M.A.O. wrote the manuscript.

SUPPLEMENTARY MATERIALS

www.sciencemag.org/content/351/6278/1192/suppl/DC1
Materials and Methods
Figs. S1 to S7
Tables S1 to S6
References (*30*–*43*)
Data S1 to S10

29 October 2015; accepted 9 February 2016
Published online 18 February 2016
10.1126/science.aad1431

BIODEGRADATION

A bacterium that degrades and assimilates poly(ethylene terephthalate)

Shosuke Yoshida,[1,2]* Kazumi Hiraga,[1] Toshihiko Takehana,[3] Ikuo Taniguchi,[4] Hironao Yamaji,[1] Yasuhito Maeda,[5] Kiyotsuna Toyohara,[5] Kenji Miyamoto,[2]† Yoshiharu Kimura,[4] Kohei Oda[1]†

Poly(ethylene terephthalate) (PET) is used extensively worldwide in plastic products, and its accumulation in the environment has become a global concern. Because the ability to enzymatically degrade PET has been thought to be limited to a few fungal species, biodegradation is not yet a viable remediation or recycling strategy. By screening natural microbial communities exposed to PET in the environment, we isolated a novel bacterium, *Ideonella sakaiensis* 201-F6, that is able to use PET as its major energy and carbon source. When grown on PET, this strain produces two enzymes capable of hydrolyzing PET and the reaction intermediate, mono(2-hydroxyethyl) terephthalic acid. Both enzymes are required to enzymatically convert PET efficiently into its two environmentally benign monomers, terephthalic acid and ethylene glycol.

Plastics with desirable properties such as durability, plasticity, and/or transparency have been industrially produced over the past century and widely incorporated into consumer products (*1*). Many of these products are remarkably persistent in the environment because of the absence or low activity of catabolic enzymes that can break down their plastic constituents. In particular, polyesters containing a high ratio of aromatic components, such as poly(ethylene terephthalate) (PET), are chemically inert, resulting in resistance to microbial degradation (*2*, *3*). About 56 million tons of PET was produced worldwide in 2013 alone, prompting further industrial production of its monomers, terephthalic acid (TPA) and ethylene glycol (EG), both of which are derived from raw petroleum. Large quantities of PET have been introduced into the environment through its production and disposal, resulting in the accumulation of PET in ecosystems across the globe (*4*).

There are very few reports on the biological degradation of PET or its utilization to support microbial growth. Rare examples include members of the filamentous fungi *Fusarium oxysporum* and *F. solani*, which have been shown to grow on a mineral medium containing PET yarns [although no growth levels were specified (*5*, *6*)]. Once identified, microorganisms with the enzymatic machinery needed to degrade PET could serve as an environmental remediation strategy as well as a degradation and/or fermentation platform for biological recycling of PET waste products.

We collected 250 PET debris–contaminated environmental samples including sediment, soil, wastewater, and activated sludge from a PET bottle recycling site (*7*). Using these samples, we screened for microorganisms that could use low-crystallinity (1.9%) PET film as the major carbon source for growth. One sediment sample contained a distinct microbial consortium that formed on the PET film upon culturing (Fig. 1A) and induced morphological change in the PET film (Fig. 1B). Microscopy revealed that the consortium on the film, termed "no. 46," contained

[1]Department of Applied Biology, Faculty of Textile Science, Kyoto Institute of Technology, Matsugasaki, Sakyo-ku, Kyoto 606-8585, Japan. [2]Department of Biosciences and Informatics, Keio University, 3-14-1 Hiyoshi, Kohoku-ku, Yokohama, Kanagawa 223-8522, Japan. [3]Life Science Materials Laboratory, ADEKA, 7-2-34 Higashiogu, Arakawa-ku, Tokyo 116-8553, Japan. [4]Department of Polymer Science, Faculty of Textile Science, Kyoto Institute of Technology, Matsugasaki, Sakyo-ku, Kyoto 606-8585, Japan. [5]Ecology-Related Material Group Innovation Research Institute, Teijin, Hinode-cho 2-1, Iwakuni, Yamaguchi 740-8511, Japan.
*Present address: Department of Polymer Chemistry, Graduate School of Engineering, Kyoto University, Nishikyo-ku, Kyoto 615-8530, Japan. **†Corresponding author. E-mail: kmiyamoto@bio.keio.ac.jp (K.M.); bika@kit.ac.jp (K.O.)**

Downloaded from on March 10, 2016

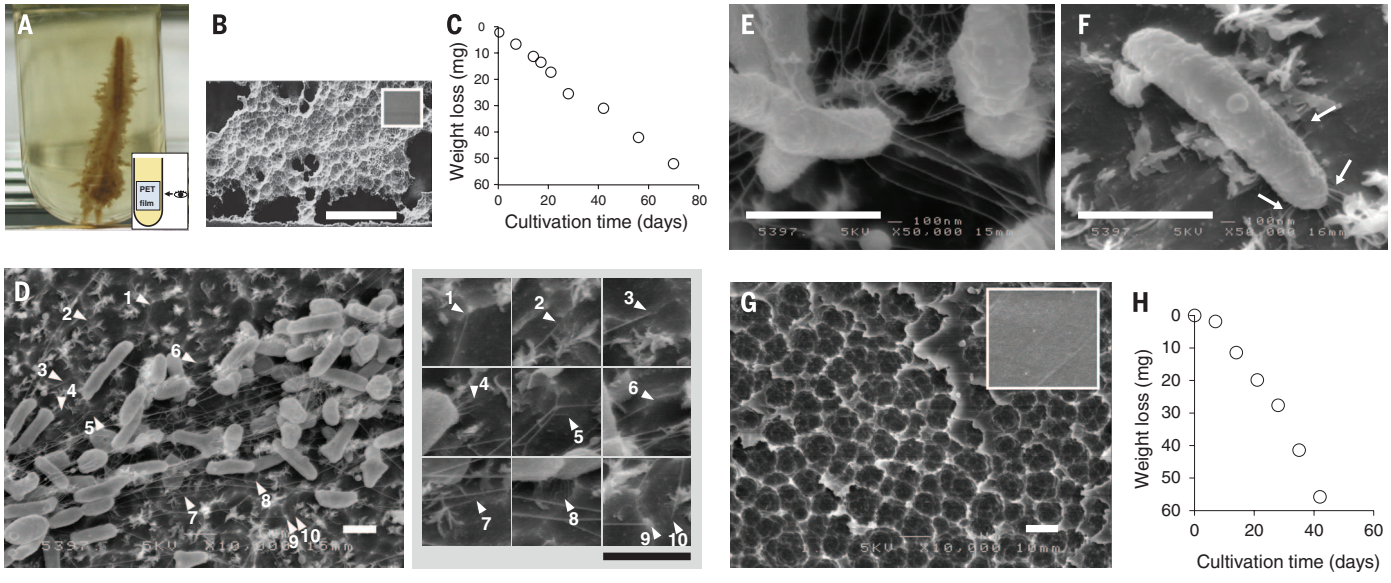

Fig. 1. Microbial growth on PET. The degradation of PET film (60 mg, 20 × 15 × 0.2 mm) by microbial consortium no. 46 at 30°C is shown in (A) to (C). The MLE (modified lettuce and egg) medium (10 mL) was changed biweekly. (**A**) Growth of no. 46 on PET film after 20 days. (**B**) SEM image of degraded PET film after 70 days. The inset shows intact PET film. Scale bar, 0.5 mm. (**C**) Time course of PET film degradation by no. 46. PET film degradation by *I. sakaiensis* 201-F6 at 30°C is shown in (D) to (H). The YSV (yeast extract–sodium carbonate–vitamins) medium was changed weekly. (**D** to **F**) SEM images of *I. sakaiensis* cells grown on PET film for 60 hours. Scale bars, 1 μm. Arrow heads in the left panel of (D) indicate contact points of cell appendages and the PET film surface. Magnifications are shown in the right panel. Arrows in (F) indicate appendages between the cell and the PET film surface. (**G**) SEM image of a degraded PET film surface after washing out adherent cells. The inset shows intact PET film. Scale bar, 1 μm. (**H**) Time course of PET film degradation by *I. sakaiensis*.

a mixture of bacteria, yeast-like cells, and protozoa, whereas the culture fluid was almost transparent (Fig. 1A). This consortium degraded the PET film surface (fig. S1) at a rate of 0.13 mg cm^{-2} day^{-1} at 30°C (Fig. 1C), and 75% of the degraded PET film carbon was catabolized into CO_2 at 28°C (fig. S2).

Using limiting dilutions of consortium no. 46 that were cultured with PET film to enrich for microorganisms that are nutritionally dependent on PET, we successfully isolated a bacterium capable of degrading and assimilating PET. The strain represents a novel species of the genus *Ideonella*, for which we propose the name *Ideonella sakaiensis* 201-F6 (deposited in the National Center for Biotechnology Information taxonomy database under identifier 1547922). In addition to being found in the culture fluid, cells were observed on the film (Fig. 1D) and appeared to be connected to each other by appendages (Fig. 1E). Shorter appendages were observed between the cells and the film; these might assist in the delivery of secreted enzymes into the film (Fig. 1, D and F). The PET film was damaged extensively (Fig. 1G) and almost completely degraded after 6 weeks at 30°C (Fig. 1H). In the course of subculturing no. 46, we found a subconsortium that lost its PET degradation capability. This subconsortium lacked *I. sakaiensis* (fig. S3), indicating that *I. sakaiensis* is functionally involved in PET degradation.

There are currently few known examples of esterases, lipases, or cutinases that are capable of hydrolyzing PET (*8*, *9*). To explore the genes involved in PET hydrolysis in *I. sakaiensis* 201-F6, we assembled a draft sequence of its genome (table S1). One identified open reading frame (ORF), ISF6_4831, encodes a putative lipase that shares 51% amino acid sequence identity and catalytic residues with a hydrolase from *Thermobifida fusca* (TfH) (fig. S4 and table S2) that exhibits PET-hydrolytic activity (*10*). We purified the corresponding recombinant *I. sakaiensis* proteins (fig. S5) and incubated them with PET film at 30°C for 18 hours. Prominent pitting developed on the film surface (Fig. 2A). Mono(2-hydroxyethyl)

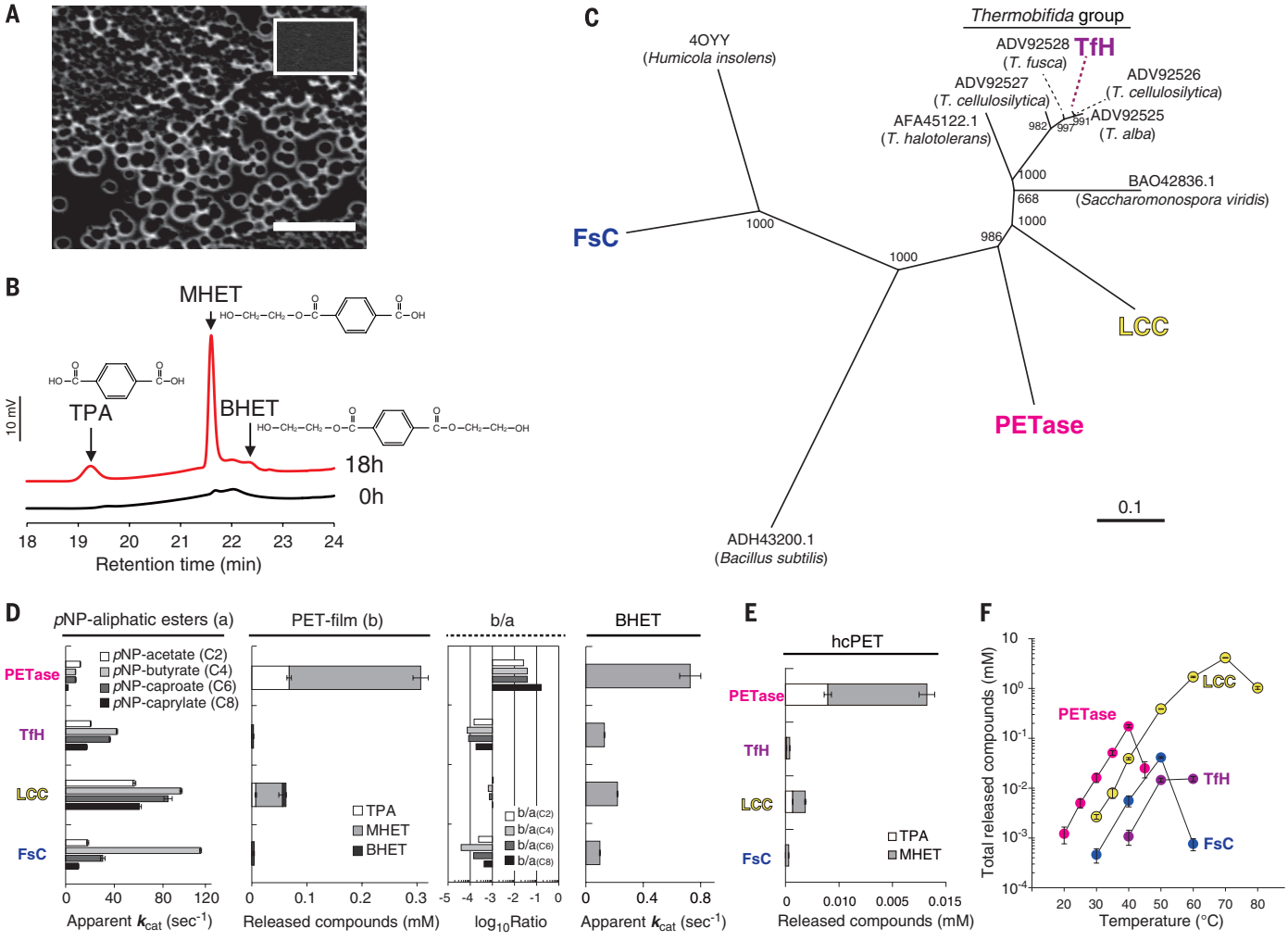

Fig. 2. ISF6_4831 protein is a PETase. Effects of PETase on PET film are shown in (A) and (B). PET film (diameter, 6 mm) was incubated with 50 nM PETase in pH 7.0 buffer for 18 hours at 30°C. (**A**) SEM image of the treated PET film surface. The inset shows intact PET film. Scale bar, 5 μm. (**B**) High-performance liquid chromatography spectrum of the products released from the PET film. (**C**) Unrooted phylogenetic tree of known PET hydrolytic enzymes. The GenBank or Protein Data Bank accession numbers (with the organism source of protein in parentheses) are shown at the leaves. Bootstrap values are shown at the branch points. Scale bar, 0.1 amino acid substitutions per single site. (**D**) Substrate specificity of four phylogenetically distinct PET hydrolytic enzymes (b/a indicates the ratio of the values in the middle-left panel to those in the leftmost panel). All reactions were performed in pH 7.0 buffer at 30°C. PET film was incubated with 50 nM enzyme for 18 hours. (**E**) Activity of the PET hydrolytic enzymes for highly crystallized PET (hcPET). The hcPET (diameter, 6 mm) was incubated with 50 nM PETase or 200 nM TfH, LCC, or FsC in pH 9.0 bicine-NaOH buffer for 18 hours at 30°C. (**F**) Effect of temperature on enzymatic PET film hydrolysis. PET film (diameter, 6 mm) was incubated with 50 nM PETase or 200 nM TfH, LCC, or FsC in pH 9.0 bicine-NaOH buffer for 1 hour. For better detection of the released products in (E) and (F), the pH and enzyme concentrations were determined based on the results shown in figs. S6 and S7, respectively. Error bars in (D) to (F) indicate SE ($n \geq 3$).

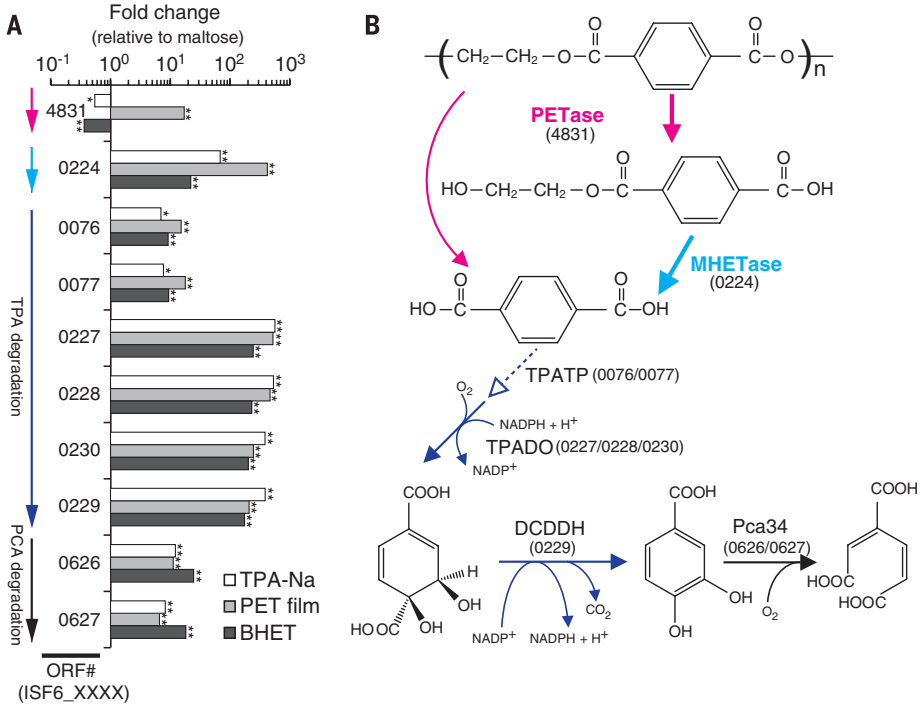

Fig. 3. PET metabolism by *I. sakaiensis*. (**A**) Transcript levels of selected genes when grown on TPA-Na, PET film, or BHET, relative to those when grown on maltose (PCA, protocatechuic acid; ORF#, last four digits of the ORF number). Two-sided *P* values were derived from Baggerly's test of the differences between the means of two independent RNA sequencing experiments (**P* < 0.05; ***P* < 0.01). Colors correspond to the steps in (B). (**B**) Predicted *I. sakaiensis* PET degradation pathway. The cellular localization of PETase and MHETase was predicted first (supplementary text, section S1). Extracellular PETase hydrolyzes PET to produce MHET (the major product) and TPA. MHETase, a predicted lipoprotein, hydrolyzes MHET to TPA and EG. TPA is incorporated through the TPA transporter (TPATP) (*17*) and catabolized by TPA 1,2-dioxygenase (TPADO), followed by 1,2-dihydroxy-3,5-cyclohexadiene-1,4-dicarboxylate dehydrogenase (DCDDH). The resultant PCA is ring-cleaved by PCA 3,4-dioxygenase (Pca34). The predicted TPA degradation pathway is further described in the supplementary text (section S2).

terephthalic acid (MHET) was the major product released by the recombinant protein, together with minor amounts of TPA and bis(2-hydroxyethyl) TPA (BHET) (Fig. 2B). These results suggest that the ISF6_4831 protein hydrolyzes PET. This protein also hydrolyzed BHET to yield MHET with no further decomposition.

We compared the activity of the ISF6_4831 protein with that of three evolutionarily divergent PET-hydrolytic enzymes identified from a phylogenetic tree that we constructed using published enzymes (Fig. 2C and table S2). We purified TfH from a thermophilic actinomycete (*10*), cutinase homolog from leaf-branch compost metagenome (LC cutinase, or LCC) (*11*), and *F. solani* cutinase (FsC) from a fungus (fig. S5) (*12*), and we measured their activities against *p*-nitrophenol–linked aliphatic esters (*p*NP-aliphatic esters), PET film, and BHET at 30°C and pH 7.0. For *p*NP-aliphatic esters, which are preferred by lipases and cutinases, the activity of the ISF6_4831 protein was lower than that of TfH, LCC, and FsC (Fig. 2D). The activity of the ISF6_4831 protein against the PET film, however, was 120, 5.5, and 88 times as high as that of TfH, LCC, and FsC, respectively. A similar trend was observed for BHET (Fig. 2D). The catalytic preference of the ISF6_4831 protein for PET film over *p*NP-aliphatic esters was also substantially higher than that of TfH, LCC, and FsC (380, 48, and 400 times as high on average, respectively) (Fig. 2D). Thus, the ISF6_4831 protein prefers PET to aliphatic esters, compared with the other enzymes, leading to its designation as a PET hydrolase (termed PETase).

PETase was also more active than TfH, LCC, and FsC against commercial bottle–derived PET, which is highly crystallized (Fig. 2E), even though the densely packed structure of highly crystallized PET greatly reduces the enzymatic hydrolysis of its ester linkages (*9*, *13*). PETase was somewhat heat-labile, but it was considerably more active against PET film at low temperatures than were TfH, LCC, and FsC (Fig. 2F). Enzymatic degradation of polyesters is controlled mainly by their chain mobility (*14*). Flexibility of the polyester chain decreases as the glass transition temperature increases (*9*). The glass transition temperature of PET is around 75°C, meaning that the polyester chain of PET is in a glassy state at the moderate temperatures appropriate for mesophilic enzyme reactions. The substrate specificity of PETase and its prominent hydrolytic activity for PET in a glassy state would be critical to sustaining the growth of *I. sakaiensis* on PET in most environments.

I. sakaiensis adheres to PET (Fig. 1, D to F) and secretes PETase to target this material. We compared the PET hydrolytic activity of PETase with that of the other three PET hydrolytic enzymes (fig. S7). The activity ratios of PETase relative to the other enzymes decreased as the enzyme concentrations increased, indicating that PETase efficiently hydrolyzed PET with less enzyme diffusion into the aqueous phase and/or plastic vessels used for the reaction. PETase lacks apparent substrate-binding motifs such as the carbohydrate-binding modules generally observed in glycoside hydrolases. Therefore, without a three-dimensional structure determined for PETase, the exact binding mechanism is unknown.

MHET, the product of PETase-mediated hydrolysis of BHET and PET, was a very minor component in the supernatant of *I. sakaiensis* cultured on PET film (fig. S8), indicating rapid MHET metabolism. Several PET hydrolytic enzymes have been confirmed to hydrolyze MHET (table S2). To identify enzymes responsible for PET degradation in *I. sakaiensis* cultures, we RNA-sequenced transcriptomes of *I. sakaiensis* cells growing on maltose, disodium terephthalate (TPA-Na), BHET,

Table 1. Kinetic parameters of MHETase. The kinetic parameters were determined in pH 7.0 buffer at 30°C. Because the enzymatic PET hydrolysis involves a heterogeneous reaction, Michaelis–Menten kinetics were not applied to PETase. ND, not detected (activity was below the detection limit of the assay).

Substrate	k_{cat} (s^{-1})	K_m (μM)
MHET	31 ± 0.8*	7.3 ± 0.6*
PET film	ND	
BHET	0.10 ± 0.004†	
*p*NP-aliphatic esters (*p*NP-acetate, *p*NP-butyrate)	ND	
Aromatic esters (ethyl gallate, ethyl ferulate, chlorogenic acid hydrate)	ND	

*Data are shown as means ± SEs based on a nonlinear regression model. †The reported k_{cat} is the apparent k_{cat} determined with 0.9 mM BHET. Shown is the mean ± SE from three independent experiments.

or PET film (fig. S9 and table S3). The catabolic genes for TPA and the metabolite protocatechuic acid (PCA) were up-regulated dramatically when cells were cultured on TPA-Na, BHET, or PET film. This contrasted with genes for the catabolism of maltose (Fig. 3A), which involves a pathway distinct from the degradation of TPA and EG, indicating efficient metabolism of TPA by *I. sakaiensis*. The transcript level of the PETase-encoding gene during growth on PET film was the highest among all analyzed coding sequences (table S4), and it was 15, 31, and 41 times as high as when bacteria were grown on maltose, TPA-Na, and BHET, respectively. This suggests that the expression of PETase is induced by PET film itself and/or some degradation products other than TPA, EG, MHET, and BHET.

The expression levels of the PETase gene in the four different media were similar to those of another ORF, ISF6_0224 (fig. S10), indicating similar regulation. ISF6_0224 is located adjacent to the TPA degradation gene cluster (fig. S11). The ISF6_0224 protein sequence matches those of the tannase family, which is known to hydrolyze the ester linkage of aromatic compounds such as gallic acid esters, ferulic saccharides, and chlorogenic acids. The catalytic triad residues and two cysteine residues found only in this family (*15*) are completely conserved in the ISF6_0224 protein (fig. S12). Purified recombinant ISF6_0224 protein (fig. S5) efficiently hydrolyzed MHET with a turnover rate (k_{cat}) of 31 ± 0.8 s^{-1} and a Michaelis constant (K_m) of 7.3 ± 0.6 μM (Table 1), but it did not show any activity against PET, BHET, *p*NP-aliphatic esters, or typical aromatic ester compounds catalyzed by the tannase family enzymes (Table 1). ISF6_0224 is nonhomologous to six known MHET-hydrolytic enzymes that also hydrolyze PET and *p*NP-aliphatic esters (table S2). These results strongly suggest that the ISF6_0224 protein is responsible for the conversion of MHET to TPA and EG in *I. sakaiensis*. The enzyme was thus designated a MHET hydrolase (termed MHETase).

To determine how the metabolism of PET (Fig. 3B) evolved, we used the Integr8 fully sequenced genome database (*16*) to search for other organisms capable of metabolizing this compound. However, we were unable to find other organisms with a set of gene homologs of signature enzymes for PET metabolism (PETase, MHETase, TPA dioxygenase, and PCA dioxygenase) (fig. S13). However, among the 92 microorganisms with MHETase homolog(s), 33 had homologs of both TPA and PCA dioxygenases. This suggests that a genomic basis to support the metabolism of MHET analogs was established much earlier than when ancestral PETase proteins were incorporated into the pathway. PET enrichment in the sampling site and the enrichment culture potentially promoted the selection of a bacterium that might have obtained the necessary set of genes through lateral gene transfer. A limited number of mutations in a hydrolase, such as PET hydrolytic cutinase, that inherently targets the natural aliphatic polymer cutin may have resulted in enhanced selectivity for PET.

REFERENCES AND NOTES

1. V. Sinha, M. R. Patel, J. V. Patel, *J. Polym. Environ.* **18**, 8–25 (2010).
2. R. J. Müller, I. Kleeberg, W. D. Deckwer, *J. Biotechnol.* **86**, 87–95 (2001).
3. D. Kint, S. Munoz-Guerra, *Polym. Int.* **48**, 346–352 (1999).
4. L. Neufeld, F. Stassen, R. Sheppard, T. Gilman, Eds., *The New Plastics Economy: Rethinking the Future of Plastics* (World Economic Forum, 2016); www3.weforum.org/docs/WEF_The_New_Plastics_Economy.pdf.
5. T. Nimchua, H. Punnapayak, W. Zimmermann, *Biotechnol. J.* **2**, 361–364 (2007).
6. T. Nimchua, D. E. Eveleigh, U. Sangwatanaroj, H. Punnapayak, *J. Ind. Microbiol. Biotechnol.* **35**, 843–850 (2008).
7. Materials and methods are available as supplementary materials on *Science* Online.
8. D. Ribitsch *et al.*, *Biocatalysis Biotransform.* **30**, 2–9 (2012).
9. W. Zimmermann, S. Billig, *Adv. Biochem. Eng. Biotechnol.* **125**, 97–120 (2010).
10. R. J. Müller, H. Schrader, J. Profe, K. Dresler, W. D. Deckwer, *Macromol. Rapid Commun.* **26**, 1400–1405 (2005).
11. S. Sulaiman *et al.*, *Appl. Environ. Microbiol.* **78**, 1556–1562 (2012).
12. C. M. Silva *et al.*, *J. Polym. Sci. A Polym. Chem.* **43**, 2448–2450 (2005).
13. M. A. M. E. Vertommen, V. A. Nierstrasz, M. Veer, M. M. C. G. Warmoeskerken, *J. Biotechnol.* **120**, 376–386 (2005).
14. E. Marten, R. J. Müller, W. D. Deckwer, *Polym. Degrad. Stabil.* **88**, 371–381 (2005).
15. K. Suzuki *et al.*, *Proteins* **82**, 2857–2867 (2014).
16. P. Kersey *et al.*, *Nucleic Acids Res.* **33**, D297–D302 (2005).
17. M. Hosaka *et al.*, *Appl. Environ. Microbiol.* **79**, 6148–6155 (2013).

ACKNOWLEDGMENTS

We are grateful to Y. Horiuchi, M. Uemura, T. Kawai, K. Sasage, and S. Hase for research assistance. We thank D. Dodd, H. Atomi, T. Nakayama, and A. Wlodawer for comments on this manuscript. This study was supported by grants-in-aid for scientific research (24780078 and 26850053 to S.Y.) and the Noda Institute for Scientific Research (S.Y.). The reported nucleotide sequence data, including assembly and annotation, have been deposited in the DNA Data Bank of Japan, European Molecular Biology Laboratory, and GenBank databases under the accession numbers BBYR01000001 to BBYR01000227. All other data are reported in the supplementary materials. The reported strain *Ideonella sakaiensis* 201-F6^T was deposited at the National Institute of Technology and Evaluation Biological Resource Center as strain NBRC 110686^T and at Thailand Institute of Scientific and Technological Research as strain TISTR 2288^T.

SUPPLEMENTARY MATERIALS

www.sciencemag.org/content/351/6278/1196/suppl/DC1
Materials and Methods
Supplementary Text
Figs. S1 to S14
Tables S1 to S5
References (*18*–*39*)

15 October 2015; accepted 29 January 2016
10.1126/science.aad6359

NEURODEVELOPMENT

CLK2 inhibition ameliorates autistic features associated with SHANK3 deficiency

Michael Bidinosti,[1]* Paolo Botta,[3]* Sebastian Krüttner,[3] Catia C. Proenca,[1] Natacha Stoehr,[1] Mario Bernhard,[1] Isabelle Fruh,[1] Matthias Mueller,[1] Debora Bonenfant,[2] Hans Voshol,[2] Walter Carbone,[1] Sarah J. Neal,[4] Stephanie M. McTighe,[4] Guglielmo Roma,[1] Ricardo E. Dolmetsch,[4] Jeffrey A. Porter,[1] Pico Caroni,[3] Tewis Bouwmeester,[1] Andreas Lüthi,[3] Ivan Galimberti[1]†

SH3 and multiple ankyrin repeat domains 3 (*SHANK3*) haploinsufficiency is causative for the neurological features of Phelan-McDermid syndrome (PMDS), including a high risk of autism spectrum disorder (ASD). We used unbiased, quantitative proteomics to identify changes in the phosphoproteome of Shank3-deficient neurons. Down-regulation of protein kinase B (PKB/Akt)–mammalian target of rapamycin complex 1 (mTORC1) signaling resulted from enhanced phosphorylation and activation of serine/threonine protein phosphatase 2A (PP2A) regulatory subunit, B56β, due to increased steady-state levels of its kinase, Cdc2-like kinase 2 (CLK2). Pharmacological and genetic activation of Akt or inhibition of CLK2 relieved synaptic deficits in Shank3-deficient and PMDS patient–derived neurons. CLK2 inhibition also restored normal sociability in a Shank3-deficient mouse model. Our study thereby provides a novel mechanistic and potentially therapeutic understanding of deregulated signaling downstream of Shank3 deficiency.

Chromosomal aberrations at 22q13 that delete or inactivate one SH3 and multiple ankyrin repeat domains 3 (*SHANK3*) allele are genetic hallmarks of Phelan-McDermid syndrome (PMDS). De novo mutations in *SHANK3* are also associated with nonsyndromic autism spectrum disorder (ASD) and intellectual disability (*1*–*4*). Genetic ablation of *Shank3* in mice yields ASD-like behavioral phenotypes and synaptic dysfunction (*5*–*10*), the latter of which

Downloaded from on March 10, 2016

has also been observed in PMDS patient–derived neurons or after Shank3 knockdown in primary rodent neurons (*11*, *12*). Shank3 is a large protein that serves as a scaffold to organize excitatory postsynaptic densities through protein-protein interactions [reviewed in (*13*)]. Reduced expression of Shank3 results in decreased dendritic spine density (*6*, *7*, *11*, *14*), whereas its overexpression enhances spine number or induces spine formation in aspiny neurons (*14*, *15*).

PMDS patients treated with insulin-like growth factor–1 (IGF-1) showed improvements in social and stereotyped behaviors (*16*). IGF-1 also alleviated deficits in Shank3-deficient mice (*17*) and PMDS neurons (*12*). Here, we used phosphoproteomics to investigate the signaling pathways that link Shank3 and IGF-1.

We used rat cortical neurons and reduced Shank3 expression by knockdown. We treated these neurons with brain-derived neurotrophic factor (BDNF) to elicit synaptic plasticity-dependent changes and then analyzed the phosphoproteome (fig. S1). Several phosphopeptides originating from protein substrates in the protein kinase B (PKB or Akt)–mammalian target of rapamycin complex 1 (mTORC1) pathway showed reduced phosphorylation levels in Shank3 knockdown neurons (Fig. 1A, table S1, and database S1). In particular, phosphorylation on GSK3β and ribosomal protein S6 (rpS6) was less than normal on Akt and mTORC1-dependent sites, respectively (Fig. 1A and table S1). Phosphorylation on B56β (*Ppp2r5b*), a PP2A phosphatase regulatory subunit (*18*), was elevated on a peptide sequence known (*19*) to regulate dephosphorylation of Akt (Fig. 1, A and B). No significant changes were observed in extracellular–signal regulated kinase (ERK) signaling (Mapk1/3) (Fig. 1A and table S1). Consistent with this, we also observed reduced pathway activity in synaptosomal fractions from a newly produced Shank3-deficient mouse model (table S2, database S2, and fig. S9). In a second method of proteomic analysis, we enriched less mTOR from Shank3 knockdown neurons on the basis of affinity for pan-kinase inhibitor conjugated beads (Kinomatrix beads) (*20*) (fig. S1 and database S3). The Akt-mTORC1 signaling pathway is linked to ASD (*21*, *22*) and is regulated by IGF-1, which is currently being explored as a therapeutic for PMDS (*12*, *16*, *17*). We therefore explored whether Shank3 deficiency in PMDS leads to reduced Akt-mTORC1 signaling by way

[1]Developmental Molecular Pathways, Novartis Institutes for Biomedical Research, Basel, Switzerland. [2]Analytical Sciences and Imaging, Novartis Institutes for Biomedical Research, Basel, Switzerland. [3]Friedrich Miescher Institute, Basel, Switzerland. [4]Neuroscience, Novartis Institutes for Biomedical Research, Cambridge, USA.
*These authors contributed equally to this work. **†Corresponding author. E-mail: ivan.galimberti@novartis.com**

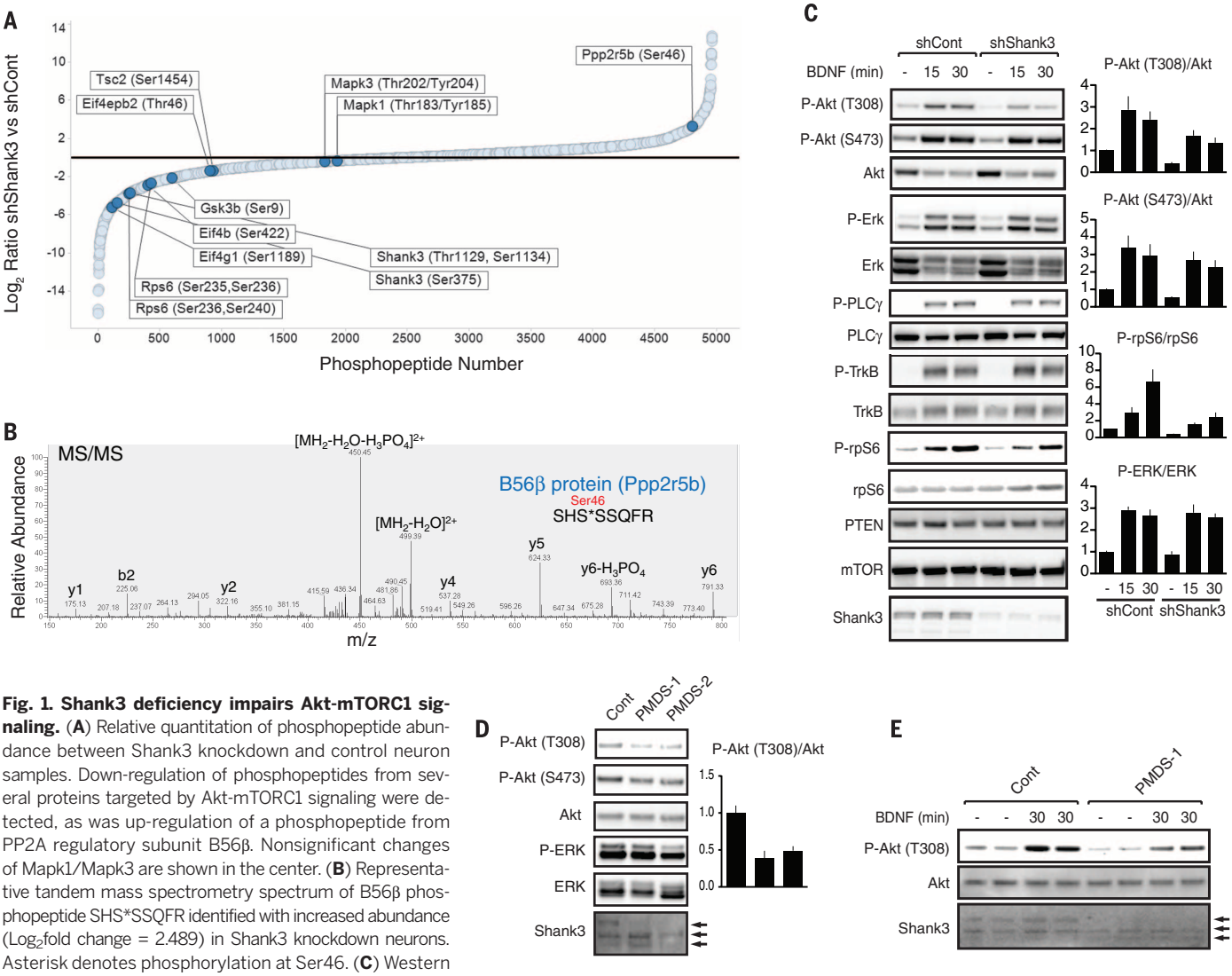

Fig. 1. Shank3 deficiency impairs Akt-mTORC1 signaling. (**A**) Relative quantitation of phosphopeptide abundance between Shank3 knockdown and control neuron samples. Down-regulation of phosphopeptides from several proteins targeted by Akt-mTORC1 signaling were detected, as was up-regulation of a phosphopeptide from PP2A regulatory subunit B56β. Nonsignificant changes of Mapk1/Mapk3 are shown in the center. (**B**) Representative tandem mass spectrometry spectrum of B56β phosphopeptide SHS*SSQFR identified with increased abundance (Log_2fold change = 2.489) in Shank3 knockdown neurons. Asterisk denotes phosphorylation at Ser46. (**C**) Western blotting validation of reduced Akt-mTORC1 signaling in Shank3 knockdown neurons. Neurons were treated with BDNF (50 ng/ml), and cell lysates were prepared in radioimmunoprecipitation assay buffer. Plots are means ± SEM. (**D**) Impaired Akt activity in PMDS iPSC-derived patient neurons. Cell lysates were prepared as in (C) at 8 weeks in vitro. Plots are means ± SEM. (**E**) Impaired Akt activation after BDNF stimulation in PMDS iPSC-derived patient neurons. Cell lysates were prepared as in (C) at 8 weeks in vitro.

of enhanced PP2A-mediated inactivation of Akt (fig. S1).

Shank3 knockdown in primary neurons caused a reduction by a factor of two of Akt phosphorylation at T308 in basal conditions or after BDNF stimulation (Fig. 1C) but had less of an effect at S473. Coincident phosphorylation of both Akt sites (T308 and S473) is required for full Akt activation. Phosphorylation of rpS6 was similarly reduced (Fig. 1C). Attenuated Akt T308 phosphorylation was observed with two additional Shank3 short hairpin RNAs (shRNAs) and was rescued by coexpression of nontargeted Shank3 (fig. S2). mTOR steady-state levels were unchanged. This indicated that reduced mTOR recovery in Kinomatrix capture, which enriches activated kinases through affinity for a promiscuous adenosine triphosphate (ATP)–competitive inhibitor resin, was due to impaired kinase activity after Shank3 knockdown. BDNF and its receptor TrkB also activate ERK and phospholipase Cγ (PLCγ) pathways (fig. S2); however, no impairment was observed in either of these pathways (Fig. 1C and fig. S2). We observed no change in Akt phosphorylation after knockdown of another postsynaptic density protein, PSD95, thus indicating that impaired Akt signaling is specific to Shank3 deficiency rather than generic reduction of synaptic proteins (fig. S2). Phosphorylation of the BDNF receptor, TrkB, and expression of phosphatase and tensin homolog (PTEN) were also unchanged (Fig. 1C), suggesting that attenuated Akt-mTORC1 signaling occurs directly through deregulated Akt phosphorylation. These findings were corroborated in human induced pluripotent stem cell (iPSC)–derived neurons from two PMDS patients who harbor deletions within the *SHANK3* locus (fig. S3). As with Shank3 knockdown, Akt T308 phosphorylation was reduced in these SHANK3-deficient neurons (Fig. 1, D and E).

Next, we examined the possibility that Akt-signaling is attenuated by elevated PP2A dephosphorylation activity. B56β, a regulatory subunit of PP2A, is expressed in the brain and defines PP2A specificity for Akt T308 dephosphorylation (fig. S1) (*18*, *23*). Phosphorylated B56β recruits PP2A catalytic (PP2Ac) and structural subunits to Akt for heterotrimeric phosphatase holoenzyme assembly and T308 dephosphorylation (*19*). In Shank3 knockdown neurons, association of Akt with PP2Ac was above normal by a factor of two (Fig. 2A). Thus, excess of B56β phosphorylation enhances recruitment of PP2A to Akt and reduces phosphorylation of Akt within the catalytic domain

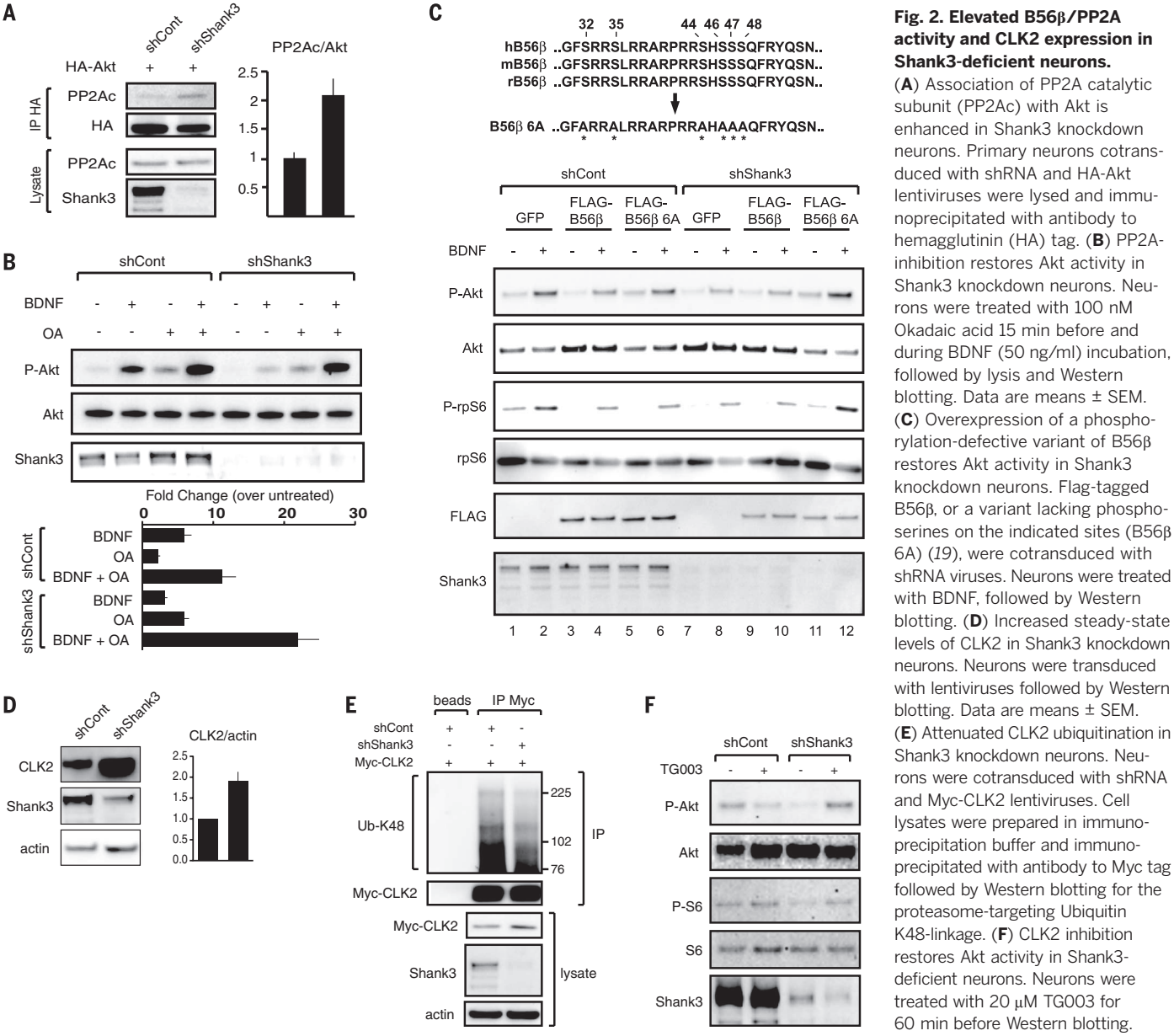

Fig. 2. Elevated B56β/PP2A activity and CLK2 expression in Shank3-deficient neurons. (**A**) Association of PP2A catalytic subunit (PP2Ac) with Akt is enhanced in Shank3 knockdown neurons. Primary neurons cotransduced with shRNA and HA-Akt lentiviruses were lysed and immunoprecipitated with antibody to hemagglutinin (HA) tag. (**B**) PP2A-inhibition restores Akt activity in Shank3 knockdown neurons. Neurons were treated with 100 nM Okadaic acid 15 min before and during BDNF (50 ng/ml) incubation, followed by lysis and Western blotting. Data are means ± SEM. (**C**) Overexpression of a phosphorylation-defective variant of B56β restores Akt activity in Shank3 knockdown neurons. Flag-tagged B56β, or a variant lacking phosphoserines on the indicated sites (B56β 6A) (*19*), were cotransduced with shRNA viruses. Neurons were treated with BDNF, followed by Western blotting. (**D**) Increased steady-state levels of CLK2 in Shank3 knockdown neurons. Neurons were transduced with lentiviruses followed by Western blotting. Data are means ± SEM. (**E**) Attenuated CLK2 ubiquitination in Shank3 knockdown neurons. Neurons were cotransduced with shRNA and Myc-CLK2 lentiviruses. Cell lysates were prepared in immunoprecipitation buffer and immunoprecipitated with antibody to Myc tag followed by Western blotting for the proteasome-targeting Ubiquitin K48-linkage. (**F**) CLK2 inhibition restores Akt activity in Shank3-deficient neurons. Neurons were treated with 20 μM TG003 for 60 min before Western blotting.

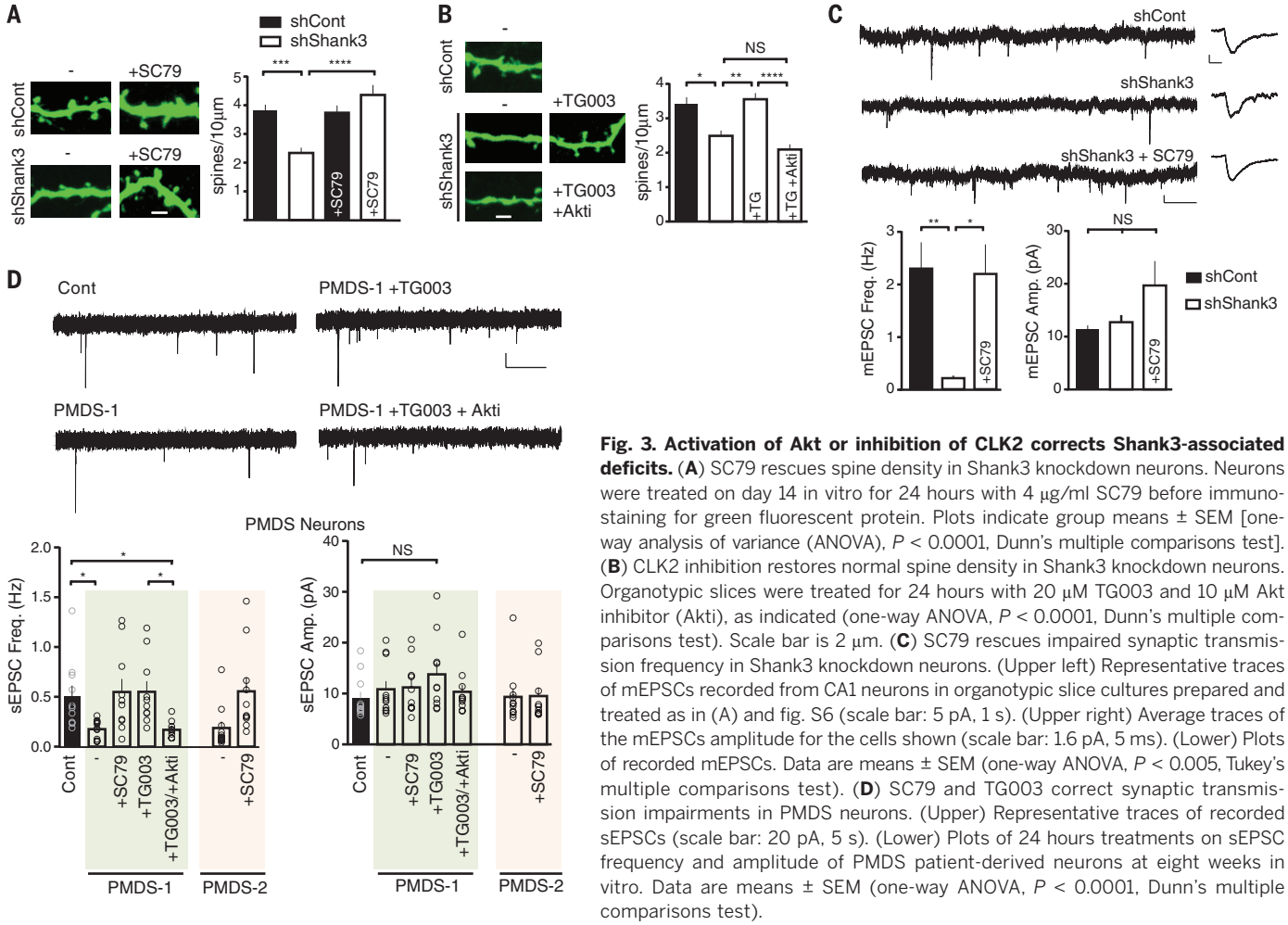

Fig. 3. Activation of Akt or inhibition of CLK2 corrects Shank3-associated deficits. (**A**) SC79 rescues spine density in Shank3 knockdown neurons. Neurons were treated on day 14 in vitro for 24 hours with 4 µg/ml SC79 before immunostaining for green fluorescent protein. Plots indicate group means ± SEM [one-way analysis of variance (ANOVA), $P < 0.0001$, Dunn's multiple comparisons test]. (**B**) CLK2 inhibition restores normal spine density in Shank3 knockdown neurons. Organotypic slices were treated for 24 hours with 20 µM TG003 and 10 µM Akt inhibitor (Akti), as indicated (one-way ANOVA, $P < 0.0001$, Dunn's multiple comparisons test). Scale bar is 2 µm. (**C**) SC79 rescues impaired synaptic transmission frequency in Shank3 knockdown neurons. (Upper left) Representative traces of mEPSCs recorded from CA1 neurons in organotypic slice cultures prepared and treated as in (A) and fig. S6 (scale bar: 5 pA, 1 s). (Upper right) Average traces of the mEPSCs amplitude for the cells shown (scale bar: 1.6 pA, 5 ms). (Lower) Plots of recorded mEPSCs. Data are means ± SEM (one-way ANOVA, $P < 0.005$, Tukey's multiple comparisons test). (**D**) SC79 and TG003 correct synaptic transmission impairments in PMDS neurons. (Upper) Representative traces of recorded sEPSCs (scale bar: 20 pA, 5 s). (Lower) Plots of 24 hours treatments on sEPSC frequency and amplitude of PMDS patient-derived neurons at eight weeks in vitro. Data are means ± SEM (one-way ANOVA, $P < 0.0001$, Dunn's multiple comparisons test).

at T308, thereby attenuating activity. Addition of the PP2A inhibitor Okadaic acid (OA), alone or together with BDNF, increased Akt T308 phosphorylation in Shank3 knockdown neurons by a factor of two, relative to control (Fig. 2B). Expression of a B56β variant lacking the regulatory phosphorylation sites (B56β 6A) (*19*) restored Akt phosphorylation in Shank3 knockdown neurons to control levels (Fig. 2C; compare lanes 1 and 2 with 11 and 12). Thus, Shank3 deficiency in neurons engenders enhanced activity of B56β/PP2A, leading in turn to excessively dephosphorylated Akt and deficiency in Akt activity.

B56β is phosphorylated by CLK2 (*19*) on serine residues in the regulatory peptide sequence. Shank3 knockdown neurons exhibited an increase by a factor of two in CLK2 protein levels (Fig. 2D), consistent with excess phosphorylation on B56β (Fig. 1, A and B). In hepatocytes, CLK2 is upregulated by insulin induction to homeostatically regulate Akt through B56β/PP2A-mediated dephosphorylation (*19*, *24*). BDNF treatment induced the accumulation of CLK2 in control neurons but not in Shank3 knockdown neurons (fig. S4). This suggests that the regulated expression of CLK2 by ubiquitination (*24*) is lost in the absence of Shank3. Proteasome inhibition caused a rapid increase of CLK2 in control neurons but not in neurons deficient in Shank3 (fig. S4). Immunoprecipitation of Myc-CLK2 showed less CLK2 ubiquitination in Shank3 knockdown neurons (Fig. 2E). Shank3 knockdown neurons exhibited no change in CLK2 mRNA levels (fig. S5). Treatment with an ATP-competitive CLK2 inhibitor, TG003 (fig. S4), restored Akt T308 phosphorylation in Shank3 knockdown neurons to control levels (Fig. 2F). Thus, increased steady-state levels of CLK2 in Shank3-deficient neurons occurs through impaired ubiquitination and causes excess Akt inactivation through elevated B56β/PP2A activity (fig. S4).

We anticipated that Akt activation, either directly or through CLK2 inhibition, would reverse neuronal impairments associated with Shank3 deficiency. Shank3 knockdown in organotypic brain slice cultures decreased dendritic spine density and was rescued by Shank3 re-expression (fig. S6) (*4*, *6*, *11*). We then exposed slices to the small-molecule Akt activator SC79 (fig. S7) (*25*) or to TG003. We observed that both treatments restored spine density in Shank3 knockdown neurons to control levels (Fig. 3, A and B). This was dependent on Akt activity because it was blocked by co-incubation with a validated Akt inhibitor (Fig. 3B and fig. S7). Reduction of CLK2 in Shank3 knockdown neurons had a similar restorative effect on spine density to that of TG003 treatment (fig. S6). We confirmed that Akt inhibition in wild-type neurons is sufficient to reduce spine density and thereby phenocopy the effect of Shank3 deficiency on reducing spine density through downstream Akt attenuation (fig. S6). Shank3 knockdown in organotypic slices reduced miniature excitatory postsynaptic current (mEPSC) frequency that was restored to control levels with SC79 treatment (Fig. 3C). iPSC-derived neurons from two unrelated PMDS patients exhibited reduced frequency of spontaneous EPSCs (sEPSCs) (Fig. 3D and fig. S8). Treatment with SC79 or TG003 again rescued these deficits in an Akt-dependent manner (Fig. 3D, highlighted groups). Thus, Akt activation alone or through CLK2 inhibition is sufficient to restore synaptic impairments occurring from Shank3 deficiency.

To determine whether our findings extend to ASD-like behaviors, we generated a Shank3-deficient mouse model by ablation of *Shank3* exon 21 (fig. S9) as previously described (*8*, *10*). The major Shank3 isoforms are absent in our

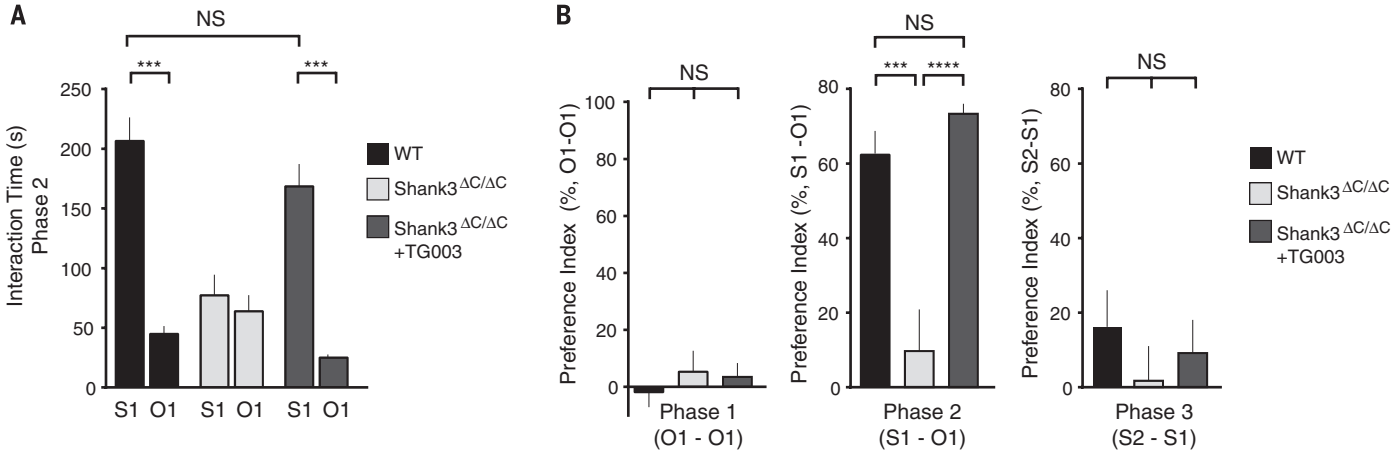

Fig. 4. CLK2 inhibition corrects impaired social motivation in Shank3$^{\Delta C/\Delta C}$ mice. (**A**) Shank3$^{\Delta C/\Delta C}$ mice display impaired motivation for social interaction that is corrected by treatment with CLK2-inhibitor TG003. Interaction times with the intruder mouse (S1) or the object (O1) are plotted for phase 2. Data are means ± SEM with paired *t* tests (wild-type, $P < 0.0005$; Shank3$^{\Delta C/\Delta C}$ +TG003, $P < 0.0005$), comparing S1 to O1 investigation times within each group. Comparison of social interaction times across groups was by one-way ANOVA with Tukey's multiple comparisons test ($P < 0.0005$ for differences among group means). (**B**) Preference index for S1 versus O1 of interaction times (see the methods) was calculated for each test phase. Data are means ± SEM (one-way ANOVA, $P < 0.0001$, Tukey's multiple comparisons test).

homozygous mice (Shank3$^{\Delta C/\Delta C}$), whereas faster-migrating, truncated fragments were detected (fig. S9). Shank3$^{\Delta C/\Delta C}$ neurons displayed excess CLK2 expression (fig. S9). Neither heterozygous (Shank3$^{+/\Delta C}$) nor Shank3$^{\Delta C/\Delta C}$ mice exhibited anxious behavior or locomotor skill impairments (fig. S10). Both Shank3$^{+/\Delta C}$ and Shank3$^{\Delta C/\Delta C}$ mice displayed avoidance behavior, assessed by marble burying, that was refractory to treatment with TG003 (fig. S10). In contrast, we observed that only Shank3$^{\Delta C/\Delta C}$ mice exhibited excess self-grooming, a trait reflecting repetitive behaviors seen in ASD (fig. S10). Treatment of these mice with TG003 significantly decreased self-grooming, although not to wild-type frequency (fig. S10). Mice were then tested in a social motivation paradigm (fig. S10). Wild-type and Shank3$^{+/\Delta C}$ mice displayed a significant preference for social investigation, whereas Shank3$^{\Delta C/\Delta C}$ mice did not (Fig. 4, A and B, and fig. S10). In contrast, Shank3$^{\Delta C/\Delta C}$ mice treated with TG003 recovered normal preference for social interaction (Fig. 4, A and B, and fig. S10). We observed that this effect persisted 3 days after treatment when a new cohort of animals was tested (fig. S10). The recovery of normal social behavior correlated with restored Akt phosphorylation in synaptosomal fractions (fig. S9). No significant preference was observed between groups when a second intruder was introduced (Fig. 4B). Thus, CLK2 inhibition rescues deficits in social behavior caused by Shank3 deficiency.

Mutations in Akt-mTORC1 pathway regulators PTEN and TSC1/2 yield clinical syndromes that include features of ASD by means of exaggerated Akt-mTORC1 activity (*21*, *22*). However, attenuated Akt-mTORC1 activity has also been associated with Angelman syndrome, another monogenic form of ASD (*26*, *27*). This suggests a bidirectional regulation of the Akt-mTORC1 pathway associated with different ASD genes. Here, we show that Shank3 deficiency leads to enhanced CLK2 expression and attenuated Akt-mTORC1 activity. Cellular and behavioral impairments attributed to Shank3 loss of function have been corrected with IGF-1 treatment (*12*, *16*, *17*). We found that IGF-1 treatment restored normal dendritic spine density to Shank3 knockdown neurons in an Akt-dependent manner (fig. S11). We suggest that IGF-1 restores balance in signaling pathways by boosting Akt phosphorylation to counteract elevated dephosphorylation by PP2A (fig. S12). Thus, we propose that direct Akt-reactivation or CLK2 inhibition may be therapeutic targets for intervention in patients with PMDS.

REFERENCES AND NOTES

1. K. Phelan, H. E. McDermid, *Molecular Syndromology* **2**, 186–201 (2012).
2. C. Redin *et al.*, *J. Med. Genet.* **51**, 724–736 (2014).
3. J. Gauthier *et al.*, *Proc. Natl. Acad. Sci. U.S.A.* **107**, 7863–7868 (2010).
4. C. M. Durand *et al.*, *Nat. Genet.* **39**, 25–27 (2007).
5. O. Bozdagi *et al.*, *Molecular Autism* **1**, 15 (2010).
6. J. Peça *et al.*, *Nature* **472**, 437–442 (2011).
7. X. Wang *et al.*, *Hum. Mol. Genet.* **20**, 3093–3108 (2011).
8. M. Kouser *et al.*, *J. Neurosci.* **33**, 18448–18468 (2013).
9. M. Yang *et al.*, *J. Neurosci.* **32**, 6525–6541 (2012).
10. L. J. Duffney *et al.*, *Cell Reports* **11**, 1400–1413 (2015).
11. C. Verpelli *et al.*, *J. Biol. Chem.* **286**, 34839–34850 (2011).
12. A. Shcheglovitov *et al.*, *Nature* **503**, 267–271 (2013).
13. Y. H. Jiang, M. D. Ehlers, *Neuron* **78**, 8–27 (2013).
14. G. Roussignol *et al.*, *J. Neurosci.* **25**, 3560–3570 (2005).
15. K. Han *et al.*, *Nature* **503**, 72–77 (2013).
16. A. Kolevzon *et al.*, *Molecular Autism* **5**, 54 (2014).
17. O. Bozdagi, T. Tavassoli, J. D. Buxbaum, *Molecular Autism* **4**, 9 (2013).
18. S. Padmanabhan *et al.*, *Cell* **136**, 939–951 (2009).
19. J. T. Rodgers, R. O. Vogel, P. Puigserver, *Mol. Cell* **41**, 471–479 (2011).
20. C. M. Gower *et al.*, *ACS Chem. Biol.* **11**, 121–131 (2016).
21. A. Goffin, L. H. Hoefsloot, E. Bosgoed, A. Swillen, J. P. Fryns, *Am. J. Med. Genet.* **105**, 521–524 (2001).
22. S. L. Smalley, P. E. Tanguay, M. Smith, G. Gutierrez, *J. Autism Dev. Disord.* **22**, 339–355 (1992).
23. B. McCright, D. M. Virshup, *J. Biol. Chem.* **270**, 26123–26128 (1995).
24. J. T. Rodgers, W. Haas, S. P. Gygi, P. Puigserver, *Cell Metab.* **11**, 23–34 (2010).
25. H. Jo *et al.*, *Proc. Natl. Acad. Sci. U.S.A.* **109**, 10581–10586 (2012).
26. S. Ricciardi *et al.*, *Hum. Mol. Genet.* **20**, 1182–1196 (2011).
27. C. Cao *et al.*, *PLOS Biol.* **11**, e1001478 (2013).

ACKNOWLEDGMENTS

We thank B. Gomez-Mancilla and T. Doll for help in accessing and reprogramming the PMDS cell lines. We thank B. Kinzel, M. Xiaohong, and D. Breustedt for help in the creation of the Shank3$^{\Delta C/\Delta C}$ mouse model and S. Legare for help with the in vivo experiments. We thank J. Knehr for the technical performance of the metapair sequencing and M. Beibel for the bioinformatics support. Sequencing data related to this study are available in the National Center for Biotechnology Information's Short Read Archive under accession number SRP067966. The PMDS iPS lines and the Kinomatrix are available from Novartis under materials transfer agreements. Novartis AG may hold patent applications related to aspects of the disclosed subject matter. The Developmental Molecular Pathways Department is part of the Novartis Institutes for Biomedical Research. The supplementary materials contain additional data.

SUPPLEMENTARY MATERIALS

www.sciencemag.org/content/351/6278/1199/suppl/DC1
Materials and Methods
Figs. S1 to S12
Tables S1 and S2
Databases S1 to S3
References

30 September 2015; accepted 22 January 2016
Published online 4 February 2016
10.1126/science.aad5487

CANCER BIOLOGY

Schedule-dependent interaction between anticancer treatments

Sheng-hong Chen,[1] William Forrester,[2] Galit Lahav[1]

The oncogene *MDMX* is overexpressed in many cancers, leading to suppression of the tumor suppressor p53. Inhibitors of the oncogene product MDMX therefore might help reactivate p53 and enhance the efficacy of DNA-damaging drugs. However, we currently lack a quantitative understanding of how MDMX inhibition affects the p53 signaling pathway and cell sensitivity to DNA damage. Live cell imaging showed that MDMX depletion triggered two distinct phases of p53 accumulation in single cells: an initial postmitotic pulse, followed by low-amplitude oscillations. The response to DNA damage was sharply different in these two phases; in the first phase, MDMX depletion was synergistic with DNA damage in causing cell death, whereas in the second phase, depletion of MDMX inhibited cell death. Thus a quantitative understanding of signal dynamics and cellular states is important for designing an optimal schedule of dual-drug administration.

Efficient killing of cancer cells often requires combinations of drugs. A major rationale underlying such approaches is that the administration of two drugs that work through different mechanisms should reduce overall drug resistance and increase tumor eradication. A related combinatorial therapy approach is to apply anticancer drugs sequentially (*1*, *2*). In this case, treatment with the first drug may modify ("rewire") the behavior of specific signaling pathways, resulting in a population of cancer cells that is more sensitive to the second treatment (*1*). Improving the efficacy of time-staggered combinatorial treatments and designing optimal schedules require a detailed quantitative understanding of how each treatment dynamically alters cellular states in individual cells.

We investigated how weakening the effects of the oncogene product MDMX (also known as MDM4 and HDMX) alters the state of individual cancer cells and how these changes affect their sensitivity to DNA damage over time. *MDMX* is amplified in many tumors, including melanoma, osteosarcoma, and breast and colorectal cancers. Overexpression of MDMX inhibits the tumor-suppressive effects of the protein p53 and leads to resistance to anticancer drugs (*3*, *4*). Antagonization of MDMX may therefore enhance the efficacy of DNA-damaging drugs (*3*, *5*). Effects of MDMX on the abundance of p53 have been measured at one or a few time points in populations of cells (*6*–*8*). However, it remains unclear how MDMX regulates the dynamics of p53, which is important in determining a cell's response to DNA damage (*9*). We examined the effects of MDMX inhibition on p53 dynamics and the susceptibility to DNA damage in individual cells.

Multiple MDMX inhibitors are under development (*10*, *11*), but the specificity and efficacy of candidate inhibitors are still under study. We therefore used small interfering RNA (siRNA) to inhibit MDMX. Immunoblots showed that amounts of MDMX were effectively reduced in cells treated with siRNA (Fig. 1, A and B), leading to a transient increase in the amount of p53, followed by a decrease below its initial basal levels (Fig. 1, A and B). Population averages were previously shown to mask p53 dynamics in single cells (*12*, *13*). We therefore quantified p53 dynamics in individual cells after MDMX depletion in a p53 reporter cell line (Fig. 1, C and D, and experimental procedures). Cells transfected with scrambled siRNA showed a pulse of p53 accumulation after mitosis, as previously reported for actively dividing cells [Fig. 1E and (*13*)]. Cells transfected with MDMX siRNA also showed this postmitotic pulse (Fig. 1F) with a similar length but larger amplitude (Fig. 1, I and J). Most cells showed the p53 postmitotic pulse within the first 25 hours, which is consistent with their cell cycle length (fig. S1A). In our experimental conditions, division time was not synchronized between individual cells (Fig. 1H); therefore, each cell showed the postmitotic pulse at a different time, giving the appearance of a prolonged increase in p53 immunoblots representing the population average (Fig. 1B). After the initial postmitotic p53 pulses, cells depleted of MDMX showed oscillations in p53 abundance that persisted during the course of the experiment (60 hours; Fig. 1, F and H). The amplitude of these oscillations was lower than that of the spontaneous p53 pulses in dividing cells expressing MDMX (Fig. 1J), leading to lower overall amounts of p53 in the cell population (Fig. 1, A and B). The response to MDMX depletion therefore has two phases in individual cells: During the first phase, cells show a high-amplitude p53 pulse, and during the second phase, cells experience low-amplitude p53 oscillations. Because these dynamics are triggered after division, each cell enters the first and second phase of the response at a different time (Fig. 1H). Similar biphasic p53 dynamics were also found in the noncancerous primary line RPE1 (fig. S2), suggesting that these MDMX-mediated dynamics are not limited to cancer cells. The p53 postmitotic pulse appeared in RPE1 within 20 hours, which is consistent with their shorter cell cycle length (fig. S1B).

The p53 oscillations during the second phase of the response resemble the p53 oscillations that occur in response to DNA double-strand breaks (DSBs) (*14*). Although the p53 oscillations resulting from MDMX depletion had lower amplitude than those induced by DSBs (MCF7: Fig. 1, G and L; RPE1: fig. S2, C and H), both shared a remarkably similar period (Fig. 1K and fig. S2G). We therefore suggest that MDMX-mediated p53 oscillations result from the core negative feedback loop between p53 and Mdm2, as was previously suggested after DNA damage [Fig. 1M and (*14*)]. Mdm2 suppression led to completely different non-oscillatory p53 dynamics (fig. S3), strengthening the model that Mdm2 is required for p53 oscillations after DNA damage and MDMX suppression. The similarity in oscillation period led us to ask whether the p53 oscillations after MDMX knockdown result from activation of the DNA-damage signaling pathway. We measured the abundance of gamma-H2AX, an indicator of DSBs, in cells transfected with scrambled or MDMX siRNA and found that MDMX depletion did not increase the gamma-H2AX signal (Fig. 1, N and O). There was also no change in the phosphorylation states of the two major DNA-damage effector kinases, Chk1 and Chk2, after MDMX knockdown (Fig. 1P), suggesting that p53 oscillations after MDMX depletion do not result from DNA-damage signaling.

We used a cell line expressing a fluorescently tagged p53 and an inducible *MDMX* fused to mKate2 (a far-red fluorescent protein) to quantify p53 dynamics after reintroducing MDMX during the oscillatory phase (Fig. 2, A to D). The addition of doxycycline led to increased amounts of mKate2-MDMX (Fig. 2, B and D), which suppressed p53 oscillations (Fig. 2E), suggesting that MDMX prevents p53 oscillations in nonstressed conditions. Amounts of MDMX decreased in response to DSBs [fig. S4A and (*15*)], raising the possibility that a decreased abundance of MDMX is required for p53 oscillations. To examine the effect of MDMX on p53 oscillations that result from DSBs, we triggered DSBs with the radiomimetic drug neocarzinostatin (NCS) and measured p53 dynamics before and after expression of mKate2-MDMX. NCS led to p53 oscillations (*16*), and accumulation of mKate2-MDMX again diminished p53 oscillations (Fig. 2F). Incubation of cells with doxycycline before treatment with NCS dampened the NCS-induced p53 oscillations (Fig. 2, G and H, and fig. S4B). Thus, MDMX suppresses p53 oscillations both in basal conditions and in cells with DSBs. MDMX degradation after DSBs is required to allow p53 oscillations.

To determine the effects of the two-phase p53 response after MDMX depletion on the transcription of p53 target genes, we quantified the amounts of transcripts of well-characterized p53 target genes in different cellular programs.

[1]Department of Systems Biology, Harvard Medical School, Boston, MA, USA. [2]Developmental and Molecular Pathways, Novartis Institutes for Biomedical Research, Cambridge, MA, USA.

Downloaded from on March 10, 2016

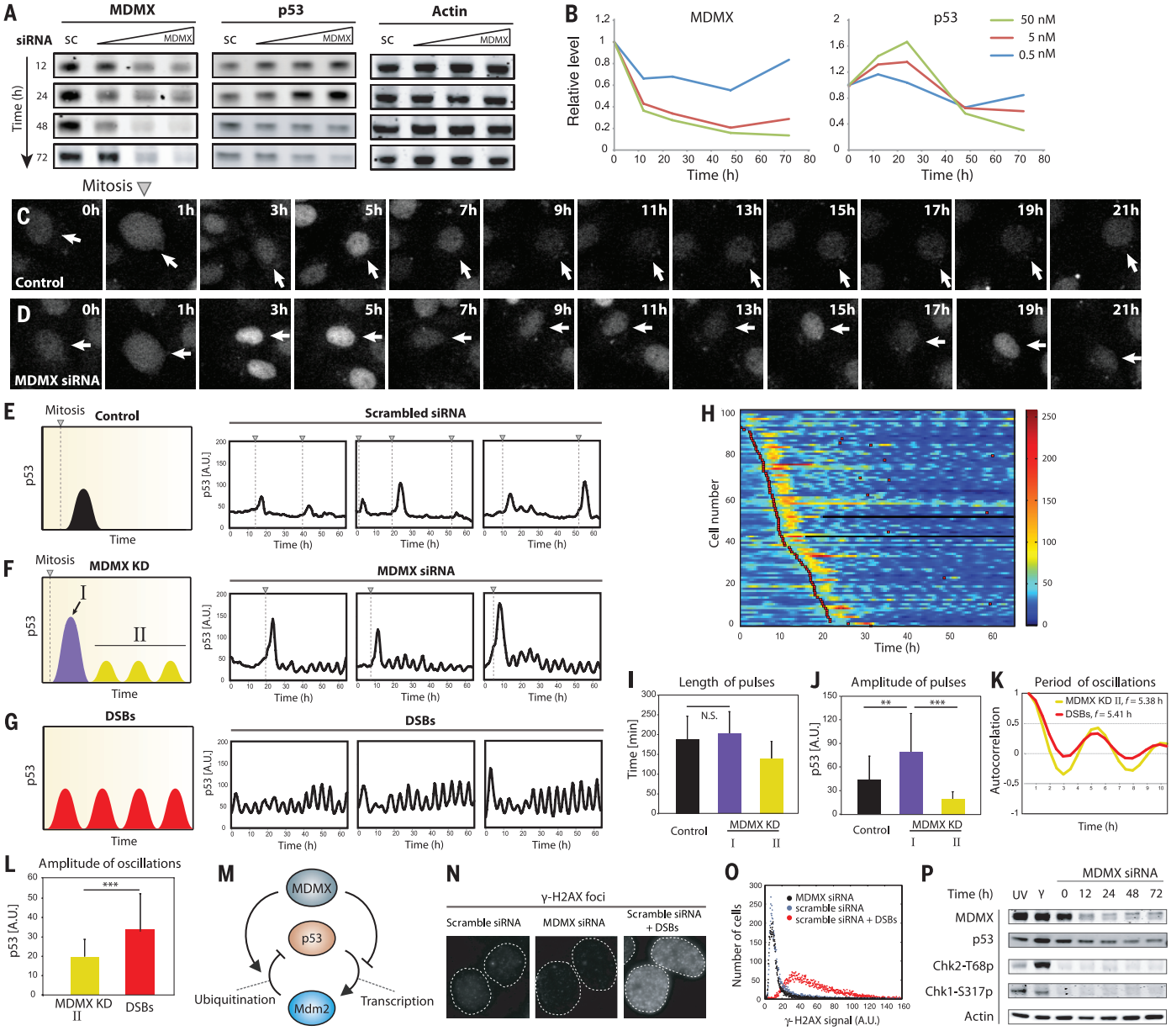

Fig. 1. Single cells show two phases of p53 dynamics after MDMX depletion. (**A**) Abundance of MDMX, p53, and actin in Western blots of extracts from MCF7 cells transfected with either scrambled siRNA (sc, 5 nM) or siRNA targeting MDMX's mRNA (0.5, 5, and 50 nM) for the indicated times. (**B**) Quantification of MDMX and p53 abundance from (A). The amount of siRNA used is shown in the upper right corner. (**C** and **D**) Time-lapse microscopy images of cells expressing p53-mCerulean after transfection with scrambled (C) or MDMX (D) siRNAs. (**E**, **F**, and **G**) Abundance of p53 in individual cells tracked as fluorescence of p53-mCerulean. Triangles with dashed lines indicate cell division. and p53-mCerulean dynamics in MDMX knockdown cells are classified into phase I (first postmitotic pulse) and phase II (low-amplitude oscillations). DSBs were introduced by NCS. Illustrations on the left summarize p53 dynamics. (**H**) Heat map of p53-mCerulean abundance in cells treated with MDMX siRNA. p53 traces of individual cells are arranged from top to bottom by the occurrence of first mitosis. Red squares indicate the time of cell division. (**I**) The mean relative widths measured by full width at half maximum [$n > 90$ p53 pulses; error bars indicate SD; the two p53 postmitotic pulses are not statistically significantly different ($P = 0.14$; P values obtained by Student's two-sample unequal variance t test, with a two-tailed distribution)]. (**J**) Amplitude of p53 pulses in control cells and MDMX KD cells [$n > 90$ p53 pulses; error bars indicate SD; $^{**}P < 10^{-8}$, $^{***}P < 10^{-19}$ (P values obtained by Student's two-sample unequal variance t test, with a two-tailed distribution)]. (**K**) Periods of p53 oscillations in MDMX knockdown (phase II) and NCS-treated cells measured by autocorrelation. (**L**) The mean relative amplitudes of p53 oscillations in MDMX knockdown (phase II) and NCS-treated cells are shown ($n > 90$ p53 pulses; error bars indicate SD, $^{***}P < 10^{-19}$ (P values obtained by Student's two-sample unequal variance t test, with a two-tailed distribution)]. A.U., arbitrary units. (**M**) A schematic diagram of MDMX regulating p53. p53 oscillations were previously shown to result from the p53-Mdm2 negative feedback loop. MDMX acts to inhibit the p53-Mdm2 oscillator through two arms: One arm inhibits p53 transcriptional activity (right arm) and the second arm degrades p53 through catalyzing Mdm2-mediated p53 ubiquitination (left arm). (**N** and **O**) The γ-H2AX signal is shown (N) and quantified (O) in MCF7 cells transfected with either scrambled or MDMX siRNAs, followed by NCS treatment. (**P**) The abundance of indicated proteins in MCF7 cells either ultraviolet- or γ-irradiated or transfected with MDMX siRNA for the indicated times, analyzed by Western blot.

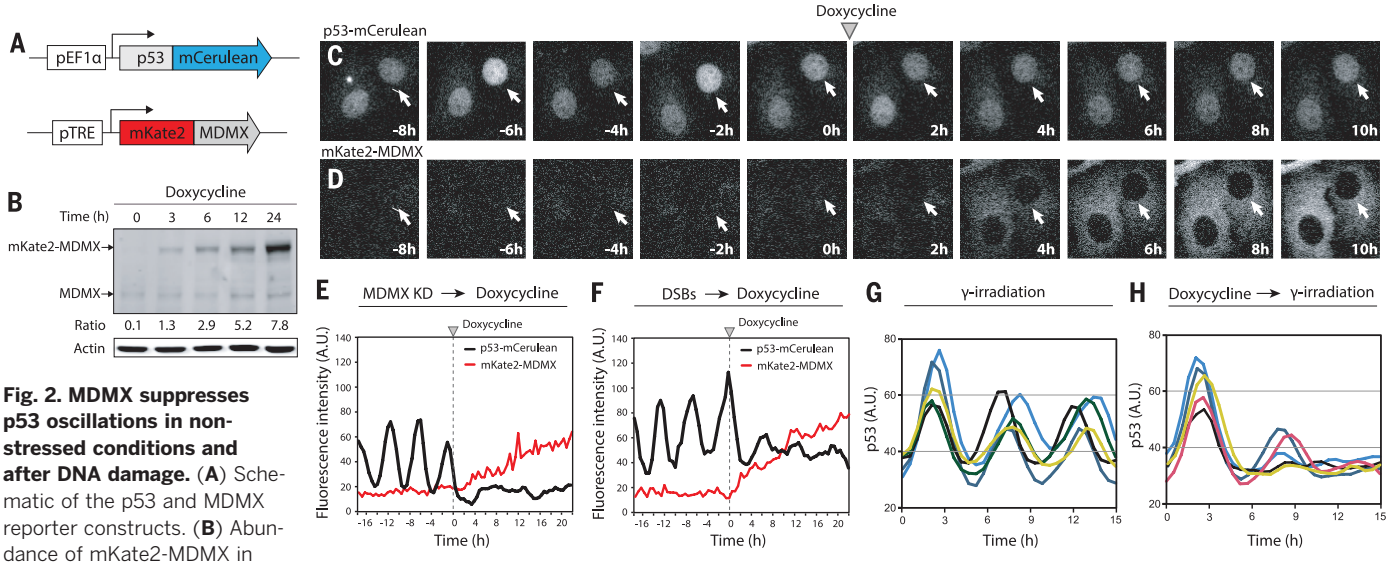

Fig. 2. MDMX suppresses p53 oscillations in non-stressed conditions and after DNA damage. (**A**) Schematic of the p53 and MDMX reporter constructs. (**B**) Abundance of mKate2-MDMX in p53-MDMX reporter cells treated with doxycycline, analyzed by Western blot. pEF1α, EF1 alpha promoter; pTRE, Tet response element promoter. (**C** and **D**) Time-lapse microscopy images of p53-mCerulean (C) and mKate2-MDMX (D) after MDMX siRNAs (30 hours), followed by doxycycline. (**E** and **F**) Trajectories of p53-mCerulean and mKate2-MDMX levels are shown for cells with either MDMX knockdown (E) or NCS (F) treatment 30 hours before doxycycline addition. (**G** and **H**) Trajectories of p53-mCerulean levels are shown for cells treated with NCS alone (G) or with prior treatment of doxycycline (H).

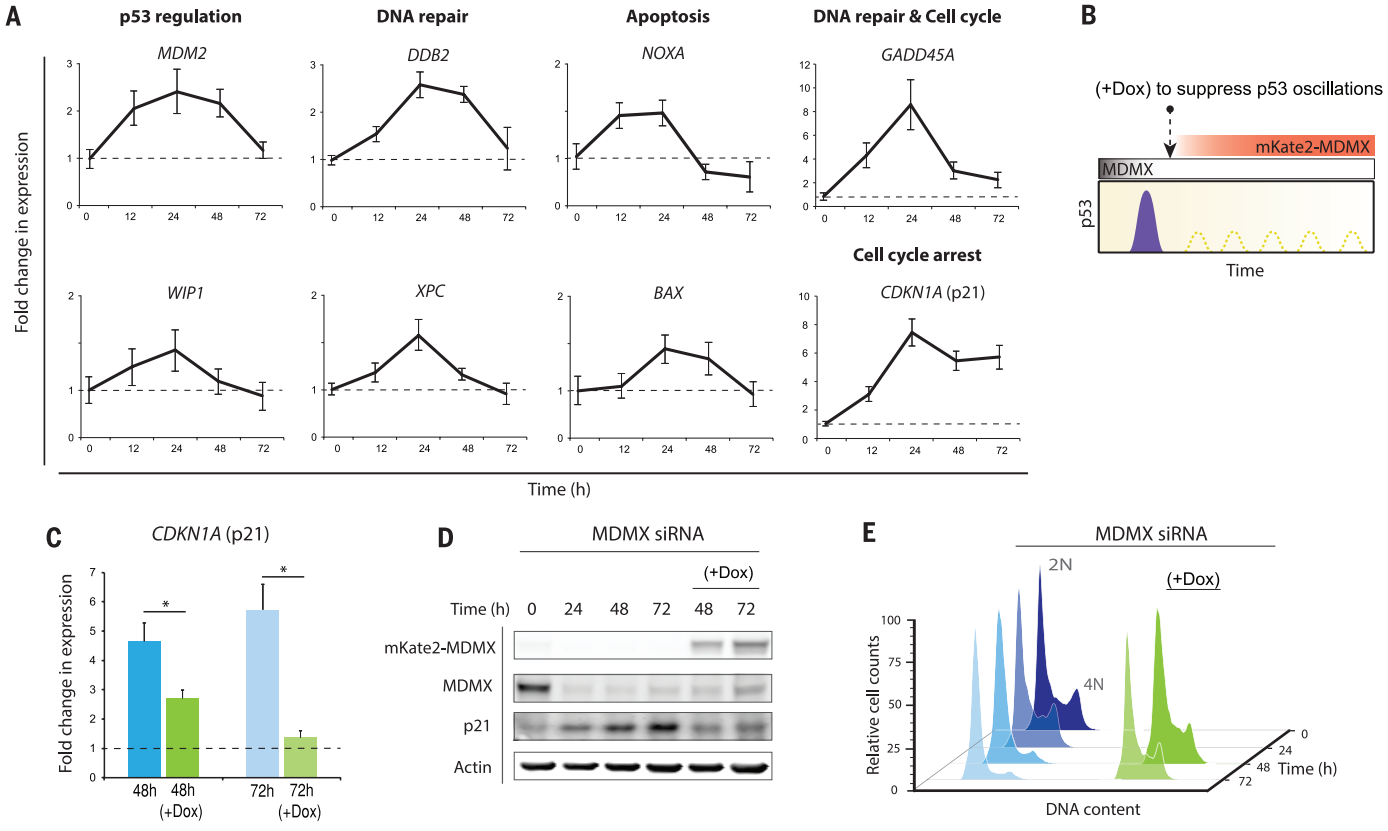

Fig. 3. Repression of p53 oscillations during phase II to maintaine p21 accumulation and cell cycle arrest. (**A**) Expression of p53 target genes measured by quantitative polymerase chain reaction after MDMX knockdown. Genes are grouped according to their function (n = 3 biological repeats; error bars represent SD). (**B**) Schematic of suppressing p53 oscillations by inducing mKate2-MDMX using doxycycline. Doxycycline was added 24 hours after MDMX siRNA transfection. (C) Abundance of transcripts of *CDKN1A* (p21) 2 and 3 days after MDMX siRNA transfection alone or followed by doxycycline addition [n = 3 biological repeats; error bars indicate SD, $^{*}P < 10^{-2}$ (P values obtained by Student's two-sample unequal variance t test, with a two-tailed distribution)]. (**D**) Abundance of p21 protein in cells depleted of MDMX alone or with doxycycline addition. (**E**) Cell cycle profile after MDMX depletion alone or with doxycycline addition.

Most p53 targets showed a mild transient increase in transcription after MDMX depletion in the first 24 to 48 hours, and returned to their basal levels by 72 hours (Fig. 3A). These genes may be sensitive to the first-phase postmitotic pulse of p53 after MDMX depletion, but less sensitive to the second oscillatory phase of p53. The behavior of *CDKN1A*, a gene encoding p21 (cyclin-dependent kinase inhibitor 1), was distinct. Amounts of *CDKN1A* transcript showed an eightfold increase at 24 hours after MDMX depletion and remained increased (more than fivefold) at 48 hours and 72 hours after depletion of MDMX (Fig. 3A, bottom right panel). Amounts of p21 protein showed a continuous increase during the entire 72-hour period after MDMX depletion, which was p53-dependent (fig. S5). MDMX depletion also led to cell cycle arrest, as indicated by the increase in the percentage of cells in the G_1 phase of the cell cycle and a decrease in the percentage of cells in S phase (Fig. 3E, left panel). Suppression of p53 low-amplitude oscillations by a delayed expression of mKate2-*MDMX* (Figs. 2E and 3B) lowered amounts of p21 mRNA and protein (Fig. 3, C and D) and rescued cells from arrest (Fig. 3E, right panel). This indicates that the p53 oscillations after MDMX knockdown are responsible for maintaining p21 and cell cycle arrest.

The complexity of the p53 response to MDMX depletion prompted us to investigate how cells respond to DNA damage at different times after depletion of MDMX. We applied DNA damage either during the first phase (postmitotic pulse) or second phase (oscillations) of the p53 response and measured p53 dynamics and cell fate (Fig. 4A). When DNA damage was applied during the first phase (12 hours after transfection with MDMX siRNA), MDMX depletion sensitized cells to death, leading to 95% cell death as compared with 66% resulting from DNA damage alone (Fig. 4B). This increase in cell death may result from increased accumulation of p53 (Fig. 4, D, F and G, and fig. S6A) and increased transcription of apoptotic genes (Fig. 3A) during this phase. In sharp contrast, when DNA damage was applied during the second, oscillatory, phase of p53 dynamics (48 hours after MDMX

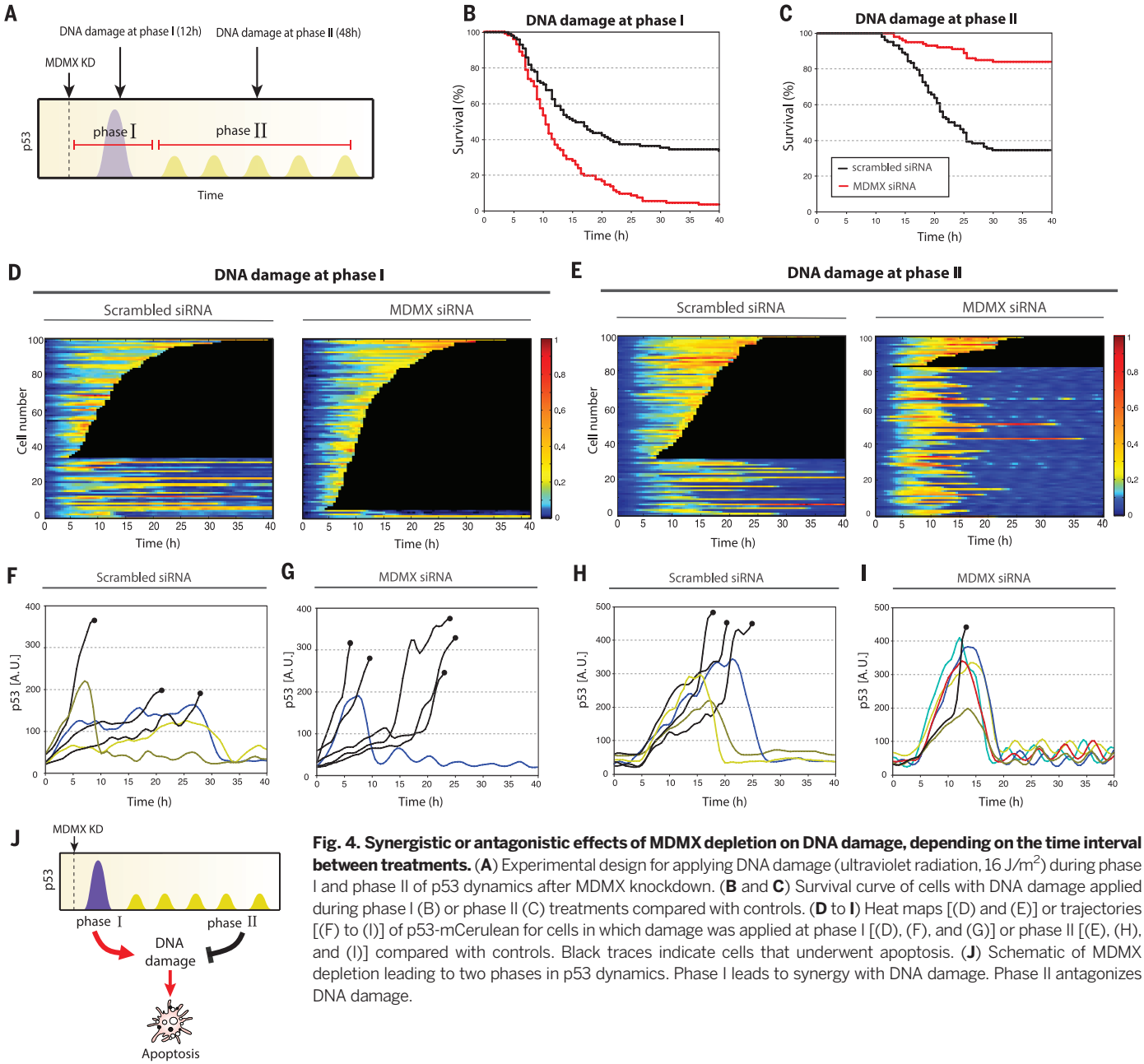

Fig. 4. Synergistic or antagonistic effects of MDMX depletion on DNA damage, depending on the time interval between treatments. (**A**) Experimental design for applying DNA damage (ultraviolet radiation, 16 J/m^2) during phase I and phase II of p53 dynamics after MDMX knockdown. (**B** and **C**) Survival curve of cells with DNA damage applied during phase I (B) or phase II (C) treatments compared with controls. (**D** to **I**) Heat maps [(D) and (E)] or trajectories [(F) to (I)] of p53-mCerulean for cells in which damage was applied at phase I [(D), (F), and (G)] or phase II [(E), (H), and (I)] compared with controls. Black traces indicate cells that underwent apoptosis. (**J**) Schematic of MDMX depletion leading to two phases in p53 dynamics. Phase I leads to synergy with DNA damage. Phase II antagonizes DNA damage.

was depleted) cell death was reduced (67 to 16%) (Fig. 4C). Similar schedule-dependent interactions were observed between MDMX suppression and four different chemotherapy agents (4NQO, doxorubicin, camptothecin, and actinomycin D) in MCF7 and the primary line RPE1 (fig. S7).

MDMX-depleted cells showed a similar amplitude of p53 accumulation to that in mock-treated cells when DNA damage was applied during phase II (Fig. 4, E, H, and I, and fig. S6B), indicating that the reduction in cell death is not caused by lower amounts of p53. Instead, we suggest that transcriptional regulation of genes by MDMX-induced p53 oscillations could make cells less susceptible to DNA damage. Indeed, p53 oscillations during the second phase after MDMX depletion induced accumulation of p21 and cell cycle arrest (Fig. 3, D and E), which provides protection from cell death (*17*). In addition, MDMX suppression led to a stronger activation of the pro-survival signal phospho-Akt after DNA damage and to a weaker accumulation of the pro-apoptotic protein PUMA as compared with those in MDMX-expressing cells (fig. S8). This suggests that, in addition to induction of p21 and cell cycle arrest by p53 oscillations, MDMX suppression shifts cells toward a pro-survival cellular state (fig. S8), which may also contribute to its protection from DNA damage–induced cell death.

The complexity of cellular signaling pathways makes it challenging to predict the response to a single perturbation, and even more challenging to predict responses to combined perturbations. In the context of combined therapeutic treatments, the schedule of administration can be crucial [Fig. 4J and (*1*, *18*, *19*)]. The results presented here unexpectedly show that the combination of DNA damage with MDMX inhibitors for cancer therapy has the potential either to improve cancer therapy or to blunt its effects. Our results have implications for the design of MDMX-combination drug regimes and perhaps for the design of combination therapies in general. Further consideration of treatment schemes in the context of other physiological rhythms, such as the cell cycle and circadian clock (*20*–*22*), can be critical for more precise and effective therapies. Such a detailed quantitative description of system behavior at the single-cell level can reveal hidden regulatory principles and the nature of cellular state changes in response to perturbations.

REFERENCES AND NOTES

1. M. J. Lee *et al.*, *Cell* **149**, 780–794 (2012).
2. S. W. Morton *et al.*, *Sci. Signal.* **7**, ra44 (2014).
3. M. Wade, Y.-C. Li, G. M. Wahl, *Nat. Rev. Cancer* **13**, 83–96 (2013).
4. A. Gembarska *et al.*, *Nat. Med.* **18**, 1239–1247 (2012).
5. C. J. Brown, S. Lain, C. S. Verma, A. R. Fersht, D. P. Lane, *Nat. Rev. Cancer* **9**, 862–873 (2009).
6. J. A. Barboza, T. Iwakuma, T. Terzian, A. K. El-Naggar, G. Lozano, *Mol. Cancer Res.* **6**, 947–954 (2008).
7. F. Mancini *et al.*, *Int. J. Biochem. Cell Biol.* **42**, 1080–1083 (2010).
8. X. Wang, J. Wang, X. Jiang, *J. Biol. Chem.* **286**, 23725–23734 (2011).
9. J. E. Purvis *et al.*, *Science* **336**, 1440–1444 (2012).
10. B. Graves *et al.*, *Proc. Natl. Acad. Sci. U.S.A.* **109**, 11788–11793 (2012).
11. D. Reed *et al.*, *J. Biol. Chem.* **285**, 10786–10796 (2010).
12. G. Lahav *et al.*, *Nat. Genet.* **36**, 147–150 (2004).
13. A. Loewer, E. Batchelor, G. Gaglia, G. Lahav, *Cell* **142**, 89–100 (2010).
14. E. Batchelor, C. S. Mock, I. Bhan, A. Loewer, G. Lahav, *Mol. Cell* **30**, 277–289 (2008).
15. H. Kawai *et al.*, *J. Biol. Chem.* **278**, 45946–45953 (2003).
16. G. Lahav, *Adv. Exp. Med. Biol.* **641**, 28–38 (2008).
17. O. D. K. Maddocks *et al.*, *Nature* **493**, 542–546 (2013).
18. M. Behar, D. Barken, S. L. Werner, A. Hoffmann, *Cell* **155**, 448–461 (2013).
19. P. Lito, N. Rosen, D. B. Solit, *Nat. Med.* **19**, 1401–1409 (2013).
20. J. Bieler *et al.*, *Mol. Syst. Biol.* **10**, 739 (2014).
21. C. Feillet *et al.*, *Proc. Natl. Acad. Sci. U.S.A.* **111**, 9828–9833 (2014).
22. A. Sancar *et al.*, *FEBS Lett.* **584**, 2618–2625 (2010).

ACKNOWLEDGMENTS

We thank A. G. Jochemsen, J. C. Marine, X. Wang, and J. Chen for sharing their experience and thoughts on MDMX regulation; R. Ward, S. Gruver, G. Gaglia, J. Porter, L. Bruett, and members of the Lahav laboratory for comments, support, and discussion; and the Nikon Imaging Center at Harvard Medical School for support with live cell imaging. This research was supported by National Institutes of Health grant GM083303 to G.L., grant F32GM105205 to S.C., and funding from the Novartis Institutes for Biomedical Research.

SUPPLEMENTARY MATERIALS

www.sciencemag.org/content/351/6278/1204/suppl/DC1
Materials and Methods
Figs. S1 to S8
References (*23*–*25*)

12 May 2015; accepted 28 January 2016
10.1126/science.aac5610

CANCER THERAPY

Disordered methionine metabolism in MTAP/CDKN2A-deleted cancers leads to dependence on PRMT5

Konstantinos J. Mavrakis,[1]* E. Robert McDonald III,[1]* Michael R. Schlabach,[1]* Eric Billy,[2]* Gregory R. Hoffman,[1]* Antoine deWeck,[2] David A. Ruddy,[1] Kavitha Venkatesan,[1] Jianjun Yu,[3] Gregg McAllister,[1] Mark Stump,[1] Rosalie deBeaumont,[1] Samuel Ho,[1] Yingzi Yue,[1] Yue Liu,[1] Yan Yan-Neale,[1] Guizhi Yang,[1] Fallon Lin,[1] Hong Yin,[1] Hui Gao,[1] D. Randal Kipp,[1] Songping Zhao,[1] Joshua T. McNamara,[1] Elizabeth R. Sprague,[1] Bing Zheng,[3] Ying Lin,[4] Young Shin Cho,[1] Justin Gu,[4] Kenneth Crawford,[3] David Ciccone,[1] Alberto C. Vitari,[3] Albert Lai,[3] Vladimir Capka,[1] Kristen Hurov,[1] Jeffery A. Porter,[1] John Tallarico,[1] Craig Mickanin,[1] Emma Lees,[1] Raymond Pagliarini,[1] Nicholas Keen,[1] Tobias Schmelzle,[2]* Francesco Hofmann,[2]* Frank Stegmeier,[1]*† William R. Sellers[1]*†

5-Methylthioadenosine phosphorylase (MTAP) is a key enzyme in the methionine salvage pathway. The *MTAP* gene is frequently deleted in human cancers because of its chromosomal proximity to the tumor suppressor gene *CDKN2A*. By interrogating data from a large-scale short hairpin RNA–mediated screen across 390 cancer cell line models, we found that the viability of MTAP-deficient cancer cells is impaired by depletion of the protein arginine methyltransferase PRMT5. MTAP-deleted cells accumulate the metabolite methylthioadenosine (MTA), which we found to inhibit PRMT5 methyltransferase activity. Deletion of MTAP in MTAP-proficient cells rendered them sensitive to PRMT5 depletion. Conversely, reconstitution of MTAP in an MTAP-deficient cell line rescued PRMT5 dependence. Thus, MTA accumulation in MTAP–deleted cancers creates a hypomorphic PRMT5 state that is selectively sensitized toward further PRMT5 inhibition. Inhibitors of PRMT5 that leverage this dysregulated metabolic state merit further investigation as a potential therapy for MTAP/CDKN2A-deleted tumors.

5-Methylthioadenosine phosphorylase (MTAP) participates in the methionine salvage pathway that metabolizes methylthioadenosine (MTA) to adenine and methionine. Because of its proximity to the tumor suppressor gene *CDKN2A* on human chromosome 9p21, the *MTAP* gene is deleted at high frequency in many human tumors, including 53% of glioblastomas, 26% of pancreatic cancers, and other tumor types (Fig. 1A). Given the critical role of MTAP in methionine metabolism, we hypothesized that the metabolic rewiring in response to MTAP loss may create new vulnerabilities.

[1]Novartis Institutes for Biomedical Research, Cambridge, MA 02139, USA. [2]Novartis Institutes for Biomedical Research, Basel CH-4002, Switzerland. [3]Novartis Institutes for Biomedical Research, Emeryville, CA 94608, USA. [4]China Novartis Institutes for Biomedical Research, Shanghai 201203, China.
*These authors contributed equally to this work. **†Corresponding authors. E-mail: william.sellers@novartis.com (W.R.S.); fstegmeier@ksqtx.com (F.S.)**

Downloaded from on March 10, 2016

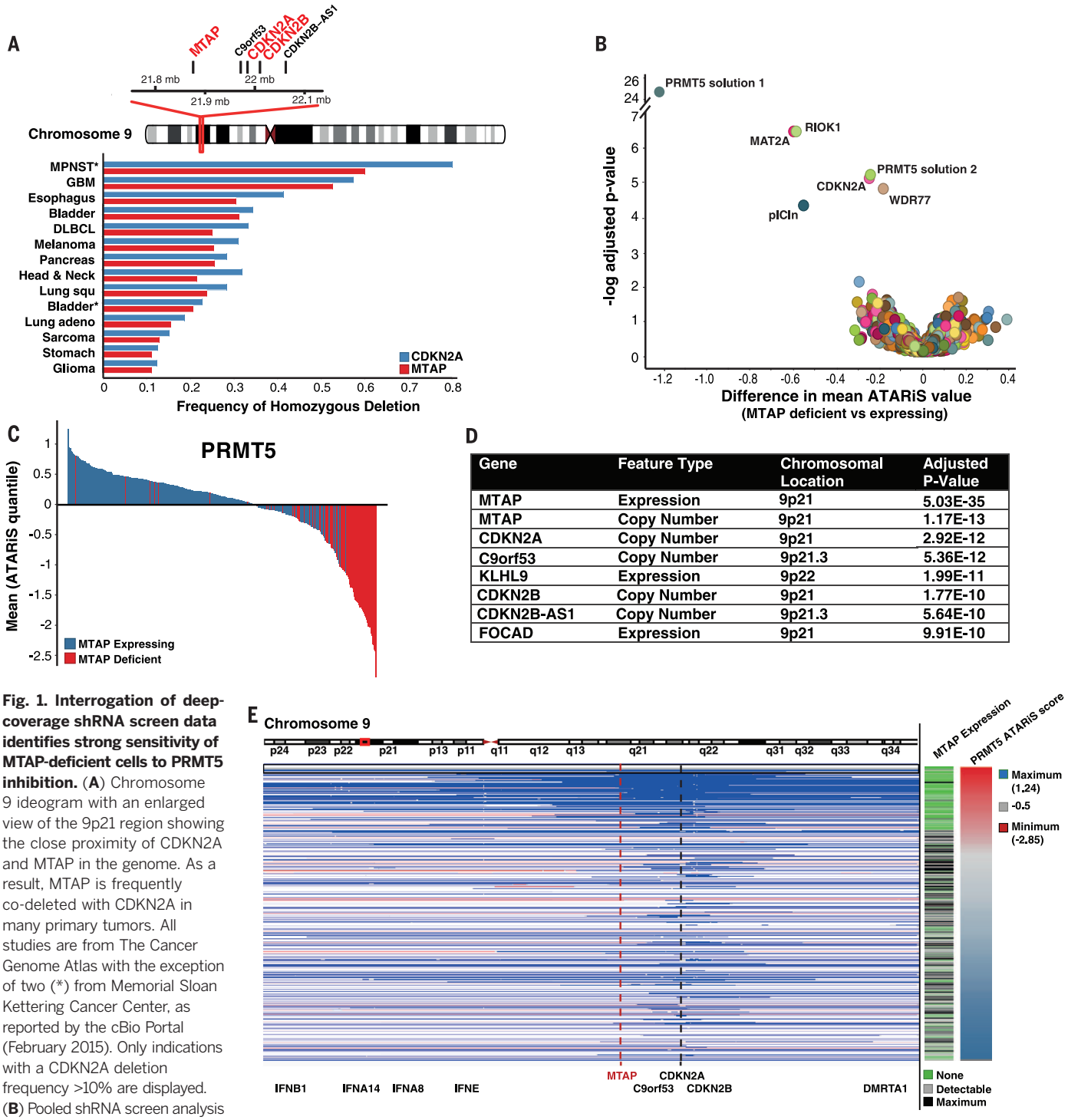

Gene	Feature Type	Chromosomal Location	Adjusted P-Value
MTAP	Expression	9p21	5.03E-35
MTAP	Copy Number	9p21	1.17E-13
CDKN2A	Copy Number	9p21	2.92E-12
C9orf53	Copy Number	9p21.3	5.36E-12
KLHL9	Expression	9p22	1.99E-11
CDKN2B	Copy Number	9p21	1.77E-10
CDKN2B-AS1	Copy Number	9p21.3	5.64E-10
FOCAD	Expression	9p21	9.91E-10

Fig. 1. Interrogation of deep-coverage shRNA screen data identifies strong sensitivity of MTAP-deficient cells to PRMT5 inhibition. (**A**) Chromosome 9 ideogram with an enlarged view of the 9p21 region showing the close proximity of CDKN2A and MTAP in the genome. As a result, MTAP is frequently co-deleted with CDKN2A in many primary tumors. All studies are from The Cancer Genome Atlas with the exception of two (*) from Memorial Sloan Kettering Cancer Center, as reported by the cBio Portal (February 2015). Only indications with a CDKN2A deletion frequency >10% are displayed. (**B**) Pooled shRNA screen analysis to identify genes that are selectively required for the proliferation of cells lacking MTAP expression. The mean difference in gene-level ATARiS scores between MTAP-deficient and MTAP-expressing cells is plotted on the *x* axis, and the degree of significance is on the *y* axis (*P* values calculated by Mann-Whitney-Wilcoxon rank sum test and adjusted by the false-discovery rate). Note that two independent gene-level solutions for PRMT5 (PRMT5 solution 1 and PRMT5 solution 2, as computed by ATARiS algorithm) scored as differentially lethal in MTAP-deficient versus MTAP-expressing setting. (**C**) Waterfall plot of PRMT5 dependence colored by MTAP RNA expression [MTAP deficient (<4.5) in red and MTAP expressing (>4.5) in blue]. (**D**) Unbiased correlation analysis of predictors of PRMT5 dependence across all CCLE features, including mutations, copy number, and expression—the most significantly associated features are listed; *P* values have been corrected for multiple-hypothesis testing, and, e.g., *P* = 5.03E-35 may be stated $P = 5.03 \times 10^{-35}$. (**E**) The Integrative Genomics Viewer chromosomal view of the 9p21.3 locus across the panel of screened cell lines, sorted according to their sensitivity to PRMT5 depletion. Cell line models that are most dependent on PRMT5 are at the top (minimum ATARiS score) and least-dependent cell lines at the bottom (maximum ATARiS score). MTAP expression (RNA) is co-plotted as a heat map. Broader deletions encompassing both MTAP and CDKN2A lead to a loss of MTAP expression (green) and PRMT5 sensitivity (red).

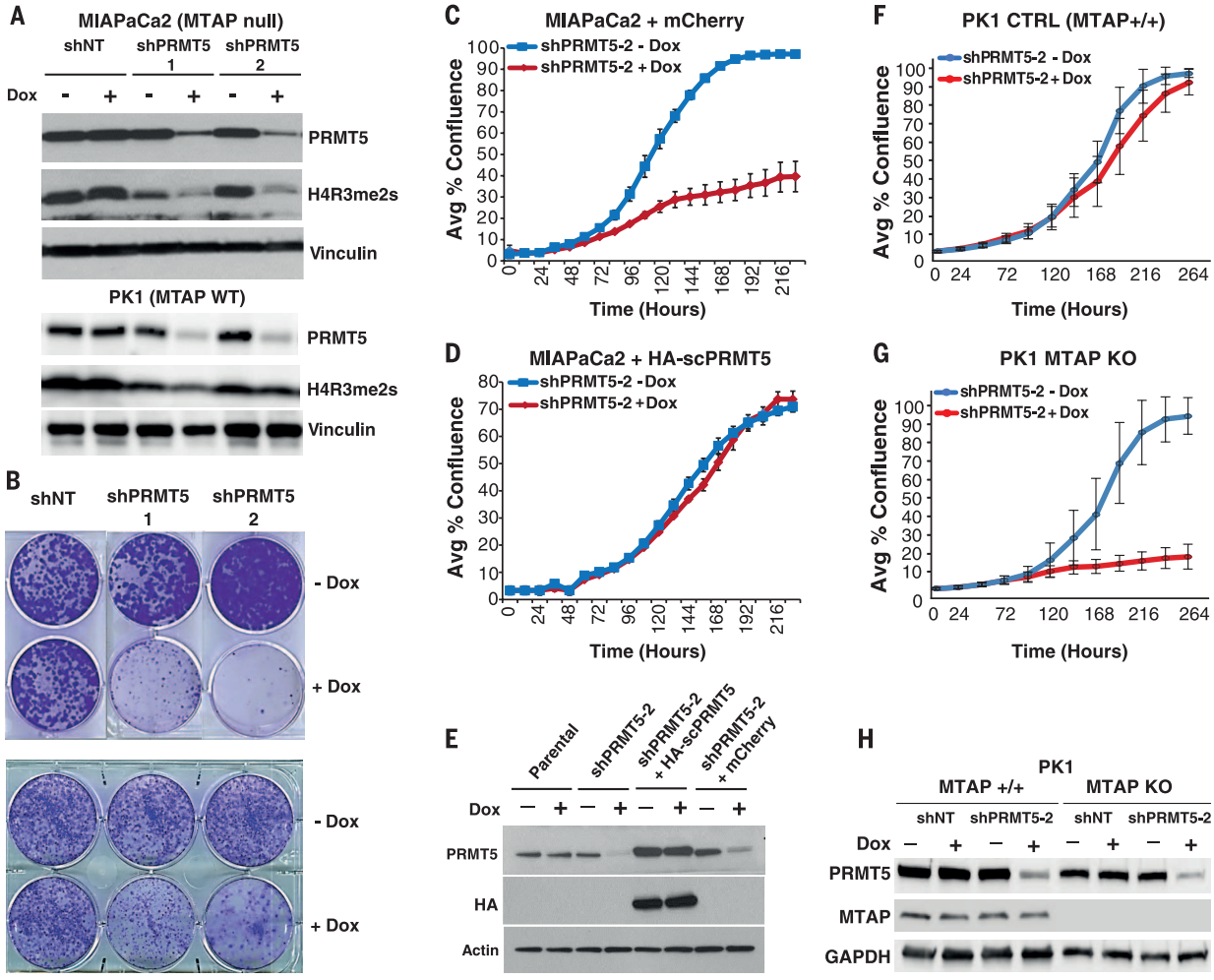

Fig. 2. Loss of MTAP renders cells sensitive to PRMT5 depletion. (**A**) Immunoblot to assess PRMT5 depletion of two independent doxycycline (Dox)–inducible hairpins (shPRMT5-1 and shPRMT5-2); shNT represents a nontargeting control shRNA. PRMT5 protein levels and H4R3me2s were assessed by immunoblotting in MTAP-null (MIAPaCa2) and MTAP-expressing (WT; PK1) pancreatic cell lines. Vinculin serves as a loading control. (**B**) Foci-formation assays of cell lines [corresponding to Western blots in (A)] transduced with the indicated inducible shRNAs. (**C**) shRNA-mediated depletion of PRMT5 substantially decreased the confluence (measured by IncuCyte) of MIAPaCa2 shPRMT5-2 cells stably expressing an empty control vector (mCherry); –Dox (blue) versus +Dox (red); $P < 0.001$. (**D**) Expression of a shRNA-resistant PRMT5 cDNA (HA-scPRMT5) fully rescued the antiproliferative effects of PRMT5 shRNA (NS, $P > 0.05$; shown are means and SD of triplicate experiments). (**E**) Immunoblot of lysates extracted from MIAPaCa2 (parental), MIAPaCa2 stably expressing shPRMT5-2, and stable MIAPaCa2 shPRMT5-2 cell lines expressing either HA-scPRMT5 or mCherry control that were probed for PRMT5, HA, and actin loading control. (**F** and **G**) In vitro proliferation assay of PK1 MTAP isogenic cell lines that have been engineered with a nontargeting control single guide RNA (sgRNA) (PK1 CTRL) (F) or with a sgRNA-targeting MTAP (PK1 MTAP KO) (G) and stably express a Dox-inducible PRMT5 shRNA (shPRMT5-2). The proliferation of cells with and without treatment with doxycycline (±Dox) over time (hours) was assessed by IncuCyte ($n = 24$ per treatment condition). (**H**) Immunoblot of cells used in (F) and (G) with and without shRNA induction and probed with the indicated antibodies.

We recently performed a pooled short hairpin RNA (shRNA) screen across 390 cancer cell lines of the Cancer Cell Line Encyclopedia (CCLE) with a library encompassing ~7500 genes at an approximate depth of 20 shRNAs per gene. To find genes that are selectively required for the viability of MTAP-deficient cells, we compared the gene-level shRNA values [using ATARiS, (*1*)] between cell line models lacking MTAP expression to those that express MTAP (fig. S1A, table S1, and table S2). This analysis identified several genes that selectively affected the growth of MTAP-deficient cells (Fig. 1B and fig. S2). One of the hits that scored as selectively lethal to MTAP-deficient cells was methionine adenosyltransferase 2A (MAT2A) ($P = 2.93 \times 10^{-7}$) (Fig. 1B), an enzyme within the *S*-adenosyl methionine (SAM) biosynthesis pathway (fig. S1C), which supported the notion that MTAP loss creates new metabolic vulnerabilities. The most differential hit was the protein arginine methyltransferase PRMT5 ($P = 1.64 \times 10^{-25}$). Several cofactors that are required for PRMT5 function, such as methylosome protein 50 (MEP50/WDR77) ($P = 1.21 \times 10^{-5}$), methylosome subunit pICIn ($P = 3.81 \times 10^{-5}$), and RIO kinase 1 (RIOK1) ($P = 2.93 \times 10^{-7}$) (*2*, *3*), also scored as differentially required for the growth of MTAP-deficient cancer cells (Fig. 1B). Similar results were obtained when the cell lines were partitioned by *MTAP* copy number rather than by expression values (fig. S1B).

To test the hypothesis that the PRMT5 complex is selectively required for the proliferation of MTAP-deficient cells, we performed a reciprocal unbiased correlation analysis of all CCLE features (including somatic mutations, copy number, and expression data) to identify which markers correlate best with PRMT5 dependence.

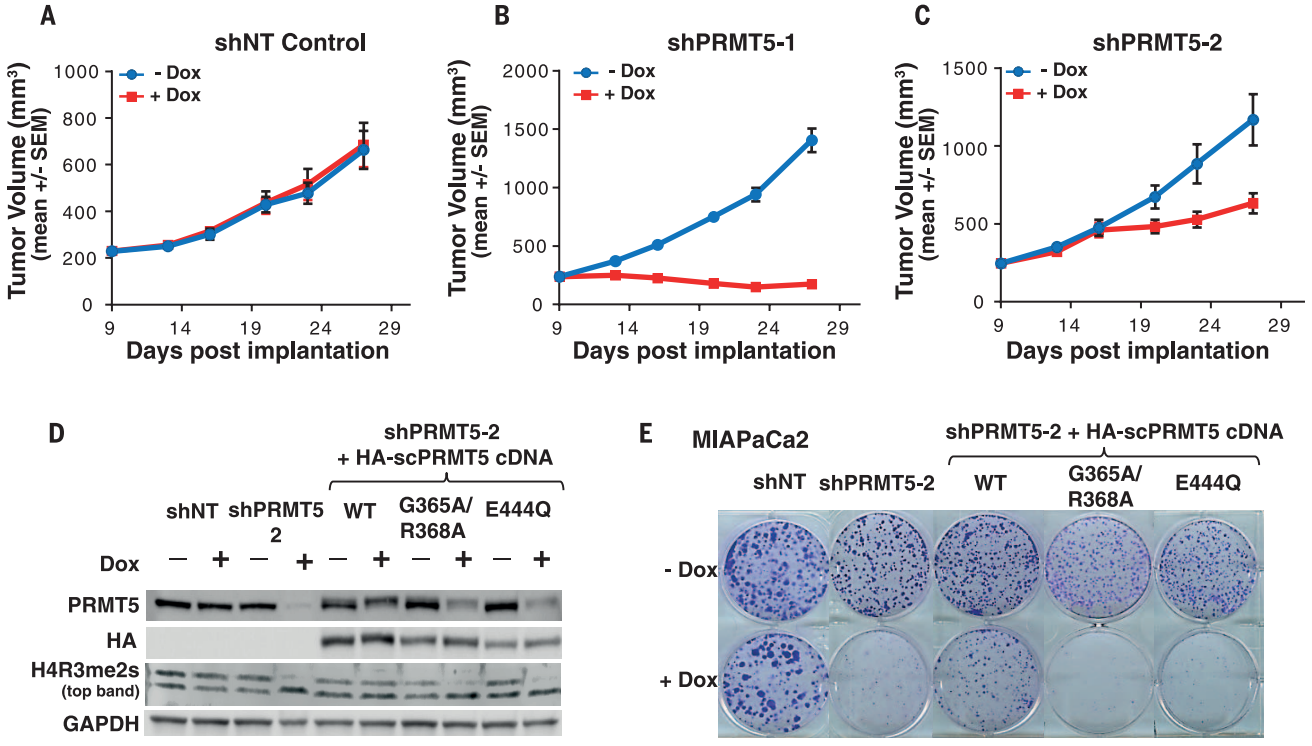

Fig. 3 PRMT5 is required for the growth of MTAP-deficient cells in vivo, and its catalytic HMT activity is essential. (**A** to **C**) MIAPaCa2 cells stably expressing shNT (A) or one of two inducible PRMT5 shRNAs—(B) shPRMT5-1 and (C) shPRMT5-2—were subcutaneously implanted, and tumor volume was monitored over a 28-day period. Dox treatment was initiated on day 9 postimplantation (±7 for each treatment arm; shown are mean tumor volumes and SEM). shNT control +Dox (red) versus −Dox (blue) (P = 0.943); shPRMT5-1 ± Dox (P < 0.001); shPRMT5-2 ± Dox (P < 0.001). (**D** and **E**) PRMT5 catalytic activity is required for growth in MTAP-deficient MIAPaCa2 cells. (D) Immunoblot of stable lines generated with shRNA-resistant mutants and probed with antibodies detecting PRMT5, HA, H4R3me2s, and glyceraldehyde-3-phosphate dehydrogenase (GAPDH) loading control. (E) Cells were transduced with the indicated shRNAs and shRNA-resistant cDNA vectors, and the relative growth was assessed by foci-formation assay. WT denotes wild-type PRMT5. G365A/R368A and E444Q are catalytically inactive PRMT5 mutants.

This analysis revealed deletion (low copy number) of *MTAP* ($P = 1.17 \times 10^{-13}$) and low expression ($P = 5.03 \times 10^{-35}$) of MTAP as the top features predictive of cancer cell dependence on PRMT5 (Fig. 1, C and D, and fig. S1D), followed by deletion of CDKN2A and CDKN2B. Although cells with concomitant loss of both CDKN2A and MTAP were strongly sensitive to PRMT5 depletion (knockdown), cells harboring focal deletions encompassing *CDKN2A*, but not *MTAP*, were generally insensitive to PRMT5 depletion (Fig. 1E). These findings indicate that loss of MTAP, rather than CDKN2A, confers sensitivity to PRMT5 inhibition. Thus, PRMT5 dependence is an example of collateral lethality (*4*) in which MTAP loss, as a consequence of CDKN2A deletion, creates a selective vulnerability to PRMT5 knockdown.

We next explored the mechanistic link between MTAP loss and PRMT5 knockdown. Knockdown of PRMT5 with two independent shRNAs (fig. S3, A and B, and fig. S4, A and B) markedly inhibited cell growth in two pancreatic MTAP-null cell line models, MIAPaCa2 and su86.86 (Fig. 2B and fig. S5). By contrast, PRMT5 depletion had only minor effects on viability in the MTAP-expressing pancreatic cell line PK1, despite displaying similar levels of PRMT5 protein knockdown (Fig. 2, A and B, and fig. S5, A to C). Expression of a shRNA-resistant version of PRMT5 fully rescued the colony formation and proliferation effects in MIAPaCa2, which indicated that growth inhibition is mediated by PRMT5 depletion and is unlikely to be a consequence of shRNA off-target effects (Fig. 2, C to E). To directly test the hypothesis that MTAP loss confers sensitivity to PRMT5 knockdown, we next evaluated the effect of PRMT5 depletion in an isogenic cell line setting. To this end, clustered regularly interspaced short palindromic repeats (CRISPR)–mediated deletion was used to inactivate MTAP in PK1 cells. In comparison with parental PK1 cells, PK1-MTAP$^{-/-}$ cells were strongly sensitized to shRNAs targeting PRMT5 (Fig. 2, F to H, and fig. S6, A to D). To examine if MTAP-deficient cells remained dependent on PRMT5 in vivo, we established tumor xenografts of the MTAP-deficient MIAPaCa2 cells expressing inducible shRNAs targeting PRMT5 or a nontargeting control and monitored tumor size over time. Induction of PRMT5 shRNAs led to reduced levels of H4R3me2s (symmetrical dimethylation on arginine 3 of histone 4), a known PRMT5 substrate (*5*–*7*), and markedly inhibited tumor growth, whereas the nontargeting control had no impact on tumor volume (Fig. 3, A to C, and fig. S7E). In keeping with the in vitro observations, this effect was specific to cells with MTAP loss, as PRMT5 knockdown did not affect the growth of the MTAP-expressing HARA xenograft model (fig. S7, A to D). Similar in vivo results were obtained with the PK1 MTAP isogenic cell lines, which confirmed that loss of MTAP is responsible for the difference in sensitivity (fig. S8). These experiments indicate that MTAP-deficient cells are sensitive to PRMT5 inhibition in vitro and in vivo.

We examined whether the methyltransferase activity of PRMT5 was required for the growth of MTAP-deficient cells. Expression of PRMT5 mutant proteins predicted to affect SAM binding (G365A/R368A; in which alanine replaces glycine 365 and arginine 368) or the methyltransferase activity (E444Q; in which glutamine replaced Glu^{444}) (*3*, *8*, *9*) failed to restore H4R3me2s levels in cells depleted for endogenous PRMT5, which confirmed their impaired catalytic activity (Fig. 3D). Despite being expressed at levels similar to those of wild-type PRMT5, the two catalytically dead PRMT5 mutants failed to rescue the growth of PRMT5-depleted cells (Fig. 3E), which

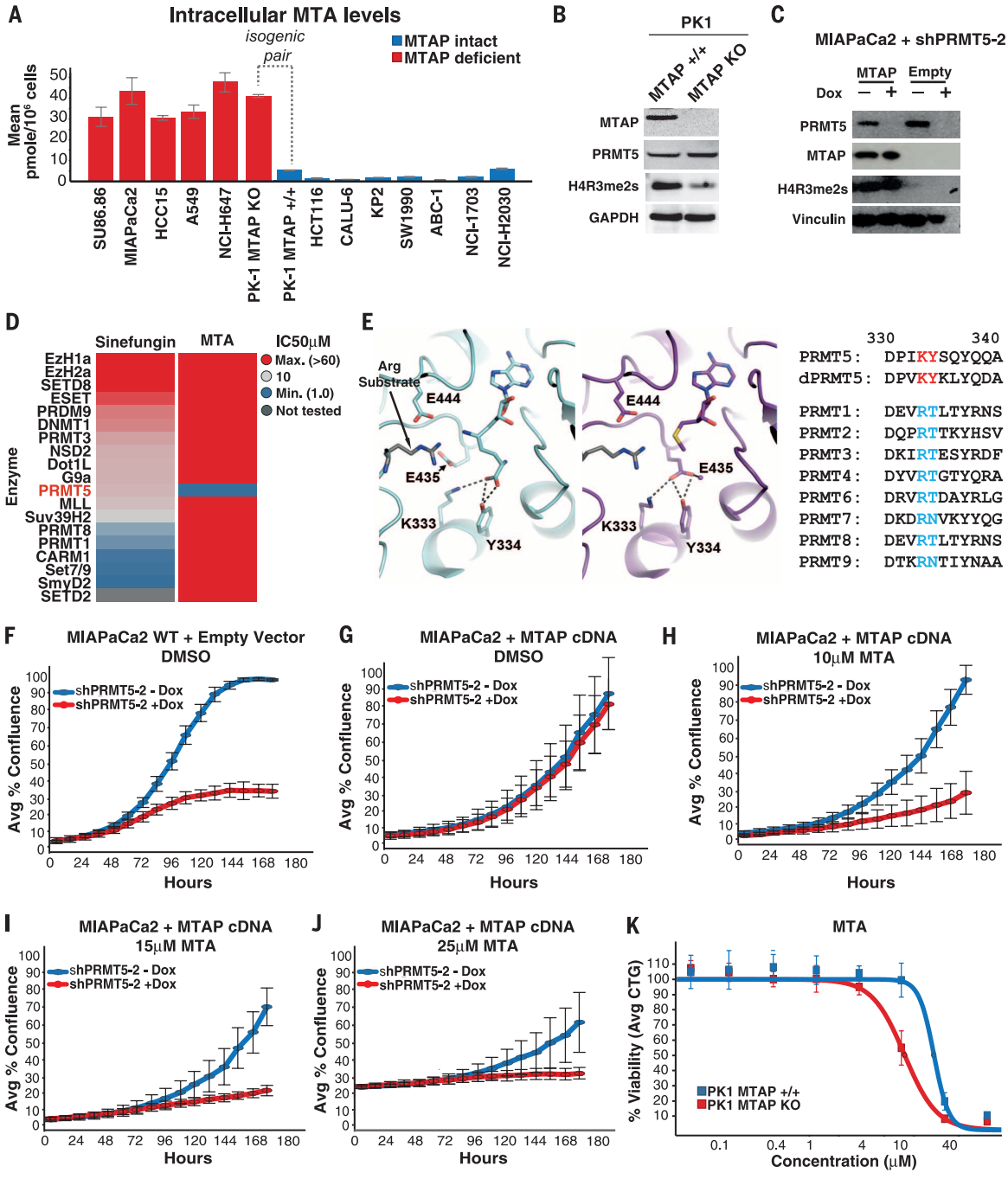

Fig. 4 Accumulation of MTA in MTAP-deficient cells selectively inhibits the catalytic activity of PRMT5. (**A**) Intracellular MTA levels were measured using liquid chromatography–mass spectrometry (LC-MS) across a panel of 14 cell lines representing six MTAP-deficient and eight MTAP-expressing cell lines, including the PK1 isogenic cell line pair (PK1 MTAP KO and PK1 MTAP$^{+/+}$, respectively); ± 3, shown are the means and SD. On average, MTAP-deficient cells have ~15 times as much intracellular MTA as MTAP-intact cells (mean MTA levels across all MTAP-deficient cells profiled = 37.9 pmol/10^6; mean MTA levels across all MTAP intact cells = 2.48 pmol/10^6 cells; $P = 6.18 \times 10^{-9}$). (**B**) Immunoblot of PK1 MTAP isogenic cell lines generated by CRISPR/Cas9 with a sgRNA nontargeting control (MTAP$^{+/+}$) or a sgRNA-targeting MTAP (MTAP KO) and probed with antibodies as indicated. (**C**) MIAPaCa2 cell lines stably expressing shPRMT5-2 and either MTAP or empty vector control (Empty) and blotted with antibodies detecting PRMT5, MTAP, H4R3me2s, and loading control (vinculin). (**D**) MTA selectively inhibits PRMT5 biochemical activity. Heat map of the IC_{50} values of MTA and sinefungin across a panel of methyltransferases in an LC-MS–based biochemical assay. (**E**) Crystal structure of the published SAM analog A9145C-bound PRMT5:WDR77 complex with the H4 peptide (left in cyan; PDB ID: 4gqb) compared with the MTA-bound form (right in purple). The arginine residue from the H4 substrate peptide is shown as gray sticks. Dashes represent hydrogen bonds between E435 or A9145C and K333, Y334, or water (purple sphere). Comparison of key residues in MTA-bound PRMT5 across other family members finds Lys^{333} and Tyr^{334} (red) to be unique to PRMT5 (PRMT5 amino acids 330 to 340; dPRMT5 refers to the *Drosophila* PRMT5; Uniprot accession codes from top to bottom: O14744, Q9U6Y9, Q99873, P55345, O60678, Q86X55, Q96LA8, Q9NVM4, Q9NR22, and Q6P2P2). (**F** and **G**) Growth inhibitory effect of PRMT5 knockdown in MTAP-deficient cells is abrogated by ectopic MTAP reexpression. MIAPaCa2 cells stably expressing inducible shPRMT5-2 were transduced with retroviral empty vector control (F) or with MTAP cDNA (G), and proliferation was assessed by confluence measurements using IncuCyte. Expression of the MTAP cDNA was constitutive, whereas shPRMT5 expression was controlled by the addition (+Dox, red) or absence (–Dox, blue) of doxycycline; ± 6, shown are means and SD. (**H** to **J**) Exogenous addition of MTA restores sensitivity of MTAP-rescued cells to PRMT5 knockdown. In vitro proliferation assay as described in (F) of MIAPaCa2 cells stably expressing MTAP and inducible shPRMT5-2 ± Dox (± 6, shown are means and SD) and treated with (H) 10 μM MTA (± Dox, $P \leq 0.001$); (I) 15 μM MTA (±Dox, $P \leq 0.001$); and (J) 25 μM MTA (± Dox, $P \leq 0.001$). (**K**) Effect of addition of exogenous MTA (concentrations indicated on *x* axis) on the proliferation of PK1 isogenic cells described in Fig. 2, F to H. Cell viability was assessed 10 days after compound treatment using Cell Titer Glo and normalized to dimethyl sulfoxide (DMSO) controls; the means and SD of quadruplicate experiments are shown.

indicated that the catalytic activity of PRMT5 is required for the proliferation of MTAP-deficient cells. It remained unclear, however, why cancer cells lacking MTAP are selectively sensitized toward PRMT5 depletion mediated by RNA interference (RNAi). MTAP catalyzes the phosphorylation of MTA to adenine and 5-methylthioribose-1-phosphate, which is further recycled to methionine (*10*) (fig. S1C), and tumors with loss of MTAP exhibit a marked increase of intra- and extracellular levels of MTA (*5*, *11*, *12*). Consistent with the prior tumor data, metabolic profiling of MTA across a number of MTAP-deficient and -proficient cancer models, as well as in the PK1 isogenic cell lines, revealed that both intra- and extracellular MTA levels were increased in cells lacking MTAP (Fig. 4A; fig. S9, A and B; and fig. S10B). By contrast, intracellular SAM levels were on average higher than MTA levels and did not stratify with MTAP status (fig. S10, A and B). Given that MTA has been proposed to act as a general inhibitor of PRMTs (*12*, *13*), we hypothesized that increased MTA levels due to MTAP loss may partially cripple PRMT5 catalytic activity and thereby sensitize cells to further PRMT5 inhibition. Indeed, deletion of MTAP in PK1 cells (MTAP-KO) led to a reduction in the levels of H4R3me2s, consistent with the hypothesis that MTAP loss leads to reduced PRMT5 activity (Fig. 4B). Conversely, reexpression of MTAP in the MTAP-deficient MIAPaCa2 cell line, which according to our model should restore PRMT5 function by lowering MTA levels, resulted in increased levels of H4R3me2s (Fig. 4C).

To investigate the inhibitory activity of MTA on PRMTs in more detail, we profiled MTA in biochemical assays across a panel of 18 histone methyltransferases (HMTs), including several PRMTs (*6*). In contrast to the pan-methyltransferase inhibitor sinefungin (*7*), MTA selectively inhibited PRMT5 activity with a median inhibitory concentration (IC_{50}) of 4.6 μM and did not affect the activity of any of the other methyltransferases profiled at concentrations up to 100 μM (Fig. 4D and table S3). This finding may help explain why MTAP-deficient cells are selectively sensitized to depletion of PRMT5 but not other PRMT family members.

To further investigate the selective inhibition of PRMT5 by MTA, we determined the crystal structure of MTA-bound PRMT5:WDR77 in complex with a H4 peptide (Fig. 4E and table S7). SAM and MTA are structurally similar (fig. S10C), and as expected, the adenine and ribose moieties of MTA are nearly identical to those described for the SAM analog (A9145C) bound to human PRMT5:WDR77 (*3*). Our analysis revealed a change in the conformation of Glu^{435} in the MTA-bound form of PRMT5; this residue no longer coordinates the arginine residue of the peptide substrate as seen in the A9145C-peptide structure (Fig. 4E; cyan) but, rather, shifts down to make a split hydrogen bond with Tyr^{334} and a salt bridge with Lys^{333} (Fig. 4E; purple). The shifted Glu^{435} side chain and an additional water molecule occupy a region similar to the 2-aminobutanoate of the SAM analog, and they form the lower wall of the MTA pocket. Whereas Glu^{435} is invariant among all arginine methyltransferase family members and has been proposed to be important for function, Lys^{333} and Tyr^{334} are unique to PRMT5 (Fig. 4E). Thus, we hypothesize that the selectivity of MTA inhibition for PRMT5 is due, in part, to the reordering of the cofactor binding pocket facilitated by the Glu^{435}-Lys^{333}/Tyr^{334} interactions.

If MTAP loss, and concomitant MTA accumulation, is responsible for inducing sensitivity to PRMT5 inhibition, then restoration of MTAP function should render MTAP-deficient cells insensitive to PRMT5 depletion. Indeed, expression of exogenous MTAP in the MTAP-deficient MIAPaCa2 cell line rescued the PRMT5 shRNA-mediated effects on proliferation (Fig. 4, F and G). Moreover, MTA supplementation resensitized this MTAP-reconstituted cell line to PRMT5 knockdown, which resulted in decreased proliferation and H4R3me2s levels (Fig. 4, H to J, and fig. S11, A and B). Higher concentrations of MTA (25 μM MTA) (Fig. 4J) by itself caused antiproliferative effects and reduced H4R3me2s to levels comparable to those seen with PRMT5 knockdown in the MIAPaCa2 wild-type (WT) scenario (fig. S11C). This effect could either be due to more complete inhibition of PRMT5 function, thus mimicking the PRMT5 null phenotype, or might be mediated by feedback inhibition of spermidine synthase, a by-product of polyamine synthesis (*10*, *14*, *15*).

EPZ015666 is a potent pharmacological inhibitor of PRMT5, and it requires SAM for efficient binding to and inhibition of the enzyme (*16*). SAM is more abundant than MTA in cells. Whereas MTAP loss leads to a profound increase in MTA levels (Fig. 4, A and B), we found that it has little impact on SAM levels (fig. S9C and fig. S10, A and B). We hypothesized that the activity of SAM cooperative inhibitors would not be differentially affected by the altered metabolic state in MTAP-deficient cancers. Indeed, when we profiled EPZ015666 across a panel of 11 MTAP-deficient and intact cell lines, including the PK1 isogenic MTAP-KO cells, we did not detect substantial selective antiproliferative effects correlating with MTAP status (fig. S12, A to D). Consistent with this, we found that complete inactivation of PRMT5 by CRISPR is lethal even in MTAP-proficient cells (fig. S13, A to C). PRMT5 biochemical assays with differing concentrations of MTA and SAM (fig. S14A) further supported our hypothesis.

Because MTA inhibits PRMT5 by competing rather than cooperating with SAM for binding to the catalytic site (fig. S14, B and C), we next explored whether MTA itself could act as an exogenous SAM-competitive inhibitor. We found that the isogenic MTAP-deleted PK1 cells were more sensitive to MTA than the parental PK1 cells (Fig. 4K). Therefore, in the MTAP-deleted setting, where an increased fraction of the MTA-bound inactive form of PRMT5 exists, enhanced sensitivity to exogenous MTA is achieved, and this is due to its SAM-competitive binding mode. Thus, we postulate that SAM-competitive inhibition of PRMT5 can be exploited to selectively alter the proliferation of MTAP-deficient cells. Overall, our data suggest a model in which complete loss of MTAP leads to partial metabolite-based inhibition of PRMT5 by altering the ratio of MTA to SAM (fig. S15).

In summary, loss of the 9p21 tumor suppressor locus is the most common deletion event across all cancer types, yet this event has remained intractable for therapeutic targeting. Our study and that of Kryukov *et al.* (*17*) indicate that deletion of the *MTAP* gene in human cancer leads to an altered metabolic state that represents an attractive opportunity for therapeutic intervention. Based on our mechanistic insights, therapeutics that mimic the mode of action of MTA on PRMT5 function (e.g., by competing with SAM for binding to PRMT5) or that preferentially bind to PRMT5 in the presence of MTA will be required to pharmacologically exploit the PRMT5 hypomorphic state found in these cancers.

REFERENCES AND NOTES

1. D. D. Shao *et al.*, *Genome Res.* **23**, 665–678 (2013).
2. G. Guderian *et al.*, *J. Biol. Chem.* **286**, 1976–1986 (2011).
3. S. Antonysamy *et al.*, *Proc. Natl. Acad. Sci. U.S.A.* **109**, 17960–17965 (2012).
4. F. L. Muller *et al.*, *Nature* **488**, 337–342 (2012).
5. A. P. Stevens *et al.*, *J. Cell. Biochem.* **106**, 210–219 (2009).
6. W. Qi *et al.*, *Proc. Natl. Acad. Sci. U.S.A.* **109**, 21360–21365 (2012).
7. J. Li, J. S. Chorba, S. P. Whelan, *J. Virol.* **81**, 4104–4115 (2007).
8. T. L. Branscombe *et al.*, *J. Biol. Chem.* **276**, 32971–32976 (2001).
9. M. C. Ho *et al.*, *PLoS ONE* **8**, e57008 (2013).
10. L. Christa, L. Thuillier, A. Munier, J. L. Perignon, *Biochim. Biophys. Acta* **803**, 7–10 (1984).
11. I. Basu *et al.*, *J. Biol. Chem.* **282**, 21477–21486 (2007).
12. K. Limm *et al.*, *Eur. J. Cancer* **49**, 1305–1313 (2013).
13. P. A. Maher, *J. Biol. Chem.* **268**, 4244–4249 (1993).
14. L. Christa, J. Kersual, J. Augé, J. L. Pérignon, *Biochem. J.* **255**, 145–152 (1988).
15. A. L. Subhi *et al.*, *J. Biol. Chem.* **278**, 49868–49873 (2003).
16. E. Chan-Penebre *et al.*, *Nat. Chem. Biol.* **11**, 432–437 (2015).
17. G. V. Kryukov *et al.*, *Science* **351**, aad5214 (2016).

ACKNOWLEDGMENTS

Use of the Industrial Macromolecular Crystallography Association Collaborative Access Team (IMCA-CAT) beamline 17-ID (or 17-BM) at the Advanced Photon Source was supported by the companies of the Industrial Macromolecular Crystallography Association through a contract with Hauptman-Woodward Medical Research Institute. Use of the Advanced Photon Source was supported by the Office of Science, Office of Basic Energy Sciences, U.S. Department of Energy, under contract no. DE-AC02-06CH11357. Novartis has filed a patent application relating to the use of inhibitors to treat MTAP-deficient diseases (62/049004).

SUPPLEMENTARY MATERIALS

www.sciencemag.org/351/6278/1208/suppl/DC1
Materials and Methods
Figs. S1 to S15
Tables S1 to S7
Data Tables S8 and S9
References (*18*–*29*)

6 October 2015; accepted 1 February 2016
Published online 11 February 2016
10.1126/science.aad5944

CANCER THERAPY

MTAP deletion confers enhanced dependency on the PRMT5 arginine methyltransferase in cancer cells

Gregory V. Kryukov,[1,2]* Frederick H. Wilson,[1,2]* Jason R. Ruth,[1,2]* Joshiawa Paulk,[1,2] Aviad Tsherniak,[2] Sara E. Marlow,[1,2] Francisca Vazquez,[1,2] Barbara A. Weir,[1,2] Mark E. Fitzgerald,[2] Minoru Tanaka,[1,2] Craig M. Bielski,[1,2] Justin M. Scott,[2] Courtney Dennis,[2] Glenn S. Cowley,[2] Jesse S. Boehm,[2] David E. Root,[2] Todd R. Golub,[2] Clary B. Clish,[2] James E. Bradner,[1,2] William C. Hahn,[1,2] Levi A. Garraway[1,2]†

The discovery of cancer dependencies has the potential to inform therapeutic strategies and to identify putative drug targets. Integrating data from comprehensive genomic profiling of cancer cell lines and from functional characterization of cancer cell dependencies, we discovered that loss of the enzyme methylthioadenosine phosphorylase (MTAP) confers a selective dependence on protein arginine methyltransferase 5 (PRMT5) and its binding partner WDR77. MTAP is frequently lost due to its proximity to the commonly deleted tumor suppressor gene, *CDKN2A*. We observed increased intracellular concentrations of methylthioadenosine (MTA, the metabolite cleaved by MTAP) in cells harboring *MTAP* deletions. Furthermore, MTA specifically inhibited PRMT5 enzymatic activity. Administration of either MTA or a small-molecule PRMT5 inhibitor showed a modest preferential impairment of cell viability for MTAP-null cancer cell lines compared with isogenic MTAP-expressing counterparts. Together, our findings reveal PRMT5 as a potential vulnerability across multiple cancer lineages augmented by a common "passenger" genomic alteration.

The gene encoding methylthioadenosine phosphorylase (MTAP) is ubiquitously expressed in normal tissues (fig. S1). However, homozygous deletion of *MTAP* occurs frequently in cancer due to its proximity to *CDKN2A*, one of the most commonly deleted tumor suppressor genes (Fig. 1A) (*1*–*7*). For example, *MTAP* is deleted in 40% of glioblastomas; 25% of melanomas, urothelial carcinomas, and pancreatic adenocarcinomas; and 15% of non–small cell lung carcinomas (NSCLC) (*8*). MTAP cleaves methylthioadenosine (MTA) to generate precursor substrates for methionine and adenine salvage pathways. Synthetic lethal strategies to exploit MTAP loss with methionine starvation or by inhibiting de novo purine synthesis have been proposed; however, clinical efficacy of such approaches has not been demonstrated (*9*–*11*).

We searched for genetic vulnerabilities associated with MTAP loss by leveraging genome-scale pooled short hairpin RNA (shRNA) screening data for 216 cancer cell lines from Project Achilles (*12*, *13*). *MTAP* deletion status for each line was determined using profiles of *MTAP* copy number and mRNA expression from the Cancer Cell Line Encyclopedia (CCLE) (data table S1) (*14*). We correlated 50,529 shRNA sensitivity profiles with *MTAP* deletion status across these lines and identified two shRNAs that strongly correlated with reduced viability of MTAP-null ($MTAP^-$) lines (n = 50) but not MTAP-positive ($MTAP^+$) lines (n = 166) (Fig. 1B and data table S2). One shRNA targeted *PRMT5* (shPRMT5 #1; two-sided Wilcoxon $P < 3 \times 10^{-15}$) and the other targeted *WDR77* (shWDR77 #1; $P < 4 \times 10^{-12}$). We observed a correlation between sensitivity to these shRNAs (Fig. 1C), suggesting that $MTAP^-$ lines sensitive to suppression with either shRNA were generally also sensitive to suppression with the other shRNA. Cell lines with loss of *CDKN2A* but not *MTAP* were generally less sensitive to *PRMT5* or *WDR77* depletion than were lines with codeletion of *CDKN2A* and *MTAP*, suggesting a correlation with *MTAP* (but not *CDKN2A*) loss (Fig. 1D and fig. S2). To provide further support for a possible dependency on *PRMT5* or *WDR77* in the setting of *MTAP* loss, we examined additional shRNAs targeting *PRMT5* and *WDR77* from the screening data set. We identified a second shRNA targeting *PRMT5* (shPRMT5 #2) and *WDR77* (shWDR77 #2) that also demonstrated a strong correlation between impaired cell viability and *MTAP* loss (Fig. 1E and data table S3).

False-positive findings can occur from genome-scale shRNA analyses because of "off-target" microRNA-like effects attributable to partial sequence complementarity with the 5′ end of the shRNA (known as the "seed" region) (*15*, *16*). To investigate this possibility, we identified shRNAs from the screening data set that shared sequence identity in the seed region with each of the four shRNAs targeting *PRMT5* or *WDR77*. None of the shRNAs with shared seed sequence identity demonstrated a correlation between cell viability and MTAP status comparable to that observed for the shRNAs targeting *PRMT5* or *WDR77*, arguing that the differential viability was not caused by a seed effect (fig. S3 and tables S1 and S2). We also confirmed on-target activity of all four shRNAs against *PRMT5* or *WDR77* by immunoblotting of lysates from shRNA-expressing cells (fig. S4).

PRMT5 and *WDR77* encode critical components of the methylosome. PRMT5 forms a complex with WDR77 and catalyzes the transfer of methyl groups to arginine side chains of target proteins, including histones (involved in chromatin remodeling and gene expression) and Sm proteins (RNA-binding proteins involved in mRNA processing) (*17*–*19*). Genetic depletion of PRMT5 has previously been reported to impair cancer cell viability by promoting G1 cell cycle arrest and apoptosis (*20*–*22*). Interestingly, shRNAs targeting either *PRMT5* or *WDR77* reduced levels of both proteins (while demonstrating specific suppression of the target transcript), consistent with depletion of the methylosome complex using either shRNA (fig. S4). $MTAP^-$ cells were also sensitive to shRNA-mediated depletion of *CLNS1A* and *RIOK1*, which encode two additional components of the methylosome (Fig. 1E) (*23*). Finally, the correlation between MTAP loss and sensitivity to *PRMT5* or *WDR77* suppression was not confounded by cell lineage. Within individual lineages (including glioma, pancreatic adenocarcinoma, and NSCLC), $MTAP^-$ cell lines were generally (but not universally) more sensitive to depletion of *PRMT5* and *WDR77* than were $MTAP^+$ lines (Fig. 1F and fig. S2).

Based on these observations, we hypothesized that MTAP loss may confer enhanced sensitivity to genetic suppression of *PRMT5* and *WDR77*. To validate this hypothesis, we examined effects of shRNAs targeting *PRMT5* and *WDR77* on cell viability in 275 additional cancer cell lines profiled through Project Achilles. This profiling data was generated using an expanded shRNA library with additional shRNAs not included in the initial study. Similar to findings from the initial screening data set, we observed that $MTAP^-$ lines (n = 47) were generally more sensitive to *PRMT5* or *WDR77* suppression than $MTAP^+$ lines (n = 228) (Fig. 1G and data table S4). Three of the four shRNAs used to establish our initial finding from the screening data set again demonstrated a strong correlation between loss of cell viability and *MTAP* status, as did an additional shRNA targeting *PRMT5* not included in the screening data set (shPRMT5 #3). In total, the overall increased sensitivity of $MTAP^-$ cells to *PRMT5* or *WDR77* depletion was demonstrated with five shRNAs (three targeting *PRMT5* and two targeting *WDR77*) from two independent functional data sets comprising 491 cancer cell lines (fig. S5).

To determine whether the effects of *PRMT5* or *WDR77* suppression on cell viability are affected by MTAP, we first introduced MTAP into four $MTAP^-$ cell lines [LU99 and H647 (NSCLC), SF-172 (glioma), and SU.86.86 (pancreatic ductal carcinoma)]. This resulted in robust MTAP protein expression in MTAP-reconstituted lines, whereas

[1]Department of Medical Oncology, Dana-Farber Cancer Institute, Harvard Medical School, Boston, MA 02215, USA. [2]The Broad Institute of MIT and Harvard, Cambridge, MA 02142, USA.
*These authors contributed equally to this work. †Corresponding author. E-mail: levi_garraway@dfci.harvard.edu

Downloaded from on March 10, 2016

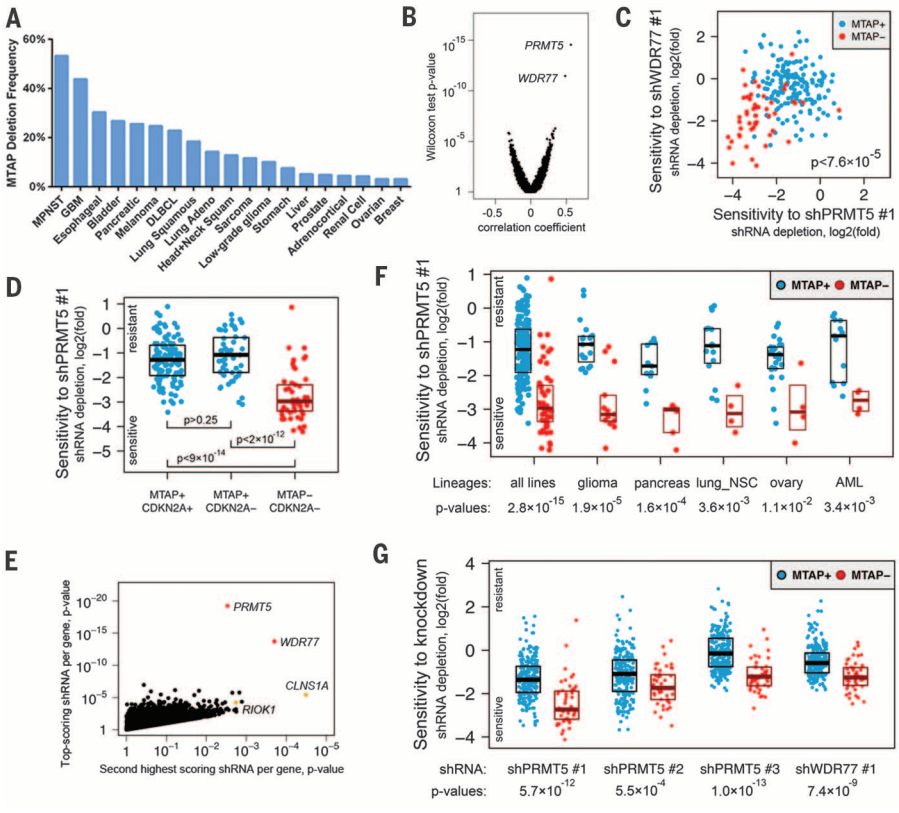

Fig. 1. Cancer cell lines with homozygous *MTAP* loss are selectively sensitive to suppression of *PRMT5* or *WDR77*. (**A**) Frequency of MTAP deletion for selected cancers is shown. Data was obtained from the cBioPortal for Cancer Genomics (http://www.cbioportal.org). MPNST, malignant peripheral nerve sheath tumor; GBM, glioblastoma; DLBCL, diffuse large B cell lymphoma. (**B**) Point biserial correlation coefficients for association with MTAP loss are plotted against Wilcoxon two-class comparison test *P* values for 50,529 shRNAs. (**C**) Log2(fold) of depletion of shPRMT5 #1 and shWDR77 #1 are shown, demonstrating a correlation between sensitivity to these shRNAs for MTAP$^-$ lines. (**D**) Log2(fold) of shPRMT5 #1 depletion is plotted for cell lines with the indicated genotypes. Median with upper and lower 25th percentiles are shown. (**E**) Pearson correlation test *P* values for the top-scoring shRNAs are plotted against *P* values for the second best-scoring shRNAs targeting the same gene. Selective sensitivity of MTAP$^-$ lines to depletion of the methylosome is supported by at least two hairpins targeting four members of the complex, including constitutive members of the complex (PRMT5 and WDR77, red) and mutually exclusive substrate adaptors (CLNS1A and RIOK1, orange). (**F**) Log2(fold) of shPRMT5 #1 depletion is plotted for all 216 cell lines (left) and for lines from the indicated lineages. lung_NSC, non–small cell lung cancer; AML, acute myeloid leukemia. (**G**) Log2(fold) depletion for the indicated shRNAs is shown for all 275 cell lines from the validation cohort.

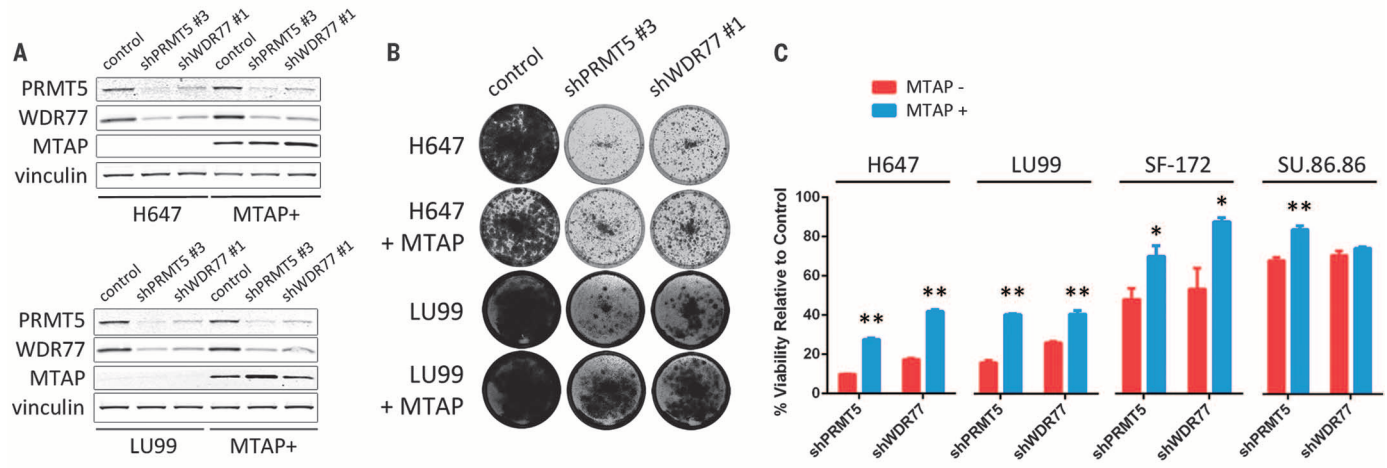

Fig. 2. Cells with MTAP loss are more sensitive to suppression of *PRMT5* and *WDR77* than isogenic MTAP-reconstituted cells. (**A**) Protein lysates were harvested from H647 (top) or LU99 (bottom) and from MTAP-reconstituted H647 or LU99 cells (MTAP$^+$) 5 days after lentiviral transduction with the indicated shRNAs or control. Lysates were fractionated by SDS–polyacrylamide gel electrophoresis (SDS-PAGE), and immunoblotting was performed with the indicated antibodies. (**B**) H647 or LU99 cells and MTAP-reconstituted H647 or LU99 cells were transduced with lentivirus harboring the indicated shRNAs and stained with crystal violet after 10 to 18 days. Media change was performed every 3 days. (**C**) Quantitation of crystal violet uptake by cells transduced with shRNAs targeting *PRMT5* or *WDR77* (normalized to control shRNA for each cell line). Mean and standard error of three to four replicates are shown. The experiment was performed two to three times for each of the four cell line pairs. $^{**}P < 0.01$; $^{*}P < 0.05$ by two-tailed Student's *t* test.

MTAP was absent from parental lines (Fig. 2A and fig. S6). We then performed colony formation assays to assess differences in cell viability after depletion of *PRMT5* or *WDR77* in the presence or absence of MTAP. We observed a reduction in cell viability for each MTAP$^-$ cell line with *PRMT5* or *WDR77* suppression, consistent with our screening and validation results (Fig. 2, B and C and fig. S6). Overall, MTAP-reconstituted lines demonstrated reduced sensitivity to *PRMT5* or *WDR77* suppression compared with isogenic MTAP$^-$ counterparts, suggesting a functional link between MTAP loss and PRMT5 or WDR77 dependency (Fig. 2, B and C and fig. S6).

Previous studies suggest that the activity of PRMT proteins may be inhibited by MTA (the substrate of MTAP) (*24*, *25*). MTA is an analog of S-adenosyl methionine (SAM), the donor substrate for PRMT-mediated methylation (*26*). We hypothesized that somatic *MTAP* loss may lead to increased intracellular MTA concentrations, which

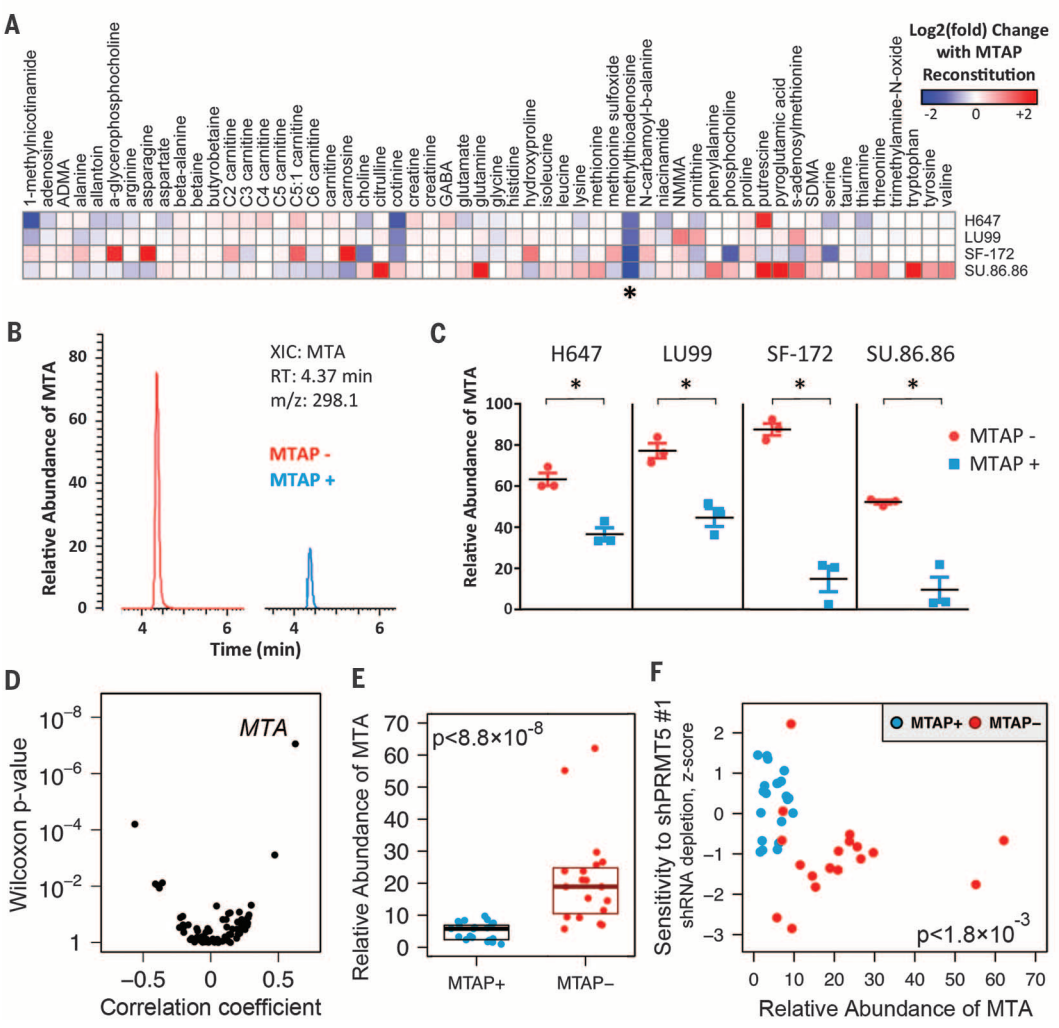

Fig. 3. Intracellular MTA is increased in MTAP$^-$ cells and correlates with sensitivity to *PRMT5* suppression. (**A**) Relative abundance of 56 profiled metabolites was compared for cell extracts from four isogenic cell line pairs. Fold change in relative abundance of each metabolite with MTAP reconstitution is shown for each isogenic pair. Results represent the mean of two independent experiments with three replicates per cell line. Findings for MTA are indicated with an asterisk. (**B**) Representative extracted ion chromatograms (XICs) from LC-MS/MS analysis of SF-172 (left) or MTAP-reconstituted SF-172 (right) cell extracts demonstrating a peak corresponding to MTA. RT, retention time; m/z, mass-to-charge ratio. (**C**) Relative abundance of MTA from cell extracts is displayed. Mean and standard error of three biological replicates are shown. The experiment was performed twice with similar findings. *$P < 0.01$ by Student's t test. (**D**) Correlation of metabolite levels with MTAP loss is shown. Point biserial correlation coefficients are plotted against Wilcoxon two-class comparison test P values for 73 metabolites profiled across 40 MTAP$^+$ and MTAP$^-$cell lines. (**E**) Relative abundance of MTA from MTAP$^+$ (n = 21) and MTAP$^-$ (n = 19) cell lines from various lineages is shown. For each cell line, mean of three biological replicates is displayed. Median with upper and lower 25th percentiles are shown for MTAP$^-$ and MTAP$^+$ lines. (**F**) Correlation of intracellular MTA levels with sensitivity to *PRMT5* depletion is shown. shPRMT5 sensitivity data from the screening and validation studies was normalized and combined using modified z scores. Z scores are plotted against relative intracellular abundance of MTA for the 40 assayed cell lines. Spearman rank correlation P value is shown.

in turn confers a partial inhibition of PRMT5 activity. Together, these effects may heighten cell sensitivity to further reductions in PRMT5 activity (e.g., through genetic suppression). To test this hypothesis, we first determined whether MTAP$^-$ cells contain elevated MTA levels. We used liquid chromatography tandem mass spectrometry (LC-MS/MS) to quantify levels of 56 metabolites (including MTA) from LU99, H647, SF-172, and SU.86.86 cells and their isogenic MTAP-reconstituted counterpart lines. The abundance of most measured metabolites was not significantly altered by ectopic MTAP expression (Fig. 3A). However, intracellular MTA abundance was reduced by a factor of 1.5 to 6, with MTAP reconstitution in each isogenic cell line pair, consistent with increased intracellular MTA in the absence of MTAP (Fig. 3, A to C).

To determine whether MTA levels are generally higher in MTAP$^-$ cell lines compared with MTAP$^+$ lines, we quantified intracellular levels of 73 metabolites from MTAP$^-$ (n = 19) and MTAP$^+$ (n = 21) cancer cell lines from various lineages, including NSCLC, melanoma, and breast. Among profiled metabolites, the abundance of MTA was most strongly correlated with MTAP loss (Fig. 3D and data tables S5 and S6). We observed an approximately 3.3-fold increase in median MTA levels in MTAP$^-$ lines compared with MTAP$^+$, consistent with the hypothesis that MTAP loss leads to increased intracellular MTA (Fig. 3E). In contrast, intracellular levels of the methyl donor SAM were not significantly different between MTAP$^-$ and MTAP$^+$ lines (fig. S7). Using shRNA sensitivity data from Project Achilles, we also observed a significant correlation between MTA levels and PRMT5 dependency across profiled cell lines (Fig. 3F, fig. S7, and data table S7).

Next, we assessed whether elevated MTA might inhibit PRMT5 activity. PRMT5 catalyzes the formation of symmetric dimethyl arginine (sDMA), whereas most other PRMTs generate asymmetric dimethyl arginine (aDMA) (*17*, *27*, *28*). Using an antibody previously shown to recognize sDMAs generated by PRMT5 (*29*), we observed decreased sDMA levels in MTAP$^-$ cells compared with isogenic, MTAP-reconstituted lines (Fig. 4A). In addition, reduced sDMA was observed in MTAP-reconstituted cells exposed to exogenous MTA, consistent with inhibition of PRMT5 enzymatic activity (Fig. 4A). Similar findings were observed with an antibody recognizing symmetric methylation of histone H4 arginine 3 (H4R3), an established substrate of PRMT5 (Fig. 4A) (*30*). In contrast, we observed only modest effects of MTAP status or exogenous MTA on levels of aDMA (Fig. 4A).

This finding raised the possibility that among PRMT family members, PRMT5 may exhibit heightened sensitivity to MTA intracellular concentrations. To investigate this, we measured the ability of MTA to inhibit the catalytic function of 31 histone methyltransferases (including PRMT5 and the PRMT5/WDR77 complex), using a radioisotope filter binding assay (data table S8) (*31*). We observed more than 100-fold

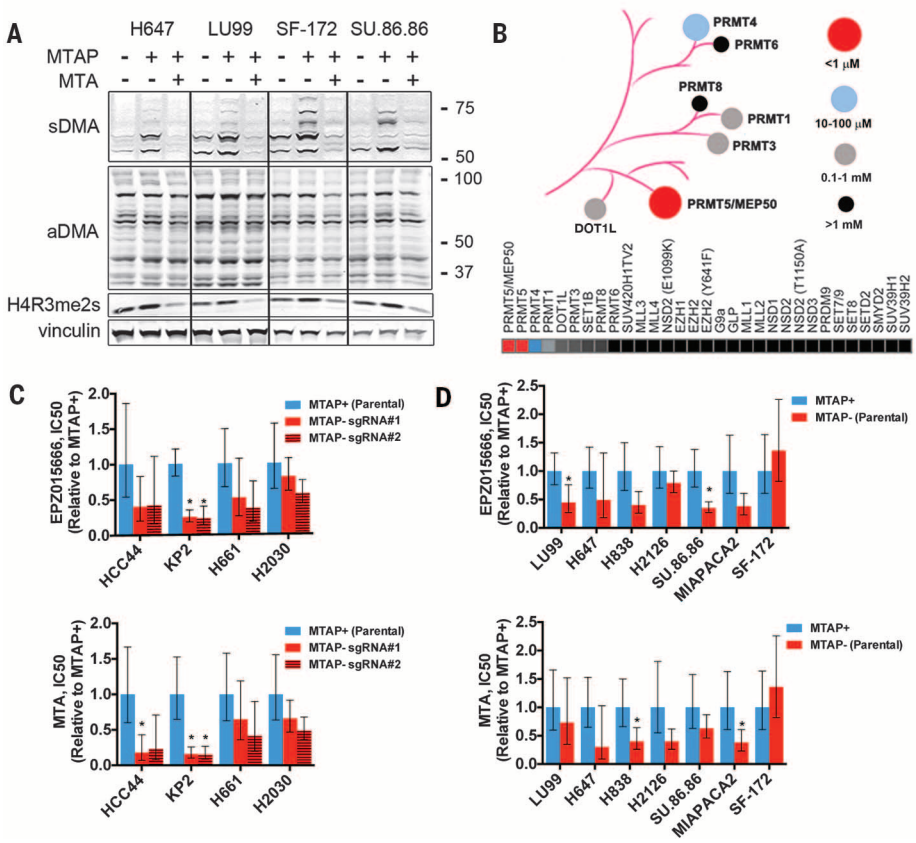

Fig. 4. Pharmacological inhibition of PRMT5. (**A**) Cells were exposed to dimethyl sulfoxide or 200 μM MTA for 48 hours. Lysates were harvested and fractionated by SDS-PAGE. Immunoblotting was performed with the indicated antibodies [recognizing symmetric or asymmetric dimethyl arginine motifs (sDMA and aDMA, respectively), symmetric dimethyl histone H4 arginine 3 (H4R3me2s), or vinculin (loading control)]. Molecular weight is indicated on the right in kDa. (**B**) Dendrogram and heat map indicating relative sensitivity of 31 histone methyltransferases to inhibition by MTA, as determined by radioisotope filter binding assay. (**C** and **D**) Relative cell viability IC_{50} (normalized to $MTAP^+$ cells for each line) for cells treated with EPZ015666 (top) or MTA (bottom), for isogenic cell lines derived from (C) MTAP-expressing parental cell lines or (D) $MTAP^-$ parental cell lines. Mean IC_{50} and 95% confidence interval of six replicates are shown for each cell line. Each experiment was performed twice for each cell line. $^*P < 0.05$ by two-tailed Student's *t* test (versus $MTAP^+$ cells).

selectivity for MTA against both PRMT5 and PRMT5/WDR77 activity compared with all other profiled methyltransferases, consistent with the hypothesis that PRMT5 function is selectively vulnerable to elevated MTA concentrations (Fig. 4B). Furthermore, we demonstrated that MTA is a SAM-competitive inhibitor of PRMT5 (fig. S8).

Next, we sought to determine whether $MTAP^-$ cell lines might exhibit increased sensitivity to pharmacologic inhibition of PRMT5 compared with $MTAP^+$ lines. We identified two inhibitors with distinct PRMT5 binding sites: the metabolite MTA itself and EPZ015666, a potent peptide-competitive and SAM-cooperative inhibitor with >10,000-fold specificity against PRMT5 relative to other methyltransferases (*32*). We tested the ability of these inhibitors to selectively impair viability of parental $MTAP^-$ cell lines compared with isogenic lines expressing MTAP, as well as parental $MTAP^+$ cell lines compared with isogenic CRISPR-mediated MTAP knockout lines (fig. S9). Among the 11 isogenic cell line pairs assayed, the IC_{50} values (concentrations of inhibitor that led to a 50% reduction in activity) for $MTAP^-$ cell lines treated with MTA or EPZ015666 were generally lower than IC_{50} values for isogenic $MTAP^+$ lines, consistent with our findings from genetic depletion of *PRMT5* (although with a smaller effect size) (Fig. 4, C and D). Although the results for any given cell line pair were consistent using either PRMT5 inhibitor (fig. S9), the differences between each isogenic cell line pair were generally modest and more pronounced for some pairs than others (the differential sensitivity was absent altogether in SF-172). Furthermore, we did not observe significant differences in mean IC_{50} values between $MTAP^+$ and $MTAP^-$ cell lines for either compound (fig. S9).

The discrepancy in effect size that we observed between genetic depletion and enzymatic inhibition of PRMT5 may be caused by several factors. For example, it is possible that the reported SAM-cooperative mechanism of action of EPZ015666 limits inhibition of PRMT5 in the setting of excess MTA and reduced SAM binding (*32*). Consistent with this, excess MTA is reported to increase the IC_{50} of EPZ015666 by an order of magnitude in assays of PRMT5 activity (*33*). In addition, we cannot exclude the possibility that a noncatalytic PRMT5 function also contributes to the dependency. In this case, therapeutic approaches to exploit this type of vulnerability may require strategies that deplete protein levels of either PRMT5 itself or the larger methylosome complex. Further work will be necessary to explore these and other mechanistic possibilities.

Collectively, our findings suggest that MTAP loss leads to increased intracellular MTA, which in turn inhibits PRMT5 activity and confers heightened susceptibility to further depletion of PRMT5 (fig. S10). Although PRMT5 has recently emerged as a possible therapeutic target in some cancers (*26*), genetic alterations correlated with sensitivity to PRMT5 inhibition have not previously been identified. Our data suggest that many $MTAP^-$ tumors are more sensitive to depletion of the methylosome, although there is an overlapping distribution of sensitivities to *PRMT5* or *WDR77* suppression between $MTAP^-$ and $MTAP^+$ cell lines (Fig. 1, D, F, and G). Thus, MTAP status alone is not sufficient to distinguish cell lines that are sensitive to PRMT5 inhibition. These observations suggest the presence of other modifiers of sensitivity to methylosome depletion that function in a manner independent of *MTAP* status. Nevertheless, our results endorse the unexpected notion that MTAP loss confers sensitivity to PRMT5 depletion. More generally, these findings highlight the value of comprehensive functional and molecular characterization of large cancer cell line collections to promote identification of potentially targetable dependencies conferred by common genetic lesions.

REFERENCES AND NOTES

1. T. Nobori *et al.*, *Proc. Natl. Acad. Sci. U.S.A.* **93**, 6203–6208 (1996).
2. Z. H. Chen, H. Zhang, T. M. Savarese, *Cancer Res.* **56**, 1083–1090 (1996).
3. P. B. Illei, V. W. Rusch, M. F. Zakowski, M. Ladanyi, *Clin. Cancer Res.* **9**, 2108–2113 (2003).
4. S. R. Hustinx *et al.*, *Cancer Biol. Ther.* **4**, 90–93 (2005).
5. E. L. Powell *et al.*, *Am. J. Surg. Pathol.* **29**, 1497–1504 (2005).
6. C. A. Karikari *et al.*, *Mol. Cancer Ther.* **4**, 1860–1866 (2005).
7. S. A. Christopher, P. Diegelman, C. W. Porter, W. D. Kruger, *Cancer Res.* **62**, 6639–6644 (2002).
8. E. Cerami *et al.*, *Cancer Discov.* **2**, 401–404 (2012).
9. J. R. Bertino, W. R. Waud, W. B. Parker, M. Lubin, *Cancer Biol. Ther.* **11**, 627–632 (2011).
10. H. L. Kindler, H. A. Burris 3rd, A. B. Sandler, I. A. Oliff, *Invest. New Drugs* **27**, 75–81 (2009).
11. P. N. Munshi, M. Lubin, J. R. Bertino, *Oncologist* **19**, 760–765 (2014).
12. H. W. Cheung *et al.*, *Proc. Natl. Acad. Sci. U.S.A.* **108**, 12372–12377 (2011).
13. G. S. Cowley *et al.*, *Scientific Data* **1**, 140035 (2014).
14. J. Barretina *et al.*, *Nature* **483**, 603–607 (2012).
15. A. L. Jackson *et al.*, *RNA* **12**, 1179–1187 (2006).
16. F. D. Sigoillot *et al.*, *Nat. Methods* **9**, 363–366 (2012).
17. V. Karkhanis, Y. J. Hu, R. A. Baiocchi, A. N. Imbalzano, S. Sif, *Trends Biochem. Sci.* **36**, 633–641 (2011).
18. W. J. Friesen *et al.*, *Mol. Cell. Biol.* **21**, 8289–8300 (2001).
19. W. J. Friesen *et al.*, *J. Biol. Chem.* **277**, 8243–8247 (2002).

20. A. Scoumanne, J. Zhang, X. Chen, *Nucleic Acids Res.* **37**, 4965–4976 (2009).
21. J. H. Lim *et al.*, *Biochem. Biophys. Res. Commun.* **452**, 1016–1021 (2014).
22. C. M. Koh *et al.*, *Nature* **523**, 96–100 (2015).
23. G. Guderian *et al.*, *J. Biol. Chem.* **286**, 1976–1986 (2011).
24. M. T. Bedford, S. Richard, *Mol. Cell* **18**, 263–272 (2005).
25. H. G. Williams-Ashman, J. Seidenfeld, P. Galletti, *Biochem. Pharmacol.* **31**, 277–288 (1982).
26. Y. Yang, M. T. Bedford, *Nat. Rev. Cancer* **13**, 37–50 (2013).
27. T. L. Branscombe *et al.*, *J. Biol. Chem.* **276**, 32971–32976 (2001).
28. B. P. Pollack *et al.*, *J. Biol. Chem.* **274**, 31531–31542 (1999).
29. F. Liu *et al.*, *J. Clin. Invest.* **125**, 3532–3544 (2015).
30. Q. Zhao *et al.*, *Nat. Struct. Mol. Biol.* **16**, 304–311 (2009).
31. K. Y. Horiuchi *et al.*, *Assay Drug Dev. Technol.* **11**, 227–236 (2013).
32. E. Chan-Penebre *et al.*, *Nat. Chem. Biol.* **11**, 432–437 (2015).
33. K. J. Mavrakis *et al.*, *Science* **351**, aad5944 (2016).

ACKNOWLEDGMENTS

Data from Project Achilles and the Cancer Cell Line Encyclopedia can be accessed at www.broadinstitute.org/achilles and www.broadinstitute.org/ccle/home, respectively. We thank members of the Garraway laboratory for helpful discussion. We thank D. Hernandez for assistance with seeding cell lines for metabolomics studies. We gratefully acknowledge the Carlos Slim Foundation for providing access to shRNA screening data (funded in part by the Slim Initiative in Genomic Medicine for the Americas project) for validation studies. Funding for this work was provided by the Novartis Institutes for BioMedical Research, the Dr. Miriam and Sheldon G. Adelson Medical Research Foundation, the Melanoma Research Alliance, a NIH PO1 Research Program Project grant (each to L.A.G.), an Integrative Cancer Biology Program grant (U54 CA112962 to T.R.G.), and an NIH U01 CA176058 (to W.C.H.). F.H.W. is supported by a Conquer Cancer Foundation of the American Society of Clinical Oncology Young Investigator Award, the 2014 AACR-Bristol-Myers Squibb Oncology Fellowship in Clinical Cancer Research (grant 14-40-15-WILS), a grant from the Karin Grunebaum Cancer Research Foundation, and a KL2/Catalyst Medical Research Investigator Training award (an appointed KL2 award) from Harvard Catalyst/The Harvard Clinical and Translational Science Center (National Center for Research Resources and the National Center for Advancing Translational Sciences, NIH Award KL2 TR001100). G.V.K., A.T., F.V., B.A.W., and C.M.B. performed computational analysis of data sets generated from Project Achilles and CCLE under the supervision of J.S.B., T.R.G., W.C.H., and L.A.G. G.S.C., D.E.R., and W.C.H. supervised the generation of Project Achilles screening data. F.H.W. and S.E.M. performed experiments to validate the computational shRNA screening findings. G.V.K., F.H.W., S.E.M., J.M.S., C.D., and C.B.C. performed metabolomic studies and analyzed data. Isogenic cell line pairs were generated and characterized by F.H.W. and J.R.R. J.R.R. conducted cell viability IC_{50} experiments and the MTA methyltransferase selectivity assay. J.P. performed the MTA mechanism of action study under the supervision of J.E.B. M.E.F. and M.T. synthesized EPZ015666 under the supervision of J.E.B. F.H.W., G.V.K., J.R.R., and L.A.G. wrote the manuscript. L.A.G. is a paid consultant for Novartis and Boehringer Ingelheim; he holds equity in, and is a paid consultant for, Foundation Medicine; and he is a recipient of a grant from Novartis. W.C.H. is a paid consultant for Novartis and recipient of a grant from Novartis. M.T. is a visiting scientist from Mitsubishi Tanabe Pharma Corporation (MTPC) and a recipient of nonresearch support from MTPC. The Broad Institute and the authors (L.A.G., F.H.W., G.V.K., and J.R.R.) have filed a patent application (BI2015/040 46783.00.2109 US PRO Pending 62/131,825) relating to the use of PRMT5 inhibitors to treat MTAP-deficient tumors.

SUPPLEMENTARY MATERIALS

www.sciencemag.org/content/351/6278/1214/suppl/DC1
Materials and Methods
Figs. S1 to S10
Tables S1 and S2
Data Tables S1 to S8
References

7 October 2015; accepted 1 February 2016
Published online 11 February 2016
10.1126/science.aad5214

TRANSCRIPTION

Measurement of gene regulation in individual cells reveals rapid switching between promoter states

Leonardo A. Sepúlveda,[1,2] Heng Xu,[1,2] Jing Zhang,[1,2] Mengyu Wang,[1,2,3] Ido Golding[1,2,3,4]*

In vivo mapping of transcription-factor binding to the transcriptional output of the regulated gene is hindered by probabilistic promoter occupancy, the presence of multiple gene copies, and cell-to-cell variability. We demonstrate how to overcome these obstacles in the lysogeny maintenance promoter of bacteriophage lambda, P_{RM}. We simultaneously measured the concentration of the lambda repressor CI and the number of messenger RNAs (mRNAs) from P_{RM} in individual *Escherichia coli* cells, and used a theoretical model to identify the stochastic activity corresponding to different CI binding configurations. We found that switching between promoter configurations is faster than mRNA lifetime and that individual gene copies within the same cell act independently. The simultaneous quantification of transcription factor and promoter activity, followed by stochastic theoretical analysis, provides a tool that can be applied to other genetic circuits.

Sequence-specific transcription factors drive the diversity of cell phenotypes in development and homeostasis (*1*). For each target gene, alternative transcription-factor binding configurations (by different transcription factors or by multiple copies of the same one) result in varied transcriptional outputs, in turn leading to alternative cell fates and behaviors (*2*, *3*). Elucidating the relations between transcription-factor configurations [which can number in the hundreds (*4*–*6*)] and the resulting transcriptional activity remains a challenge. Application of traditional genetic and biochemical approaches usually requires a genetically modified system or assays of purified components in vitro (*7*). Ideally, however, one would like to map transcription-factor configuration to promoter activity inside the cell, with minimal perturbation to the endogenous system.

Multiple factors hinder such direct measurement. First, individual cells vary in both transcription-factor concentration and the resulting transcriptional activity (*8*, *9*); averaging over many cells thus filters out details of the regulatory relation. Second, even within the single cell, more than one copy of the regulated gene is typically present, with each copy individually regulated (*10*). Finally, even at the level of a single gene copy, multiple binding configurations are possible at a given transcription-factor concentration (*11*, *12*). The relative probabilities of these different configurations and the rate of switching between them will define the stochastic activity of the regulated promoter (*13*).

We simultaneously measured, in individual cells, the concentration of a transcription factor and the number of mRNAs produced from the regulated gene. We also measured how the gene copy number changes through the cell cycle. We then analyzed the full single-cell data using a theoretical model, which allowed us to identify the contributions of different transcription-factor binding configurations to the stochastic activity of the promoter.

Specifically, we examined the lysogeny maintenance promoter of phage lambda, P_{RM}. The regulation of this promoter by its own gene product, the lambda repressor (CI), is a paradigm for how alternative binding configurations drive transcriptional activity and the resulting cell fate—stable lysogeny or lytic induction resulting in cell death (*7*). The number of possible CI configurations is very large [>100 (*4*, *5*)]. Briefly, as CI concentration increases, CI dimers gradually occupy three proximal ($O_{R1\text{-}3}$) and three distal ($O_{L1\text{-}3}$) operator sites, leading first to activation, then repression, of P_{RM} (Fig. 1A). Cooperative CI binding, and looping of DNA between the O_R and O_L sites, play important roles in shaping the P_{RM}(CI) regulatory curve (*14*).

In a lysogen (a bacterium carrying a prophage), CI concentration is believed to be such that P_{RM} fluctuates between the activated and repressed states (*15*) (Fig. 1A), and this has been suggested to stabilize the lysogenic state against random fluctuations in CI levels (*14*). However, the nature of the lysogenic "mixed state" (activated/repressed) is unknown: Are the promoter fluctuations slow

[1]Verna and Marrs McLean Department of Biochemistry and Molecular Biology, Baylor College of Medicine, Houston, TX 77030, USA. [2]Center for Theoretical Biological Physics, Rice University, Houston, TX 77005, USA. [3]Graduate Program in Structural and Computational Biology and Molecular Biophysics, Baylor College of Medicine, Houston, TX 77030, USA. [4]Center for the Physics of Living Cells, University of Illinois at Urbana–Champaign, Urbana, IL 61801, USA.
***Corresponding author. E-mail: golding@bcm.edu; igolding@illinois.edu**

Downloaded from on March 10, 2016

enough, such that two distinct cell populations coexist, exhibiting high and low P_{RM} expression, respectively? Alternatively, are promoter fluctuations fast, such that all cells exhibit an intermediate, well-defined level of P_{RM} expression (Fig. 1B)?

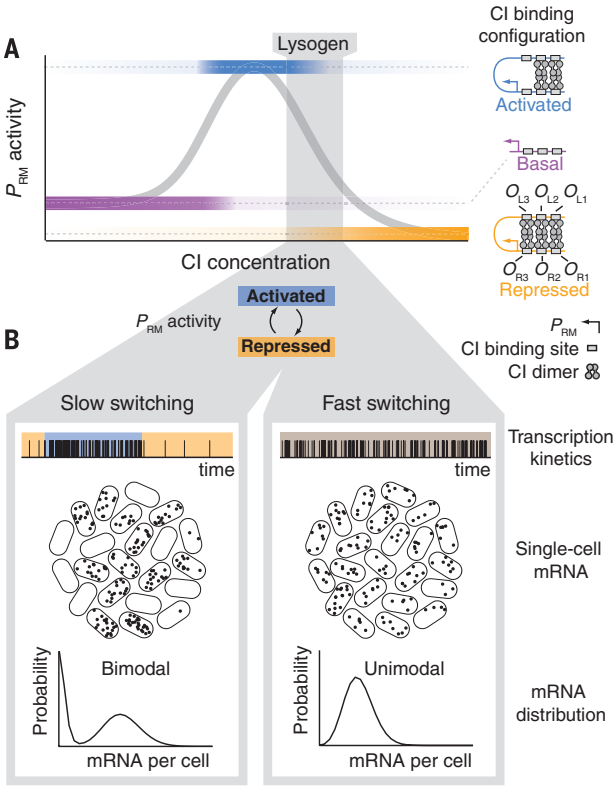

Fig. 1. Schematic of P_{RM} regulation by CI. (**A**) As the concentration of CI increases, the probabilities of different binding configurations of CI dimers at the O_R and O_L operators change (color shading), resulting in varying P_{RM} activity (gray curve). Three configurations, expected to be the most probable, are depicted. In lysogenic cells, P_{RM} has comparable probabilities of being in the activated and repressed promoter states (gray shading). (**B**) The rate of switching between activated and repressed states drives the stochastic activity of P_{RM} in lysogenic cells. Two alternative hypotheses are illustrated: If switching is slow relative to the mRNA lifetime (left), two subpopulations of cells will exist, with low and high mRNA levels. If switching is fast (right), the mRNA distribution in the population will be unimodal.

To measure CI concentration in individual cells, we used antibody labeling (immunofluorescence). Lysogenic cells (see table S1) exhibited a strong CI signal, whereas nonlysogenic (uninfected) cells showed only a weak background signal (Fig. 2A and fig. S1). To verify that the antibody signal reliably represents CI levels, we expressed a CI–yellow fluorescent protein (YFP) fusion protein (*16*) in nonlysogenic cells and compared the YFP fluorescence to the signal exhibited by the antibody to CI in each cell. The two signals were linear with each other (fig. S2A), and single-molecule imaging revealed that most YFP molecules were colocalized with an antibody to CI, as expected (fig. S2B).

To convert the antibody signal to CI concentration in each cell, we needed to know the fluorescence value corresponding to a single antibody–labeled CI molecule [a CI dimer, which is the dominant species in the cell (*17*)]. To obtain this calibration constant, we used two methods (*18*) (Fig. 2, B and C): In the first method, we used automated image analysis to identify individual fluorescent particles (spots, fig. S3). These spots displayed a well-defined intensity value, distinct from the corresponding signal found in negative samples (Fig. 2B). We identified the positive-sample spot intensity as corresponding to individual CI dimers (fig. S4A) (each one decorated by ~20 fluorescent dyes, due to the stoichiometry of antibody labeling; fig. S5) and used it to convert cell fluorescence to CI concentration. In the second method, we used the fact that the Poisson statistics of random protein positions within the cell lead to a linear relation between the

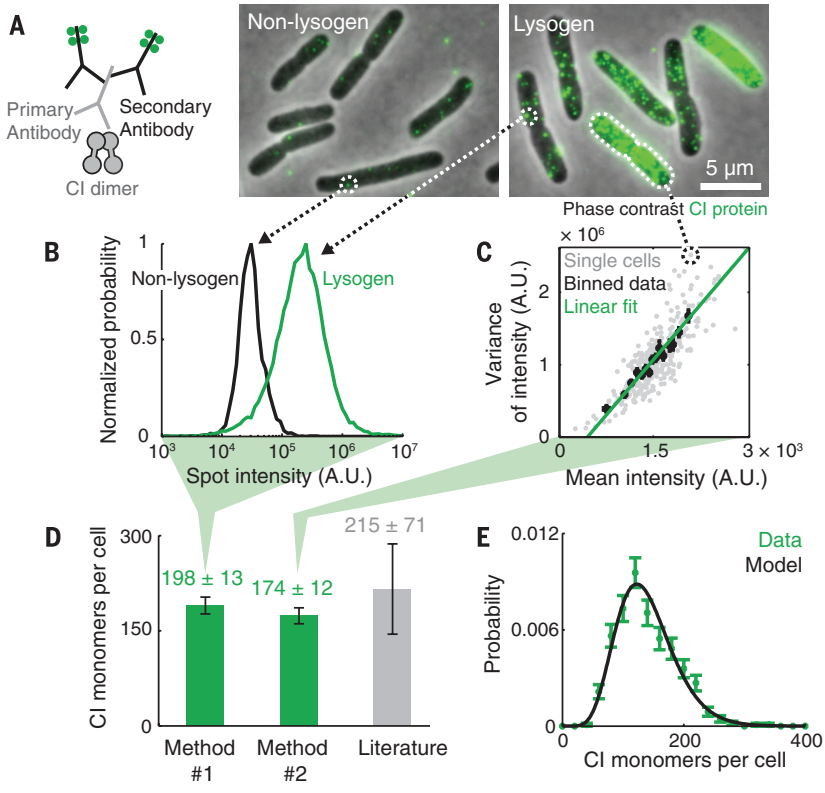

Fig. 2. Measuring the number of CI molecules in individual cells. (**A**) CI proteins were labeled with antibodies to CI and fluorescently labeled secondary antibodies (left). Under the microscope, lysogenic *E. coli* cells exhibited a strong CI signal (right) whereas nonlysogens showed a weak background signal (center). (**B**) Method 1 for measuring the number of CI proteins per cell. The typical fluorescence of a single CI dimer was obtained from the spot intensity distribution in lysogenic cells (green, N = 23,631 spots), distinguishable from that of the negative sample (black, N = 1764 spots). (**C**) Method 2 for measuring the number of CI proteins per cell. The variance versus the mean of pixel intensity in individual cells (gray, N = 324) was fitted to a linear function (green). The slope of this line was used to estimate the fluorescence intensity of a single CI dimer. (**D**) The estimated number of CI molecules in a lysogen, obtained with the two single-cell methods (green, mean ± SEM from six experiments, 327 to 704 cells each). Also shown is the value reported in the literature [gray, mean ± SD from three studies (*19*–*21*)]. (**E**) The distribution of CI copy number in lysogenic cells (green; N = 560 cells). The data are described well by a gamma distribution (black).

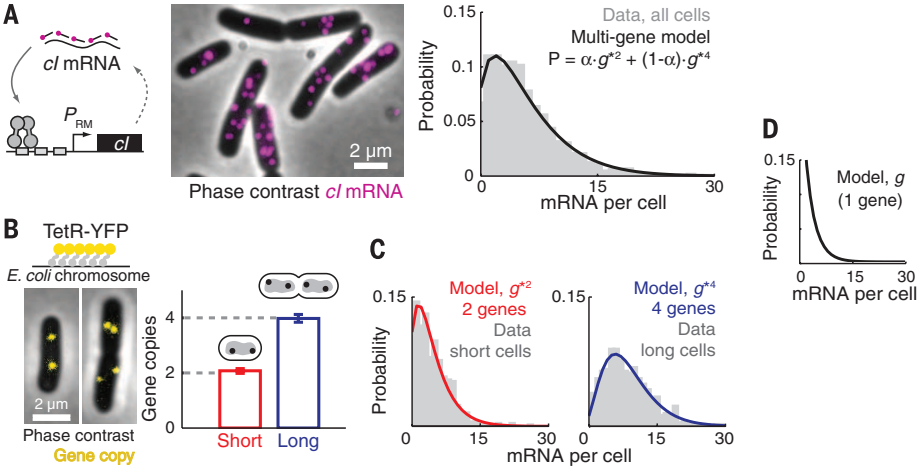

Fig. 3. Measuring the transcriptional activity of a single P_{RM} copy. (**A**) (Left and center) *cI* mRNA in lysogenic cells was labeled by smFISH. (Right) The measured distribution of *cI* mRNA number per cell from the whole population (gray, N = 2893 cells) consists of contributions from cells containing two and four gene copies [black; see (B) to (D)]. α is the fraction of cells with two copies of the P_{RM}-*cI* gene. (**B**) Estimating the number of P_{RM}-*cI* gene copies in lysogenic cells. TetR-YFP binds to an array of *tetO* sites inserted next to the gene locus, resulting in visible foci (left). (Right) Newborn cells (length percentile 5 to 20, "short," red, N = 493) contained two copies of the P_{RM}-*cI* locus, whereas cells about to divide (length percentile 80 to 95, "long," blue, N = 493) contained four copies. Error bars indicate SEM. (**C**) The measured distributions of *cI* mRNA numbers for short (left) and long (right) cells. Both were well fitted by a model assuming independent stochastic activity of each gene copy. (**D**) The theoretical fit from (C) was used to reconstruct the *cI* mRNA distribution from a single gene copy. This distribution was then used to predict the distribution for the whole population (A).

fluorescence mean and the pixel-to-pixel variance within each cell (Fig. 2C and fig. S6). Measuring the slope of this line allowed us to identify the fluorescence corresponding to a single labeled protein (fig. S7). Using either method to estimate CI concentration in lysogens gave similar results (Fig. 2D and fig. S4B). These measured values also agreed with those reported in the literature (*19*–*21*) (Fig. 2D and table S2).

The two imaging-based methods allowed us to measure CI numbers in individual lysogenic cells (Fig. 2E). Fitting the CI distribution to a stochastic model of protein production (*22*) indicated that, on average, the ~200 CI monomers in the cell are produced in ~10 random bursts, of ~20 proteins each, during the 30-min cell cycle (table S3). The estimated burst frequency is consistent with a (more accurate) value that we obtained from *cI* mRNA statistics (Fig. 3). It is also consistent with the measured stability of the lysogenic state [which depends exponentially on the CI burst frequency (*23*)].

To measure the activity of the P_{RM} promoter in individual lysogenic cells, we used single-molecule fluorescence in situ hybridization (smFISH) (*24*, *25*) to label and count *cI* mRNAs, produced from P_{RM} (Fig. 3A). Fluorescent spots were identified by means of an automated algorithm (*25*) (fig. S3), and the fluorescence intensity corresponding to a single mRNA was identified (fig. S8). We used this intensity to convert the total spot intensity in each cell to the number of *cI* mRNAs (*25*). The copy-number distribution of *cI* mRNA in a lysogen (Fig. 3A) represents the combined contribution from multiple copies of the P_{RM}-*cI* gene in each cell (*26*). To identify the contribution of a single gene copy, we first examined how the *cI* gene copy number varies during the cell cycle. We engineered an array of 140 Tet operators (*tetO*) (*27*) into the *gal* locus of *Escherichia coli* (~16 kb away from the lambda integration site). The gene locus was detected through the binding of a Tet repressor (TetR)–YFP fusion (*27*) (Fig. 3B). We used automated image analysis to count the number of YFP foci in each cell. Gating the cell population by length, we found that newborn cells had on average 2.1 ± 0.1 (mean ± SEM) foci per cell. Cells about to divide had 4.0 ± 0.1 foci per cell (Fig. 3B). These values are in good agreement with the expected copy number of the *cI* locus under our experimental conditions (*26*). We used these measured copy numbers to delineate the transcriptional activity of individual gene copies. If the stochastic activity of each copy is independent of the other copies in the same cell, then the *cI* mRNA distribution for cells having two gene copies will be given by the autoconvolution of the distribution for a single gene copy (a distribution that we cannot measure directly). Similarly, the mRNA distribution for four-copy cells will be equal to the one-copy distribution taken to the fourth convolution power. The experimental histograms agreed well with these predictions (Fig. 3C and fig. S9). Furthermore, knowing the fraction of cells in the population that have two and four copies allowed us to then predict the *cI* mRNA distribution for the whole population. The predicted distribution agreed well with the experimentally measured one (Fig. 3A).

Analyzing the single-gene mRNA distribution (Fig. 3D) revealed that a single copy of P_{RM} produces a burst of *cI* mRNA every ~6 min on average (table S4). When accounting for the presence of two to four gene copies per cell (Fig. 3B), this value is consistent with the burst frequency estimated from the CI protein histogram (Fig. 2E). Comparing the protein and mRNA data also allowed us to directly calculate the number of CI proteins produced from each *cI* mRNA, ~6 on average (table S3). This value is in good agreement with a previous theoretical calculation (*23*).

To measure the regulatory relation between CI concentration and P_{RM} activity, we used a reporter system in which the autoregulatory feedback from CI to P_{RM} existing in the lysogen is broken: CI is expressed from an inducible promoter, whereas P_{RM} transcribes the *lacZ* gene rather than *cI* (*14*) (Fig. 4A). To simultaneously measure CI concentration and P_{RM} activity in the same cell, we combined immunofluorescence (using antibody to CI) with smFISH (using *lacZ* probes) (*18*) (Fig. 4B and fig. S10) and measured the corresponding protein and mRNA numbers as described above. Performing this measurement over a range of CI levels, then plotting *lacZ* mRNA numbers versus CI concentration from many individual cells, produced highly scattered data (Fig. 4C), as expected from the stochasticity of the regulation and transcription processes (*9*). Averaging within finite windows of CI concentration revealed the mean regulatory relation between CI and P_{RM}, known as the gene regulation function (*16*) (Fig. 4C and fig. S11). The shape of the regulation function agreed with that from previous reports, with P_{RM} activity first increasing, then decreasing, with CI concentration (*4*, *14*, *28*). However, our measurement provides the absolute numbers for both the input (CI concentration) and output (mRNA numbers), rather than relative expression levels (*4*, *5*, *14*, *28*). The absolute values are crucial for the subsequent steps in our analysis of P_{RM} regulation.

As the first step in this analysis, we wrote down a theoretical model in which the probabilities of different CI binding configurations are given by their thermodynamic weights (*15*) (fig. S12A). This thermodynamic model successfully reproduced the regulation function (Fig. 4C and fig. S13). In performing this procedure, most free-energy values used in the model were identical to those reported (*15*) (table S5). The model also provided the probabilities of observing the different promoter activity states—basal, activated [with the DNA between O_R and O_L either looped or unlooped (*15*)], and repressed—as a function of CI concentration (Fig. 4D). The overlap between the different states underlines the challenge in identifying the transcriptional signature of a single promoter state: For example, the probability of P_{RM} being in the activated state does not surpass ~50%.

To reveal the activity of individual promoter states, we introduced a stochastic version of the theoretical model (Fig. 4E and fig. S12). In the model, the CI binding configurations are grouped based on the expected promoter activity: basal, activated unlooped, activated looped, and repressed

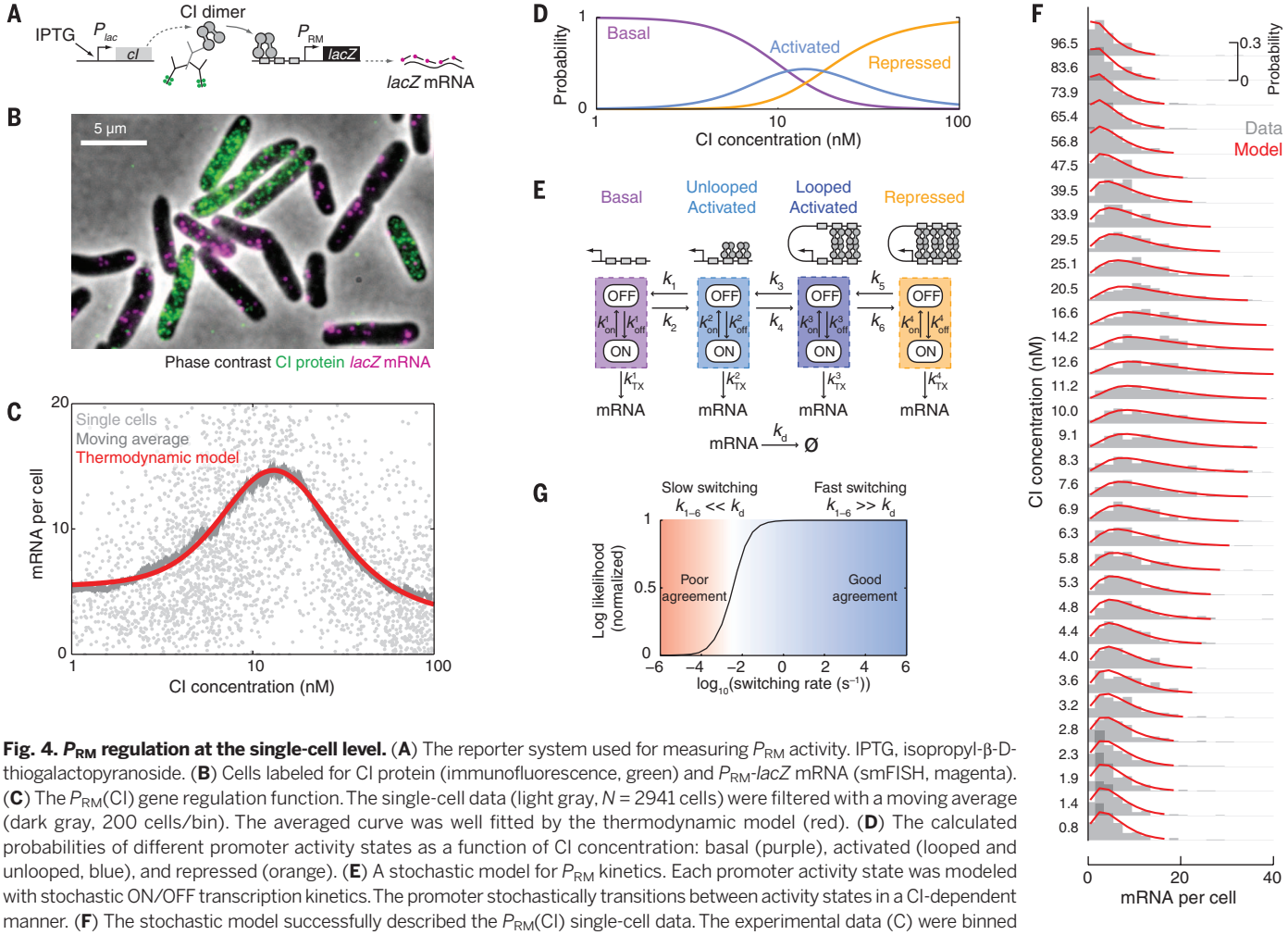

Fig. 4. P_{RM} regulation at the single-cell level. (**A**) The reporter system used for measuring P_{RM} activity. IPTG, isopropyl-β-D-thiogalactopyranoside. (**B**) Cells labeled for CI protein (immunofluorescence, green) and P_{RM}-*lacZ* mRNA (smFISH, magenta). (**C**) The P_{RM}(CI) gene regulation function. The single-cell data (light gray, $N = 2941$ cells) were filtered with a moving average (dark gray, 200 cells/bin). The averaged curve was well fitted by the thermodynamic model (red). (**D**) The calculated probabilities of different promoter activity states as a function of CI concentration: basal (purple), activated (looped and unlooped, blue), and repressed (orange). (**E**) A stochastic model for P_{RM} kinetics. Each promoter activity state was modeled with stochastic ON/OFF transcription kinetics. The promoter stochastically transitions between activity states in a CI-dependent manner. (**F**) The stochastic model successfully described the P_{RM}(CI) single-cell data. The experimental data (C) were binned into 100-cell histograms (gray) and fitted to the model (red) by maximum likelihood estimation. (**G**) Consistency of measured mRNA statistics with rapid switching between promoter states. Solving the stochastic model for different switching rates, and fitting the model results to the measured mRNA statistics, resulted in a good fit for fast switching (right, blue); slow switching yielded a poor fit (left, red).

(*15*). Each promoter activity state is described by stochastic bursty kinetics of mRNA production (*29*). P_{RM} stochastically switches between its four activity states. The switching rates are initially unknown, but the thermodynamic model above provides us with the equilibrium constant (ratio between switching left and right) for each pair of states, at a given CI concentration. For each set of parameters, the stochastic model can be solved to yield the expected mRNA copy-number distribution for the population of multicopy cells.

We used the stochastic model to analyze the full P_{RM}(CI) single-cell data set (Fig. 4C). Applying maximum-likelihood estimation, we found good agreement between the experimental and theoretical mRNA distributions over the full range of CI concentrations (Fig. 4F, fig. S14, and movie S1). The fitting procedure allowed us to extract the mRNA statistics corresponding to the different activity states of P_{RM} (fig. S15). The calculated distributions were in good agreement with those obtained with genetic controls: cells expressing no CI (basal), and cells overexpressing CI in wild-type P_{RM} (repressed) and in a mutant lacking the O_L operator (activated unlooped) (*14*) (fig. S15B and table S6). The stochastic kinetics of each promoter state exhibited a similar relation between expression level and burst size to that measured in other *E. coli* promoters (*29*) (fig. S15C).

Even though the measured mRNA distribution at each CI concentration represents a mixture of multiple promoter states, each of the histograms is unimodal and can be described by a simple kinetic model with a single burst size and frequency (Fig. 4F and fig. S16). The parameter that determines the shape of the "mixed state" mRNA distribution is the rate of switching between promoter states (Fig. 1B). Previous in vitro studies of O_R-O_L looping suggested that the switching between looped and unlooped promoter configurations is fast (~seconds) (*30*), but similar studies of looping in the cell left the question open (*31*). Our stochastic model predicts that if promoter switching is very slow relative to mRNA lifetime [here ~2 min (*29*)], the observed mRNA distribution will be the weighed sum of the underlying single-promoter-state distributions. Our experimental data strongly disagreed with this prediction (Fig. 4G). By contrast, if switching is fast, the observed distribution will be given by a (weighed) convolution of the underlying single-promoter-state distributions, and if the underlying states can each be described by simple bursty kinetics, the new mixed state can be as well. This is indeed what we observed (Fig. 4, F and G, and fig. S16). Thus, P_{RM} switches rapidly between different promoter states, resulting in a stochastic signature that (at a given CI concentration) is indistinguishable from that of a single promoter state, but with renormalized kinetic parameters. Our finding of rapid switching explains why, in the lysogen, we did not detect distinct "active" and "repressed" populations in either the protein (Fig. 2E) or mRNA (Fig. 3A) histograms, but instead both data sets indicated a single, well-defined promoter activity.

Precise single-cell measurements, accompanied by theoretical analysis, can reveal new features even in well-studied model systems. When combined with genetic and synthetic-biology approaches (*13*), this strategy may allow prediction of the stochastic characteristics of promoter activity,

a prediction that remains a challenge to our understanding of gene regulation (*9*, *32*).

REFERENCES AND NOTES

1. B. Pulverer, *Nat. Rev. Mol. Cell Biol.* **6**, S12–S13 (2005).
2. M. Ptashne, A. Gann, *Genes and Signals* (Cold Spring Harbor Laboratory Press, Cold Spring Harbor, NY, 2002).
3. E. H. Davidson, M. S. Levine, *Proc. Natl. Acad. Sci. U.S.A.* **105**, 20063–20066 (2008).
4. L. M. Anderson, H. Yang, *Proc. Natl. Acad. Sci. U.S.A.* **105**, 5827–5832 (2008).
5. L. Cui, I. Murchland, K. E. Shearwin, I. B. Dodd, *Proc. Natl. Acad. Sci. U.S.A.* **110**, 2922–2927 (2013).
6. E. H. Davidson, *The Regulatory Genome: Gene Regulatory Networks in Development and Evolution* (Elsevier Academic, Burlington, MA 2006).
7. M. Ptashne, *A Genetic Switch* (Cold Spring Harbor Laboratory Press, Cold Spring Harbor, NY, 2004).
8. A. Eldar, M. B. Elowitz, *Nature* **467**, 167–173 (2010).
9. A. Sanchez, I. Golding, *Science* **342**, 1188–1193 (2013).
10. M. J. Levesque, P. Ginart, Y. Wei, A. Raj, *Nat. Methods* **10**, 865–867 (2013).
11. M. A. Shea, G. K. Ackers, *J. Mol. Biol.* **181**, 211–230 (1985).
12. E. Segal, T. Raveh-Sadka, M. Schroeder, U. Unnerstall, U. Gaul, *Nature* **451**, 535–540 (2008).
13. D. L. Jones, R. C. Brewster, R. Phillips, *Science* **346**, 1533–1536 (2014).
14. I. B. Dodd, A. J. Perkins, D. Tsemitsidis, J. B. Egan, *Genes Dev.* **15**, 3013–3022 (2001).
15. I. B. Dodd *et al*., *Genes Dev.* **18**, 344–354 (2004).
16. N. Rosenfeld, J. W. Young, U. Alon, P. S. Swain, M. B. Elowitz, *Science* **307**, 1962–1965 (2005).
17. K. S. Koblan, G. K. Ackers, *Biochemistry* **30**, 7817–7821 (1991).
18. H. Xu, L. A. Sepúlveda, L. Figard, A. M. Sokac, I. Golding, *Nat. Methods* **12**, 739–742 (2015).
19. Z. Hensel *et al*., *Nat. Struct. Mol. Biol.* **19**, 797–802 (2012).
20. A. Levine, A. Bailone, R. Devoret, *J. Mol. Biol.* **131**, 655–661 (1979).
21. L. Reichardt, A. D. Kaiser, *Proc. Natl. Acad. Sci. U.S.A.* **68**, 2185–2189 (1971).
22. N. Friedman, L. Cai, X. S. Xie, *Phys. Rev. Lett.* **97**, 168302 (2006).
23. C. Zong, L. H. So, L. A. Sepúlveda, S. O. Skinner, I. Golding, *Mol. Syst. Biol.* **6**, 440 (2010).
24. A. Raj, P. van den Bogaard, S. A. Rifkin, A. van Oudenaarden, S. Tyagi, *Nat. Methods* **5**, 877–879 (2008).
25. S. O. Skinner, L. A. Sepúlveda, H. Xu, I. Golding, *Nat. Protoc.* **8**, 1100–1113 (2013).
26. K. Nordström, S. Dasgupta, *EMBO Rep.* **7**, 484–489 (2006).
27. M. C. Joshi *et al*., *Proc. Natl. Acad. Sci. U.S.A.* **108**, 2765–2770 (2011).
28. D. Lewis, P. Le, C. Zurla, L. Finzi, S. Adhya, *Proc. Natl. Acad. Sci. U.S.A.* **108**, 14807–14812 (2011).
29. L. H. So *et al*., *Nat. Genet.* **43**, 554–560 (2011).
30. C. Manzo, C. Zurla, D. D. Dunlap, L. Finzi, *Biophys. J.* **103**, 1753–1761 (2012).
31. Z. Hensel, X. Weng, A. C. Lagda, J. Xiao, *PLOS Biol.* **11**, e1001591 (2013).
32. A. Coulon, C. C. Chow, R. H. Singer, D. R. Larson, *Nat. Rev. Genet.* **14**, 572–584 (2013).

ACKNOWLEDGMENTS

We are grateful to the following people for generous advice and for providing reagents: I. Dodd, M. Elowitz, L. Finzi, H. Garcia, T. Gregor, T. Kuhlman, L. McLane, R. Phillips, A. Raj, E. Rothenberg, A. Sanchez, K. Shearwin, R. Singer, S. Skinner, L-H. So, A. Sokac, L. Zeng, and C. Zong. Work in the Golding lab is supported by grants from NIH (R01 GM082837), NSF (PHY 1147498, PHY 1430124 and PHY 1427654), The Welch Foundation (Q-1759), and The John S. Dunn Foundation (Collaborative Research Award). H.X. is supported by the Burroughs Wellcome Fund Career Award at the Scientific Interface. We gratefully acknowledge the computing resources provided by the Computational and Integrative Biomedical Research Center of Baylor College of Medicine.

SUPPLEMENTARY MATERIALS

www.sciencemag.org/content/351/6278/1218/suppl/DC1
Materials and Methods
Figs. S1 to S17
Tables S1 to S6
Movie S1
Supplementary Caption for Fig. 1
References (*33*–*47*)

20 July 2015; accepted 25 January 2016
10.1126/science.aad0635

BOYALIFE
博雅控股集团

All about BIOTECHNOLOGY

All for Human Development and Health Improvement

Boyalife Group is an enterprise centered on innovation in the biotechnology field covering stem cell technology and bio-pharm. Found in 2009, Boyalife Group has more than 30 wholly-owned subsidiaries and holding companies currently, becoming the leading brand in healthcare and pharmaceutical center in China.

Our operative segments all for better health are including:

- Stem Cell Technology
- Pharmaceutical
- Gene Harbor
- Cloning Factory
- Health Management
- Regenerative Medicine
- Disease Models

For more information, visit : www.boyalifegroup.com

Don't miss the debut of *Science Immunology*.

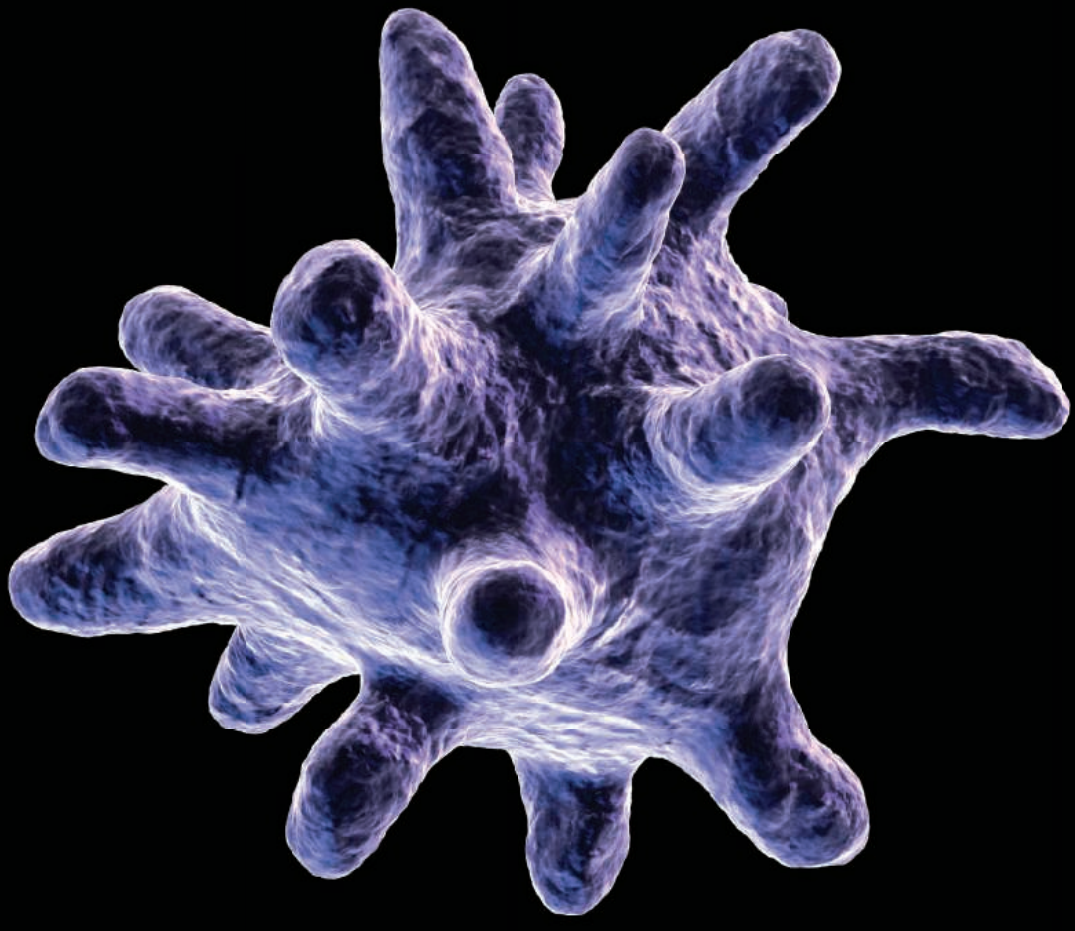

Image: Eraxion / iStockPhoto

NOW ACCEPTING PAPERS

Science is expanding its reach into immunology—now offering the newest online-only, weekly journal in the *Science* family of publications. *Science Immunology* will provide original, peer-reviewed research articles that report critical advances in all areas of immunological research, including studies that provide insight into the human immune response in health and disease.

Be a part of the *Science Immunology* debut issue publishing Summer 2016!

Submit your manuscript today at **ScienceImmunology.org.**

Science Immunology

AAAS

myIDP: A career plan customized for you, by you.

For your career in science, there's only one Science

my IDP
Science Careers

Recommended by leading professional societies and the NIH

Features in myIDP include:

- Exercises to help you examine your skills, interests, and values.
- A list of 20 scientific career paths with a prediction of which ones best fit your skills and interests.
- A tool for setting strategic goals for the coming year, with optional reminders to keep you on track.
- Articles and resources to guide you through the process.
- Options to save materials online and print them for further review and discussion.
- Ability to select which portion of your IDP you wish to share with advisors, mentors, or others.
- A certificate of completion for users that finish myIDP.

Visit the website and start planning today!
myIDP.sciencecareers.org

Science Careers In partnership with:

advancing the life sciences 1912-2012 FASEB Federation of American Societies for Experimental Biology

UCSF University of California San Francisco

Medical College of Wisconsin

Burroughs Wellcome Fund

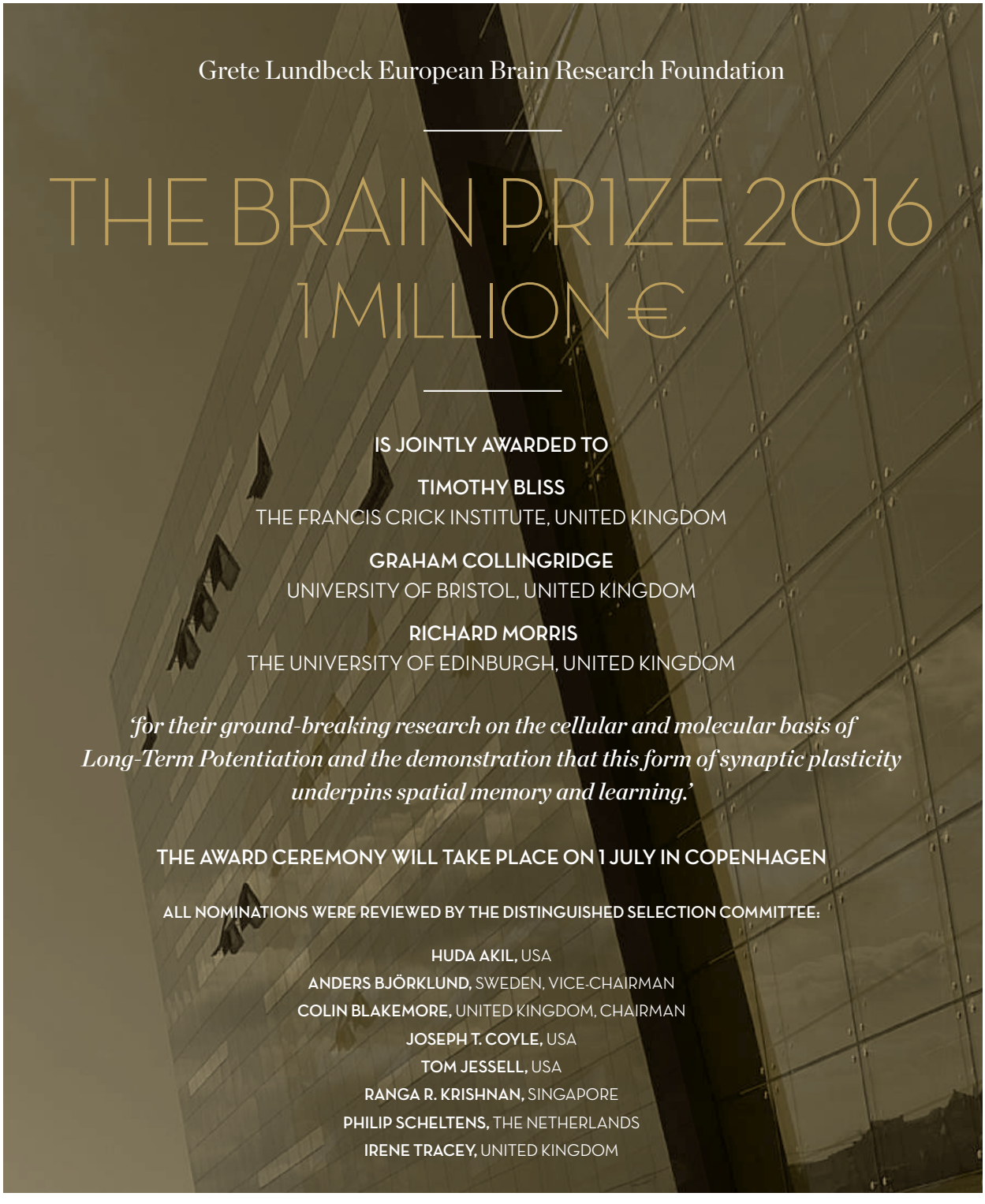

Grete Lundbeck European Brain Research Foundation

THE BRAIN PRIZE 2016

1 MILLION €

IS JOINTLY AWARDED TO

TIMOTHY BLISS
THE FRANCIS CRICK INSTITUTE, UNITED KINGDOM

GRAHAM COLLINGRIDGE
UNIVERSITY OF BRISTOL, UNITED KINGDOM

RICHARD MORRIS
THE UNIVERSITY OF EDINBURGH, UNITED KINGDOM

'for their ground-breaking research on the cellular and molecular basis of Long-Term Potentiation and the demonstration that this form of synaptic plasticity underpins spatial memory and learning.'

THE AWARD CEREMONY WILL TAKE PLACE ON 1 JULY IN COPENHAGEN

ALL NOMINATIONS WERE REVIEWED BY THE DISTINGUISHED SELECTION COMMITTEE:

HUDA AKIL, USA
ANDERS BJÖRKLUND, SWEDEN, VICE-CHAIRMAN
COLIN BLAKEMORE, UNITED KINGDOM, CHAIRMAN
JOSEPH T. COYLE, USA
TOM JESSELL, USA
RANGA R. KRISHNAN, SINGAPORE
PHILIP SCHELTENS, THE NETHERLANDS
IRENE TRACEY, UNITED KINGDOM

GRETE LUNDBECK EUROPEAN BRAIN RESEARCH FOUNDATION

THE BRAIN PRIZE

The Brain Prize recognizes and rewards outstanding contributions to European neuroscience, from basic to clinical

BOYALIFE & Science Award in Stem Cells and Regenerative Medicine

Science Translational Medicine

Stem cells and regenerative medicine is the new frontier in life sciences. Boyalife, Science and Science Translational Medicine jointly establish a global award to recognize significant contributions in advancing basic science to clinical applications in this field.

The award is to recognize and reward scientists in the fields of stem cells and/or regenerative medicine with a focus on developing cell-based treatments for cancer, degenerative disorders, immunotherapy and stem cells transplantation.

You could be next to win this prize and to receive

★ A Grand Prize of **$25,000** and a Runner-Up Prize of **$5,000** will be awarded.

★ The Grand Prize Winning Essay will be published in Science; a brief abstract of the Runner-Up Essay will be published in Science.

The 2016 Award is now open. The award ceremony will be held in San Francisco, on 23rd June, 2016.

For more information, please visit: *http://www.sciencemag.org/prizes/boyalife*

BOYALIFE StemCell

Science AAAS

Science Translational Medicine AAAS

eppendorf & Science

PRIZE FOR NEURO BIOLOGY

2015 Winner
Shigeki Watanabe, Ph.D.
Johns Hopkins University
For research on synaptic vesicle endocytosis

Call for Entries

Application Deadline
June 15, 2016

Eppendorf & Science Prize for Neurobiology
The annual Eppendorf & Science Prize for Neurobiology is an international award which honors young scientists for their outstanding contributions to neurobiological research based on methods of molecular and cell biology. The winner and finalists are selected by a committee of independent scientists, chaired by Science's Senior Editor, Dr. Peter Stern. Researchers who are not older than 35 years are invited to apply.

You could be next to win this prize and to receive
> Prize money of US$25,000
> Publication of your work in Science
> Full support to attend the Prize Ceremony held in conjunction with the Annual Meeting of the Society for Neuroscience in the USA
> An invitation to visit Eppendorf in Hamburg, Germany

It's easy to apply!
Learn more about the Prize and its past winners at:

www.eppendorf.com/prize

eppendorf Science AAAS

AAAS® and Science® are registered trademarks of the American Association for the Advancement of Science, USA. Eppendorf® and the Eppendorf logo are registered trademarks of Eppendorf AG, Germany. U.S. Design Patents are listed on www.eppendorf.com/ip. All rights reserved, including graphics and images. Copyright © 2016 by Eppendorf AG. Kurstin Roe Photography.

AAAS Travels

TANZANIA
Wildlife & Eclipse Safari
August 23–September 3, 2016

See the Annular Solar Eclipse, September 1, 2016!

Join us on a Wildlife & Eclipse Safari in Tanzania to see the Annular Solar Eclipse. Enjoy splendid days looking for lions, leopards, elephants, rare rhinos, hippos, spectacular birds, and other wildlife in the finest wildlife parks in East Africa! $5,295 pp + air

For a detailed brochure, call (800) 252-4910
All prices are per person twin share + air

BETCHART EXPEDITIONS Inc.
17050 Montebello Rd, Cupertino, CA 95014
Email: AAASInfo@betchartexpeditions.com
www.betchartexpeditions.com

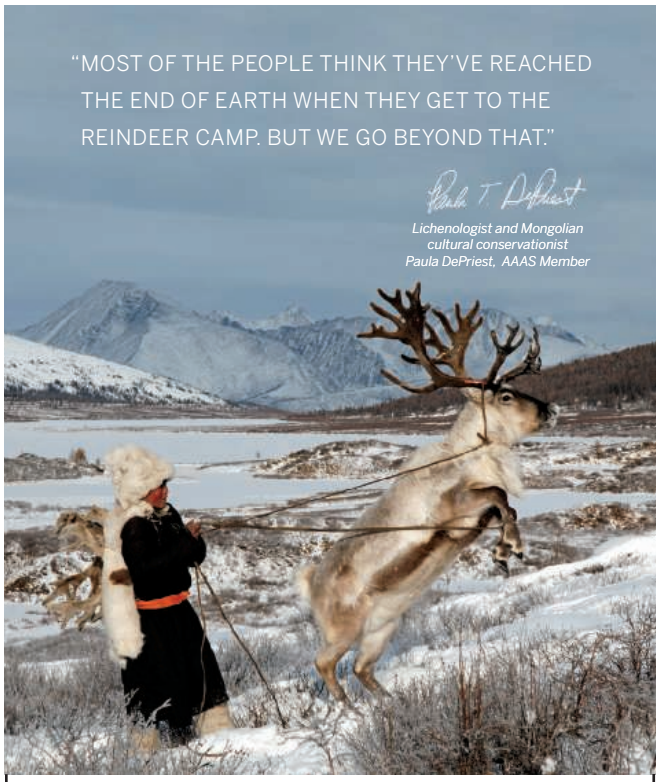

Every scientist has a *story*

Read her story at membercentral.aaas.org

AAAS MEMBERCENTRAL

HIV Cure Funding Opportunity

Gilead Sciences has spent 25 years working to improve treatments for people living with HIV, with an ultimate goal in mind: finding a cure.To that end, we've set aside fundingto support academic institutions,nonprofit organizations and communitygroups committed to HIV cure activities.

Visit www.gilead.com/HIV-Cure-FOA to learn more and apply for funding.

GILEAD

Inflammation Panels

To understand the role that inflammation plays in diseases such as cancer, heart disease, and diabetes, researchers must understand the complex interplay of many inflammatory proteins. With the Bio-Plex Pro Human Inflammation Panels, complex immune responses can be profiled in a single assay for the first time. The kits detect and quantify key inflammation biomarkers from the tumor necrosis factor (TNF), type 1 and 2 interferon (IFN), matrix metalloproteinase (MMP), and interleukin-10 (IL-10)/regulatory T cell (Treg) cytokine families. By studying up to 37 inflammatory proteins in one assay, researchers save time and money and increase sample throughput. Results can be generated in as little as three to four hours. Premixed, ready-to-use screening kits are available in 37-plex and 24-plex formats. Additionally, a Treg pathway-focused 12-plex assay kit is available. Researchers also have the added flexibility of ordering singleplex or custom kits for more focused investigations.

BioRad
For info: 800-424-6723
www.bio-rad.com/inflamassay

Stem Cell Counting Technology

Since the beginnings of mammalian tissue stem cell biology, counting has been the bane of both basic research and clinical stem cell studies. Biomarkers, such as CD34 and CD133, do not identify tissue stem cells with sufficient specificity for counting them. Asymmetrex's AlphaSTEM technology, developed with AlphaSTAR Corporation, provides precise determinations of the number, viability, and self-renewal pattern (asymmetric versus symmetric) of stem cells in complex tissue cell preparations, including both research and medical specimens. AlphaSTEM technology uses computer simulation to extract tissue stem cell properties from specially prescribed serial culture data. The AlphaSTEM tissue stem cell counting technology has many exciting applications, including determining the number of stem cells in experimental samples, determining the stem cell dose for transplantation treatments, identifying agents that can improve the vitality of transplanted tissue stem cells, and identifying agents that are toxic to tissue stem cells.

Asymmetrex
For info: 617-990-6819
www.asymmetrex.com

Transplant Genotyping Array

The Axiom Transplant Genotyping Array has been designed to improve transplantation success and individualize donor/patient selection and treatment. The array comprises ~780,000 markers, including over 30,000 variants that may contribute to transplant rejection or other complications. Researchers will also find the array useful in the study of immunology and drug treatments for disease; meta-analyses may be conducted combining data with other genotype databases such as the UK Biobank cohort, a collection of more than 500,000 volunteers genotyped using the Affymetrix UK Biobank Axiom Array. Research with this new transplant array focuses on finding transplant-related variants that will provide insight into early detection of graft-versus-host disease as well as genomic markers associated with the metabolism of immunosuppressant drugs. In addition, Affymetrix Axiom HLA Analysis software enables affordable, high-throughput, accurate analysis of 11 classical loci at four-digit resolution by imputing human leukocyte antigen (HLA) type from Axiom array-generated genotype data.

Affymetrix
For info: 888-362-2447
www.affymetrix.com

GC Column

The Zebron ZB-5MS$_{PLUS}$ is a highly inert 5% phenyl-arylene phase gas chromatography (GC) column for challenging separations. Designed with rigorous fused-silica deactivation and quality control processes, the ZB-5MS$_{PLUS}$ virtually eliminates active sites on the column's surface that can negatively affect peak shapes for challenging compounds. Most GC chromatographers are accustomed to using a 5% phenyl-arylene phase, and many work with active compounds. These researchers can switch to the new inert column for higher responses and lower detection limits without redeveloping their methods. The ZB-5MS$_{PLUS}$ produces better peak shapes without retention time shifts and ultimately increases a lab's productivity. GC chromatographers will often use a thicker-film column to compensate for active compounds' proclivity to stick to the column surface. The new deactivated column reduces the need to compensate for this activity. The ZB-5MS$_{PLUS}$ features completely redesigned packaging using both recycled and recyclable materials and is easier to open and store.

Phenomenex
For info: 310-212-0555
www.phenomenex.com

Analytical Column

The second generation CIMac r-Protein A Analytical Column is a short-bed, high-performance monolithic column primarily intended for fast, efficient, and reproducible qualitative and quantitative analyses of immunoglobulin G (IgG). It is suitable for use with high performance liquid chromatography (HPLC) and ultra-performance liquid chromatography (UPLC) systems. Quantification of IgG is possible between 0.20 µg and 20 µg. Its small volume and short column length allow operation at high volumetric flow rates (up to 3 mL/min). The information about product quantity and purity is thus generated in just 1 minute. The column has innovative symmetric design for bidirectional flow, also extending column lifetime. The CIMac r-Protein A is therefore the chromatographic tool of choice for in-process (process analytical technology) and final control of IgG purified from cell culture supernatant or human plasma.

BIA Separations
For info: +386-(0)-59-699-500
www.biaseparations.com

Electronically submit your new product description or product literature information! Go to www.sciencemag.org/about/new-products-section for more information.

Newly offered instrumentation, apparatus, and laboratory materials of interest to researchers in all disciplines in academic, industrial, and governmental organizations are featured in this space. Emphasis is given to purpose, chief characteristics, and availability of products and materials. Endorsement by *Science* or AAAS of any products or materials mentioned is not implied. Additional information may be obtained from the manufacturer or supplier.

want new technologies?

antibodies
apoptosis
biomarkers
cancer
cytometry
data
diseases
DNA
epigenetics
genomics
immunotherapies
medicine
microbiomics
microfluidics
microscopy
neuroscience
proteomics
sequencing
toxicology
transcriptomics

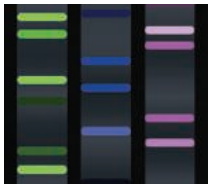

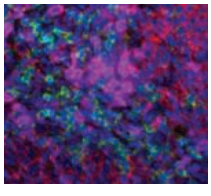

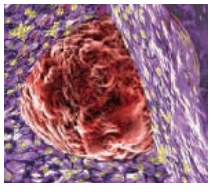

watch our webinars

Learn about the latest breakthroughs, new technologies, and ground-breaking research in a variety of fields. Our expert speakers explain their quality research to you and answer questions submitted by live viewers.

VIEW NOW!
webinar.sciencemag.org

Science
AAAS

Brought to you by the *Science*/AAAS Custom Publishing Office

@SciMagWebinars

Are your exosomes telling you everything they know?

Extracellular vesicles like exosomes can provide useful insights into cellular physiology and are a great source of circulating biomarkers. But are you getting all the information you can from them?

Let the experts at System Biosciences (SBI) help with our start-to-finish exosome profiling services:

Exo-NGS • Proteomics • Nanosight • Lipidomics

Just send us your samples, we'll take care of the rest. Order individual services or bundle and save.

Learn more at systembio.com/biomarker-discovery

SBI System Biosciences
Harnessing innovation to drive discoveries

Science Careers Advertising

For full advertising details, go to ScienceCareers.org and click For Employers, or call one of our representatives.

Tracy Holmes
Worldwide Associate Director
Science Careers
Phone: +44 (0) 1223 326525

THE AMERICAS

E-mail: advertise@sciencecareers.org
Fax: +1 (202) 289 6742

Tina Burks
Phone: +1 (202) 326 6577

Nancy Toema
Phone: +1 (202) 326 6578

Online Job Posting Questions
Phone: +1 (202) 312 6375

EUROPE / INDIA / AUSTRALIA / NEW ZEALAND / REST OF WORLD

E-mail: ads@science-int.co.uk
Fax: +44 (0) 1223 326532

Sarah Lelarge
Phone: +44 (0) 1223 326527

Kelly Grace
Phone: +44 (0) 1223 326528

Online Job Posting Questions
Phone: +44 (0) 1223 326528

JAPAN

Katsuyoshi Fukamizu (Tokyo)
E-mail: kfukamizu@aaas.org
Phone: +81 3 3219 5777

Hiroyuki Mashiki (Kyoto)
E-mail: hmashiki@aaas.org
Phone: +81 75 823 1109

CHINA / KOREA / SINGAPORE / TAIWAN / THAILAND

Ruolei Wu
E-mail: rwu@aaas.org
Phone: +86 186 0082 9345

All ads submitted for publication must comply with applicable U.S. and non-U.S. laws. *Science* reserves the right to refuse any advertisement at its sole discretion for any reason, including without limitation for offensive language or inappropriate content, and all advertising is subject to publisher approval. *Science* encourages our readers to alert us to any ads that they feel may be discriminatory or offensive.

ScienceCareers
FROM THE JOURNAL SCIENCE AAAS

ScienceCcareers.org

POSITIONS OPEN

Lecturer with Potential Security of Employment - Biological Sciences

The Department of Ecology, Evolution, and Marine Biology and the Department of Molecular, Cellular, and Developmental Biology at the University of California Santa Barbara jointly invite applications for a position of Lecturer with Potential Security of Employment (PSOE). The successful candidate will assume responsibility for courses in Introductory Biology for majors and non-majors, and a course in the candidate's area of expertise. Courses will cover topics in biochemistry, cell biology, development, genetics, animal and plant physiology, ecology and evolution. Applicants should have a record of teaching excellence with experience and expertise in the appropriate disciplines. The appointment is for the academic year with the option of additional summer quarter teaching. Salary will be commensurate with qualifications. This position requires a Ph.D. in biology or a closely related field at the time of appointment.

Applicants should submit a Curriculum Vitae, a statement of their teaching experience and interests, a statement of teaching philosophy, teaching evaluations (if available), and three to four letters of recommendation from persons with the ability to evaluate the candidate. Submit applications electronically at website: **https://recruit.ap.ucsb.edu/apply/JPF00687.** Information about the Departments can be obtained from the website **http://www.lifesci.ucsb.edu**. The review of applications will begin **March 25, 2016** and will continue until the position is filled.

The University of California is an Affirmative Action/Equal Opportunity/Americans with Disabilities Act Employer. The Departments are especially interested in candidates who can contribute to the diversity and excellence of the academic community through teaching, service and research. All qualified applicants will receive consideration for employment without regard to race, color, religion, sex, sexual orientation, gender identity, national origin, disability status, protected veteran status, or any other characteristic protected by law.

AAAS is here –
helping scientists achieve career sucess.

Every month, over 400,000 students and scientists visit ScienceCareers.org in search of the information, advice, and opportunities they need to take the next step in their careers.

A complete career resource, free to the public, *Science* Careers offers hundreds of career development articles, webinars and downloadable booklets filled with practical advice, a community forum providing answers to career questions, and thousands of job listings in academia, government, and industry. As a AAAS member, your dues help AAAS make this service available to the scientific community. If you're not a member, join us. Together we can make a difference.

To learn more, visit
aaas.org/plusyou/sciencecareers

AAAS + U = Δ

Join the Conversation!

Twitter is a great way to connect with AAAS members and staff about the issues that matter to you most. Be a part of the discussion while staying up-to-date on the latest news and information about your personal member benefits.

Follow us @AAASmember and join the conversation with #AAAS

AAAS MEMBERCENTRAL
MemberCentral.aaas.org

Do you want to make a difference?

Apply for a position at Karolinska Institutet – a medical university in Stockholm, Sweden

Faculty funded career positions in Medical Sciences
Karolinska Institutet seeks talented researchers with outstanding scientific merits and future potential:

- Up to 6 positions as Senior Researcher in Medical Science
- Up to 8 positions as Assistant Professor in Medical Science

Want to study at doctoral (PhD) level?

- 8 doctoral positions are now available

Apply now at ki.se/job
Closing date: 22 March 2016

Karolinska Institutet

ROTHAMSTED RESEARCH

Rothamsted Research Strategic Research Opportunities

Rothamsted Research (www.rothamsted.ac.uk) is at an exciting phase of its tremendous history of advancing scientific knowledge and providing solutions with global impact for agriculture. Our purpose is to transform agriculture through integrated cutting edge-science that will deliver knowledge and accelerate innovation for the sustainable intensification of agricultural systems. We focus on arable and grassland-livestock systems, nationally and internationally.

We are currently recruiting for eight outstanding, highly motivated, strategic thinkers who have high potential to be or already are established research group leaders to fill the following positions:

- **Genome Engineering Specialist**
- **Molecular Crop Physiologist**
- **Quantitative Statistical Genomicist**
- **Computational Systems Biologist**
- **Systems Agronomist**
- **Grazing Livestock Systems Specialist**
- **Nutrient Management Specialist**
- **Agro-Eco Informatician**

A highly competitive benefits package and start-up funds covering staff and basic research costs (flexible in specific allocations) will be available for the successful candidates.

More detailed information on these positions and how to register your interest can be found at:

www.rothamsted.ac.uk/careers

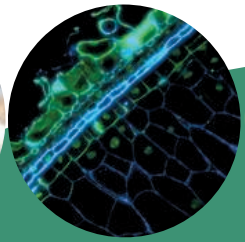

POSITIVE ABOUT DISABLED PEOPLE

Athena SWAN Bronze Award

The closing date for receipt of applications is **31 March 2016**

Auburn University
School of Fisheries, Aquaculture and Aquatic Sciences

The School of Fisheries, Aquaculture and Aquatic Sciences (sfaas.auburn.edu) at Auburn University (www.auburn.edu) seeks two scientists. The expected start date for both positions is August 16, 2016. Review of applications will begin on **April 1, 2016** and continue until the positions are filled. Only complete applications will be considered.

Reproductive Biologist – We seek a scientist with expertise in applied reproductive biology of aquatic animals. The successful candidate will teach a course in hatchery management and develop an externally funded research program related to the reproduction of aquatic animals of interest to aquaculturists, fishery managers, and conservation biologists. The position is tenure track at the level of assistant professor. A Ph.D. from an accredited institution in Animal Science, Aquaculture, Biology, Endocrinology, Fisheries, Physiology or related discipline is required. Postdoctoral experience and a publication record in applied reproductive biology of aquatic animals are also required. Experience in the reproduction of a range of aquatic animals, the potential to attract external funding to support research, and the degree to which the applicant's research interests complement those of the School faculty will be considered. Salary is negotiable and start-up funds are available. Questions about the position and application process may be directed to **Dr. Eric Peatman (peatmer@auburn.edu)**.

Extension Specialist/Aquaculture – We seek an individual to conduct extension (50%) and research (50%) activities in support of the catfish industry in West Alabama. The successful candidate will be assigned to the Alabama Fish Farming Center in Greensboro, AL and develop extension and on-farm research programs both independently and in collaboration with researchers in Auburn. An M.S. or Ph.D. from an accredited institution in Animal Science, Aquaculture, Biology, Fisheries or closely related discipline is required. For candidates with an M.S. degree, a Ph.D. from an accredited institution in Animal Science, Aquaculture, Biology, Fisheries or closely related discipline must be completed within 8 years. A publication record (ideally, in both research and extension) in warm water aquaculture is required. Experience in the catfish industry, fish nutrition, and fish health will also be considered. Salary is negotiable and start-up funds are available. Questions about the position and application process may be directed to **Dr. Allen Davis (davisda@auburn.edu)**.

To apply for the **Extension Specialist position**, go to **http://aufacultypositions.peopleadmin.com/postings/1472**. To apply for the **Reproductive Biologist** position, go to **http://aufacultypositions.peopleadmin.com/postings/1471**. For either position, submit a cover letter addressing the candidate's experience pertinent to the responsibilities of the position, (2) current curriculum vitae, (3) unofficial copies of academic transcripts, and(4) reprints of up to three articles. When prompted, please provide the names, phone numbers, and email addresses of five people who have agreed to serve as references.

Auburn University is an EEO/Vet/Disability Employer.

SCHOOL OF SCIENCE
THE UNIVERSITY OF TOKYO

Open Position for Full Professor in the Department of Chemistry, Graduate School of Science at The University of Tokyo

The Department of Chemistry in the Graduate School of Science at The University of Tokyo invites candidates for a tenured full professor position starting January 1, 2017 or thereafter. Candidates must have a Ph.D. in chemistry or a related field. Candidates with research and teaching interests in chemical biology or photon science will be considered. We particularly, but not exclusively, encourage applications from highly qualified non-Japanese researchers. The successful candidate is expected to teach at both the undergraduate and graduate levels, develop a research group, supervise students, and be involved in service to The University of Tokyo.

Job Title: Full Professor (Tenured)

Specialized Field: Chemical Biology or Photon Science

Work location: Tokyo, JAPAN

Qualifications: Excellent research expertise in chemical biology or photon science; outstanding research achievements; strong motivation for conducting research, supervising undergraduate and graduate students, and teaching at both the undergraduate and graduate levels; a Ph.D. in chemistry or a related field.

Position Start Date: January 1, 2017 or later

Application Materials: (1) Cover letter, (2) Curriculum vitae (with a face picture), (3) List of publications, invited talks, research grants, and teaching experience, (4) Copies of 10 representative publications, (5) Description of previous research achievements and their scientific significance (letter size, two pages maximum), (6) Description of future research plans (letter size, two pages maximum), (7) Two letters of recommendation

Application Deadline: April 30, 2016

How to Submit: Combine all the application materials into a single PDF and send it to Department Chair & Professor Hiroshi Nishihara (chemistry07@chem.s.u-tokyo.ac.jp) by the application deadline.

Further Information (Inquiries about the Position):

(Chemical Biology)
Prof. Hiroaki Suga, Vice Chair of Search Committee
Bioorganic Chemistry Laboratory
E-mail: hsuga@chem.s.u-tokyo.ac.jp
TEL: +81-3-5841-8372

(Photon Science)
Prof. Kaoru Yamanouchi, Vice Chair of Search Committee
Quantum Chemistry Laboratory
E-mail: kaoru@chem.s.u-tokyo.ac.jp
TEL: +81-3-5841-4334

Advance your career with expert advice from *Science* Careers.

Download Free Career Advice Booklets!
ScienceCareers.org/booklets

Featured Topics:
- Networking
- Industry or Academia
- Job Searching
- Non-Bench Careers
- And More

ScienceCareers
FROM THE JOURNAL SCIENCE AAAS

Career Feature:
Cancer Research
Issue date: April 8
Reserve space by March 22 *

There's only one *Science*.

Why choose this feature for your advertisement?

- Relevant ads lead off the career section with a special cancer research banner
- Bonus distributions:
  American Association for Cancer Research, April 16–20, New Orleans, LA
  AACR Career Fair, April 16, New Orleans, LA.

*Ads accepted until April 1 if space allows.
Produced by the until *Science*/AAAS Custom Publishing Office.

SCIENCECAREERS.ORG

ScienceCareers
FROM THE JOURNAL SCIENCE AAAS

To book your ad:
advertise@sciencecareers.org

The Americas
202 326 6582

Japan
+81 3 3219 5777

Europe/RoW
+44 (0) 1223 326500

China/Korea/Singapore/Taiwan
+86 186 0082 9345

University of Zurich[UZH]

Faculty of Science

The Faculty of Science at the University of Zurich invites applications for a

Professor of Biophysics

in order to join our team of experts at the Department of Physics.

We seek innovative applicants with a strong record in research and teaching, who will strengthen our expertise in biophysics.

The successful applicant is expected to develop a complementary and independent research program in biophysics. Your research is based on experiments and the quantitative analysis of living systems. Ideally, your field of interest is closely linked to other research (c.f. physics, biology, medicine) at our University and open up collaborations with these research groups. Contributing to the existing undergraduate and graduate teaching efforts (in English or German) in physics will also constitute an integral part of the position.

The successful applicant must have a background in physics and will be located at the University of Zurich. You are further expected to acquire external funding. The position is advertised at the level of tenure-track assistant or associate professor, but applications of more senior applicants are also welcome.

The University of Zurich provides generous research support, including dedicated funds for personnel and running expenses, and competitive start-up packages. Zurich's scientific environment includes a rich spectrum of research activities in physics and biology, and provides extensive opportunities for collaborations with research groups at the Faculty of Science of the University of Zurich, as well as teams at the nearby ETH Zurich. The University of Zurich and the city of Zurich also offer a stimulating cultural environment and are family-friendly.

Application packages should include a one-page summary; motivation letter; a full curriculum vitae; a vision statement of research and teaching interests outlining major unsolved problems and how they could be tackled; and the names and addresses of three potential referees (see http://www.mnf.uzh.ch/PBPt for guidelines). Documents should be addressed to Prof. Dr. Bernhard Schmid, Dean of the Faculty of Science, University of Zurich, and uploaded as a single PDF file to http://www.mnf.uzh.ch/PBP by April 15, 2016. For further information, please contact Prof. Dr. Andreas Schilling at schilling@physik.uzh.ch.

The University of Zurich is an equal opportunities employer.

ScienceCareers online @sciencecareers.org

TEXAS TECH UNIVERSITY
HEALTH SCIENCES CENTER
School of Medicine

Tenure-Track Faculty Positions

The Department of Cell Biology and Biochemistry at the Texas Tech University Health Sciences Center in Lubbock, TX invites applications for three tenure-track positions at the Assistant, Associate, or Professor level in any area of Biochemistry, Cellular, or Molecular Biology. The department (http://www.ttuhsc.edu/SOM/cbb/) currently has fourteen full-time faculty members and seeks accomplished scientists to complement existing research programs in cancer, reproductive biology, diabetes, membrane protein structure and function, development, and neurodegenerative diseases. Appointments will be in the School of Medicine and the Graduate School of Biomedical Sciences and come with a highly competitive start-up package and state-supported salary. Qualified candidates at the Professor level may be eligible for an endowed chair in Cancer Biology. Applicants should have a Ph.D., and/or M.D. degree, and will be expected to participate in the research and teaching missions of the department. Applicants with funded programs or strong evidence of funding potential will be given the strongest consideration. The Department of Cell Biology and Biochemistry is committed to diversity in education and employment, and strongly encourages applications from women and minorities.

Interested candidates must apply online (job **6733BR**, **6734BR**, or **6737BR**) at **http://www.ttuhsc.edu/som/cbb/positions.aspx**. Candidates should submit a single document in PDF format containing a cover letter describing their interest in the department (including possible collaborations with current faculty), a curriculum vitae, and a brief summary of their research interests. Candidates should also arrange to have three letters of recommendation sent in electronic format to cellbiology.biochemistry@ttuhsc.edu. Review of applications will continue until the positions are filled.

The TTUHSC is an Equal Opportunity /Affirmative Action/Veterans/ Disabilities Employer.

Marine Biological Laboratory

Senior Scientist, Marine Biology

Position Summary: The position of Senior Scientist in Marine Invertebrate Biology will play a key role at the Marine Biological Laboratory to develop new strategic programs in marine biology, with a focus on the development of novel model organisms to inform our understanding of topics such as neuroscience, regeneration, development, and response to environmental change.

Additional Information: The incumbent will develop an extramurally funded research program in a relevant area of marine biology, genomics, and neuroscience, while also leading program development in areas of strategic importance to the MBL, including informing research relevant to human health. To do so, the incumbent will be expected to collaborate broadly with scientists and students who come to the MBL and in particular to the Marine Resources Center, developing new programs and resources that contribute to the MBL's convening power.

Basic Qualifications: Qualified candidates will possess a PhD in a relevant area of Biology, with suitable postdoctoral experience in fields such as Physiology, Molecular Genetics, or Neurobiology. Candidates will also have at least 10 years of experience developing externally funded research programs, including experience at program leadership. Qualified applicants should have demonstrated expertise in marine organisms research. Candidates should have demonstrated commitment to studies at the nexus of marine biology, genetics/genomics, and ecological and environmental dynamics.

APPLY ONLINE: https://mbl.simplehire.com

The Marine Biological Laboratory is an Affirmative Action/Equal Opportunity/Disabled/Veterans Employer.

Science | AAAS

Associate Editor for *Science*

Join the editorial team at *Science*! We are seeking a full time Associate Editor to work either in our Washington, DC, USA or Cambridge, UK office.

We are looking for a scientist who is outgoing with broad interests, a lively curiosity, and experience with cutting-edge research in biomedicine. We would prefer a candidate with a background in genomics and in preclinical or translational research with knowledge of models of disease and gene- and cell-based therapies.

Candidates are expected to travel internationally to scientific meetings and institutions, and to interact extensively with the scientific community in order to encourage excellent manuscripts to come to *Science*. Responsibilities include managing the selection, review, and editing of research manuscripts; working with authors on revisions; soliciting review articles and special issues; and fostering contacts and communication with the scientific community.

A Ph.D. in a scientific discipline, postdoctoral experience and multiple publications are required, as is the ability to work constructively as a member of a team. Previous editing experience is a plus. Evidence of an aptitude and passion for the communication of science is essential.

Science is published by the AAAS, the world's largest general scientific membership organization.

For consideration, please apply using the link below, or send a cover letter and resume, along with your salary requirements, to **jobs@aaas.org**.

http://jobs.sciencecareers.org/job/398220/associate-editor-for-science/

AAAS is an Equal Opportunity Employer.

Download the *Science* Careers jobs app from Science

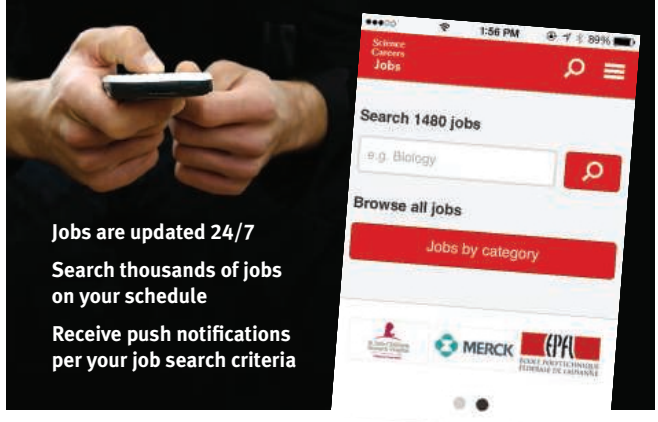

Jobs are updated 24/7

Search thousands of jobs on your schedule

Receive push notifications per your job search criteria

Get a job on the go.

Search worldwide for thousands of scientific jobs in academia, industry, and government. The application process is seamless, linking you directly to job postings from your customized push notifications.

Scan this code to download app or visit **apps.sciencemag.org** for information.

ScienceCareers | AAAS
FROM THE JOURNAL SCIENCE

ScienceCareers.org

Cold Spring Harbor Laboratory

Director - Banbury Center at Cold Spring Harbor Laboratory

The Banbury Center at Cold Spring Harbor Laboratory (CSHL) is recognized worldwide as a unique venue for discussion meetings on topics in the biomedical sciences. Participation is restricted to 20 to 30 invited scientists at the leading edge of research in molecular biology and genetics, human genetics, genomics, neuroscience and mental health. The scope of the Center extends to meetings on bioscience policy and global health. The Banbury Center also hosts a series of workshops and discussion courses currently part of the Laboratory's Meetings & Courses program. Since the first conference in 1978, Banbury has held over 650 meetings with some 13,000 participants drawn from over 40 countries.

We are seeking a highly motivated, versatile individual whose primary responsibility will be to develop the Banbury Center program of conferences by identifying topics of scientific and clinical importance, working with organizers in developing the agenda for each meeting, overseeing the selection of conference participants, and addressing any strategic issues that may arise. The position also includes developing and achieving budget targets for each meeting, and securing funding for meetings through corporate sponsorship, foundation and federal grants.

The successful candidate will also be responsible for managing the Banbury Center staff and for liaising with other departments which interface with the Banbury program. The Center is an integral part of Cold Spring Harbor Laboratory and the director interacts extensively with other senior staff, most notably the CSHL President and the Executive Director of the Meetings and Courses Program, to whom the current position will report.

An applicant must have a PhD or M.D. in the biological or biomedical sciences and a minimum of ten years postdoctoral experience. Essential qualifications include wide-ranging interests across the biomedical sciences; a willingness to learn new fields; excellent writing skills and the ability to work independently. Scientists who have left research to work, for example, in editorial positions at major scientific journals or in foundations are invited to apply.

Further information about the Banbury Center and Cold Spring Harbor Laboratory will be found at https://www.cshl.edu/banbury and at https://www.cshl.edu
Please send your CV and the names of three references to: **stewart@cshl.edu**

Dr. David J. Stewart
Executive Director
Meetings & Courses Program
Cold Spring Harbor Laboratory
One Bungtown Road
Cold Spring Harbor, NY 11724

Applicants are also required to apply via the CSHL website at: **https://www.cshl.edu/careers**. Position number **00267-E**

Cold Spring Harbor Laboratory is a world-renowned research and educational institution recognized internationally for its excellence in ground-breaking research programs in cancer, neuroscience, plant biology, genomics, and bioinformatics and broad educational mission.

CSHL is an EO/AA Employer. All qualified applicants will receive consideration for employment and will not be discriminated against on the basis of race, color, religion, sex, sexual orientation, gender identity, national origin, age, disability or protected veteran status. VEVRAA Federal Contractor

Los Alamos NATIONAL LABORATORY EST.1943

Los Alamos National Laboratory (LANL), a multidisciplinary research institution engaged in science on behalf of national security, has an opportunity available in their Theory, Simulation & Computation Directorate.

THEORETICAL DEPUTY DIVISION LEADER (Job IRC48593)

The Theoretical (T) Division at Los Alamos National Laboratory has a storied history of discovery and mission impact dating back to the Manhattan Project and today is focused on advancing the frontiers of theoretical science across a broad range of disciplines. T Division is a 250-person organization with an annual budget greater than $100 M. The Deputy Division Leader assists in leading, managing, setting strategic direction, and cultivating the careers of the Division's workforce.

The successful candidate will have an outstanding record of scientific research or programmatic accomplishment in an area of Theoretical Division-relevant research as evidenced by publications, citations, presentations, grants or programmatic support, and/or leadership of large technical projects. A Ph.D. in physics, materials science, chemistry, life sciences, applied mathematics, or a related discipline, or an equivalent combination of education and experience in related areas that are relevant to the mission of the Division, is required.

To apply and learn more about this position and others, please visit careers.lanl.gov - Job IRC48593 (R&D Manager 5). For full consideration, submit your application materials by April 10, 2016.

EOE

DUKE NUS GRADUATE MEDICAL SCHOOL SINGAPORE

Faculty Position for Research Director of the Animal BSL3 Facility at Duke-NUS

(Assistant/Associate Professor Level)

The Duke-NUS Medical School (Duke-NUS) is unique in bringing post-baccalaureate, research-intensive medical education to Asia. It represents a truly global partnership between two leading universities: National University of Singapore and Duke University, North Carolina, USA. The Programme in Emerging Infectious Diseases (EID) led by Professor Linfa Wang is one of the five signature research programmes of Duke-NUS Medical School, and has a strong core of researchers conducting cutting-edge infectious diseases research that will enhance healthcare in Singapore and the region. Areas of current focus for the programme include dengue, influenza, hepatitis and zoonotic diseases (see **www.duke-nus.edu.sg**).

The EID Programme is recruiting a new faculty member to lead research in the recently opened Animal Biosafety Level 3 (ABSL3) facility. We are seeking a candidate with PhD, MD or DVM qualification, a strong track record in infectious disease research and proven research experience in an ABSL3 facility. Past experience with BSL3 animal infection studies will be desirable. The successful candidate is expected to spend 70% time leading his or her own research projects and 30% directing and facilitating the overall science projects conducted within the ABSL3 facility.

Depending on track record and past work experience, the candidate is invited to apply for a position at Assistant/Associate Professor Level with either research- or tenure-track options.

The package for the faculty recruit will include full salary as well as start-up funding to ensure smooth start of research. The successful candidate is expected to apply for competitive grants to sustain his or her research in the long term.

For further information, please contact the search committee co-chairs:

- Dr. Eng Eong Ooi (**engeong.ooi@duke-nus.edu.sg**)
- Dr. Viji Vijayan (**viji.vijayan@duke-nus.edu.sg**)

Interested candidates should send a full application with CV and the names of three referees to the EID, Duke-NUS Medical School by email to: **eid.contact@duke-nus.edu.sg** by **31st March, 2016**.

By **Rachel Bernstein**

The water watchdog

Water treatment and corrosion expert Marc Edwards made headlines recently for his work to uncover and address the elevated lead levels in drinking water in Flint, Michigan. Edwards says he originally chose to become an environmental engineer because it "sounded like a great, altruistic career." Altruism has led the professor at Virginia Polytechnic Institute and State University in Blacksburg to some risky professional decisions. He has taken on the U.S. Centers for Disease Control and Prevention and the Environmental Protection Agency for failing to intervene effectively in Flint and, a decade earlier, in Washington, D.C., when it was experiencing its own water crisis. This interview has been edited for clarity and brevity.

Q: Why did you pursue water safety research?
A: What gives me joy is creating new knowledge, especially knowledge that helps normal people. I've always gravitated toward the work that had the biggest real-world impacts and was being overlooked. My research on building plumbing systems has profound health and economic implications, but no one wanted to take responsibility for the issue.

Q: When you've discovered problems, how have you gotten them addressed?
A: Science by itself is powerless when you're dealing with government agencies. I had to cross the line and become an activist, filing Freedom of Information Act requests and working with politicians and people on the ground. You have to reach this critical mass where you can put enough pressure on these agencies to make them take action, and you will never do that with science alone.

If you're not going to fight to the bitter end, don't get started. You have to decide: Are you willing to do whatever it takes to see this through, and can you accept the likelihood that you are going to fail? The odds are against you. I'm one of the lucky ones. It makes me feel so humble to think about all of those who put their professional lives on the line and whose careers were destroyed.

Q: How do your colleagues view your activism?
A: I engage in activism as a last resort, after every scientific path has failed. Since I personally find activism distasteful, I forgive the academics who also view it negatively. The majority of my colleagues are indifferent or bemused, focused on their own problems and getting their next research dollar.

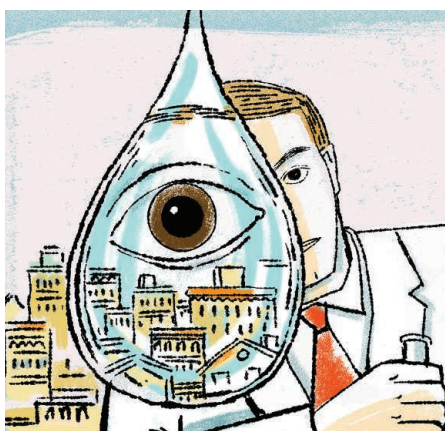

"It's about seeing something that's wrong and being unwilling to accept it."

Q: How does the current academic culture affect research like yours?
A: We have to address the pressures to publish and get funding so that we can ask ourselves whether our research is doing good for the world. I'm very fearful of the perverse incentives of academia right now. We spend all our time sucking up to funding agencies. We're all such cowards—and with good reason, because the system does not reward good heroic actors. At the same time, because cowardice is the norm, it creates a tremendous opportunity for those who want to go this path, because no one else is doing it and there is so much injustice.

We are still attracting some great people who I firmly believe are ethical, altruistic scientists, but at some point they might become the minority. My biggest fear is that the culture of academia is going to get to the point where these scientists ask, "Can I have a career without cutting corners or cheating?" I don't want us to get to the point where I might have to tell young people, "I'm not sure that you can."

Q: What motivates you to carry on despite the challenges?
A: I am the most optimistic person in the world. You have to be optimistic to think that you can change things. It's not blind optimism; it's about seeing something that's wrong and being unwilling to accept it. You have to say, "I'm going to fight to make this world a better place." And you have to make sure that the world doesn't change you. It's only the people that the world doesn't change who are going to change the world. ■

Rachel Bernstein is the editor of Science *Careers. Send your story to SciCareerEditor@aaas.org.*

ILLUSTRATION: ROBERT NEUBECKER

Downloaded from on March 10, 2016

Published by AAAS